Real-time mass spectrometric monitoring of chemical processes

by

Isaac Obeng Omari
M.Sc., Queen's University, 2014
B.Sc., Kwame Nkrumah University of Science and Technology, 2012

A Dissertation Submitted in Partial Fulfillment
of the Requirements for the Degree of

DOCTOR OF PHILOSOPHY

in the Department of Chemistry

Supervisory Committee

Real-time mass spectrometric monitoring of chemical processes

by

Isaac Obeng Omari
M.Sc., Queen's University, 2014
B.Sc., Kwame Nkrumah University of Science and Technology, 2012

Supervisory Committee

Dr. Jason Scott McIndoe, Department of Chemistry
Supervisor

Dr. Erik Krogh, Department of Chemistry
Departmental Member

Dr. Lisa Reynolds, Department of Biochemistry and Microbiology
Outside Member

Abstract

Reactions can be monitored in real-time or off-line for qualitative and quantitative information on reaction systems under study. The work presented in this dissertation was focused on the application of reaction monitoring techniques by means of electrospray ionization mass spectrometry (ESI-MS), and ultraviolet-visible (UV-Vis) spectroscopy to solve various problems. For example, in a complex petroleum matrix, naphthenic acids were selectively derivatized using a charge-tagging technique and all the acid derivatives were identified by tandem electrospray ionization mass spectrometry (ESI-MS/MS). To understand the increased visibility of analytes profiled with charge-tagged reagents in ESI-MS, ESI response of permanently charged analytes of different sizes and structures were examined. It turned out that factors, such as the analyte structure, molecular weight and solvent could influence the signal strength of analytes. In a separate study on the effect of magnesium (Mg^{2+}) on Maillard reaction, ESI-MS was used to characterize reaction species, and it was found through UV-Vis spectroscopy that, magnesium can accelerate Maillard chemistry in a dose-dependent manner. ESI-MS was also employed to investigate hydrolysis of aryltrifluoroborates in real-time complemented by pH analysis, whereby a dynamic series of equilibria for numerous ions was determined. As well, by using ESI-MS for on-line reaction monitoring, reaction intermediates of a palladium-catalyzed cyclization reaction of carbamates, and an acid-catalyzed cyclization reaction of benzoxazine were identified.

Furthermore, to ensure uniform stirring in reactions conducted simultaneously, a 3D printed circular vial holder enabled standardized stirring conditions in ten vials; and ESI-MS revealed data reproducibility could be achieved through the standardized stirring conditions offered by the vial holder. In a nutshell, the findings given provide practical considerations, and some insights into fundamental ESI-MS science.

Table of Contents

List of Tables

List of Figures

List of Schemes

Acknowledgments

I would like to express my sincere gratitude to Professor Scott McIndoe for his continuous support, guidance, patience, and sound advice throughout the entire period of my studies.

I am grateful to Haoxuan Zhu, Parmissa Randhawa, Jaiya Randhawa, Jenny Yu, Atzin San Roman, Darlene Gitaari, Lindsey Frederiksen, Alexa Fugina, Hannah Charnock, Dr. Euan Thomson for their assistance with various parts of the data collection; and Dr. Ori Granot for his technical support. As well, thankful to Anuj Joshi for his contributions towards the attainment of this dissertation.

Lastly, my heartfelt gratitude is extended to my family for their unending love, support, and encouragement.

Dedication

To Mom and Dad

Chapter 1 Literature review and research objectives

1.1 Brief history of mass spectrometry

Mass spectrometry is a widely used analytical technique that facilitates identification and quantitation of analytes of interest according to their mass-to-charge ratios. The principle of mass spectrometry dates back to the 1900s when J.J. Thomson established that neon was comprised of two isotopes (^{20}Ne and ^{22}Ne) after separation by means of electric and magnetic fields.[1] Later, Arthur Dempster designed the first mass spectrometer in 1918 which served as a foundation for building contemporary mass spectrometers.[2] Dempster's contribution to mass spectrometry also included developing an ionization source known as electron ionization (EI).[2]

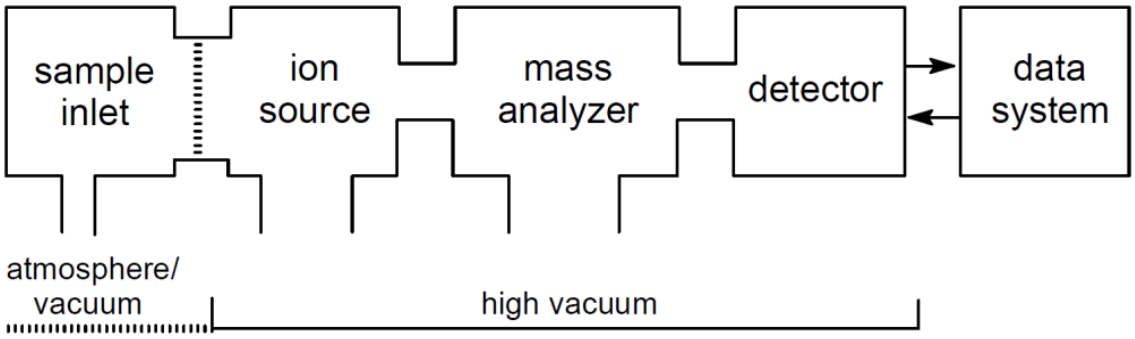

Figure 1.1. General layout of a mass spectrometer.[3]

1.2 Ionization sources

Electron impact or electron ionization (EI) gained popularity due to its ability to analyze neutral organic compounds.[2,4,5] The ionization process involves interaction of gas phase molecules with energetic electrons; the analyte ejects an electron after absorption of energy, and as a result, produces a molecular ion sufficiently energized that fragment ions promptly form. The mass spectrum obtained through this technique is interpreted by examining the fragmentation pattern of the remaining species. The intensity of the molecular ion is often low because of this fragmentation, and accordingly EI is known as a 'hard' ionization technique. To preserve molecular ions during ionization, 'soft' ionization techniques, such as chemical ionization (CI), matrix assisted laser desorption (MALDI) and electrospray ionization (ESI) were developed.

CI was developed in the mid-20th century by Munson and Field.[6,7] The ionization process is an extension of EI but in CI, the beam of energetic electrons collides first with an excess reagent gas to generate metastable protonated ions, such as $[CH_5]^+$ that (comparatively) gently interact with the neutral analyte.[3] The excess amount of reagent gas protects the analyte molecules from direct ionization by the energized electrons. The ion-neutral molecule interaction produces charged molecules through charge transfer or proton transfer. Charge transfer produces a radical ion ($M^{+\cdot}$) of minimum internal energy whereas proton transfer yields protonated $[M+H]^+$ or deprotonated $[M-H]^-$ species.[3]

Currently the most employed 'soft' ionization techniques are MALDI and ESI. MALDI was introduced by Tanaka in the late 1980s, and has since become famous in the biological community owing to its capability to analyze very large analyte molecules,

such as proteins of 200000 Da or more in mass.[8–10] It is also a popular technique for polymer studies.[11] In MALDI, an organic matrix in excess is co-crystallized with an analyte on a plate and a UV or IR laser is used to energize the matrix. Upon laser irradiation, the sample vaporizes into the gas phase and the analyte molecules interact with the matrix in the gas phase to produce charged molecular ions (Figure 1.2).

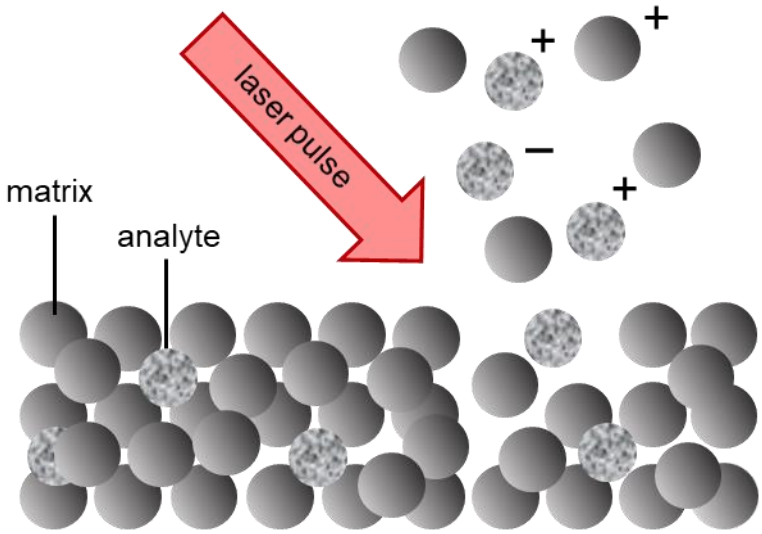

Figure 1.2. Desorption of a co-crystallized sample in matrix upon laser irradiation.

ESI was developed by Yamashita and Fenn[12] in the 1980s after its invention by Dole[9] in 1968. In electrospray ionization, a solution of analyte ions is passed through a charged capillary (2 – 5 kV) at atmospheric pressure into a chamber.[13] As the solution exits the capillary, a mist of fine droplets is emitted from a Taylor cone[14] (see Figure 1.3).

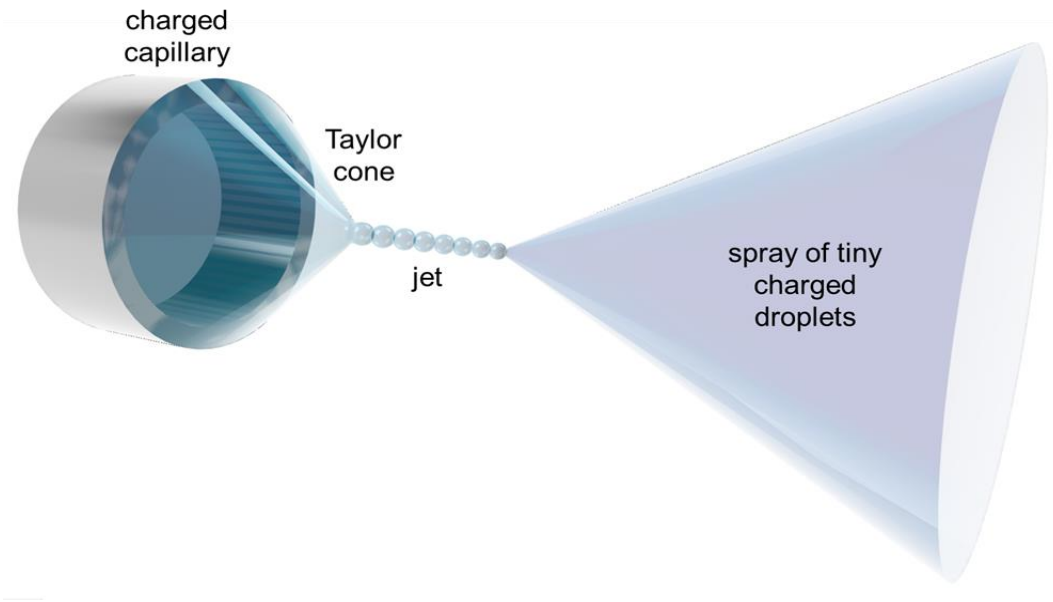

Figure 1.3. Illustration of the electrospray ionization process at a macro level (internal diameter of capillary 100 µm).

These droplets gradually shrink in a counterflow of desolvation gas (usually nitrogen) which evaporates the solvent, thus increasing the charge density. Surface active ions evaporate into the gas phase *or* the ions in the droplet repel each other as the charge increases leading to a Coulombic explosion (charge residue model (CRM)) which releases the ions (Figure 1.4).[9,15–17] Our group reported that ion evaporation was directly observable in a study on lanthanide water clusters.[18]

.

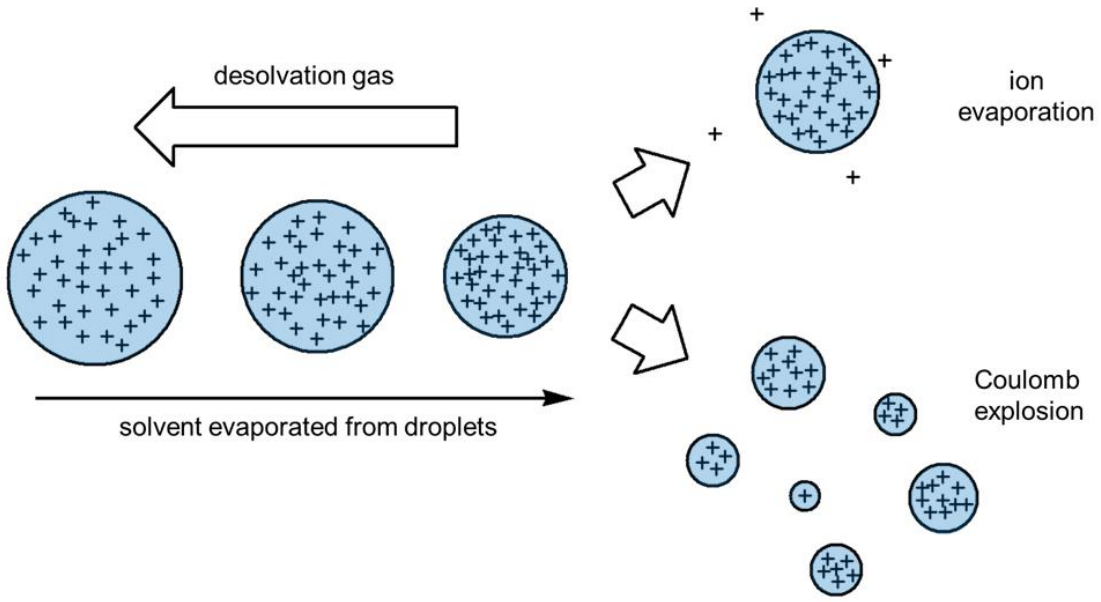

Figure 1.4. Illustration of the desolvation process in ESI through either ion evaporation or Coulomb explosion. Modified from reference 19.

It has been proposed that the ion evaporation mechanism is more appropriate for small ions (such as hydroxonium) while the Coulombic explosion (CRM) is applicable to large ions (such as proteins).[20] Nevertheless, the ions generated have little or no fragmentation.[21] Chapter 3 of this dissertation explores further on the ESI process.

ESI-MS has been used for characterizing large molecules, such as protein,[22–24] peptides[25,26] and biomolecules[27–29] given its soft ionization and its ability to identify multiply charged analytes. Also, organometallic systems have been extensively investigated, because ESI-MS is very sensitive and can preserve weak intermolecular interactions, reveal reaction intermediates; and offers fast analysis and excellent separation of different species, allowing the analysis of complex mixtures.[30–33]

Subsequent chapters of this dissertation elaborate diverse applications of this powerful technique.

1.3 Mass analyzers

After the ionization process, ions enter the mass analyzer under high to ultra-high vacuum (10^{-3}-10^{-12} mbar) for separation according to their mass-to-charge (*m/z*) ratios; and the sorted ions are then counted and registered by a detector.[3] Many mass analyzers have been developed since the invention of a mass spectrometer. Some examples are magnetic sector, time-of-flight (TOF), quadrupole, quadrupole-TOF (Q-TOF), Fourier transform ion cyclotron resonance (FT-ICR) and orbitrap.

In a magnetic sector mass spectrometer, an ion beam passes through a magnet sector whereby it is dispersed according to mass-to-charge ratios due to Lorentz force being exerted on the ions in the magnetic field.[19]

A quadrupole mass analyzer, as shown in Figure 1.5, comprises four cylindrical metal rods parallel to each other. In this analyzer, alternating DC and RF potentials are applied between a pair of the metal rods. As a result, yields a dynamic field that influences the direction of ions entering the quadrupole and the path of ions through the quadrupole. Based on the *m/z* of the ions, a stable trajectory can be achieved when a set of DC and RF potentials is appropriately chosen. In the process of a potential sweep, ions can be sorted according to their mass-to-charge ratio.[19,34] This principle of separation as well as that of the magnetic sector, laid out the foundation for the development of high-resolution mass spectrometers with Q-TOF, FT-ICR and orbitrap analyzers.[35]

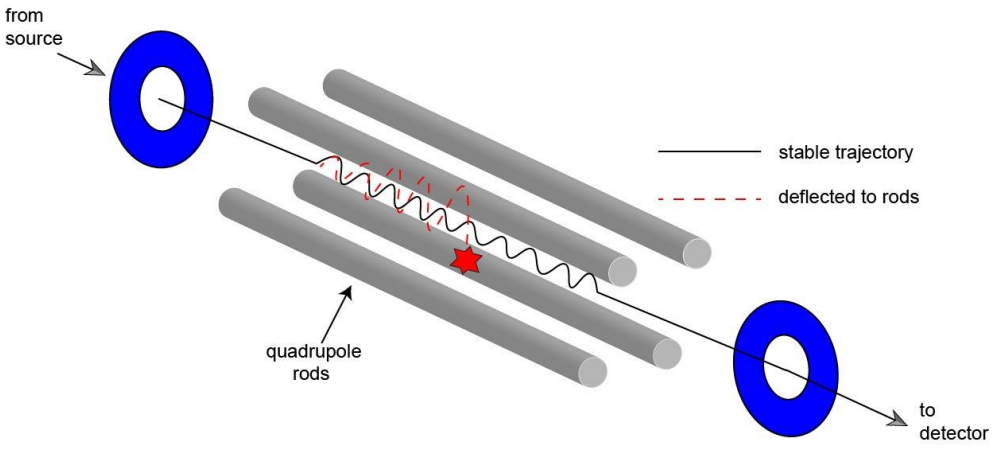

Figure 1.5. Representation of a quadrupole mass analyzer illustrating the trajectory of ions in a dynamic field.

TOF instruments were developed by W.C Wiley and I. H. McLaren in the mid-1950s.[35] A TOF mass analyzer consists of a drift tube through which accelerated pulsed ions from the ion source are separated based on their *m/z* values. The FT-ICR mass analyzer was developed by M. B. Comisarow and A. G. Marshall in 1974.[35] In FT-ICR, ions introduced into the analyzer are trapped in a magnetic field; excited by a radio frequency which produces a transient ion image signal, and upon application of a Fourier transform, a mass spectrum is generated.[3] The Orbitrap mass analyzer was developed by Makarov in the late 1990s but was available on the market in 2005.[36,37] The Orbitrap is made up of an ion trap which contains a central electrode. Ions introduced into an Orbitrap are trapped in the ion trap; they orbit around the central electrode, which generates an image current signal. After application of a Fourier transform, the *m/z* of the trapped ions can be determined from their individual oscillation frequencies.[3] FT-ICR and orbitrap

instruments are well-known for their remarkably high resolution (10^5 to 10^6) which allows accurate mass measurements.[38,39]

1.4 Tandem mass spectrometry

Tandem mass spectrometry is a technique in which two (MS/MS or MS^2) or more (MS^n) mass analyzers employ tandem in space or a mass analyzer, such as FT-ICR employs tandem in time (does not require other analyzers) for mass separation following ionization of the analyte under study.[40,41] Typical examples of instruments that employ MS^2 are Q-TOF and triple quadrupole mass spectrometers. In this dissertation, a Waters Acquity triple quadrupole detector (TQD) mass spectrometer was used for most of the research as well as a quadrupole-time of flight (Q-TOF) SYNAPT G2-Si instrument. The TQD features two mass analyzers combined in a linear fashion (with a hexapole collision cell in between) to facilitate tandem mass spectrometric experiments. A Q-TOF consists of a linear combination of quadrupole and a collision cell (usually a hexapole or an octapole) fixed orthogonally to a reflectron TOF (Figure 1.6). The quadrupole and TOF scan and sort species according to their *m/z* values whereas the collision cell plays the role of an ion guide or carries out fragmentation of ions with an inert gas and an applied collision voltage. For MS/MS experiments in a Q-TOF, a precursor ion is selected in the quadrupole (MS1), which undergoes collision induced dissociation (CID) in the collision cell, and the product ion spectrum is collected using the TOF (MS2) (Figure 1.6).

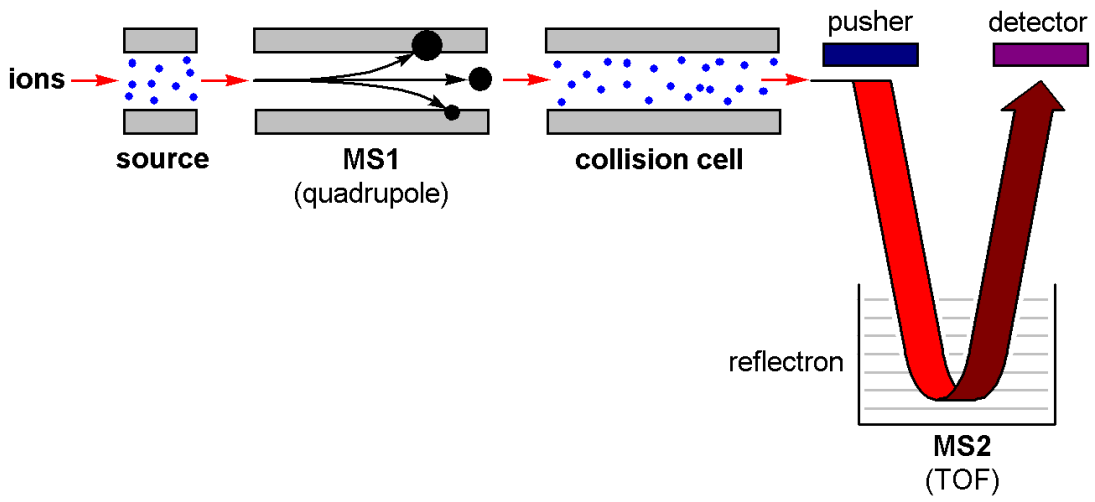

Figure 1.6. Illustration of an MS/MS in a quadrupole/time-of-flight (Q-TOF) mass spectrometer. Modified from reference 19.

In a TQD, the first and last quadrupole are scanning quadrupoles that allow separation of species based on their *m/z* while the second 'quadrupole' (in a form of a hexapole or octapole) serves as an ion guide or a collision cell for CID experiments. The layout of a TQD permits several types of MS/MS experiments, such as product ion scan, precursor ion scan, neutral loss scan and selected reaction monitoring (also known as multiple reaction monitoring).

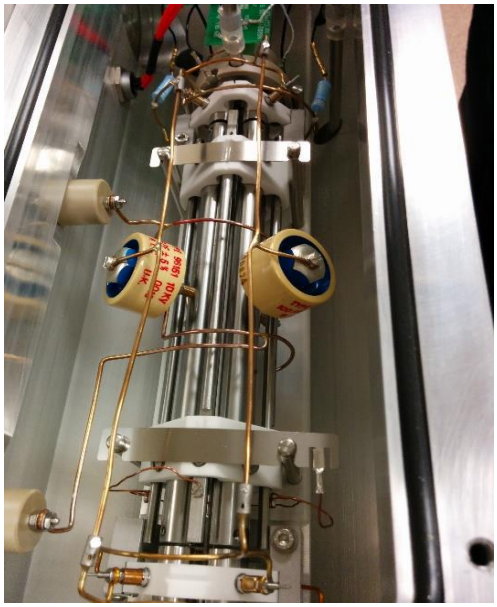

Figure 1.7. Quadrupole of a Waters Ultima triple quadrupole mass spectrometer.

The product ion scan experiment is the fundamental MS/MS experiment that provides structural information of species of interest through CID. In a product ion scan, only ions of a specific *m/z* are selected and filtered through the first mass analyzer (Q1) to the collision cell (q2) for CID in the presence of an inert gas and an applied collision voltage. The fragments produced are scanned through the last mass analyzer (Q3) to the detector (see Figure 1.8). This experiment is useful for characterizing unknown compounds by examination of the characteristic product ions formed.

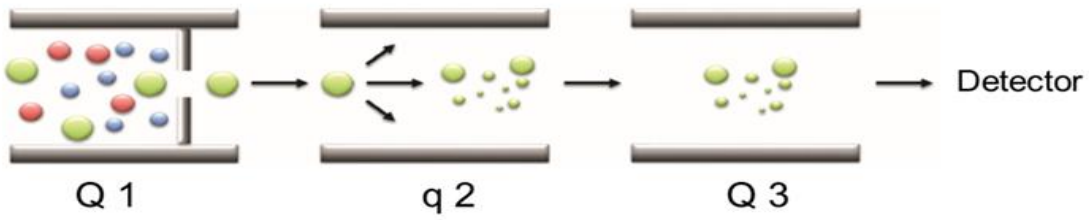

Figure 1.8. Representation of a product ion scan experiment. Modified from reference 42.

Precursor ion scan experiments can be conducted after determining a common product ion of the species of interest through product ion scan. Hence product ion scan complements precursor ion scan. In precursor ion scan, all ions are scanned in Q1, undergo CID in q2; and ions with a common product ion are selected in Q3 (Figure 1.9). Neutral loss scans reveal precursor ions with a common neutral loss (e.g. H_2O). Prior to a neutral loss scan experiment, a product ion scan is conducted to determine a common neutral loss. This implies that selected ions produce ions at a lower *m/z* consistent with the loss of a neutral moiety at an applied collision voltage. After determining the common neutral loss, the neutral loss scan experiment proceeds by scanning all ions in Q1. These scanned ions go through q2 where they undergo fragmentation; and ions with an offset of the common neutral species are scanned through Q3 to the detector.

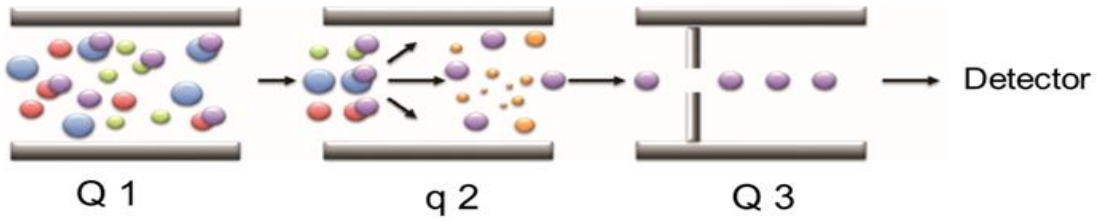

Figure 1.9. Representation of a precursor ion scan experiment. Modified from reference 42.

After determining the precursor and product ions of target species, one or more selected reaction(s) can be monitored by means of multiple reaction monitoring (MRM) using a triple quadrupole mass spectrometer. This MS/MS experiment involves selecting a precursor ion in Q1 to undergo fragmentation in q2, and the product ion of the target precursor ion is selected in Q3 for detection. MRM offers increased sensitivity considering that only selected masses of species are scanned as compared with a full MS

scan that highlights all ions being scanned. As well, increased signal-to-noise ratio can be achieved after careful optimization of both cone and collision voltages. Given these exceptional features of a triple quadrupole mass spectrometer, it has been extensively used for quantitative analytical studies.[43–46]

1.5 Characteristics of analytes suitable for ESI-MS

A major requirement for analytes in ESI-MS is that they should be charged or capable of carrying a charge due to the presence of functional groups.[12] Analytes that are inherently charged are easily favoured by the electrospray ionization process. In view of this, intrinsically-charged reaction intermediates in oxidation reactions of organometallic systems have been reported suitable for investigation by ESI-MS.[47,48] A compound can also be charged by means of protonation, deprotonation, loss of a halide or aggregation with alkali metals, such as sodium and potassium (see Figure 1.10); in addition, can be charged by installing a permanently charged species through charge-tagging (explored in Chapter 2).

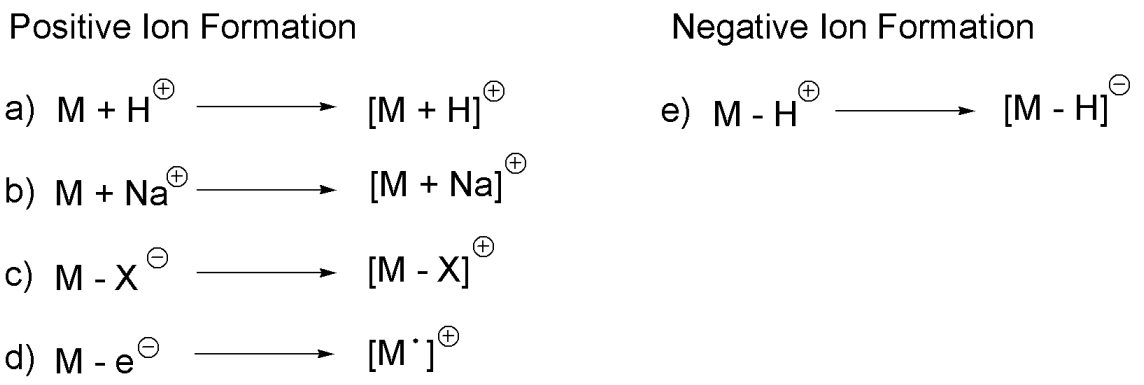

Figure 1.10. Fundamental Ionization pathways: a) basic site protonation b) association of an alkali metal to a basic site c) halide dissociation d) oxidation e) acidic site deprotonation.

Charge-tagging serves as a simple, fast derivatization technique that facilitates appearance of usually undetectable species of interest through ESI-MS. This technique mimics bioconjugation reactions by which a reactive functional group on a derivatizing agent couples to the functional group of specific macromolecules.[49]

Production of gas-phase ions in ESI-MS is contingent on ionization efficiency of ions of interest; hence, employing a charge-tagging technique is beneficial for increasing the ionization efficiency of target analytes.[19] In relation to this concept, charge-tagged reagents are designed to have a high surface activity. As well, these tags are paired with weakly coordinating anions to minimize ion-pairing and promote detection of species through ESI-MS. The charge-tagging technique has served as a useful tool for studying neutral reaction intermediates via ESI-MS.[50–52] Other applications are discussed in Chapter 2.

1.6 Reaction monitoring with ESI-MS

Reactions can be monitored off-line or on-line in ESI-MS as desired by experimentalists. Off-line reaction monitoring is predominantly used for time-dependent reactions by diluting a sample aliquot at various stages during a reaction and transferring it into a mass spectrometer for analyte characterization. Other analytical techniques, such as UV-Vis spectroscopy, IR spectroscopy and NMR also work efficiently with off-line reaction monitoring. Although this conventional approach for studying reactions in ESI-MS is widely used, a major drawback is its inability to reveal transient or unstable reaction intermediates in that sampling is not conducted continuously. Also, data precision could be affected when samples must undergo dilution prior to analysis, and decomposition can be problematic. These challenges can be resolved when reaction systems are probed on-line for real-time data. In on-line reaction monitoring, species in a reaction could be continuously tracked as they evolve over time (Figure 1.11).

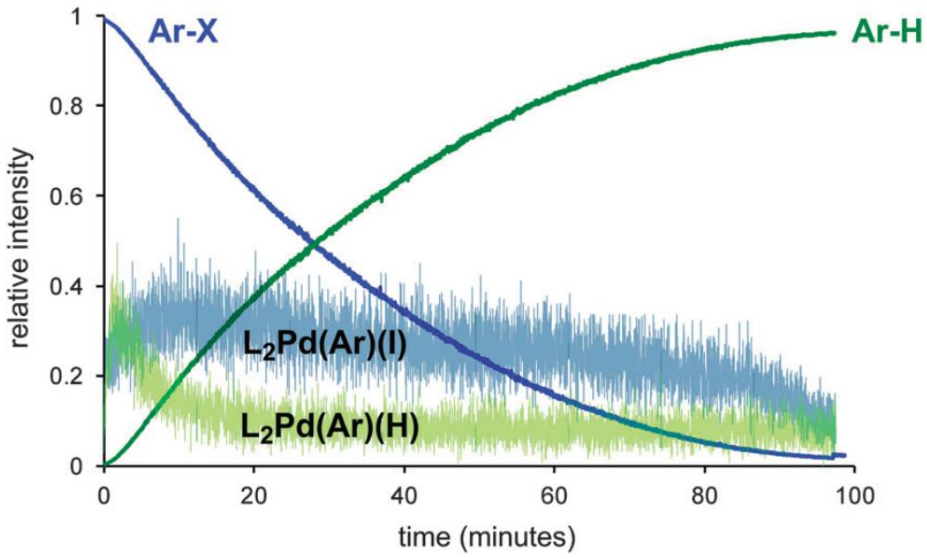

Figure 1.11. Illustration of reaction monitoring with ESI-MS for the investigation of hydrodehalogenation. Reproduced with permission from "A mechanistic investigation of hydrodehalogenation using ESI-MS" Z. Ahmadi and J. S. McIndoe, *Chem. Commun*., 2013,**49**, 11488. Copyright © 2013 The Royal Society of Chemistry.

Heitbaum and co-workers performed the first on-line reaction monitoring with a thermal spray quadrupole mass spectrometer in 1986 to investigate electrochemical reactions.[53] Covey *et al*. followed up with an alternative approach for obtaining real-time data by direct sample infusion to the ion source of a triple quadrupole mass spectrometer.[54] Membrane interface coupled to a mass spectrometer has been reported for on-line monitoring in atmospheric analysis,[55] biological systems monitoring,[56,57] organic synthesis[58] and water analysis.[59,60] An illumination-assisted droplet spray ionization (IA-DSI) coupled to a mass spectrometer to track reaction species in a photolytic reaction in real-time has also been successful.[61] In addition, a miniature mass spectrometer with a continuous flow nanoelectrospray ionisation was designed by Cooks and co-workers to

monitor several reactions in different reaction vessels concurrently.[62] Cooks and co-workers also used inductive ESI-MS for *in situ* reaction monitoring of Negishi cross-coupling, reductive amination and Pd/C-catalyzed hydrogenolysis; they found that it is an efficient technique for studying solution-phase air and moisture sensitive organometallic reactions as well as organic reactions.[32] Another addition to the innovations for ESI-MS reaction monitoring is a pressurized sample infusion (PSI) system designed by our group to enable transfer of a reaction solution directly into a mass spectrometer.[63,64] The PSI set-up comprises a Schlenk flask/tube charged with a reaction solution and sealed with a rubber septum; the septum is punctured with one end of a PEEK (polyether ether ketone) tubing and placed into the reaction mixture; and the other end of the tubing is connected to the inlet of a mass spectrometer. The Schlenk flask is pressurized with an inert gas (usually argon or nitrogen) which drives a reaction solution through the PEEK tubing into the mass spectrometer. The flow rate of the sample entering the mass spectrometer can be evaluated by the Hagen-Poiseuille equation using the following parameters: inner diameter and length of PEEK tube; viscosity of the solvent used; and pressure applied to the tube. The pressure of inert gas and the flow rate of solution can be in the range of 1-5 psi and 5-10 µl/min, respectively.[63,64] This sample introduction resembles the cannula transfer technique popularly employed in air-sensitive organometallic chemistry.[64] PSI has assisted investigation of various reaction systems since its inception; these include, air or moisture sensitive reactions[65–69] and organic reaction systems.[70–73]

Recently, the PSI set-up has been adapted to include a condenser for experiments conducted at reflux (see Figure 1.12).[74] Further, the set-up can be tailored to enable complementary reaction monitoring with other analytical instruments, such as UV-Vis and IR spectrometers.[65,75] Various studies on reaction monitoring using PSI-ESI-MS are elaborated in Chapters 5, 6 and 7.

Figure 1.12. Representation of a pressurized sample infusion (PSI) customized flask.

1.7 Reaction monitoring with UV-VIS spectroscopy

UV-Vis spectroscopy is an analytical technique in which light is absorbed by analytes in the UV-Vis region (2-800 nm)[76] of the electromagnetic spectrum for qualitative and quantitative information. Generally, the presence of light-absorbing groups referred to as chromophores and the splitting of d-orbitals in transition metal complexes are responsible for the observed optical properties of coloured analytes after absorption of visible light.[76,77] However, analyte detection is dependent on the analyte's molecular structure and the extent of light absorption (absorptivity). The Beer-Lambert law shows the relationship between absorbance and the concentration of an analyte as directly proportional.[76,77] Absorbance is measured when an electron transitions from a ground state (low energy orbitals) to a higher energy excited state (high energy orbitals). The energy required for the electronic transition in an analyte depends on the gap between the energy levels/orbitals. This implies that, for a large gap, more energy is required for the electronic excitation, which results into absorption of light of a shorter wavelength. Nevertheless, the exact wavelength of absorption of any species relies on its interaction with a quantum of light (photons of corresponding energy).[76,77]

In practice, UV-Vis spectroscopy can be employed for studying reaction kinetics of reaction systems (typically millimolar concentration range), given that the rate of change in concentration of reaction species can be determined by measuring the change in absorbance of analytes over time.[76] In respect of this, UV-Vis has been used to investigate many systems through reaction monitoring (see Figure 1.13); a handful of

examples include cross-coupling reactions with Pd nanoparticles,[78–80] olefin hydrogenation with supercritical CO_2,[81] Michael addition reactions[82] and olefin epoxidation.[83] Although UV-Vis is known for good limits-of-detection, it can be problematic when absorbing species overlap. However, in relation to identifying neutral species that are not detected by ESI-MS, UV-Vis could be of significance. Hence, UV-Vis has been used simultaneously with ESI-MS to study reactions.[65] This dissertation features off-line reaction monitoring with UV-Vis spectroscopy in Chapter 4.

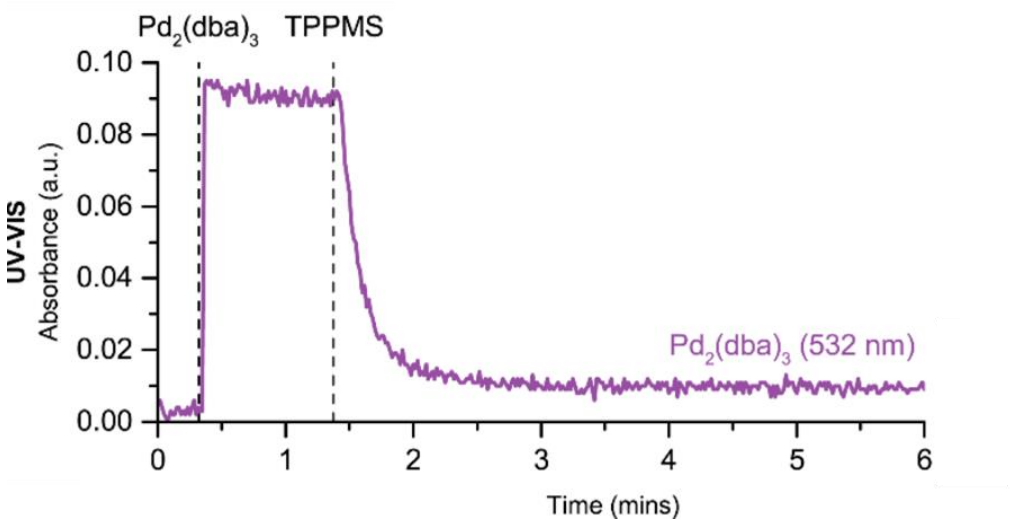

Figure 1.13. Illustration of reaction monitoring with UV-Vis during the activation of $Pd_2(dba)_3$ with $[TPPMS]^-$. Modified with permission from "Real-time analysis of $Pd_2(dba)_3$ activation by phosphine ligands" E. Janusson, H.S. Zijlstra, P.P.T. Nguyen, L. MacGillivray, J. Martelino, and J. S. McIndoe, *Chem. Commun*., 2017, **53**, 854.

1.8 Summary and objectives

ESI-MS and UV-Vis spectroscopy have found applications in reaction monitoring given their sensitivity and rapid analysis. The work in this dissertation aims to: identify target analytes in complex matrices with ESI-MS (Chapters 2 and 4); investigate the correlation between the concentration of a given analyte and its ESI signal intensity (Chapter 3); use UV-Vis spectroscopy to examine a reaction system through off-line reaction monitoring (Chapter 4), and ESI-MS to study reaction systems through on-line reaction monitoring (Chapters 5, 6 and 7); and develop a method to facilitate execution of small-scale experiments (Chapter 6).

Chapter 2 Acid-selective mass spectrometric analysis of a petroleum fraction

This chapter has been published and appears in the following publication: “Acid-selective mass spectrometric analysis of petroleum fractions” I. Omari, H. Zhu, G.B. McGarvey and J.S. McIndoe, International Journal of Mass Spectrometry, 2019, 435, 315-320.

2.1 Introduction

Petroleum is a highly complex matrix, typically composed of hydrocarbons as well as a wide variety of polar molecules. The hydrocarbons constitute about 90% whereas the polar species form a small fraction of about 10%, incorporating nitrogen, oxygen and sulfur heteroatoms as well as heavy metals (vanadium, iron and nickel).[84] These polar components have been a major concern in the petroleum industry, given their ability to corrode refinery units, inhibit catalytic activities in refinery processes and as well, pollute the environment.[85,86]

Naphthenic acids are a fraction of oxygen-containing cyclic compounds in petroleum that have recently gained attention, owing to their corrosiveness in oil extraction and processing facilities as well as pipelines..[87] Naphthenic acids comprise cyclohexyl, cyclopentyl and phenyl groups with long chain hydrocarbon backbone attached to a carboxylic acid group or long chain hydrocarbons attached to a carboxylic group (Figure 2.1), which is formed as a result of the oxidation of naphtha in petroleum.[88,89] They are described with the chemical formula: $C_nH_{2n+z}O_2$, where n is the number of carbons and z can be zero or a negative integer to indicate the hydrogen deficiency due to the presence

of multiple rings.[90] Naphthenic acids are present in petroleum in a considerable amount of up to 4% by weight.[91] The acidity of petroleum is evaluated by measuring the total acid number (TAN), which is equal to as the mass of potassium hydroxide required to neutralize a given mass of petroleum.[92] However, Turnbull and co-workers reported that the size and structure of naphthenic acids play a significant role in their corrosiveness.[93] Thus, the TAN method of addressing corrosiveness in crude oil is not a reliable method. In view of this, it is imperative to investigate other characterization techniques to account for the acid fraction of petroleum.

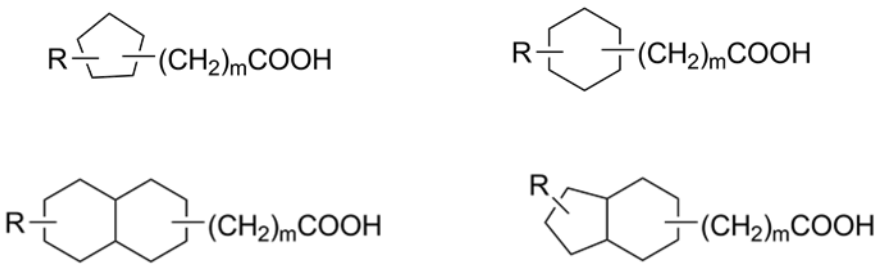

Figure 2.1. Representation of naphthenic acid structures where R is an alkyl chain, and m is the number of CH_2 units.

Various analytical techniques have been developed to enhance characterization of naphthenic acids in petroleum. These include: Fourier transform infrared (FTIR) spectroscopic analysis, gas chromatography (GC) and high performance liquid chromatography (HPLC).[94,95] These techniques are generally employed to determine the total naphthenic acid concentration.[96,97] Unfortunately, considering only the acid concentration in assessing corrosiveness of naphthenic acids in petroleum is not sufficient; but employing techniques that will also determine the size and structure of naphthenic acids would be a more useful approach. In order to determine the size and

structure of naphthenic acids in petroleum, several studies have been conducted using state-of-the-art mass spectrometry methods. EI was employed to characterize naphthenic acids, and detected about 1500 naphthenic acids.[98] As well, chemical ionization (CI),[99,100] fast atom bombardment (FAB),[101,102] atmospheric pressure chemical ionization (APCI)[103] and electrospray ionization (ESI) methods were compared to determine the molecular distribution of naphthenic acids extracted from petroleum.[104,105] However, for the study of complex mixtures, soft ionization techniques such as ESI are preferred over hard ionization techniques such as EI.[106–109] The latter yields similar fragments leading to a complicated mass spectrum; whereas the former simplifies the mass spectrum by preserving the molecular ion of the species of interest in a complex mixture.[110]

The use of Fourier-transform ion cyclotron resonance mass spectrometry (FT-ICR MS) has been a preferred technique for petroleum characterization given its ultra-high resolution and ultra-high mass accuracy.[111–114] Qian and co-workers combined HPLC with ESI-FT-ICR-MS to characterize acid fractions in crude oil and this technique was able to identify fifteen different chemical formulas of naphthenic acids.[115] Barrow *et al*. employed FT-ICR-MS to conduct a study on the degradation of naphthenic acids in the environment.[116] Clingenpeel *et al*. also employed FT-ICR-MS for characterization of naphthenic acids; and reported that during the petroleum refining process, naphthenic acids could contribute to the formation of stable emulsions.[117] In addition, Rowland and co-workers used modified aminopropyl silica (MAPS) chromatography coupled with negative ion electrospray ultrahigh resolution mass spectrometry to characterize naphthenic acids in a petroleum mixture.[118]

In this chapter, a petroleum fraction supplied by Imperial Oil was examined for naphthenic acids. Imperial Oil was interested in a fast and sensitive qualitative technique that could be employed to detect naphthenic acids in petroleum fractions. Thus, a rapid, simple, and inexpensive method by means of ESI-MS was used to characterize model naphthenic acids as well as naphthenic acids in a petroleum fraction. ESI is a soft ionization technique which can generate positively charged ions when basic species are protonated with a weak acid. ESI also generates negatively charged ions when acidic species are deprotonated with a weak base.[119] Alternatively, derivatization methods could be used to promote the detection of species of interest in ESI-MS.[73]

A charge-tagging technique which has been successful in detecting thiols and phenols in petroleum fractions was employed.[72,73] A charge-tagged alcohol (3-[4-(hydroxymethyl) benzyl]-1-methylimidazolium hexafluorophosphate) and a charge-tagged carbodiimide compound (1-[3-(dimethylamino) propyl]-3-ethylcarbodiimide methiodide) were employed in this study for naphthenic acid derivatization reactions. Derivatization of naphthenic acid with a charge-tagged alcohol mimics Fischer esterification of carboxylic acids, which is a simple and prominent reaction of carboxylic acids.[120–122]

The role of the charge-tagged alcohol and carbodiimide compounds is to facilitate detection of the naphthenic acid derivatives. A carbodiimide is a functional group with the chemical formula RN=C=NR.[123] Compounds containing the carbodiimide functional group are used as a dehydrating agent to activate carboxylic acids for coupling with primary amines to yield amide compounds.[49] Carbodiimide is also a well-known tool in the field of bioconjugation, peptide synthesis and modification of polysaccharides.[124,125] In addition, the charge-tagging technique will be compared with a deprotonation method.

The deprotonation method involves the use of ammonium hydroxide to deprotonate naphthenic acids present in the petroleum fraction and a commercial naphthenic acid mixture.

2.2 Derivatization and deprotonation of model naphthenic acids

After synthesis of the charge-tagged alcohol (see Figure 2.1), the charge-tagged mixture contained impurities such as sodium bromide, which has similar solubility as the charge-tagged alcohol, so purification was a challenge. Nevertheless, the efficiency of the charge-tagged alcohol was tested in an esterification reaction with a model naphthenic acid, 2-methoxyphenylacetic acid. The charge-tagged alcohol unexpectedly decomposed during the reaction and the derivatized product with *m/z* 351 was not of sufficient intensity to be easily identified (Figure 2.2). The inefficacy of this method of analysis could be attributed to low (intended) reactivity of the charge-tagged alcohol, long reaction time, solvent restrictions (both charge-tagged and analyte need to be soluble), and harsh reaction conditions of esterification and purification problems. Thus, a charge-tagged carbodiimide (**1**) was employed as an alternative for derivatization.

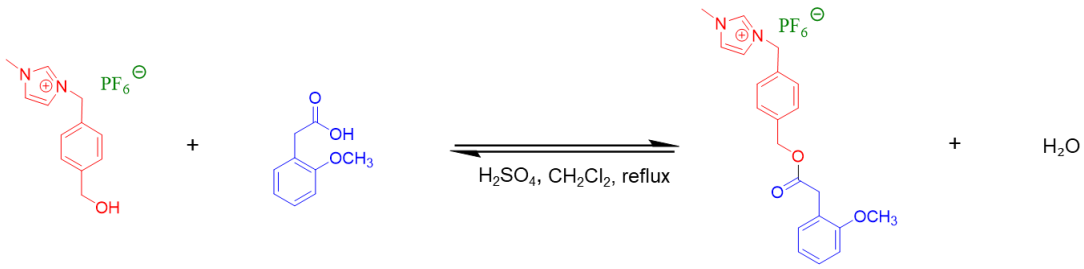

Scheme 2.1. Representation of esterification reaction between 2-methoxyphenylacetic acid (naphthenic acid) and a charge-tagged alcohol.

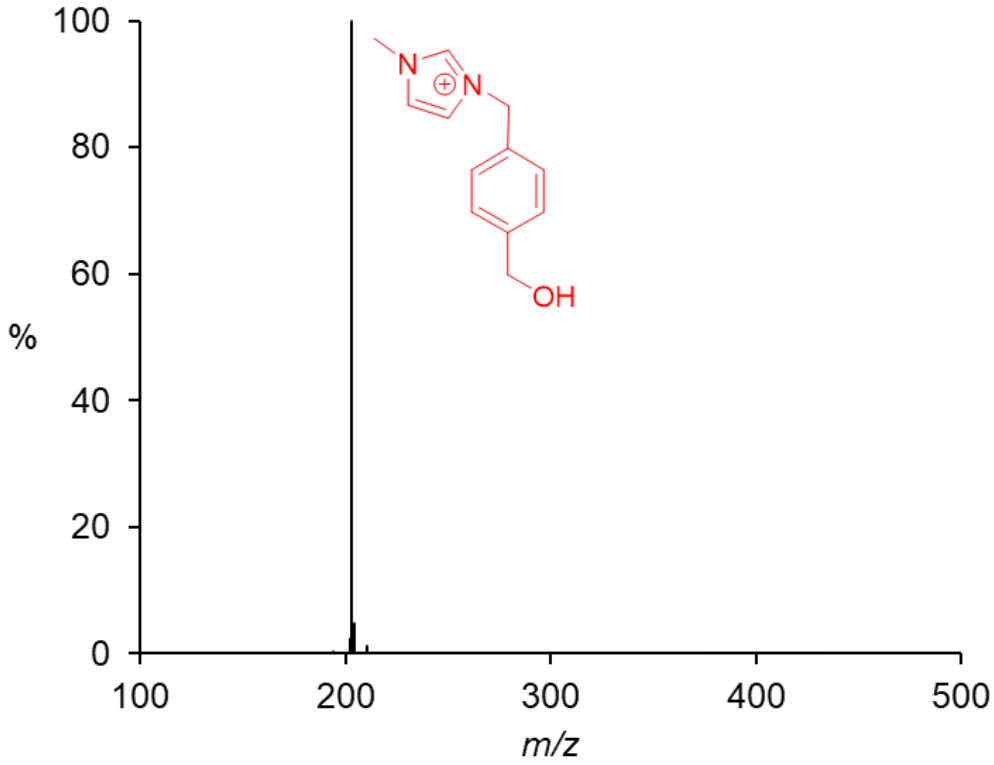

Figure 2.2. Positive ion mode ESI-MS of charge-tagged alcohol after synthesis at 70°C in water.

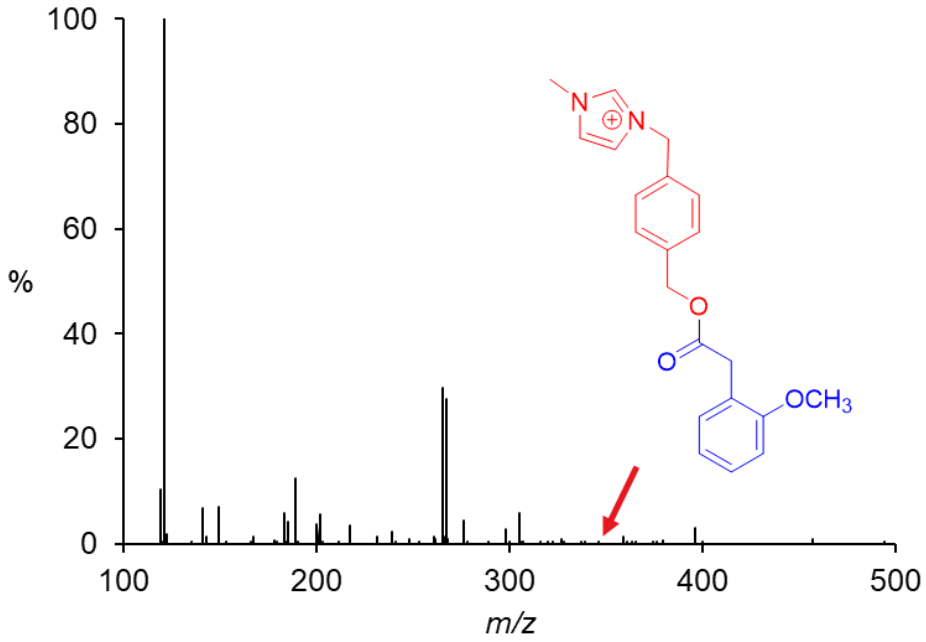

Figure 2.3. Positive ion mode ESI-MS mass spectrum after 3-hour esterification reaction with a charge-tagged alcohol in dichloromethane.

The reactivity of a charge-tagged carbodiimide (**1**) was studied via on-line reaction monitoring in positive ion mode ESI-MS (Scheme 2.2).

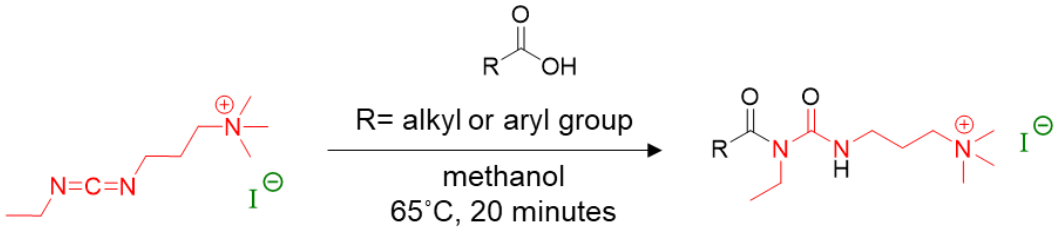

(**1**)

Scheme 2.2. Representation of a derivatization reaction between naphthenic acids and a charge-tagged carbodiimide (**1**).

This derivatization was conducted by adding a mixture of different model naphthenic acids (cyclopentanecarboxylic acid, cyclohexanepentanoic acid and cyclohexaneacetic acid in the same molar amount) to a solution containing the charge-tagged carbodiimide (**1**) at 65°C. The reaction between charge-tagged carbodiimide (**1**) and cyclohexaneacetic acid was used to establish a detection limit (Figure 2.3). Response of the naphthenic acid derivative was determined to be linear for micro- to millimolar quantities of the naphthenic acid. The response of the lowest detectable naphthenic acid derivative was used to determine the limit of detection (signal to noise ratio = 3) and limit of quantitation (signal to noise ratio = 10); which were found to be 0.7 μM and 2.3 μM respectively. However, the reactivity, concentration of target analytes as well as differences in petroleum distillate matrices could limit the derivatization process. Thus, the detection limit established was only an approximation and will differ between matrices.

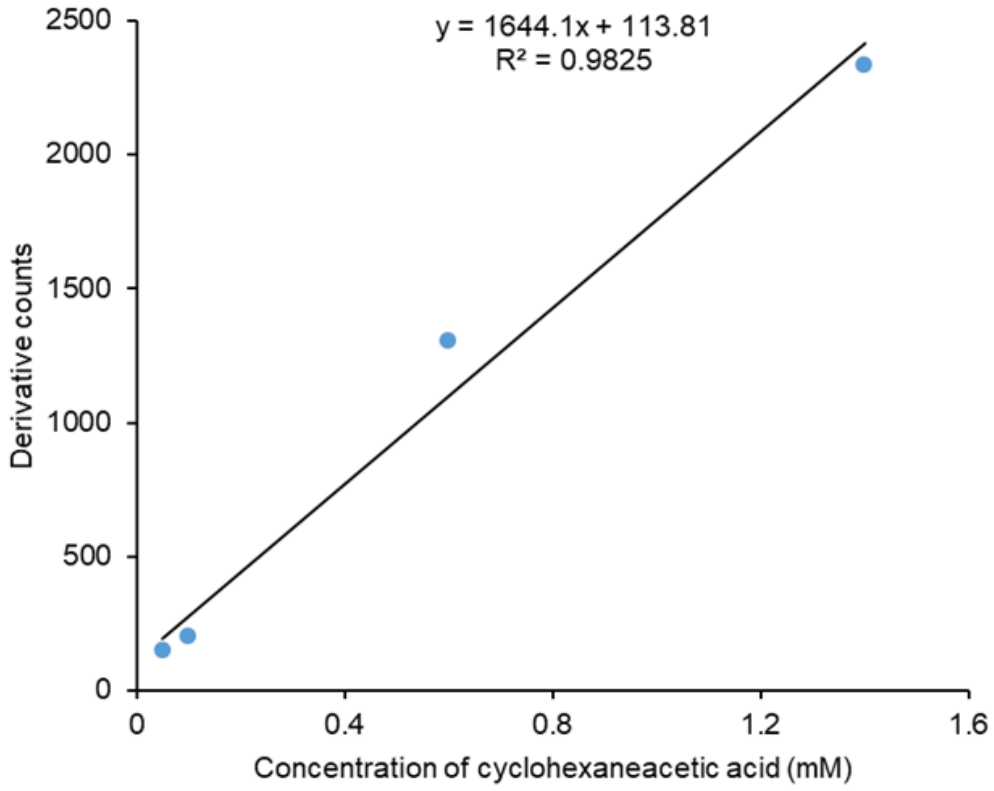

Figure 2.4. Response of naphthenic acid derivative following the reaction between cyclohexaneacetic acid and 0.286 mM (**1**).

Figure 2.5 shows a pseudo zero-order reaction whereby derivatization of cyclohexanepentanoic acid (green) was faster than cyclohexaneacetic acid (blue) and cyclopentanecarboxylic acid (red). This could be explained by steric hindrance of the cyclohexyl and cyclopentyl groups in cyclohexaneacetic acid and cyclopentanecarboxylic acid respectively, since both groups are close to the carboxyl group. Hence, the reaction rate decreased. In the case of cyclohexanepentanoic acid, the steric effect was relatively less due to the presence of four CH_2 groups keeping the bulky group away from the carboxyl group; therefore, the rate of reaction increased correspondingly. The pseudo

zero-order nature of each trace points to a reaction insensitive to the concentration of the carbodiimide (**1**).

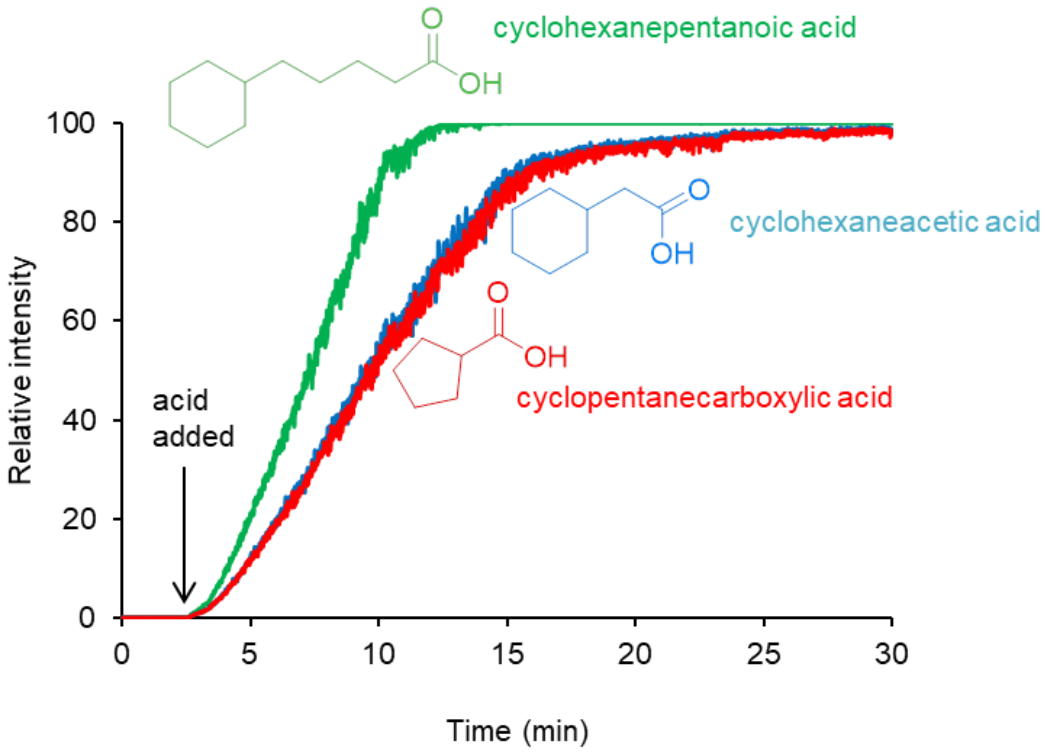

Figure 2.5. Positive ion mode ESI-MS of an on-line reaction monitoring between (**1**) and a mixture of three naphthenic acid model compounds (cyclopentanecarboxylic acid, cyclohexanepentanoic acid and cyclohexaneacetic acid) at 65°C in methanol.

A commercial naphthenic acid mixture was examined to evaluate the usefulness of the charge-tagged carbodiimide (**1**). The commercial acid mixture served as a model petroleum fraction given that it is composed of isolated naphthenic acids from petroleum.[126,127] Figure 2.6 displays a homologous series of naphthenic acid derivatives with *m/z* from 300 ($C_{16}H_{34}N_3O_2$) to 784 ($C_{52}H_{96}N_3O_2$); within this range, species with between zero and five double bond equivalents (DBE) were observed.

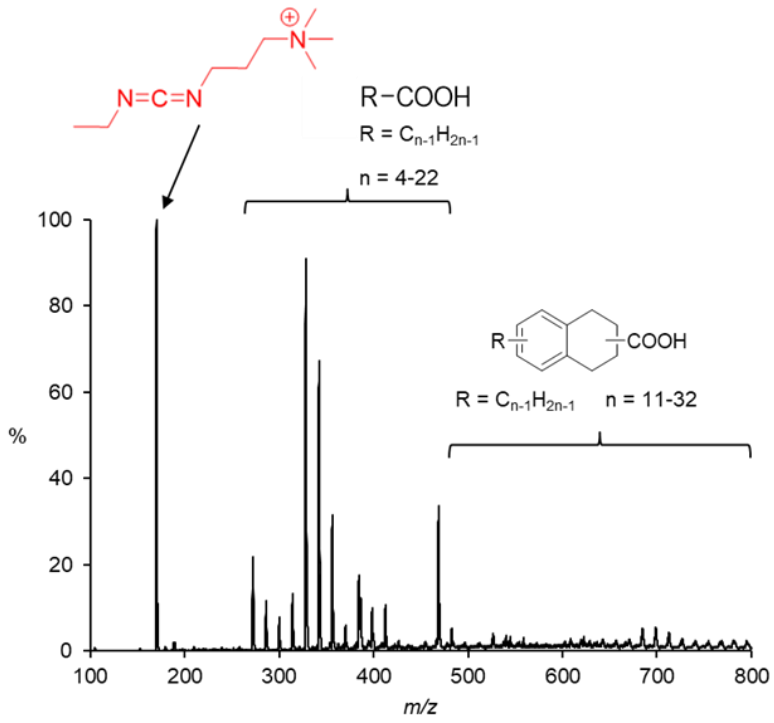

Figure 2.6. Positive ion mode ESI-MS spectrum of naphthenic acids in a commercial naphthenic acid mixture which were derivatized with (**1**) in methanol at 65°C.

Constituents of the commercial naphthenic acid mixture were also determined via deprotonation with ammonium hydroxide. Deprotonated naphthenic acid species were detected as $[M-H]^-$ (Figure 2.7). The ESI (-) MS spectrum of Figure 2.7 depicts a homologous series of naphthenic acids with *m/z* from 101 ($C_4H_7O_2$) to 613 ($C_{43}H_{75}O_2$). Within this series, naphthenic acids with *m/z* from 101 to 339 were identified as species with 0 DBE and naphthenic acids with *m/z* greater than 339 were identified as 5 DBE species.

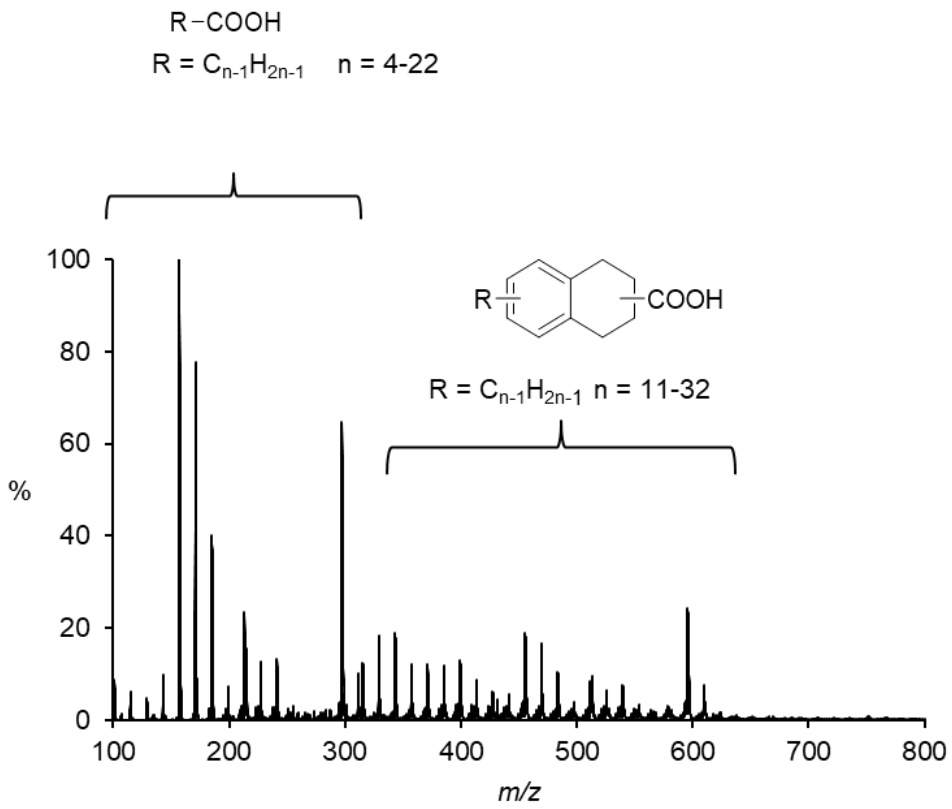

Figure 2.7. Negative ion mode ESI-MS spectrum of naphthenic acids in a commercial naphthenic acid mixture which were deprotonated with ammonium hydroxide in methanol at room temperature.

In a direct comparison between the derivatized and deprotonated commercial naphthenic acid mixture (Figure 2.7), naphthenic acid derivatives of relatively low intensities at *m/z* from 500 to 784 were observed, whereas the deprotonated acid species of same distribution were more conspicuous. It is possible that the higher mass carboxylates are exhibiting considerably higher surface activity than their lower mass counterparts, and are hence overrepresented, whereas the relative abundance of the charge-tagged variants are dependent more on the nature of the charge-tagged itself (note the masses of the latter span ~*m/z* 300-700, whereas the former are ~*m/z* 100-500).

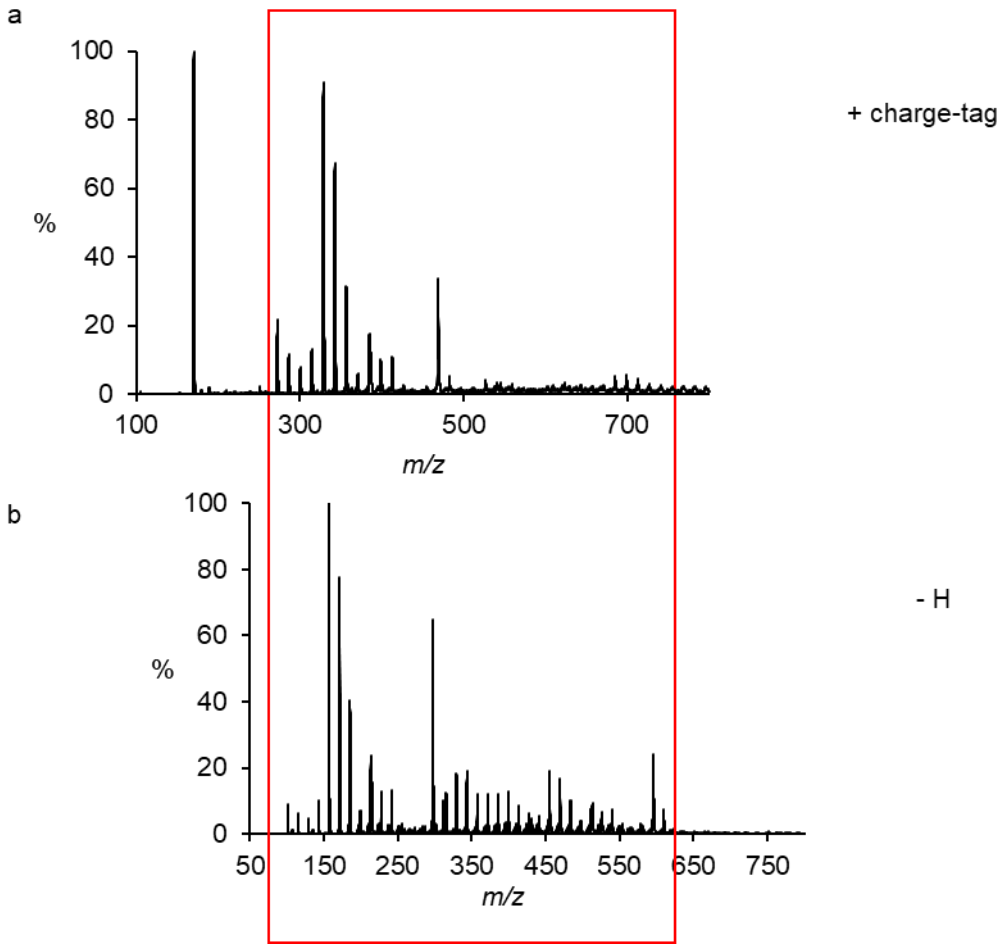

Figure 2.8. Comparison between a) derivatized naphthenic acid species; and b) deprotonated naphthenic acid species (ions with an offset of the charge-tag) of a commercial naphthenic acid mixture

2.3 Derivatization and deprotonation of naphthenic acids in a petroleum fraction

To determine various naphthenic acids present in a petroleum fraction, the charge-tagged carbodiimide (**1**) was employed and its performance was assessed with respect to selectivity in a highly complex matrix. On addition of the petroleum fraction to the charge-tagged (**1**), acid derivatives were detected from *m/z* 328 ($C_{18}H_{38}N_3O_2$) to 600 ($C_{38}H_{70}N_3O_2$); but with relatively low intensities (Figure 2.9). An explanation to this observation could be low concentration of naphthenic acids present in the petroleum fraction (after distillation by Imperial Oil); thus, the naphthenic acids exhibited poor signal to noise ratio.

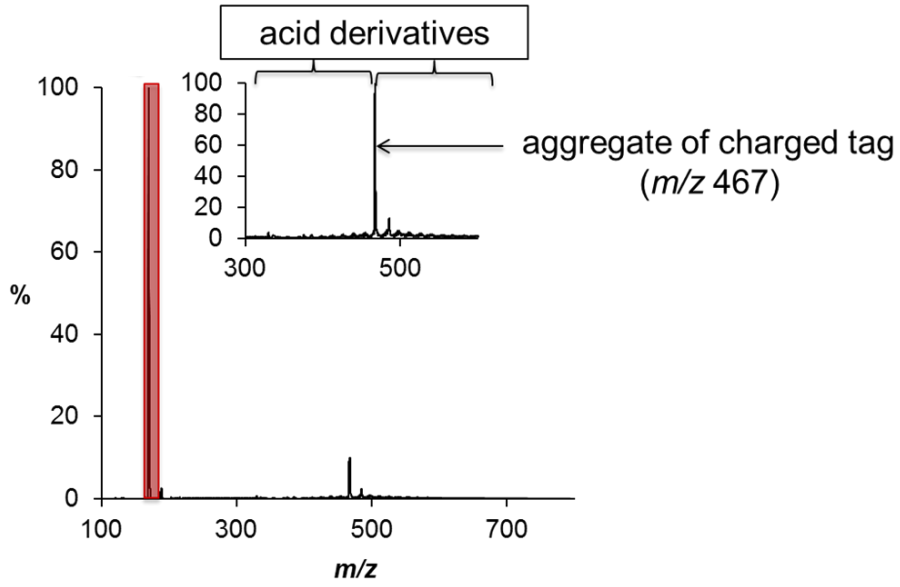

Figure 2.9. Positive-ion ESI-MS of naphthenic acids in petroleum fraction which were derivatized with (**1**) in methanol at 65°C (note: as shown in inset, *m/z* 328 – 466 and *m/z*

468 – 600 are acid derivatives; but species at *m/z* 467 is an aggregate of the charge-tagged species).

However, a better approach to facilitate assignment of these derivatized species was via tandem mass spectrometry; whereby product and precursor ions of species in a complex matrix could be deduced. In view of this, a product ion experiment was conducted after a full MS scan as shown in Figure 2.10, to determine a common product ion of the naphthenic acid derivatives in the petroleum fraction. The common product ion was determined as the base peak at *m/z* 170 (Figure 2.10).

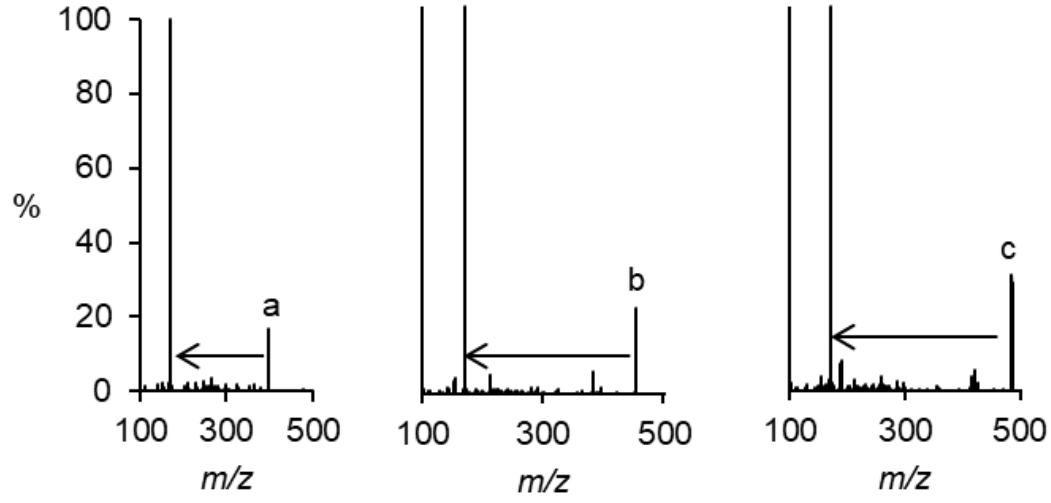

Figure 2.10. Representation of product ions of derivatized naphthenic acids at (a) *m/z* 398; (b) *m/z* 454; (c) *m/z* 498; and a common product ion at *m/z* 170.

With this established, a precursor ion experiment was conducted to determine the precursor ions of the common product ion in the complex matrix. A significant feature of this experiment is the improved signal to noise ratio of species of interest. This was apparent after the precursor ion experiment by which a variety of acid derivatives from *m/z* 328 ($C_{18}H_{38}O_2N_3$) to 600 ($C_{38}H_{70}O_2N_3$) with 0 to 7 DBE were detected (Figure 2.11). However, after conducting an orbitrap mass spectrometric analysis, naphthenic acid species of similar nominal mass were identified with the formulae $C_nH_{2n+2}O_2N_3$ (n = 26-29) and $C_nH_{2n-12}O_2N_3$ (n = 27-30); interpreted as 0 and 8 DBE species respectively (Table 2.1).

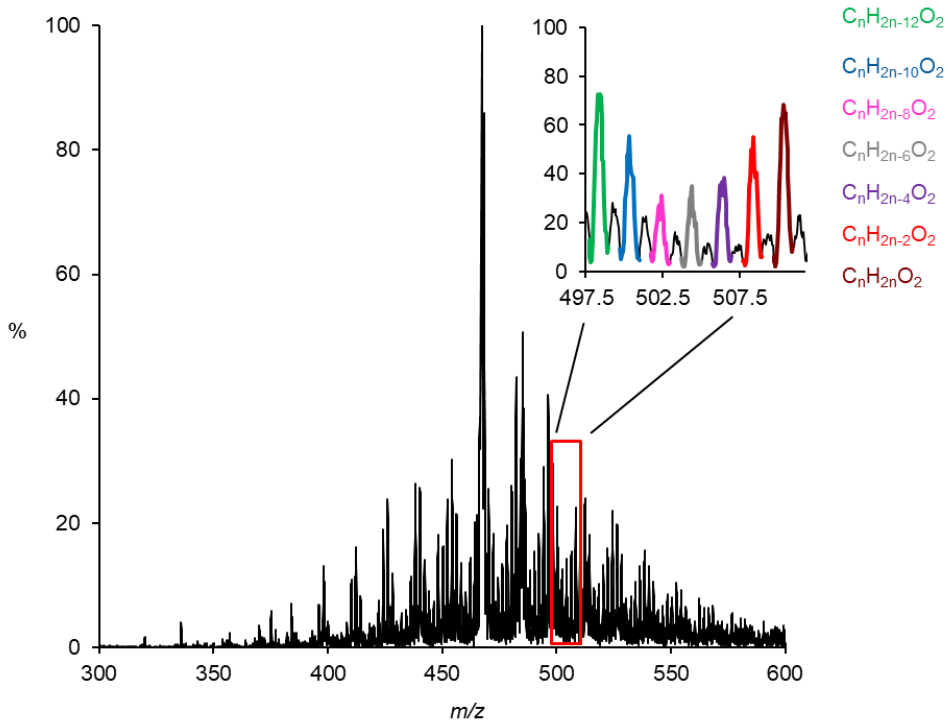

Figure 2.11. Representation of precursor ions of derivatized naphthenic acids in petroleum fraction with colour-coded acid species from *m/z* 498 to 510.

Table 2.1. The orbitrap result of acid derivatives with similar nominal mass.

m/z	Composition	Accuracy (ppm)
440.32771	$C_{27}H_{42}O_2N_3$	1.3
440.42511	$C_{26}H_{54}O_2N_3$	-1.0
454.34355	$C_{28}H_{44}O_2N_3$	1.6
454.43623	$C_{27}H_{56}O_2N_3$	-0.8
468.35921	$C_{29}H_{46}O_2N_3$	1.6
468.45224	$C_{28}H_{58}O_2N_3$	-0.2
482.37515	$C_{30}H_{48}O_2N_3$	1.2
482.46791	$C_{29}H_{60}O_2N_3$	-0.2

Petroleum fractions were also deprotonated in a similar fashion as the commercial acid mixture; but a complex spectrum was produced (Figure 2.12). As a result, assignment of naphthenic acids in petroleum fraction was not as simple as the commercial naphthenic acid mixture, in that after deprotonation, all protic species present could be detected. Nevertheless, a range of various naphthenic acids from *m/z* 157 ($C_9H_{17}O_2$) to 429 ($C_{29}H_{49}O_2$) with 0 to 8 DBE were identified; and they were in agreement with results obtained by Dalmaschio and co-workers.[86]

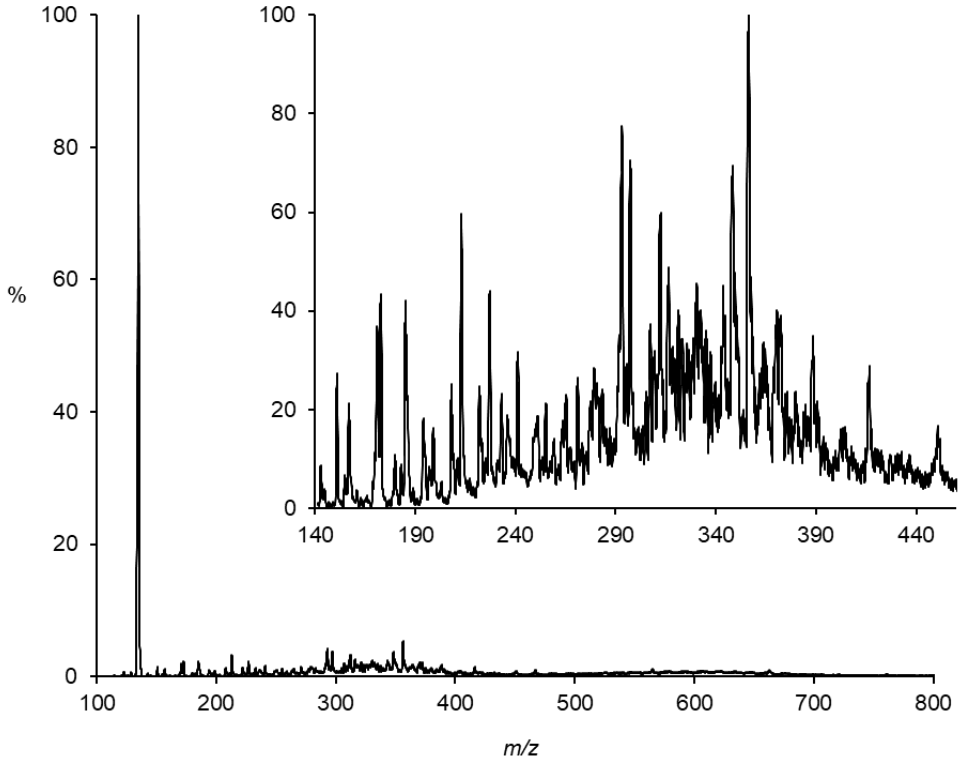

Figure 2.12. Negative ion mode ESI-MS spectrum of naphthenic acids in petroleum fraction, which were deprotonated with ammonium hydroxide in methanol at room temperature. Inset: expansion of the *m/z* 140-440 range.

2.4 Conclusions

Charge-tagging is a simple and selective methodology which facilitates detection of desired species through ESI-MS; but considering the performance of the charge-tagged alcohol in this study, it can be inferred that Fischer esterification of naphthenic acids with a charge-tagged alcohol is problematic given the harsh conditions and solvent restrictions (both charge-tagged and analyte need to be soluble) involved. However, charge-tagged carbodiimide enhances detection of model naphthenic acids; and as well, offers rapid and selective analysis of naphthenic acids in petroleum fractions which is useful for qualitative studies. The results of this study have also proved that deprotonation is relatively sensitive; but the complexity of mass spectrum involved, in relation to petroleum fractions, gives the charge-tagging technique an advantage of selectivity in characterizing naphthenic acids.

2.5 Experimental

Chemicals and Samples

All chemicals and solvents employed were purchased from Sigma-Aldrich or Alfa Aesar. The petroleum fraction used in this study is a distillate of crude oil supplied by Imperial Oil, Ontario, Canada.

NMR

A Bruker Avance 300 MHz spectrometer was used to obtain ^{1}H NMR spectra with solutions prepared in $CDCl_3$ and CD_3OD.

ESI-MS

ESI-MS of the synthesized product as well as the charged-tag reactions with the naphthenic acid models, a commercial naphthenic acid mixture and petroleum fractions were conducted in the positive ion mode on a Waters Acquity TQ Detector mass spectrometer. The parameters used were: capillary voltage, 3 kV; cone voltage, 15 V; extraction voltage, 2 V; source temperature, 70°C; desolvation temperature, 170°C; cone gas flow rate, 100 L/h; desolvation gas flow rate, 200 L/h. Scan time was set to 1 s. Also, ESI-MS of the deprotonated naphthenic acid mixture and petroleum fractions were conducted in the negative ion mode using the same instrument parameters. Pressurized sample infusion (PSI) experiments using ESI-MS (+) were employed for the derivatization reactions. The PSI experiments involved derivatization reactions at 65°C in methanol, in a Schlenk flask. The derivatized material was fed into the ESI source by means of PEEK tubing and 3 psi of argon gas. The derivatization reactions included: reaction between charge-tagged carbodiimide (**1**) (1 mmol, 1 eq) and naphthenic acid model compounds (10 mmol, 10 eq); reaction between charge-tagged carbodiimide (1 mM) and a commercial naphthenic acid mixture (10% v/v) as well as petroleum fractions (10% v/v). After the PSI experiment for the petroleum fraction, the reaction solution was further diluted to 10 ppm using HPLC grade methanol. An Exactive Plus Orbitrap Mass Spectrometer from Thermo Fisher Scientific (Waltham, MA, USA) was used to analyze the diluted reaction solution in the positive ion mode. The capillary temperature of the Orbitrap Mass Spectrometer was set to 250°C, the spray voltage was set to 3.5 kV, sheath

gas flow rate was set to 30, auxiliary gas flow rate was set to 10 and the auxiliary gas temperature was set to 175°C. A mass accuracy of less than 2 ppm and a resolving power of 100,000 (at *m/z* 400) assisted in data collection over the mass range of *m/z* 140–2000 in the full scan mode. An integrated syringe pump was used whereby the flow rate was set to 50–100 μL min^{-1}. An integrated syringe pump was used whereby the flow rate was set to 50 -100 μL min^{-1}.

Off-line experiments were also carried out prior to characterization. These involved: deprotonation of petroleum fractions (10% v/v); and a commercial naphthenic acid mixture (10% v/v) in methanol with ammonium hydroxide (30 μL, 2% v/v in methanol). In addition, a charge-tagged alcohol (1 mmol, 1 eq) was used to derivatize a naphthenic acid model compound, 2-methoxyphenylacetic acid (10 mmol, 10 eq). A concentrated sulfuric acid served as a catalyst through gentle reflux under argon for about 3 hours in 50 mL of dichloromethane in the presence of activated 4Å molecular sieves. All solutions after the off-line experiments were fed into the ESI source by means of a syringe pump and an analytical syringe connected to PEEK tubing.

MS/MS experiments were carried out with a Waters Acquity TQ Detector to obtain structural information using the parameters as follows: collision voltage, 10 V; high mass and low mass resolution at 15 V each. Interpretation of the mass spectra was facilitated using chemcalc.org.[128]

Synthesis of 3-(4-(bromomethyl) benzyl)-1-methylimidazolium hexafluorophosphate

1-Methylimidazole (0.46 mL, 5.77 mmol) reacted with excess α,α′-dibromo-p-xylene (2.049 g, 7.76 mmol) through gentle reflux under argon for about 16 hours in 50 mL of THF. A white powder was recovered from acetonitrile through vacuum filtration which

was vacuum dried for 24 hrs. The 3-(4-bromomethyl)benzyl)-1-methylimidazolium bromide (0.220 g) was dissolved in 25 mL of 50% v/v aqueous methanol, followed by the addition of sodium hexafluorophosphate (0.330 g). The solution was stirred for 12 hours. A white powder was recovered from the reaction solution via vacuum filtration (28.9% yield). ^{1}H NMR (300 MHz, CD_3OD): δ (ppm) = 3.93 (s, 3H), 4.59 (s, 2H), 5.41 (s, 2H), 7.61-7.40 (m, 6H), 8.95 (s, 1H). QTOF ESI (+): $[M]^+$ *m/z* 265.1; ESI (-): $[M]^-$ *m/z* 145.1.

Synthesis of 3-[4-(hydroxymethyl) benzyl]-1-methylimidazolium hexafluorophosphate (charge-tagged alcohol)

3-(4-(bromomethyl)benzyl)-1-methylimidazolium hexafluorophosphate (0.65 g, 1.59 mmol) was reacted with NaOH (6 g, 0.15 mol) solution in 50 mL distilled water at 70°C. The solution was mechanically stirred for 10 hrs. The reaction solution was filtered, and the filtrate was vacuum dried. The powder was redissolved in a minimum amount of methanol and a white precipitate was formed after leaving the solution at 4°C overnight. The white precipitate was recovered from the reaction solution through vacuum filtration (15% yield). ^{1}H NMR (300 MHz, $CDCL_3$): δ (ppm) = 3.90 (s, 3H), 5.05 (s, 2H), 5.29 (s, 2H), 7.50-7.29 (m, 6H), 8.64 (s, 1H). QTOF ESI (+): $[M]^+$ *m/z* 202.1; ESI (-): $[M]^-$ *m/z* 145.1.

Chapter 3 Structure, anion, and solvent effects on cation response in ESI-MS

This chapter has been published and appears in the following publication: “Structure, anion, and solvent effects on cation response in ESI-MS” I. Omari, P. Randhawa, J. Randhawa, J. Yu and J.S. McIndoe, Journal of the American Society for Mass Spectrometry, 2019, 30, 1750-1757.

3.1 Introduction

Electrospray ionization (ESI) is well-known to exhibit differing ion responses depending on the nature of the analyte under study.[129–131] This effect extends beyond the propensity of the analyte to acquire a charge in the solution phase (the more basic a compound is, the more readily it is protonated),[132] as permanently charged ions provide different intensities depending on their structure. Prior studies in this area have principally focused on the most intuitively important factor, the extent of ionization of a given analyte, which depends on factors such as solution pH and the basicity of the molecule in question.[133–135] Signal strength in a mass spectrum does not transparently reflect solution composition.[136]

The ion response describes the surface activity of species in a mass spectrum, which implies that surface-active analytes have a stronger ESI response than less surface-active analytes.[137–140] Possible parameters that correlate with the ESI response of analytes include morphology of the analyte, cation-anion interaction and solvation strength.[141,142] The nature of the solvent is a contributory factor to the manner of ESI response of

species, given that the response is contingent on the solvation strength.[141–144] However, the extent of solvation of ions may differ in polar and non-polar solvents eligible for ESI-MS.[145–147] Hydrophilic and hydrophobic species tend to be more solvated in polar and non-polar solvents respectively, thereby exhibiting poor surface activity. In this regard previous work from our research group reported that chloride aggregates of 1-butyl-3-methylimidazolium $[(BMIM)_2+Cl]^+$ showed a better ESI-MS response than bistriflimide ($[NTf_2]^-$) aggregates of the same cation $[(BMIM)_2+NTf_2]^+$ in dichloromethane, due to lower solvation of the chloride aggregates in the non-polar solvent.[148] In an experiment to investigate the ESI response of ionic liquids, Bortolini *et al*. found that a cobalt based ionic liquid with bistriflimide counterion was more responsive in methanol than in dichloromethane.[149] These findings apparently indicate that intensity is related to the solvation strength. Strong solvation of analytes can occur because of hydrogen bonding and other intermolecular forces.[150–156] For example, solvation of chloride in methanol or water/acetonitrile systems comes about because of ion-dipole interactions. Spatial effects in terms of source geometry can also affect relative ESI-MS response.[157]

Analytes with flexible alkyl groups are identified as hydrophobic and are likely to occupy surface sites in a droplet of polar solvent. Considering the morphology of such analytes, Song and co-workers reported an anomaly in a trend of surface activity for quaternary ammonium species with flexible alkyl chains in an aqueous sodium chloride system.[158] They suggested that as the alkyl chain length increases (above 14 carbon atoms), aggregates are formed with less or no surface activity depending on the environment of the species.[158] However, their assessment was based on surface tension measurements of

Gemini surfactants (also known as dimeric surfactants)[158], and not a mass spectrometric study.

In this chapter, parameters that could influence the ESI response of analytes were investigated. An equimolar mixture of six cations [cesium, tetraethylammonium, tetrabutylammonium, tridodecylmethylammonium, bis(triphenylphosphoranylidene)ammonium and tetradodecylammonium, i.e., Cs^+, $[NEt_4]^+$ (Et = ethyl), $[NBu_4]^+$ (Bu = butyl), $[NDo_3Me]^+$ (Do = dodecyl; Me = methyl), $N(PPh_3)_2^+$ (Ph = phenyl) and NDo_4^+], was paired with various anions (chloride, hexafluorophosphate, tetrafluoroborate and bistriflimide, i.e., Cl^-, $[PF_6]^-$, $[BF_4]^-$ and $[NTf_2]^-$) in standard ESI solvents (Figure 3.1).

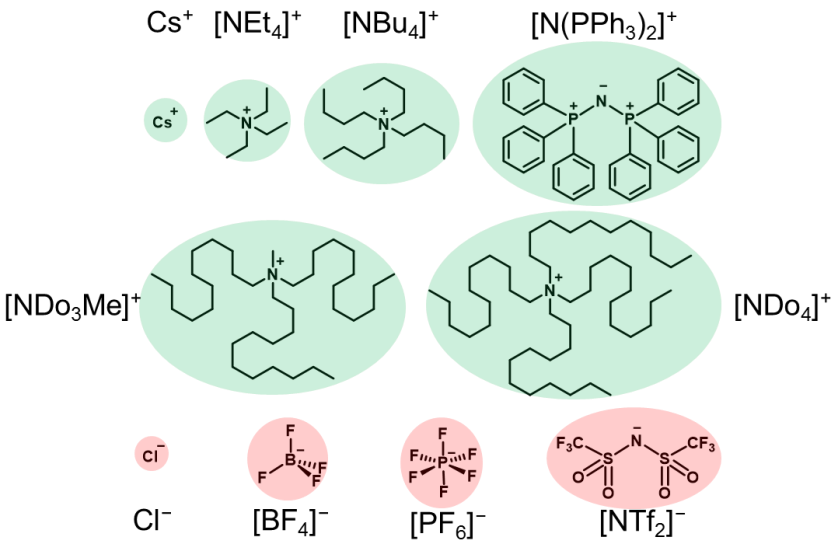

Figure 3.1. Representation of various sizes of cations and anions employed in this study.

These salts were selected to provide a variety of molecular weights and structural variety. Ionic surfactants, such as tetraalkylammonium halides have been reported by Bruins and co-workers as suitable model analytes for fundamental ESI-MS studies, given their surface activity and insusceptibility to solution pH.[159] Salts with counterions larger than chloride were prepared by switching the chloride counterion of the six cations by employment of silver tetrafluoroborate ($AgBF_4$), silver hexafluorophosphate ($AgPF_6$) and silver bistriflimide ($AgNTf_2$), exploiting the very low solubility of AgCl. The correlation between rigidity and ESI response of structurally different species was also investigated. A solid understanding of these factors is important when using ESI-MS to gather kinetic data,[33,160–165] because while corrections can be applied when studying solution components such as reactants and products (which can be individually isolated and measured), such precautions are often impossible when dealing with reactive intermediates.[166]

3.2 ESI response and molar conductivity of analytes in various solvents

An equimolar mixture of cations (Cs^+, $[NEt_4]^+$, $[NBu_4]^+$, $[NDo_3Me]^+$, $[N(PPh_3)_2]^+$, $[NDo_4]^+$) was paired with one of four anions ($Cl^–$, $[BF_4]^–$, $[PF_6]^–$, $[NTf_2]^–$) in methanol, acetonitrile, water/acetonitrile and dichloromethane; however, CsCl in dichloromethane was excluded, given its insolubility. This exclusion also included pairing of the other anions with cesium in dichloromethane. The relative responses of these species were measured in positive mode ESI-MS.

Figure 3.2 shows the relative intensities of salts in acetonitrile. The differential response with chloride as a counterion (Figure 3.2a) showed high intensity for $[NEt_4]^+$, $[NBu_4]^+$ and $[N(PPh_3)_2]^+$, moderate intensity for $[NDo_3Me]^+$ and $[NDo_4]^+$, and near-zero response for Cs^+. The low response of Cs^+ is possibly due to a high level of solvation and/or ion-pairing for this ion,[167] and the lower response of the ammonium salts with dodecyl groups could probably be related to Song's explanation for the formation of non-surface active aggregates in relation to surface activity of long chain ammonium salts.[158] Swapping the chloride for increasingly hydrophobic counterions (Figure 3.2b, c and d) changes the distribution in favour of the lowest molecular weight species, and for $[NTf_2]^-$, the spectrum is dominated by $[NEt_4]^+$ with the next most intense ion, $[NBu_4]^+$; $[N(PPh_3)_2]^+$ being less than 25% and all others at baseline levels. At the same time as ion differentiation increased, ion intensity dropped overall.

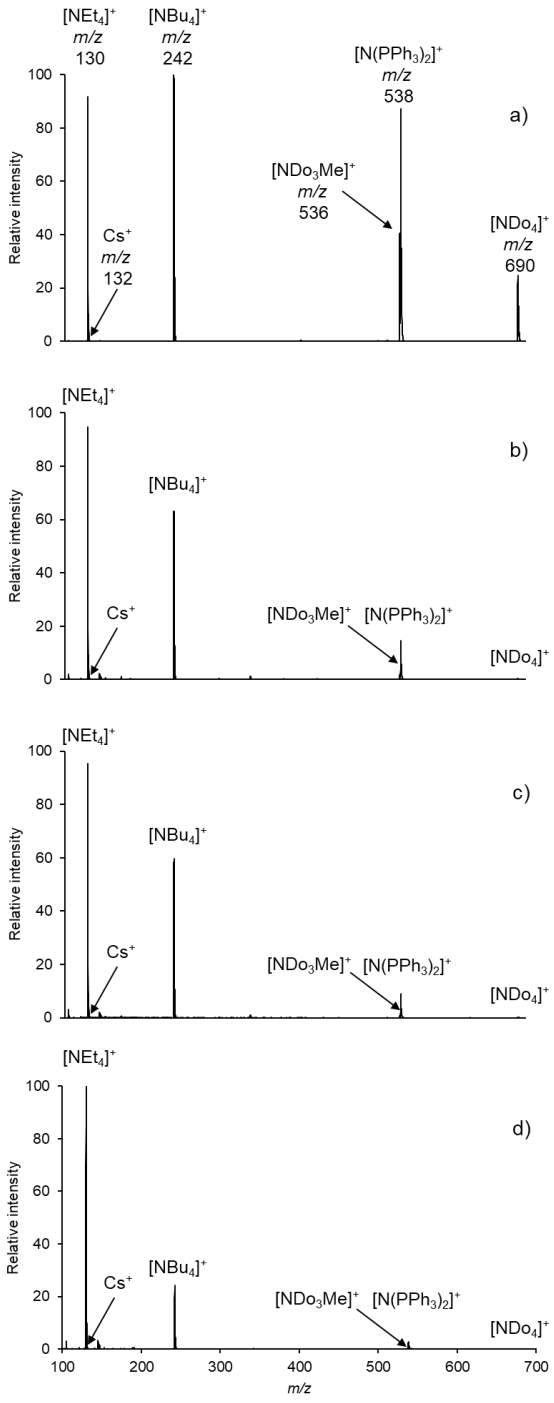

Figure 3.2. Positive ion ESI mass spectrum of an equimolar mixture of six cations $[NEt_4]^+$ (*m/z* 130), Cs^+ (*m/z* 132), $[NBu_4]^+$ (*m/z* 242), $[N(PPh_3)_2]^+$ (*m/z* 538), $[NDo_3Me]^+$ (*m/z* 536), $[NDo_4]^+$ (*m/z* 690), paired with various counterions in acetonitrile: a) Cl^-; b) $[BF_4]^-$; c) $[PF_6]^-$; and d) $[NTf_2]^-$.

A representation of reproducible peak area distribution for species in acetonitrile also depicted a similar trend (see Figure 3.3). Also, in a dichloromethane system (Figure 3.4), we observed that all cations paired with chloride were over-represented compared to cations paired with relatively hydrophobic anions ($[BF_4]^-$, $[PF_6]^-$ and $[NTf_2]^-$), considering that the cations paired with chloride were less solvated. Comparing the relative intensity (Figure 3.2) and peak area (Figure 3.3 and Figure 3.4) of the hydrophobic rigid cation $[N(PPh_3)_2]^+$ to that of the bulky hydrophobic flexible cations [NDo_3Me^+ and NDo_4^+] in both acetonitrile and dichloromethane, the hydrophobic flexible species were under-represented, though less so than the Cs^+ (in acetonitrile), which was almost invisible, suppressed by the more surface-active ions.

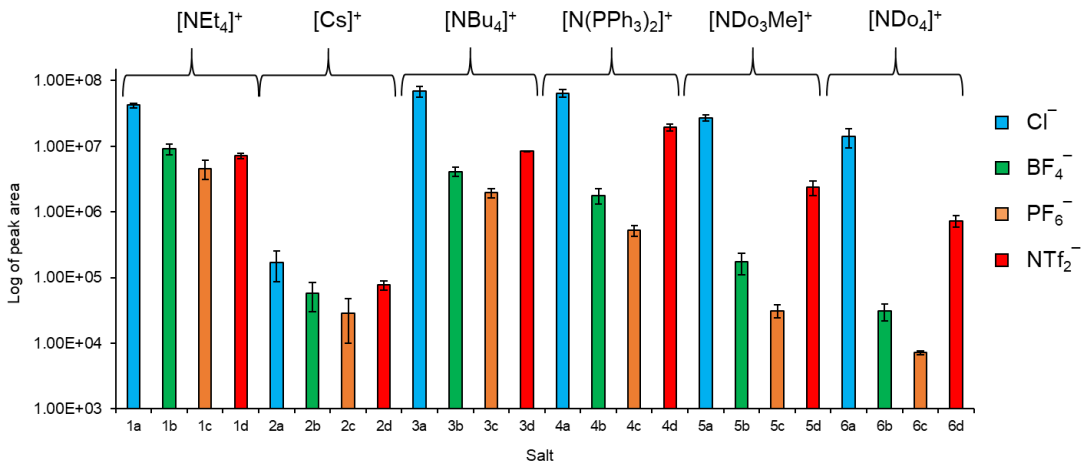

Figure 3.3. Peak area distribution in positive ion ESI-MS of salts in acetonitrile. The cations are represented as: 1= $[NEt_4]^+$; 2 = Cs^+; 3 = $[NBu_4]^+$; 4 = $[N(PPh_3)_2]^+$; 5 = $[NDo_3Me]^+$; 6 = $[NDo_4]^+$ and the anions are represented as: a = Cl^-; b = $[BF_4]^-$; c = $[PF_6]^-$; and d = $[NTf_2]^-$. The standard deviation of the mean (n = 3) is represented by the vertical bars.

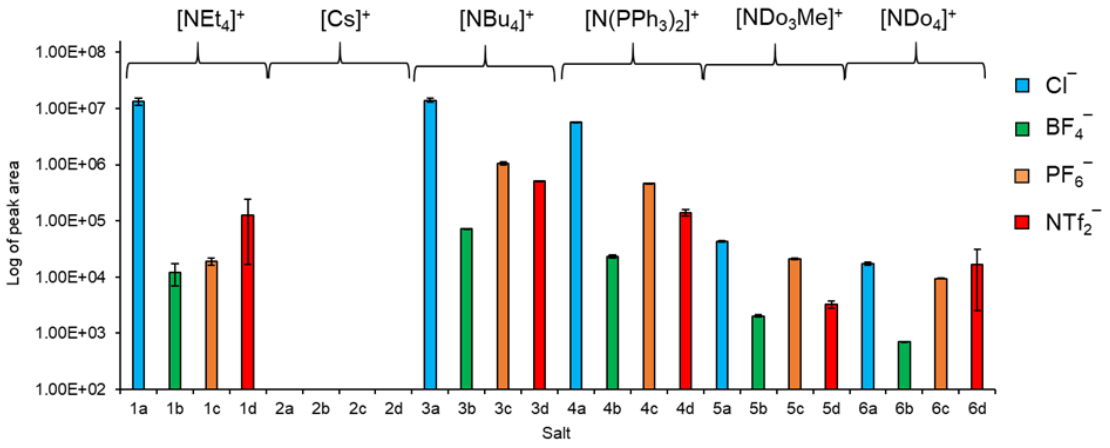

Figure 3.4. Peak area distribution in positive ion ESI-MS of salts in dichloromethane. The cations are represented as: 1= $[NEt_4]^+$; 2 = Cs^+; 3 = $[NBu_4]^+$; 4 = $[N(PPh_3)_2]^+$; 5 = $[NDo_3Me]^+$; 6 = $[NDo_4]^+$ and the anions are represented as: a = Cl^-; b = $[BF_4]^-$; c = $[PF_6]^-$; and d = $[NTf_2]^-$. Note: there is no peak area representation for all cesium salts given that cesium chloride is insoluble in dichloromethane, hence salt metathesis for the other counterions was not conducted. The standard deviation of the mean (n = 3) is represented by the vertical bars.

In polar solvents, such as, methanol and water/acetonitrile systems, polarity of the solvents could have influenced the solvation strength (between chloride and the solvents); as well, hydrogen bonding could also contribute to the solvation strength.[148] Figure 3.5 and Figure 3.6 show that cations paired with chloride anions as providing the highest ion counts.

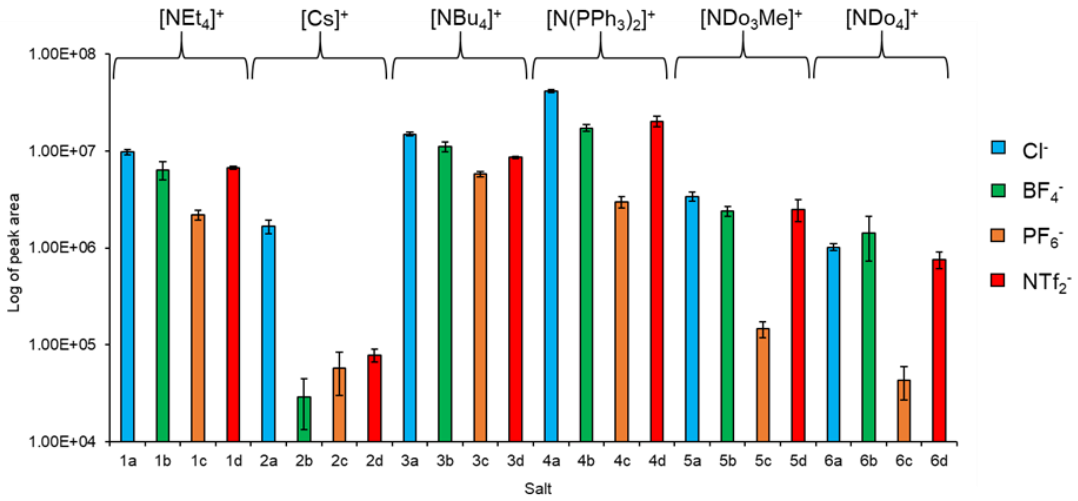

Figure 3.5. Peak area distribution in positive ion ESI-MS of salts in methanol. The cations are represented as: 1= $[NEt_4]^+$; 2 = Cs^+; 3 = $[NBu_4]^+$; 4 = $[N(PPh_3)_2]^+$; 5 = $[NDo_3Me]^+$; 6 = $[NDo_4]^+$ and the anions are represented as: a = Cl^-; b = $[BF_4]^-$; c = $[PF_6]^-$; and d = $[NTf_2]^-$. The standard deviation of the mean (n = 3) is represented by the vertical bars.

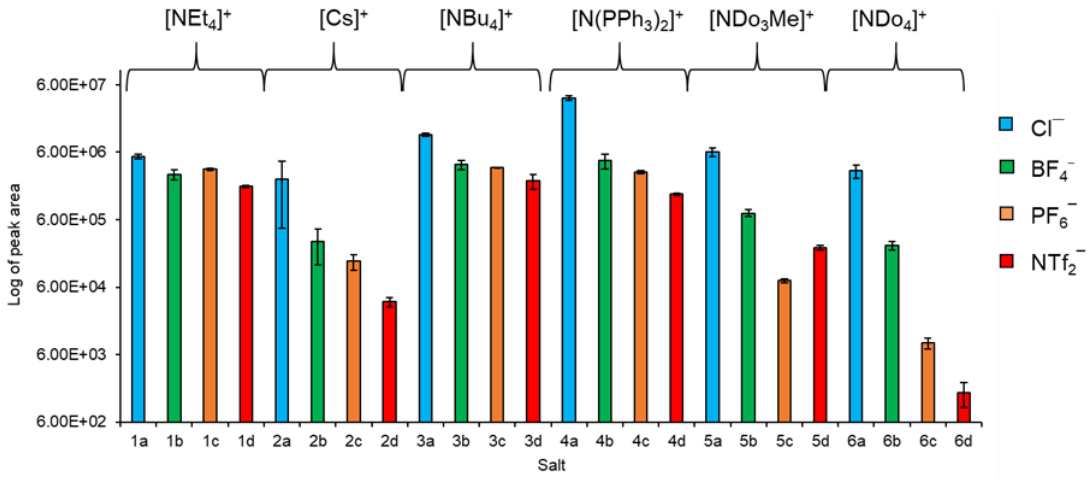

Figure 3.6. Peak area distribution in positive ion ESI-MS of salts in water/acetonitrile. The cations are represented as: 1= $[NEt_4]^+$; 2 = Cs^+; 3 = $[NBu_4]^+$; 4 = $[N(PPh_3)_2]^+$; 5 = $[NDo_3Me]^+$; 6 = $[NDo_4]^+$ and the anions are represented as: a = Cl^-; b = $[BF_4]^-$; c = $[PF_6]^-$; and d = $[NTf_2]^-$. The standard deviation of the mean (n = 3) is represented by the vertical bars.

It is possible that this is the case due to chloride being more easily oxidized than any of the other counterions, thus the ESI process as shown in Figure 3.7, generates a greater excess of charge for a given capillary voltage.[168–171]

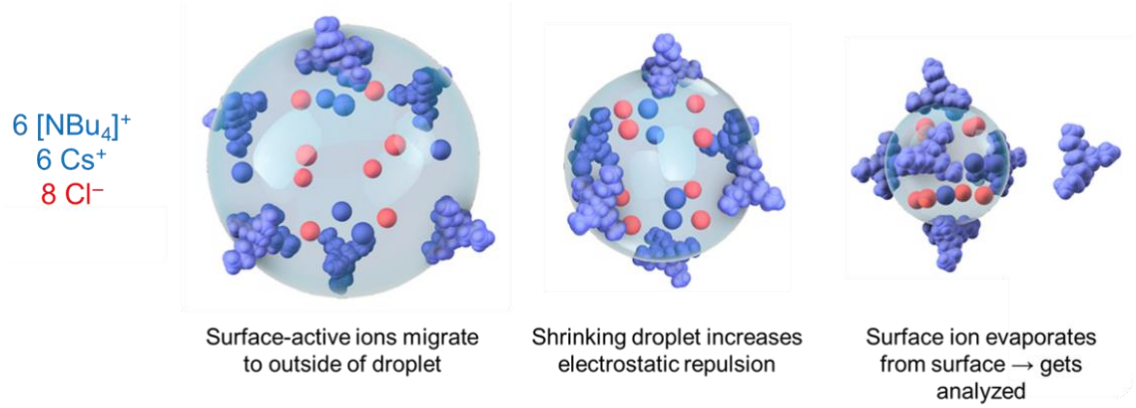

Figure 3.7. Ion evaporation process during electrospray ionization of analytes in a polar solvent.

The highest response exhibited by species paired with chloride anion could be attributed to their increase in conductivity as shown in Table 3.1. In respect of this, the molar conductivity of all electrolytes examined followed a trend whereby, halide species (except CsCl in acetonitrile) had a relatively higher molar conductivity as compared to polyatomic species (see Table 3.1). This result could be interpreted as, halide species being more conductive in solution; possibly due to a relatively less ion-ion interaction[172,173] in all solvent systems employed.

Table 3.1. Molar conductivities (units in Scm^2mol^{-1}) of solutions (10 μM) at room temperature.

Salt	Molar conductivity measured in MeOH	Molar conductivity measured in H_2O: MeCN (1:1)	Molar conductivity measured in MeCN	Molar conductivity measured in CH_2Cl_2
CsCl	101.01	90.91	33.33	-
$CsBF_4$	89.29	72.46	147.06	-
$CsPF_6$	95.24	74.07	135.14	-
$CsNTf_2$	91.74	75.76	117.65	-
NEt_4Cl	117.65	83.33	103.09	47.62
NEt_4BF_4	92.59	64.52	65.79	39.53
NEt_4PF_6	98.04	66.66	61.73	40.00
NEt_4NTf_2	94.34	69.44	106.38	37.59
NBu_4Cl	109.89	65.36	133.33	56.50
NBu_4BF_4	86.96	50.00	100.00	54.95
NBu_4PF_6	90.91	54.05	99.00	55.55
NBu_4NTf_2	83.33	54.64	95.24	52.08
$[N(PPh_3)_2]Cl$	75.76	71.43	101.01	36.36
$[N(PPh_3)_2]BF_4$	63.29	56.18	90.91	34.72
$[N(PPh_3)_2]PF_6$	66.66	58.48	98.04	35.09
$[N(PPh_3)_2]NTf_2$	58.82	60.61	90.09	33.33
NDo_3MeCl	58.48	67.57	86.96	33.33
NDo_3MeBF_4	54.64	55.55	83.33	31.75
NDo_3MePF_6	54.05	57.14	80.65	32.26
NDo_3MeNTf_2	55.55	58.48	84.75	31.06
NDo_4Cl	50.00	62.50	82.64	27.62
NDo_4BF_4	45.25	46.51	50.00	26.95
NDo_4PF_6	46.51	47.62	46.08	27.03
NDo_4NTf_2	40.00	55.55	80.00	26.32

In Figure 3.5 and Figure 3.6, it can be observed that the bulky hydrophobic flexible cation species $[NDo_3Me]^+$ and $[NDo_4]^+$ had a low response again; probably due to the formation of less surface-active premicellar species.[158] As shown in Figure 3.3, Figure 3.5 and Figure 3.6, tetraethylammonium and cesium ions (*m/z* 130 and *m/z* 132 respectively) have different peak area distributions in acetonitrile, methanol, and water/acetonitrile systems. Cs^+ had a poor response in the polar solvents, probably due to strong ion pairing that existed in the cesium species (e.g. CsCl);[167,174] as well as the overall relatively small size of the cesium species, thereby, the solvation strength was larger as compared to the tetraethylammonium species.

Furthermore, $[NBu_4]^+$ species had a better response in acetonitrile and dichloromethane as compared to $[N(PPh_3)_2]^+$ species, possibly due to a relatively higher molar conductivity in acetonitrile and dichloromethane (see Table 3.1); however, was less favoured in methanol and water/acetonitrile systems. These observations have clearly revealed that when an equimolar mixture of cations of different sizes were paired with weakly coordinating counterions ($[BF_4]^-$, $[PF_6]^-$, $[NTf_2]^-$) in polar and non-polar standard ESI solvents, there was no striking effect in their ESI response. Discrimination between masses of all species employed can be observed regardless of their equal amounts in solution due to possible non-uniform ion transmission in the mass analyzer (triple quadrupole) employed.[175,176]

Another notable observation was the highest relative intensity and peak area distribution for analytes in acetonitrile (Figure 3.2, and Figure 3.3) compared to analytes in the other solvent systems. This result agreed with previous findings by our group where it was observed that the aprotic polar solvent (acetonitrile) could solvate ions to a somewhat similar extent regardless of their morphology.[148]

3.3 Relationship between rigidity and response of analytes in ESI-MS

The correlation between rigidity and response of analytes was investigated by assessing an equimolar mixture of structurally different species of approximately the same molecular weights (*m/z* 353±14) in both polar and non-polar ESI solvents as shown in Figure 3.8.

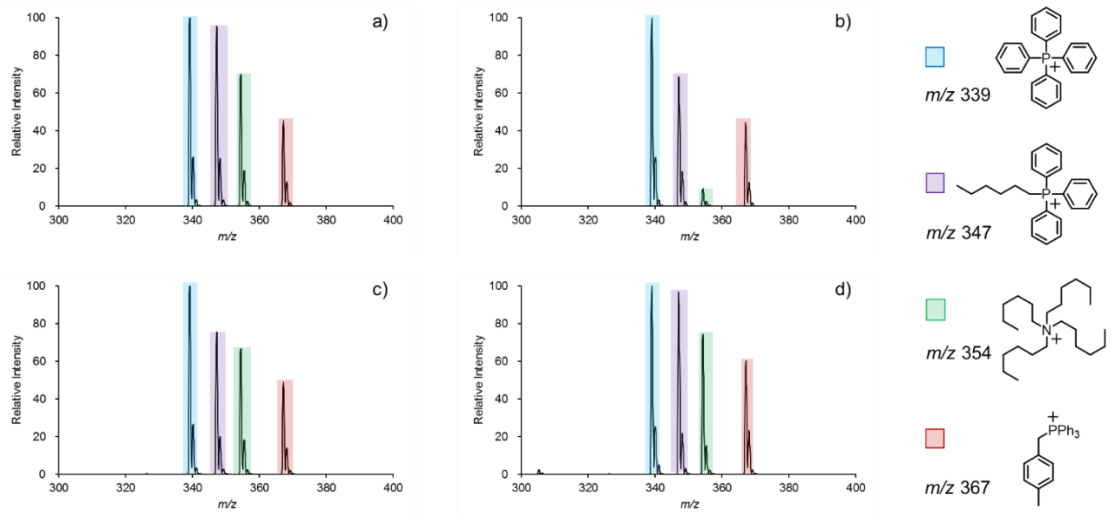

Figure 3.8. Positive ion ESI mass spectrum of an equimolar mixture of four cations paired with bromide counterion in: a) acetonitrile; b) water/acetonitrile; c) methanol; and d) dichloromethane.

In Figure 3.8, it can be observed that phosphonium species with rigid groups at *m/z* 339, $[PPh_4]^+$ and *m/z* 347, $[PPh_3C_6H_{13}]^+$ were more responsive than the ammonium species with flexible alkyl chains at *m/z* 354, $[N(C_6H_{13})_4]^+$ in both polar and non-polar solvents; however, a difference in design of the phosphonium species at *m/z* 367, $[Ph_3PCH_2C_6H_4CH_3]^+$ affected its response (relatively less surface-active) in all solvents employed.

These observations were also apparent in Figure 3.9, where $[PF_6]^-$ was the counterion, i.e. the counterion seems to play only a minor role in affecting the relative response of the various cations.

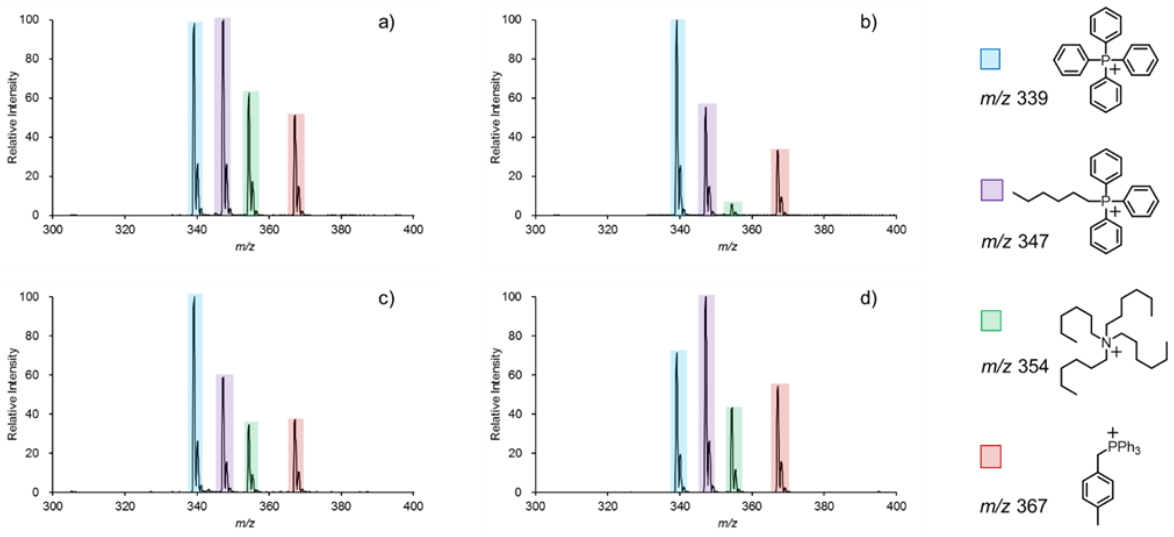

Figure 3.9. Positive ion ESI mass spectrum of an equimolar mixture of four cations paired with hexafluorophosphate counterion in: a) acetonitrile; b) water/acetonitrile; c) methanol; and d) dichloromethane.

The structural effect was further probed by evaluating an equimolar mixture of phosphonium salts in the form of $[Ph_3PCH_2C_6H_4R]^+[X]^-$, where R = H, CH_3, $CH(CH_3)_2$, CO_2CH_3; X = $[PF_6]^-$, in both polar and non-polar solvents. In this case, all four ions share a common structural feature. We have previously shown that such ions tend to show similar responses in reactions tracked by ESI-MS, whether measured directly[52] or observable by a flat total ion current for the duration of the transformation of one ion into another.[160,177,178] Figure 3.10 captures the relative intensities of the phosphonium analytes examined.

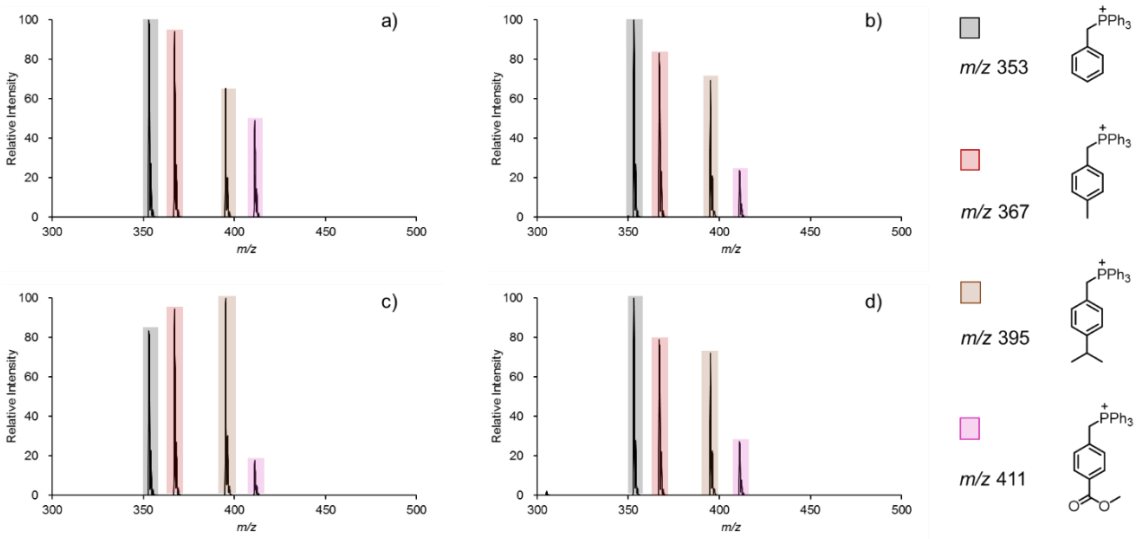

Figure 3.10. Positive ion ESI mass spectrum of an equimolar mixture of four phosphonium species paired with hexafluorophosphate counterion in: a) acetonitrile; b) water/acetonitrile; c) methanol; and d) dichloromethane.

In relation to Figure 3.10, the relative intensities of the species decreased upon changes in R group (H > CH_3 > $CH(CH_3)_2$ > CO_2CH_3) in acetonitrile, water/acetonitrile, and dichloromethane solvents. In methanol, hydrophobic species at *m/z* 395, $[Ph_3PCH_2C_6H_4CH(CH_3)_2]^+$; *m/z* 367, $[Ph_3PCH_2C_6H_4CH_3]^+$; and *m/z* 353, $[Ph_3PCH_2C_6H_5]^+$ (decreasing hydrophobicity from higher mass to lower mass) were all more responsive than the ester-functionalized phosphonium ion at *m/z* 411, $[Ph_3PCH_2C_6H_4CO_2CH_3]^+$. The higher polarity of this species increases its affinity for the solvent, making it less likely to migrate to the surface of the droplet and in turn migrate to the gas phase through ion evaporation.

3.4 Conclusions

An examination of a variety of solvents, cation structures, cation functionality, and counterion identities in the context of electrospray ionization response has revealed that all these factors play a part in dictating peak height. Polar protic solvents tend to discriminate between different ions most strongly; contrastingly, acetonitrile was the best in terms of most closely representing concentration with peak area. Smaller species tend to have higher responses overall, most likely due to an increase in conductivity and/or ease of oxidation. These effects were particularly marked for species paired with chloride over the other analytes investigated (all polyatomic). Any effect due to reduced ion pairing due to a larger counterion seems very minor. Cations that have long flexible groups are significantly under-represented in mass spectra compared to rigid ions of the

same *m/z* ratio. Cations with functional groups capable of forming stronger intermolecular forces with the solvent are also likely to be under-represented. Collectively, these observations should provide experimentalists with some explanatory power in explaining discrepancies between different analytes; and help them design experiments to either mitigate or exacerbate these effects as desired.

3.5 Experimental

All chemicals were purchased from Sigma-Aldrich and employed as received. Salts with hexafluorophosphate $[PF_6]^-$, tetrafluoroborate $[BF_4]^-$ and bistriflimide $[NTf_2]^-$ counterions were prepared by reaction of an equimolar mixture of the salts with $AgBF_4$, $AgPF_6$ and $AgNTf_2$ in methanol (MeOH), acetonitrile (MeCN), water/acetonitrile (H_2O/MeCN 1:1) and dichloromethane (CH_2Cl_2) at room temperature. For example, the salt with hexafluorophosphate counterion in methanol was prepared by reaction of an equimolar mixture of the chloride salts (1 equivalent, 10 mmol in methanol) with silver hexafluorophosphate (1 equivalent, 10 mmol in methanol) at room temperature; a gray precipitate was formed and removed by gravity filtration. The filtrate was characterized by electrospray ionization mass spectrometry (ESI-MS) whereby $[PF_6]^-$ counterion was identified as *m/z* 145 in the negative ion mode (see Appendix B). This procedure was carried out in acetonitrile, water/acetonitrile, and dichloromethane.

Phosphonium salts were prepared by a general procedure as follows: Triphenylphosphine (10 mmol) and a bromobenzyl compound (10 mmol) were dissolved in 20 mL of toluene; were stirred at room temperature under nitrogen for 48 hrs. The precipitate was filtered out of solution by vacuum filtration which produced a white solid. A saturated aqueous solution of the product obtained was added to a saturated aqueous sodium hexafluorophosphate solution to swap the bromide counterion for hexafluorophosphate counterion at room temperature; a white precipitate was recovered through vacuum filtration.

Prior to ESI-MS analysis, all analytes were further diluted to 10 μM. The ESI-MS spectra were obtained by means of a Waters Acquity Triple Quadrupole Detector (TQD). The instrument parameters employed were: capillary voltage, 2.5 kV; cone voltage, 15 V; extraction voltage, 1.0 V; source temperature was, 80°C for methanol; 110°C for water/acetonitrile; 90°C for acetonitrile; and 50°C for dichloromethane; desolvation temperature was 180°C for methanol; 200°C for water/acetonitrile; 190°C for acetonitrile and 150°C for dichloromethane. Cone gas flow rate, 100 L/h; desolvation gas flow rate, 100 L/h. Scan time was 3 s. All diluted analytes were fed into the mass spectrometer with a gastight analytical syringe connected to PEEK tubing and a syringe pump at a flow rate of 10 μL/min. A conductivity experiment was also carried out by measuring the solution resistances of analytes at room temperature using a potentiostat (Gamry Instruments, Reference 600, Warminster, PA, USA); the solution resistances measured were converted to molar conductivities.

Chapter 4 Magnesium-accelerated Maillard reactions in beer brewing

This chapter has been published and appears in the following publication:

"Magnesium-accelerated Maillard reactions drive differences in adjunct and all-malt brewing" I. Omari, H. Charnock, A. Fugina, E. Thomson, and J.S. McIndoe, Journal of the American Society of Brewing Chemists, 2020.

4.1 Brief background on Maillard reaction

Maillard reaction is a non-enzymatic browning reaction discovered by Louis Maillard in the early 20th century.[179] The reaction occurs when sugar (or a compound with carbonyl group) reacts with amino acid (or a compound with amino group) in the presence of heat.[179] The Maillard reaction is responsible for the formation of colour, flavour and aroma in foods.[179]

The colour compounds formed during Maillard reaction are nitrogenous or non-nitrogenous low molecular weight (LMW) compounds, and high molecular weight (HMW) polymeric compounds (>5 kDa).[180,181] The LMW compounds are formed because of the decomposition of Amadori products whereas the HMW compounds (known as melanoidins) are formed due to enolization, decarboxylation, condensation, and polymerisation of the LMW compounds.[182] The colour produced (colour ranges from pale yellow to dark brown) during Maillard reaction is influenced by the reactants involved in the reaction and the reaction time;[183–185] and the flavour and aroma

compounds (such as, Strecker aldehydes, furfurals and furanones) formed during the reaction is attributed to the decomposition of amino acid and sugar (termed, "Strecker degradation").[180,186]

Following Maillard's discovery, Amadori investigated further and found that *N*-glycosides were reactive products of Schiff bases in a Maillard reaction.[179] These reactive products were later referred to as "Amadori products".[179] However, Heyns also identified a variant of Amadori product from ketoses which was termed "Heyns product".[187] Scheme 4.1 shows the first reaction scheme of the Maillard reaction proposed by John Hodge[188] in 1953.

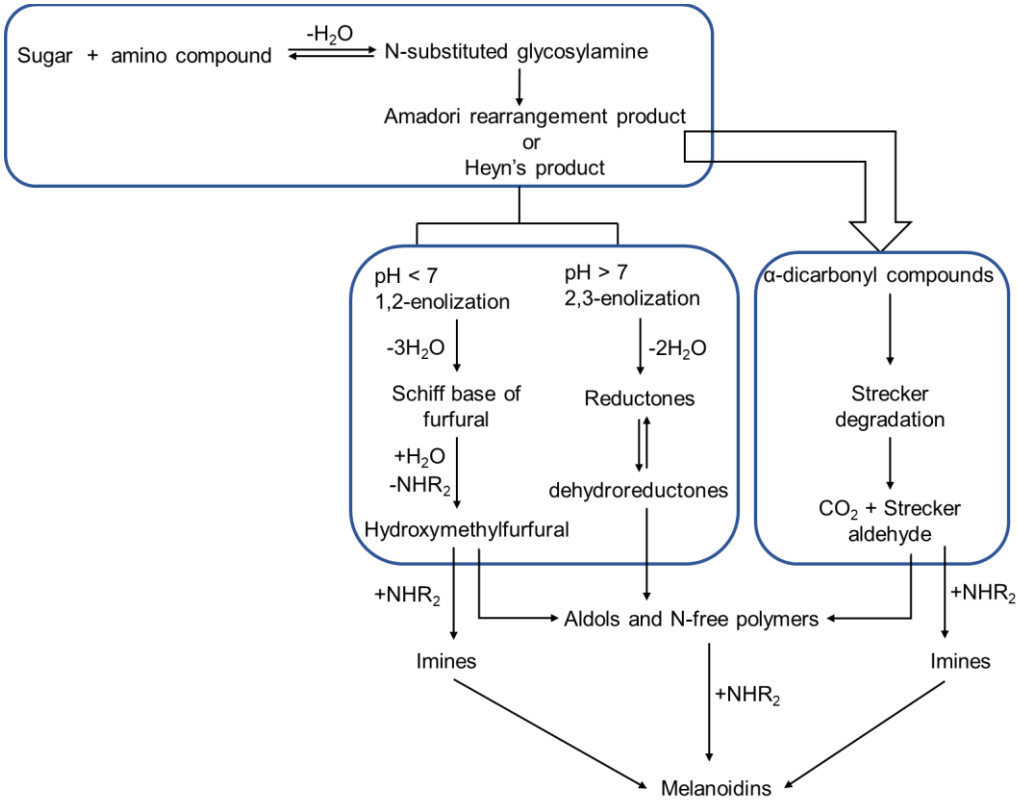

Scheme 4.1. Proposed Maillard reaction scheme by Hodge.[188]

4.2 Magnesium-catalyzed Maillard reaction in beer brewing

Beer is traditionally brewed with malted barley because of its high enzymatic content, which enables the fast conversion of starch to fermentable sugars that give rise to alcohol, carbon dioxide and flavour compounds during fermentation by yeast. As the industry has evolved, brewers have introduced alternative or adjunct grains and derivatives such as corn, rice, sorghum, wheat, oats, corn syrup and corn starch, which in the absence of malted barley are generally incapable of producing full starch conversion. Brews falling short of sufficient enzyme activity for starch conversion typically require exogenous enzyme addition; therefore, it is technically possible for a beer to contain a greater proportion of adjunct grains than malted barley. While certain of these materials serve cost efficiency motives, each contributes different textures and flavours to beer along with micronutrients required by yeast in fermentation.[189] In relation to flavours in beer, divalent cations such as calcium and magnesium are known to play key roles in pH, mouthfeel and bitterness in beer brewing.[190–194] Grains are the primary source of cations in beer and in the early stages of brewing are milled and mixed with hot water to trigger enzyme activity. Typically, brewers account for calcium shortfalls by adding calcium chloride and calcium sulfate, and the balance of these can impact bitterness and body in the finished product.[191,195–198] Despite the growing consensus among food scientists that magnesium plays an important role in Maillard chemistry,[199–201] gaps remain in our understanding of its impact on beer flavour development.

Magnesium concentration is known to have diverse impacts on quality outcomes of brewing.[194] Its impact on bitterness was documented half a century ago in a study demonstrating that at 158 ppm, magnesium drives humulone isomerization 200-fold above background levels in a model solvent system.[190] Likewise, Bastgen *et al.* recently showed that hop utilization, measure of the heat-induced isomerization of hop acids that serves as the main driver of bitterness in beer, is pushed beyond the 30-40% limit typically observed by brewers by increasing the concentration of magnesium by 40 ppm.[202] Magnesium was shown to promote the activity of proteinases during barley and sorghum germination, key steps in the malting process, indicating a potential parallel role in the low-temperature mashing steps that define many traditional and craft brewing operations.[203] Impacts of magnesium on yeast physiology have been explored.[204,205] Although one group found no effect of modifying the magnesium to calcium ratio on yeast fermentation performance,[206] Walker was able to demonstrate a protective effect of magnesium on yeast viability following ethanol and heat shock.[205] Magnesium was also found to counteract the agglomerating effect of calcium on yeast cells.[206]

While these studies illustrate the diversity of impacts that magnesium exerts on various qualities of beer, its effects on food science more generally are far-reaching. The acceleration of Maillard chemistry by magnesium is proposed to occur through reduction of water mobility.[207,208] An increase in the rate of browning (melanoidin pigment formation) using model Maillard reactions (e.g. xylose-glycine system) in the presence of magnesium has been reported.[200] Melanoidins exhibit both antioxidant and pro-oxidant

properties, which contribute to the stabilization of colour, aroma, flavour and foam.[209–217] While pale beers were assumed to have shorter shelf life than dark beers, given the relatively low concentration of melanoidin present in pale beers,[212,218] recent work indicates increased oxidative potential in beer containing darker malts owing to the heat-triggered release of bound iron during specialty malt processing.[219,220] It stands to reason that these impacts would extend to other foods (nuts, coffee, and meats, for example) that depend on development of Maillard reactions for sensory qualities.

During routine analysis of soluble metals concentration by staff at Phillips Brewing & Malting Co. (Figure 4.1), high magnesium levels in unfermented beer compared with other metals (see Figure 4.2) led to an investigation of magnesium levels in commercial beers brewed from barley and mixed grains, such as a combination of rice, corn and barley.

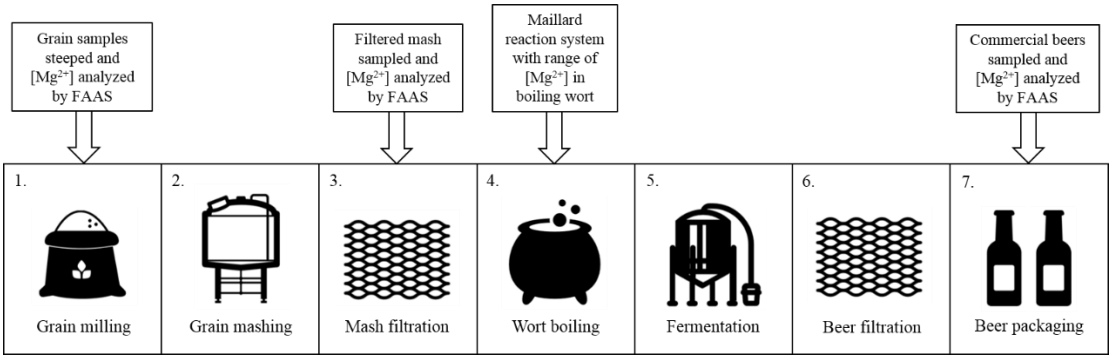

Figure 4.1. Sampling and experimental events associated with brewing process steps at Phillips Brewing & Malting Co. To generate a nutrient-rich sugar solution suitable fermentation by brewing yeast, grain is milled to a flour consistency (1), mashed with water at approximately 65°C (2), and filtered to remove grain particulate (3). At this stage, the liquid is known as wort, which is boiled after the addition of hops for approximately 1 hour (4) prior to chilling and fermentation by yeast (5). Upon completion of fermentation, solids including yeast and hops are removed by filtration (6) to generate finished beer ready for packaging (7). Arrows above processes indicate sampling points in this study.

In their examination, they found a relatively high magnesium content in beers brewed from barley compared with that of mixed grains (see Figure 4.3). At this point, they were interested in understanding the importance of magnesium concentration in brewing, with a focus on Maillard chemistry, which contributes to the flavour quality of beer. In this chapter, the influence of magnesium on colour formation during key brewing steps was studied by simulating Maillard chemistry under optimized reaction conditions. Model systems combined maltose with amino acids proline, phenylalanine, and leucine, subjected to increasing concentrations of magnesium. The Maillard reaction products were characterized using electrospray ionization mass spectrometry (ESI-MS). Ultraviolet-visible spectroscopy (UV-Vis) was used to monitor changes in colour during reactions. Results obtained from the model systems provided a benchmark for analysis of brewhouse wort, a grain extract comprising a complex assortment of sugars, amino acids, and micronutrients. This work describes chemical mechanisms that may underpin colour formation driven by magnesium in both simplified reaction systems and simulated brewhouse chemistry.

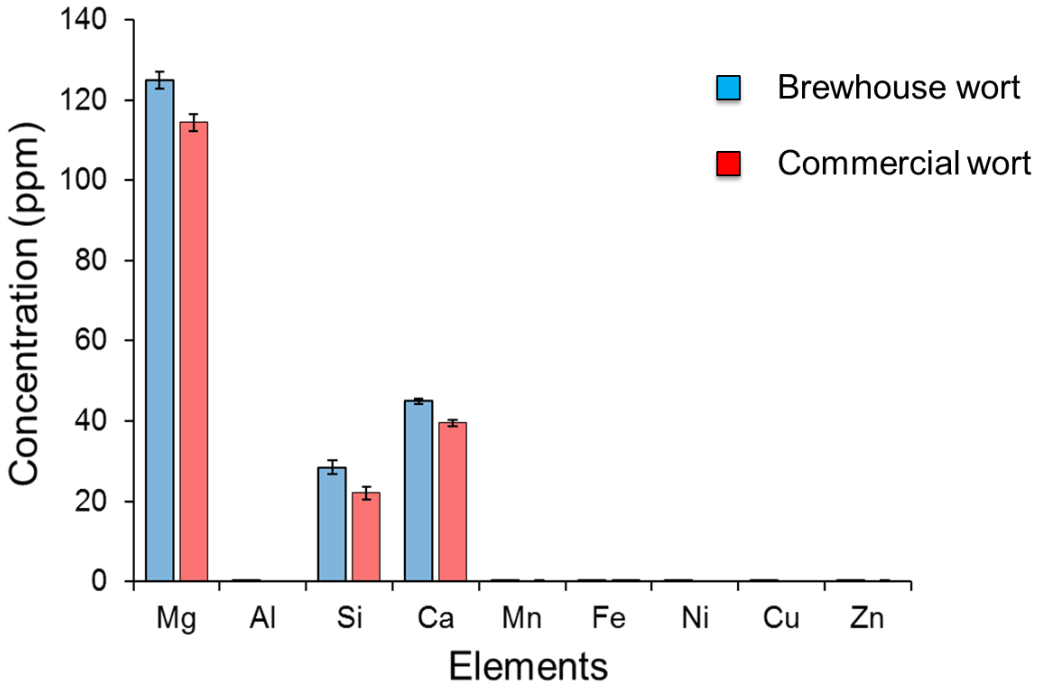

Figure 4.2. Metal concentration in wort (unfermented beer). These concentrations were measured by means of flame atomic absorption spectroscopy (FAAS) by staff at Phillips Brewing & Malting Co.

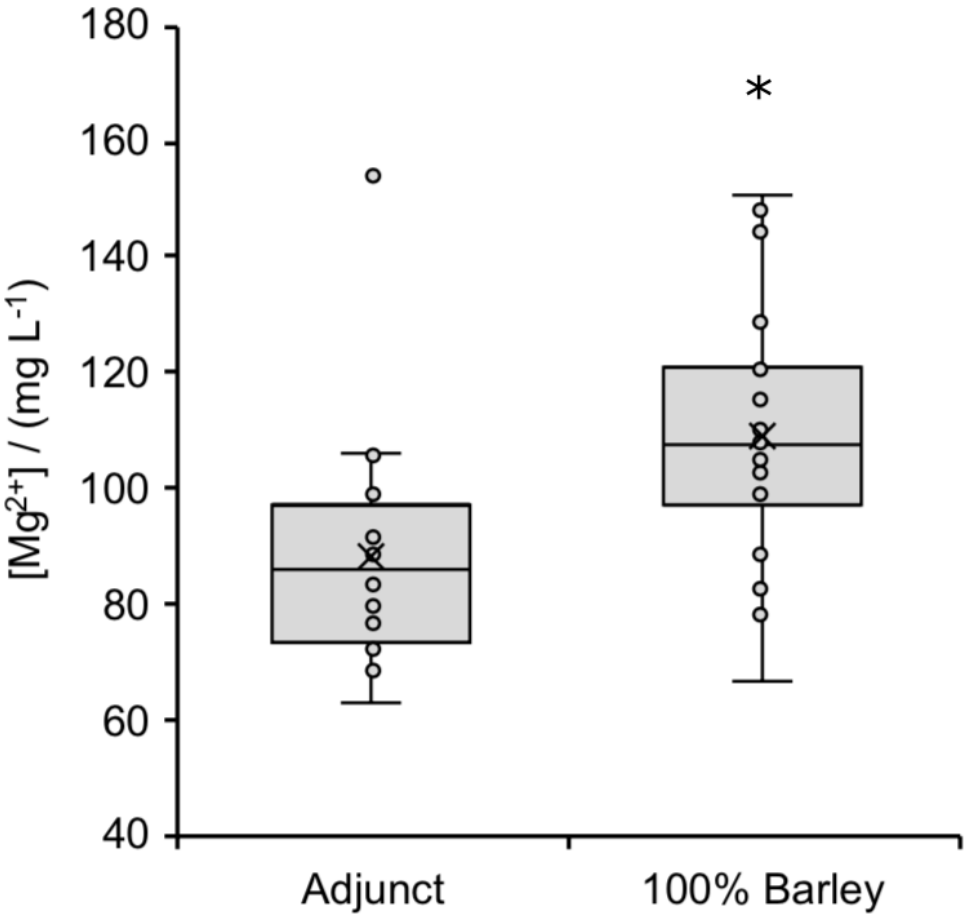

Figure 4.3. Magnesium content of commercial beers brewed with barley plus adjunct grains (17 beers) or 100% barley (21 beers). The top and bottom of each box represents the first and third quartiles, respectively, with the interior horizontal line representing the median (exclusive) distance between regions. The upper and lower whiskers represent the maximum and minimum, respectively, with calculated outliers positioned outside of the whiskers. The mean is indicated with a cross marker. Star denotes significant difference between groups. These concentrations were measured by means of flame atomic absorption spectroscopy (FAAS) by staff at Phillips Brewing & Malting Co.

4.3 Analysis of Maillard chemistry by UV-Vis spectroscopy

UV-Vis spectroscopy was employed to measure appearance of Maillard reaction products at various concentrations using model systems and brewhouse wort, with increasing absorbance at 430 nm indicating the formation of coloured Maillard reaction products. All model systems produced visible yellow colour during the reaction, indicating Maillard product formation. Correspondingly, absorbance values increased with reaction time (Figure 4.4, Figure 4.5). The presence of magnesium in the Maillard reaction increased the absorbance values with reference to the control (0 ppm Mg^{2+}), and when magnesium concentration was increased from 2 ppm through 200 ppm, absorbance values increased correspondingly. The trend shown matched results obtained for the maltose-leucine system (see Appendix C). The maltose-phenylalanine system (Figure 4.5) shows slightly higher absorbance values than the maltose-proline (Figure 4.4) and maltose-leucine systems (Figure 4.6) after 10 minutes, possibly due to differences in the reactivity of the amino acids as established by Kwak *et al.*,[221] where phenylalanine was found to be more reactive than proline and leucine (phenylalanine>proline~leucine).[221]

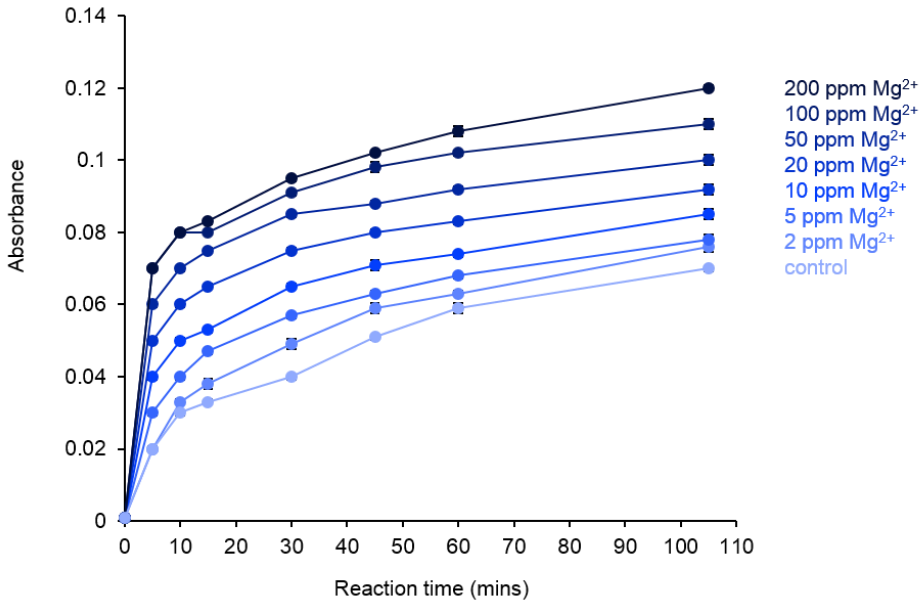

Figure 4.4. Influence of magnesium on absorbance (430 nm) of a maltose-proline model system. Standard deviation (n = 3) is represented by vertical bars.

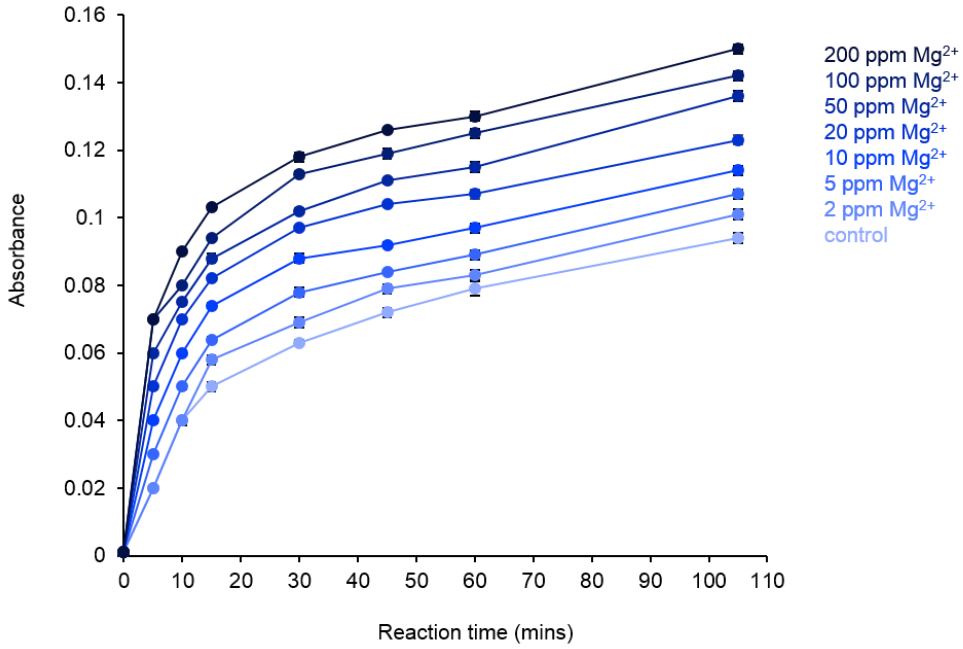

Figure 4.5. Influence of magnesium on absorbance (430 nm) of a maltose-phenylalanine model system. Standard deviation (n = 3) is represented by vertical bars.

In the maltose-proline-phenylalanine-leucine model system (Figure 4.6), regardless of the presence of magnesium, absorbance values were higher for all reaction times than those shown in single amino acid systems (Figure 4.4, Figure 4.5, Figure 4.6). This likely reflects increased complex species formation from a greater diversity of Maillard reaction products.

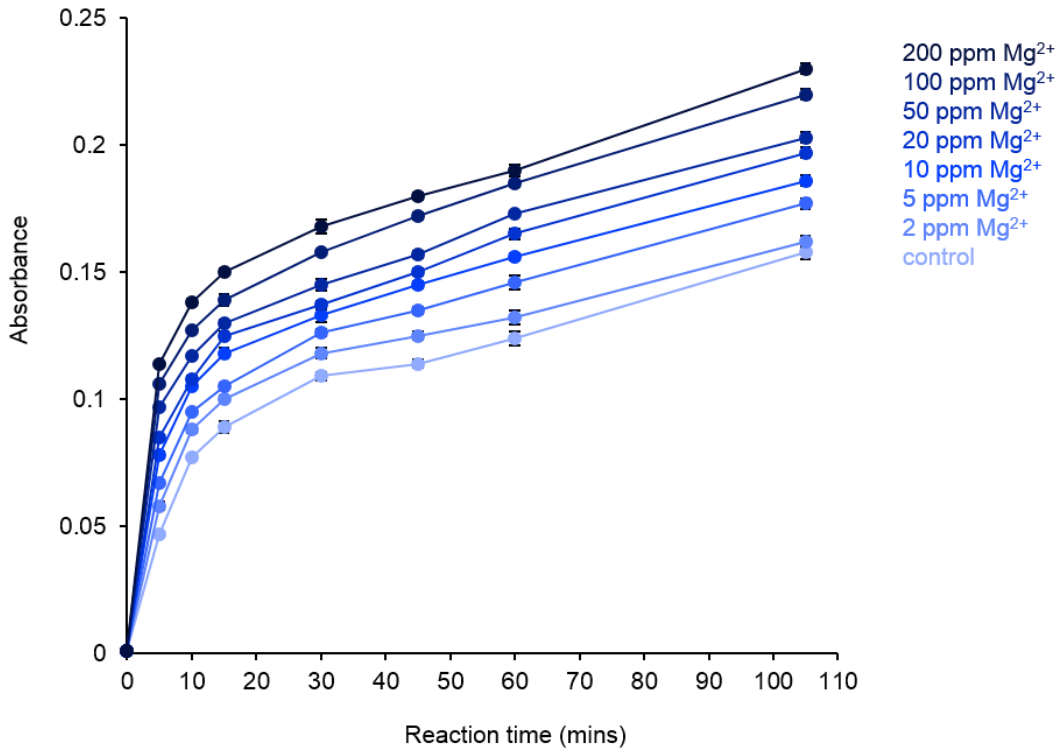

Figure 4.6. Influence of magnesium on absorbance (430 nm) of a maltose-proline-phenylalanine-leucine model system. Standard deviation (n = 3) is represented by vertical bars.

To test these model system findings against simulated brewing conditions, the effect of magnesium concentration on Maillard chemistry was investigated at different concentrations in boiling wort. The wort used had an amber colour prior to the reaction, and unlike in model systems, it showed no visible colour change in the course of reaction. However, similar to the results for the model systems (Figure 4.4, Figure 4.5, Figure 4.6), absorbance values increased across the reaction period for all treatments (Figure 4.7). This suggests a central position of magnesium relative to other metals in catalyzing Maillard reactions, given that in this system the spiked magnesium was supplementary to the existing metal content of the wort (as shown in Figure 4.2). The higher starting absorbance of wort (0.240) than that measured in the model systems is due to the contribution of Maillard reaction products from specialty kilned and toasted malts in the brew recipe. The complex mixture of unreacted maltose, other reducing sugars and amino acids in the wort[222,223] is likely responsible for the additional Maillard reactions observed during the boil.

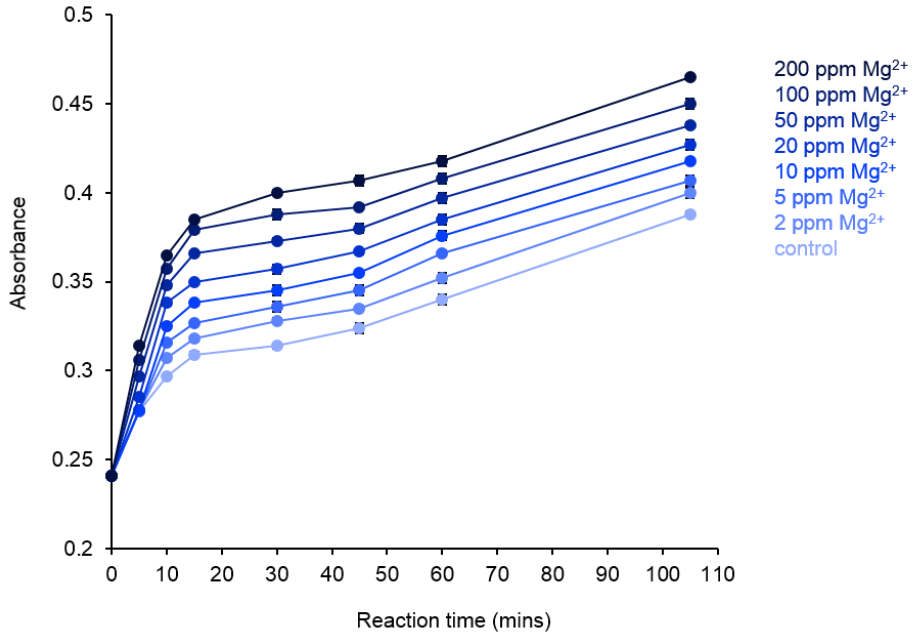

Figure 4.7. Representation of the influence of Mg^{2+} on the change of absorbance over time of wort. Standard deviation (n = 3) is represented by the vertical bars.

Change in absorbance at 430 nm serves as a proxy for change in concentration of the Maillard reaction products over time, given the direct relationship between absorbance and concentration.[224,225] This suggests that the increased absorbance values in the presence of magnesium is related to an increase in concentration of Maillard reaction products. The influence of magnesium could be explained by the findings of Matiacevich *et al*., whereby magnesium chloride was employed to decrease water mobility and increase Maillard reaction rates of a model system.[207] In the context of their findings, it is likely that as the magnesium concentration increased from 2 ppm through 200 ppm, the water mobility decreased correspondingly, and accelerating Maillard reactions in all systems. However, for the wort system, other salts present could have possibly contributed to the decrease in water mobility (diffusion of water molecules).[193] In addition, the presence of magnesium ions in Maillard reaction could facilitate

nucleophilic addition reactions between the carbonyl groups and amino groups after Lewis acid activation of the carbonyl group,[226] given that Maillard chemistry occurs between carbonyl groups of reducing sugars and amino groups of amino acids, peptides or proteins.[223,227–229]

In all reactions studied - model systems and wort alike - the highest rate occurred early, followed by a change in slope to a value that was essentially uniform for all magnesium concentrations. Nonetheless, the reaction rate at early stages of the reaction is substantial, giving the Maillard reaction a substantial kickstart. One possible explanation is that magnesium ions get effectively sequestered by chelating agents generated through Maillard reactions or already present in the mixture,[230–232] and the magnesium ions lose efficacy as rate accelerators. This was modeled by adding 20 ppm magnesium at the start of the reaction and adding repeat aliquots of 20 ppm magnesium at 20, 40, 60 and 80 minutes (Figure 4.8). Additions at 20 minutes and onward had no effect on absorbance measurements, suggesting that deactivating agents are present in sufficient quantity to render additional magnesium ineffective.

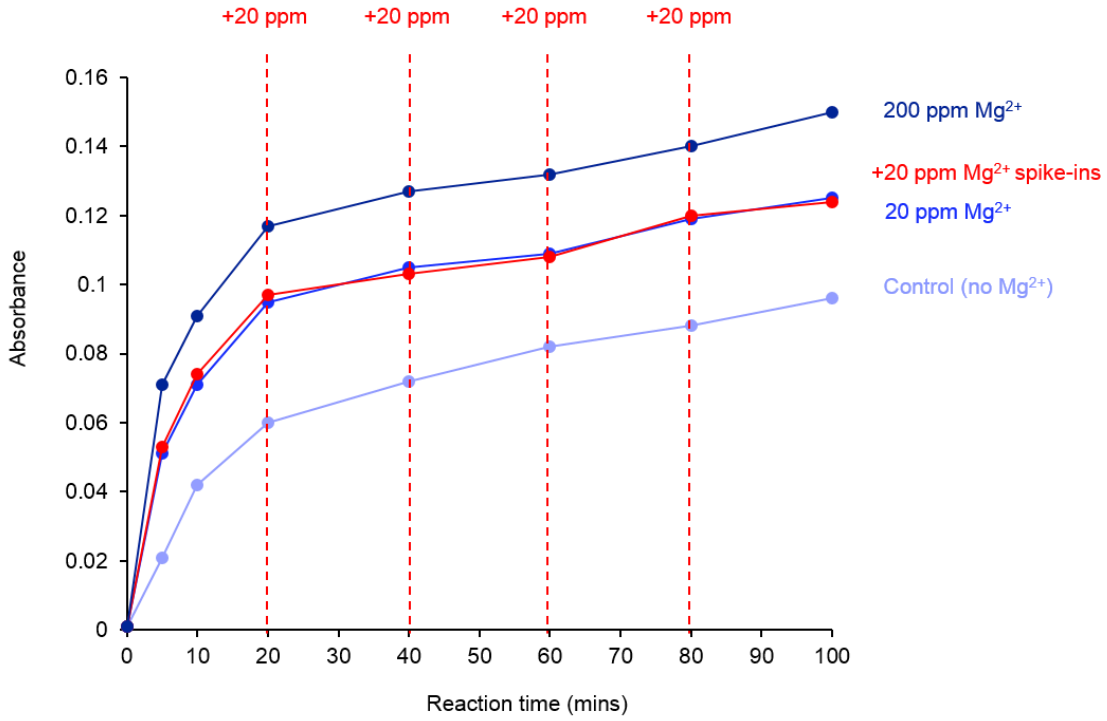

Figure 4.8. Representation of the influence of Mg^{2+} on the change of absorbance over time on the reaction between maltose and phenylalanine. Four experiments are represented here: no added Mg^{2+}, 20 ppm added Mg^{2+}, 200 ppm added Mg^{2+}, and 20 ppm Mg^{2+} repeatedly spiked at 0, 20, 40, 60 and 80 minutes.

4.4 Characterization of Maillard reaction products with ESI-MS

Investigation by ESI-MS revealed Maillard reaction species in the positive ion mode in a Mal/Pro system (Figure 4.9.). The reaction products were identified as low molecular weight species. The base peak in Figure 4.9 represents a protonated proline species at *m/z* 116.1167 ($C_5H_{10}NO_2$). A reaction scheme leading to the formation of the observed ions is shown in Scheme 4.2. The other model systems followed a similar reaction scheme (see Scheme 4.3 and Scheme 4.4)

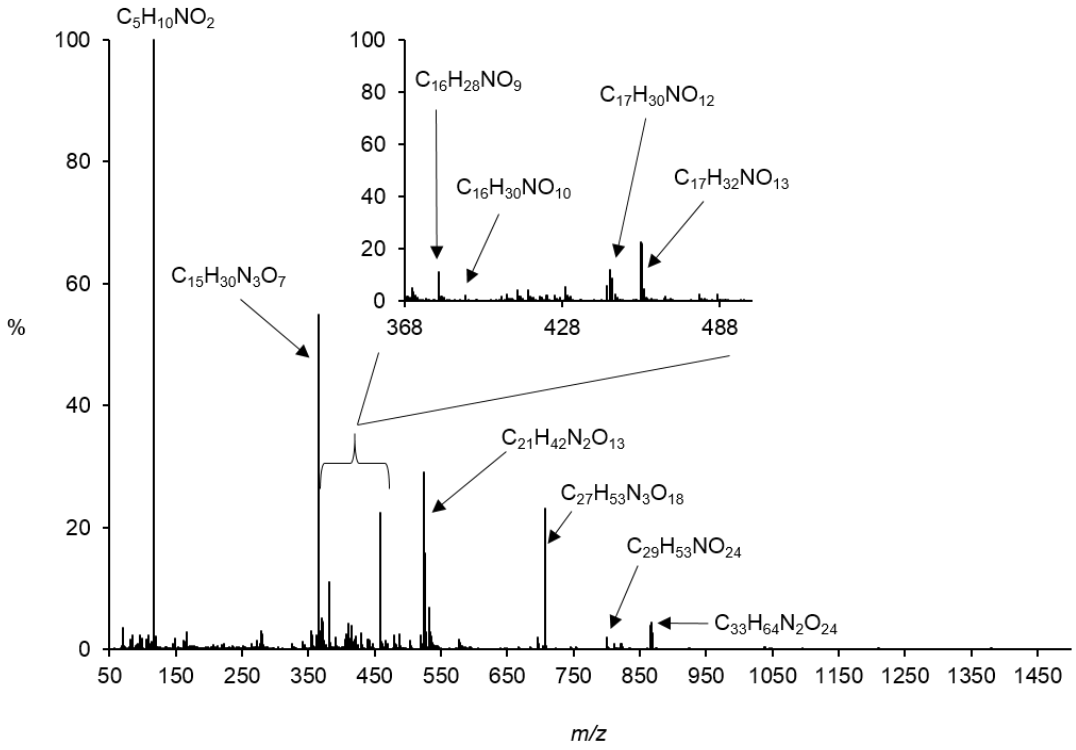

Figure 4.9. Positive ion mode ESI-MS of the Maillard reaction species of a maltose-proline system after reflux at 130^{o}C for 1 hour. Inset: expansion of the *m/z* 368-488 range.

The Maillard reaction proceeded through a nucleophilic addition between the carbonyl group of the reducing sugar and the amino group of the amino acid to produce a Schiff base which rearranged to form an Amadori product,[227,233–236] seen at *m/z* 440.0258 ($C_{17}H_{30}NO_{12}$) (Figure 4.9). The reaction continued via decarboxylation and dehydration to yield products at *m/z* 396.0127 ($C_{16}H_{30}NO_{10}$) and *m/z* 378.0646 ($C_{16}H_{28}NO_9$) respectively. The Amadori product further reacted with maltose to produce the species at *m/z* 799.5289 ($C_{29}H_{53}NO_{24}$). The species at *m/z* 364.6972 ($C_{15}H_{30}N_3O_7$) was identified as an aggregate of proline and water; this aggregate ion formed a cluster with maltose, observed at *m/z* 706.9716 ($C_{27}H_{53}N_3O_{18}$). An aggregate ion comprising the Amadori product and water was seen at *m/z* 458.0182 ($C_{17}H_{32}NO_{13}$). A cluster of the decarboxylated product at *m/z* 396.0127 ($C_{16}H_{30}NO_{10}$) and water was identified at *m/z* 414.0393 ($C_{16}H_{33}NO_{11}$). This species also formed a cluster with proline, and the aggregate ion was observed at *m/z* 529.6497 ($C_{21}H_{42}N_2O_{13}$). In addition, the observed ion at *m/z* 870.4815 ($C_{33}H_{64}N_2O_{24}$) represented an aggregate ion of maltose and the species at *m/z* 529.6497 ($C_{21}H_{42}N_2O_{13}$).

To obtain further information on the reaction products, product ion scan experiments (ESI-MS/MS) were carried out. For example, the Amadori product at *m/z* 440.0258 ($C_{17}H_{30}NO_{12}$) produced a product ion at *m/z* 422.0425 ($C_{17}H_{28}NO_{11}$) by losing 18 Da (H_2O) (Figure 4.10). This implied that the Amadori product readily undergoes dehydration.

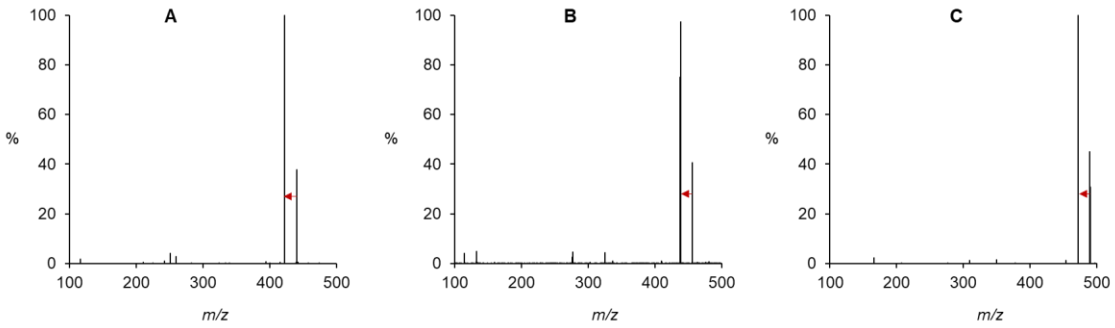

Figure 4.10. ESI-MS/MS spectra of the Amadori product (precursor ion) at: A) *m/z* 440.0258 and a product ion at *m/z* 422.0425 of a maltose-proline system; B) *m/z* 456.0224 and a product ion at *m/z* 438.2437 of a maltose-leucine system; C) *m/z* 490.0257 and a product ion at *m/z* 472.0215 of a maltose-phenylalanine system.

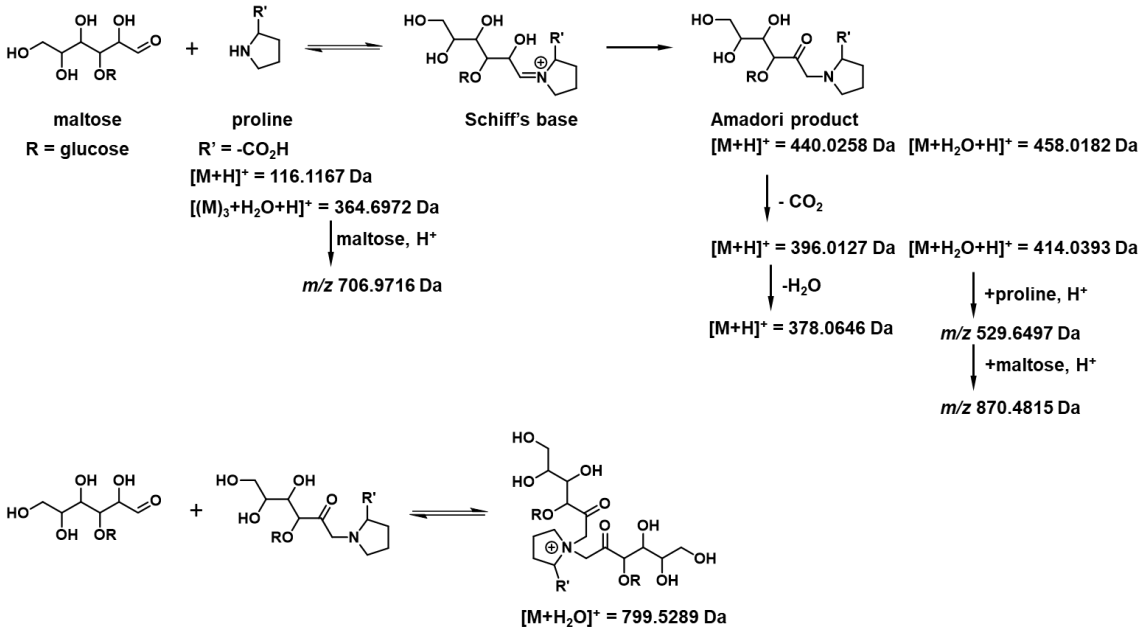

Scheme 4.2. Maillard reaction scheme of a maltose-proline system with mass-to-charge ratios of the reaction species.

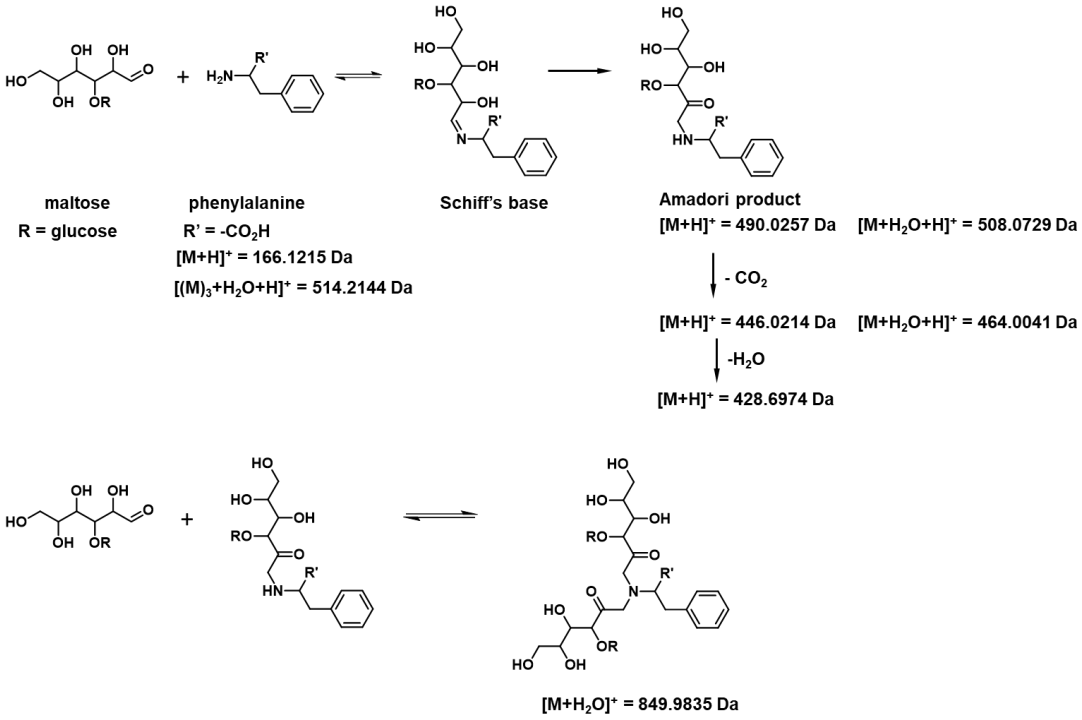

Scheme 4.3. Maillard reaction scheme of a maltose-phenylalanine system with mass-to-charge ratios of the reaction species.

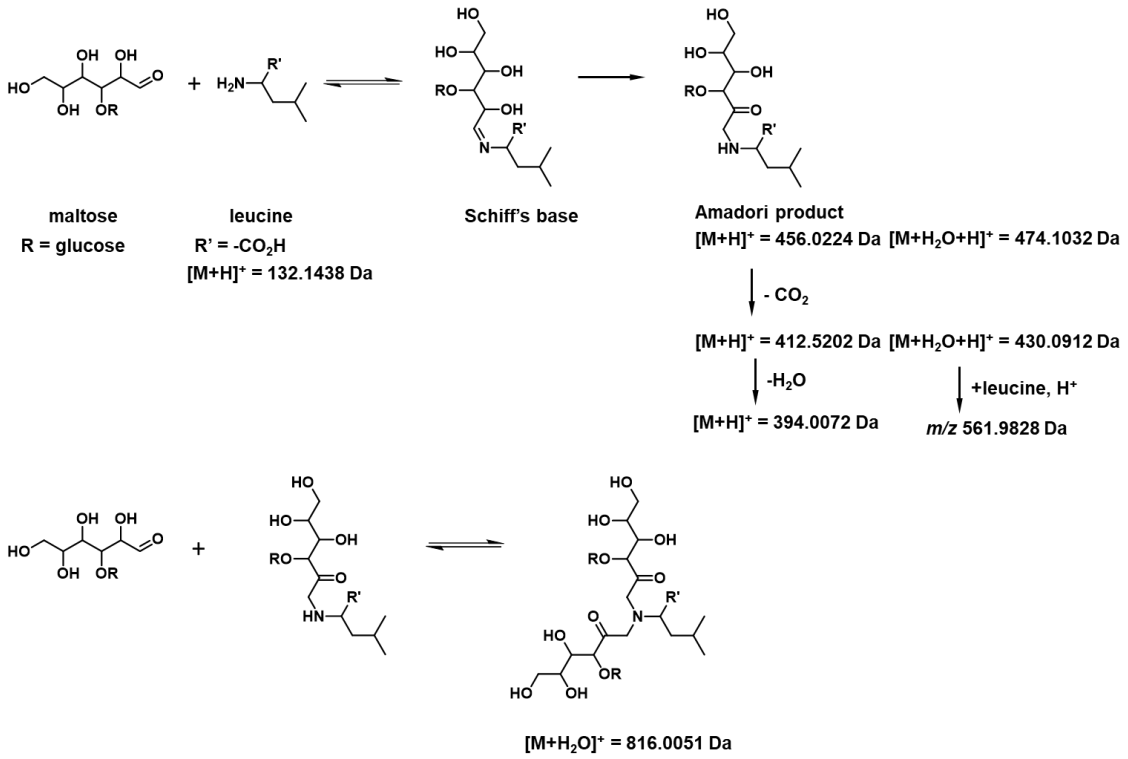

Scheme 4.4. Maillard reaction scheme of a maltose-leucine system with mass-to-charge ratios of the reaction species.

Furthermore, no difference was observed in mass spectra for the various reaction times employed at reflux (5 mins through 105 mins); meanwhile, varying the magnesium concentration did not change the distribution of species in the mass spectra of all systems (see Figure 4.11 and Appendix C) It is likely that any high molecular weight species formed were less surface active, thereby exhibiting poor ESI response. We have previously reported that such behaviour can occur depending on the environment of the analytes under study.[237] Also, a significant difference in the mass spectra could have been achieved for longer reaction times (ten hours or more) as reported by Hemmler *et al*.[238] However, not more than 105 mins was employed in order to simulate real world effects, whereby wort is typically boiled for 45-90 mins before yeast fermentation.[239]

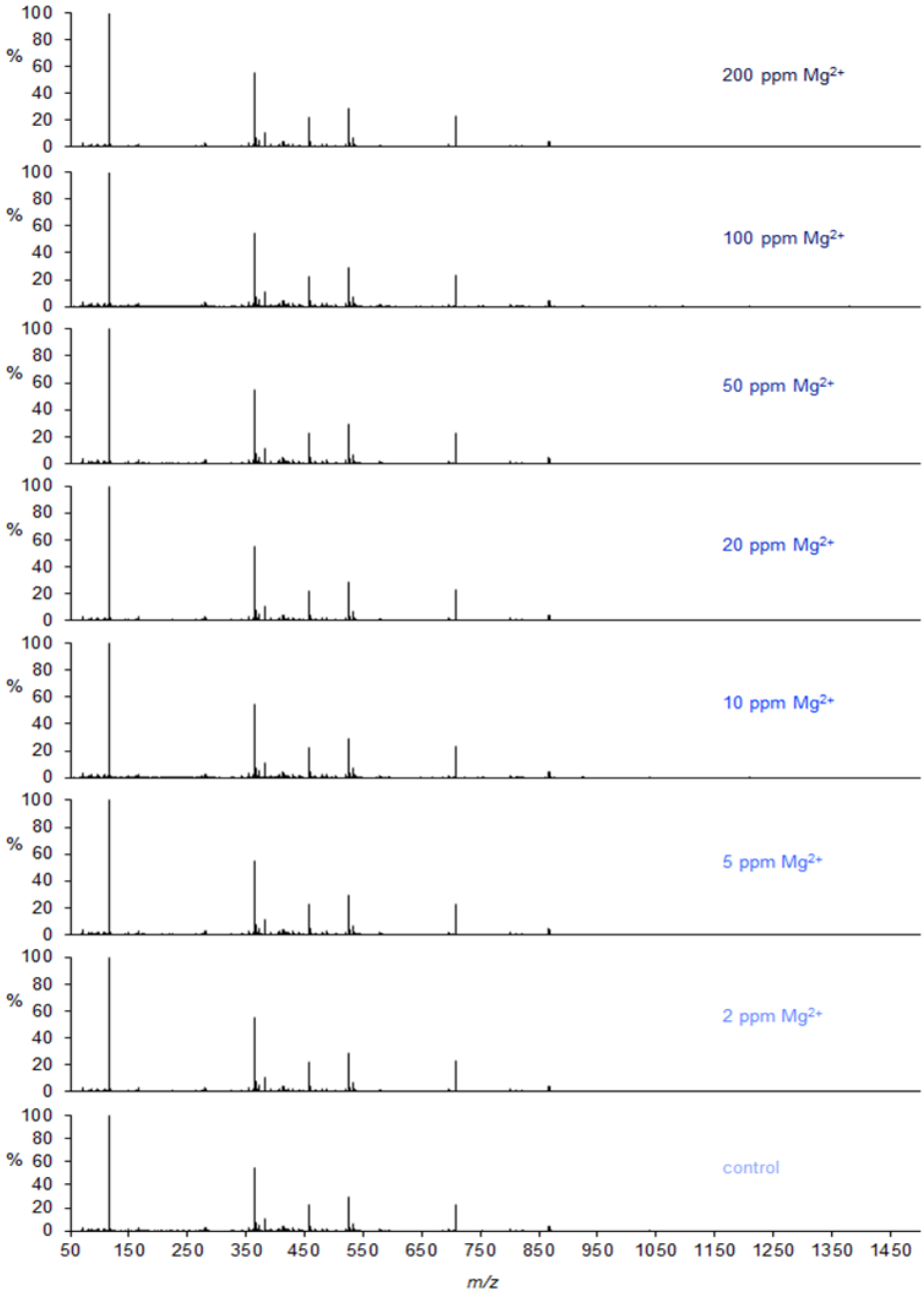

Figure 4.11. Positive ion mode ESI-MS of the Maillard reaction species of maltose-proline system after reflux at 130°C for 105 mins with various concentrations of magnesium.

4.5 Conclusions

Addition of magnesium at levels typically found in barley facilitates Maillard reactions between sugars and amino acids by acting as a Lewis acid catalyst. Low molecular weight Maillard reaction species were characterized by ESI-MS. Examination of the reaction by UV-Vis spectroscopy showed that the catalytic effect of magnesium is significant but short-lived, persisting for about 20 minutes, at which point all reactions proceeded at the same rate regardless of magnesium supplementation. Further additions of magnesium at later stages in the reaction also had no accelerating effect on the rate of reaction. The results suggest that a contributing factor to the colour and flavour of beer is the concentration of magnesium present at the start of the wort boil and that monitoring magnesium could offer improved control over Maillard product formation in beers for flavour and colour development.

4.6 Experimental

Chemicals and reagents

Maltose monohydrate (95%), L-proline (99%), L-leucine (⩾ 98%), D-phenylalanine (⩾ 98%), magnesium chloride ($MgCl_2$) and formic acid were purchased from Fisher Scientific (Ottawa, ON). Brewhouse wort was supplied by Phillips Brewing & Malting Co. (Victoria, BC, Canada). All chemicals were used as received. Deionized water was obtained from a Millipore Milli-DI water purification system.

Maillard reaction

Model systems of maltose-proline [Mal (10 mmol, 10 eq)/Pro (1 mmol, 1 eq)], maltose-phenylalanine [Mal (10 mmol, 10 eq)/Phe (1 mmol, 1 eq)], maltose-leucine [Mal (10 mmol, 10 e)/Leu (1 mmol, 1 eq)] and maltose-proline-phenylalanine-leucine [Mal (10 mmol, 10 eq)/Pro (1 mmol, 1 eq)/Phe (1 mmol, 1 eq)/Leu (1 mmol, 1 eq)] were prepared. Deionized water containing 0 ppm, 2 ppm, 5 ppm, 10 ppm, 20 ppm, 50 ppm, 100 ppm or 200 ppm $MgCl_2$ was added to the model systems and to brewhouse wort. Maltose was chosen as reducing sugar given its predominance in brewing worts.[222] Amino acids were selected based on the ability of brewing yeast to produce them from exogenous sources, where proline is non-essential, leucine is important and phenylalanine is vital to yeast growth and healthy fermentation.[240] However, each of these amino acids could contribute to the flavour or visual quality of beer.[241,242] The range of magnesium concentration (0 – 200 ppm) was selected to exceed the range of magnesium concentrations measured in commercial beers (as shown in Figure 4.3). All analytes were prepared in triplicate and

heated to reflux at 130ºC for 5 mins, 10 mins, 15 mins, 30 mins, 45 mins, 60 mins and 105 mins; and cooled to room temperature.

UV-Vis spectroscopy

Prior to absorbance measurements, the cooled analytes were gravity filtered, and the filtrates were diluted with deionized water. Spectroscopy was performed using an ASEQ Instruments LR-1 compact spectrometer (version 2.1, Configuration B). Absorbance was measured at 430 nm for all analytes.

ESI-MS

Prior to ESI-MS analysis, the cooled analytes were gravity filtered; the filtrates were diluted to 0.001% v/v with deionized water, and 0.1% v/v formic acid was added to the analytes. The ESI-MS spectra were obtained by means of a quadrupole-time of flight (Q-TOF) SYNAPT G2-Si instrument (Waters Corp., Manchester, UK). Instrument parameters were set as follows: capillary voltage 3 kV, cone voltage 20 V, source offset 30 V, source temperature 100°C, desolvation temperature 200°C, cone gas flow rate 100 L/h, desolvation gas flow rate 100 L/h, nebuliser 2.5 bar, scan time 3 s. All analytes were fed into the mass spectrometer with a Hamilton GASTIGHT® syringe connected to PEEK tubing and a syringe pump at a flow rate of 10 μL/min. MS/MS experiments were performed with a trap collision energy between 2-20 V. Interpretation of mass spectra was facilitated using chemcalc.org.[243]

Chapter 5 Dynamic ion speciation during hydrolysis of aryltrifluoroborates

This chapter has been published and appears in the following publication: “Dynamic ion speciation during hydrolysis of aryltrifluoroborates” I. Omari, L.P.E.Yunker, J. Penafiel, D. Gitaari, A.S. Roman and J.S. McIndoe, Chemistry – A European Journal, 2020.

5.1 Introduction

Many organoboronic acids are known to be inherently unstable to oxidation or protolytic deboronation; making their benchtop handling and storage difficult.[244,245] As an alternative, chemists sometimes use stable, easy to handle organoborate salts. As such, organotrifluoroborates, along with N-methyliminodiacetic acid (MIDA) boronates,[246–249] have become common organoboron sources in the Suzuki-Miyaura reaction.[250–259] They require hydrolysis[260–262] prior to the coupling reaction and the Lloyd-Jones research group has extensively studied this hydrolysis reaction by nuclear magnetic resonance (NMR).[263–265] They proposed that in THF-water (including a base), a biphasic system with three mechanisms of hydrolysis is at work (Scheme 5.1). The hydrolysis is catalyzed in path A by acid and is correspondingly retarded by base.[263] Fluoride dissociation by path B is accelerated by base, and a third path C is active in the aqueous phase for hydrophilic substituents and is accelerated by base.[263] They noticed that the biphasic system needed to reach a critical pH (induction period) for the reaction to start through path A.[263] Considering that organotrifluoroborates are anionic, the dynamics of ions formed during its hydrolysis (i.e. $[RBF_n(OH)_{3-n}]^-$, n = 0-3) were investigated by pressurized sample infusion (PSI) coupled with electrospray ionization mass

spectrometry (ESI-MS).[64,266] In addition, changes in pH due to speciation during hydrolysis could be measured in parallel using a pH meter.

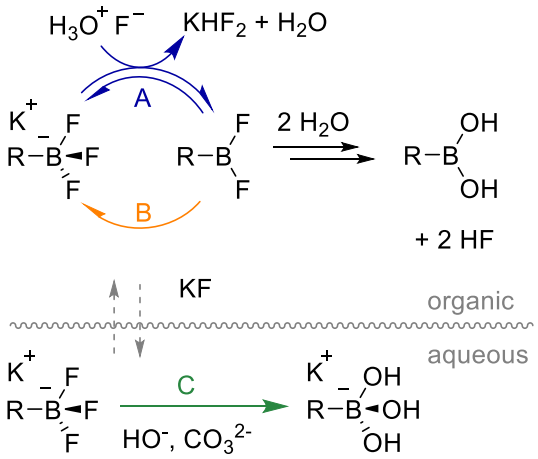

Scheme 5.1. Trifluoroborate hydrolysis pathways proposed by Lloyd-Jones and Perrin (R = alkyl, aryl).[263,267]

5.2 Real-time monitoring of trifluoroborate hydrolysis by ESI-MS and pH analysis

Five organotrifluoroborate potassium salts (p-tolyltrifluoroborate, p-methoxyphenyltrifluoroborate, cyclohexyltrifluoroborate, isopropyltrifluoroborate and phenyltrifluoroborate) were employed for the investigation. The first four borates were shown by Perrin[267] and Lloyd-Jones[263] to be the fastest hydrolyzing examples, and therefore were the best match for our methodology (PSI-ESI-MS gathers spectra on a timescale of seconds, so dense data can be collected in minutes). However, we also explored the reactivity of phenyltrifluoroborate (found to be a slow hydrolyzing example by Perrin[267] and Lloyd-Jones[263]), for an insight into its rate of hydrolysis using our technique. The hydrolysis was studied with a 1:3 ratio of organotrifluoroborate to base (Cs_2CO_3) and a THF/H_2O ratio of 10:1. In order to avoid saturation issues in our mass spectrometer, concentration of the borate was kept at 1.8 mM. The reaction at slow (~168 rpm) and fast (~600 rpm) stir rates were examined in a round-bottomed flask and in a Schlenk tube. Reactions were also monitored separately using a pH meter.

The anionic speciation profile of the reaction mixture prior to addition of base and water was simple, showing signals only for $[ArBF_3]^-$ (Figure 5.1A) and its corresponding aggregate ion $[(ArBF_3)_2K]^-$ (generated due to an increase in concentration of the borate in the droplet formed during the electrospray ionization process[268–270]). Addition of base and water soon resulted in a profusion of new peaks (Figure 5.1B). These peaks could be assigned to partially hydrolyzed, dehydrated, and aggregate ions.

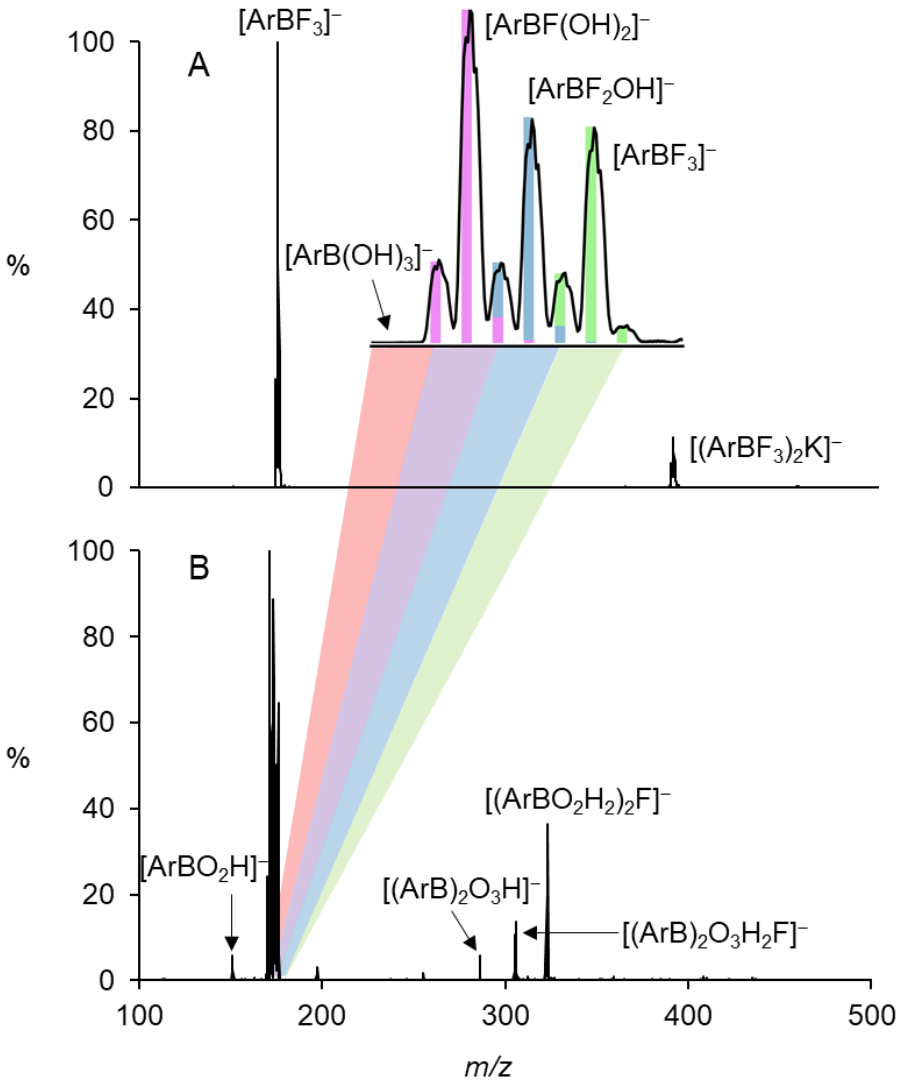

Figure 5.1. (A) negative ion mass spectrum of $KArBF_3$ in THF. (B) negative ion mass spectrum of the same solution, 20 minutes after addition of water and Cs_2CO_3. Inset: magnification of the $[ArBF_n(OH)_{3-n}]^-$ (n = 0-3) region of the spectrum at t = 20 minutes.

Table 5.1. Mass and assignment of species observed during hydrolysis of potassium p-methoxyphenyltrifluoroborate substrate.

m/z	Assignment
175	$[ArBF_3]^-$
173	$[ArBF_2(OH)]^-$
171	$[ArBF(OH)_2]^-$
169	$[ArB(OH)_3]^-$
151	$[ArBO_2H]^-$
285	$[(ArB)_2O_3H]^-$
305	$[(ArB)_2O_3H_2F]^-$
323	$[(ArBO_2H_2)_2F]^-$
389	$[(ArBF_3)_2K]^-$
483	$[(ArBF_3)_2Cs]^-$

Each progressive species in the conversion from $[RBF_3]^-$ (**1**) through to $[RB(OH)_3]^-$ (**7**) (Scheme 5.3) was expected, but the equilibria are more complex. Aggregates, such as $[(RBF_3)_2M]^-$ (M = K or Cs), dehydrated species, such as $[RBO_2H]^-$ (**8**) and $[R_2B_2O_3H]^-$ (**9**); and mixed dimers, such as $[R_2B_2O_3H_2F]^-$ (**10**) were observed. Given that dehydrated boronic acids are known to adopt cyclic structures,[271–274] **9** was assigned as a hydrogen-bond stabilized boroxine-type structure.

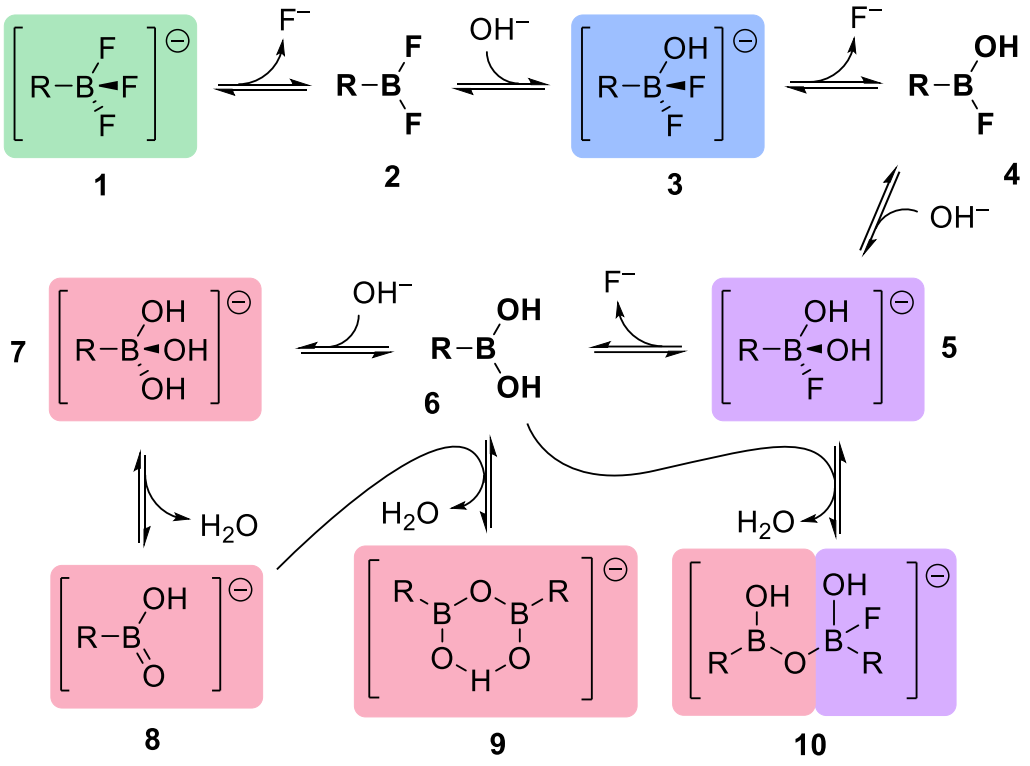

Scheme 5.2. Proposed equilibria for trifluoroborate hydrolysis. Highlighted species are ionic and observable by ESI-MS. Structural connectivity is proposed based on structures of these molecular formulae in the literature.[275]

Species **8** is of relevance for a Suzuki-Miyaura reaction, as it is structurally part of a pre-transmetallation intermediate proposed by Denmark.[275,276] For substrates with electron withdrawing R groups,[267] such as phenyltrifluoroborate, *p*-methoxyphenyltrifluoroborate or *p*-tolyltrifluoroborate, the formation of **8** will be more favored (due to $RB(OH)_2$ being less stabilized)[263] than for the cyclohexyltrifluoroborate and isopropyltrifluoroborate ($RB(OH)_2$ is more stabilized due to π-donation or hyperconjugation[263]) salt hydrolysis. The ratio of intensities for ions **7**:**8** was found to vary for each different R group of the borates in all reactions, and also varied with pH (Figure 5.2).

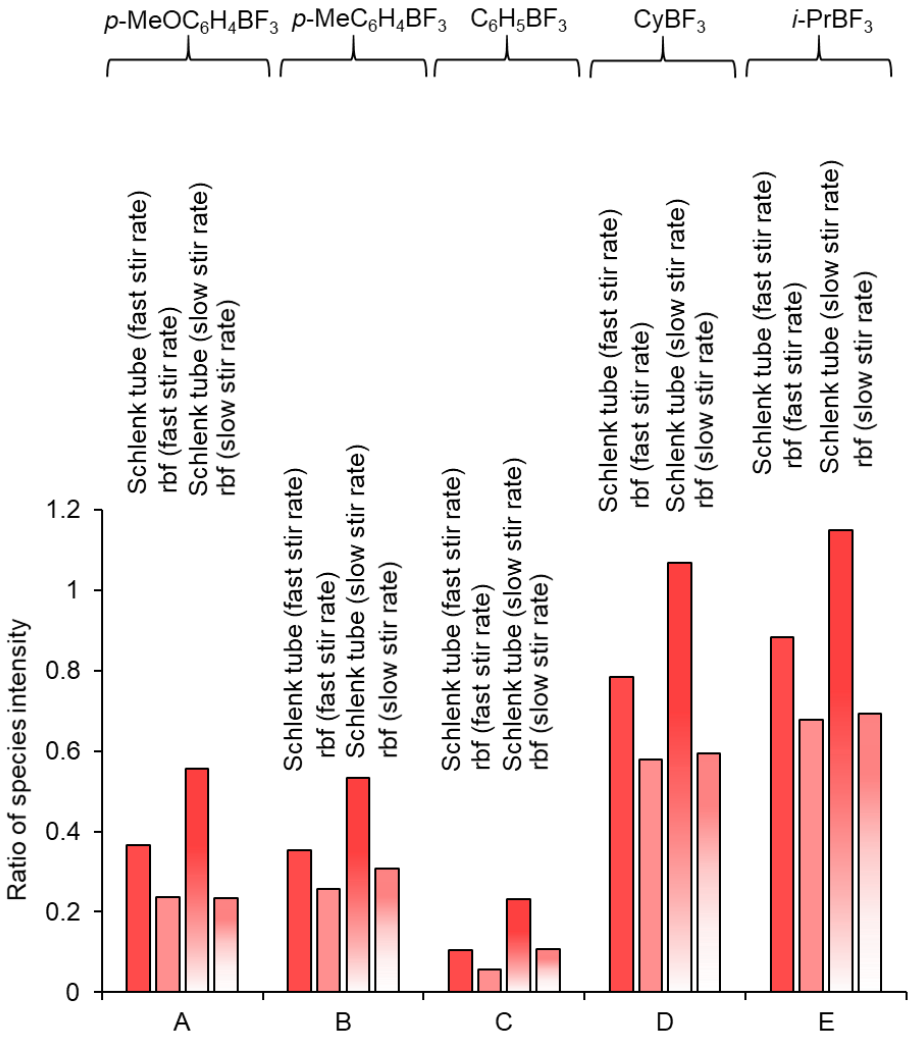

Figure 5.2. Representation of ratio of **7**:**8** during hydrolysis of potassium salts of A) p-methoxyphenyltrifluoroborate B) p-tolyltrifluoroborate C) cyclohexyltrifluoroborate in THF/H_2O (10:1) containing Cs_2CO_3; reaction was conducted in a Schlenk tube and round-bottomed flask at fast and slow stir rates. **7** and **8** represents $[ArB(OH)_3]^-$ and $[ArBO_2H]^-$ respectively. Fully shaded bars represent fast stir rate while the half-shaded bars represent slow stir rate.

No species corresponding to $[KF_2]^-$, $[CsF_2]^-$, $[BF_4]^-$, nor $[B(OH)_4]^-$ were observed. $[KF_2]^-$ and $[CsF_2]^-$ are byproducts of path A,[263] and $[BF_4]^-$ and $[B(OH)_4]^-$ are protodeboronation byproducts.[277] All numbered species exhibited dynamic behaviour and could be classified into different types according to their degree of hydrolysis. All species related to each $[ArBF_{3-n}(OH)_n]^-$ (n = 0-3, i.e., **1**, **3**, **5** and **7** respectively) through aggregation or dehydration were grouped together for the sake of simplicity of interpretation. Since different ions provide different ESI-MS response,[278] and neutrals are not detected at all (unless associated with a charged entity), traces of species in this study do not directly correspond to concentrations. Rather, they indicate the approximate proportion of the charged components of a mixture that can be attributed to a particular ion (or group of related ions).

The combination of pH measurements with ESI-MS confirmed the relation between pH and the system's dynamics. Upon addition of a base to a THF solution of the trifluoroborates, the pH increased immediately from approximately 7 to 10 with a brief or long induction period (induction period here is the interval between the time when the base is added to the system and the time when the substrate begins to decay) which agreed with ESI-MS results in most cases (Figure 5.3-5.5). The end of the induction period was indicated by an abrupt pH drop for most substrates (Figure 5.3-5.5 and Appendix D), possibly due to mopping up of HF by the base.[263] After the pH drop, there was a slow pH recovery and expansion. In a parallel analysis with ESI-MS, a first order decay in trifluoroborate was observed in most cases at the end of the induction period.

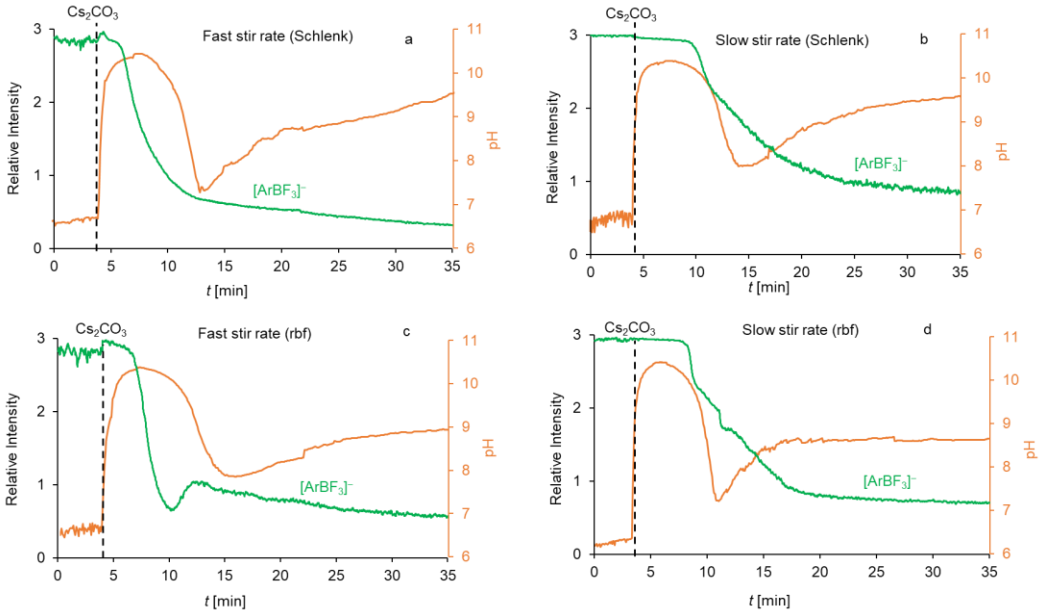

Figure 5.3. Relative species intensity and pH values for the hydrolysis of potassium p-methoxyphenyltrifluoroborate in THF/H_2O (10:1) containing Cs_2CO_3 at 55°C; reaction was performed in: a) Schlenk tube (fast stir rate); b) Schlenk tube (slow stir rate); c) rbf (fast stir rate); d) rbf (slow stir rate). The relative intensity values were determined by multiplying the intensities of F containing species by the number of F available; the sum of the result from each species represents the relative intensities of the $[ArBF_3]^-$ trace (green trace).

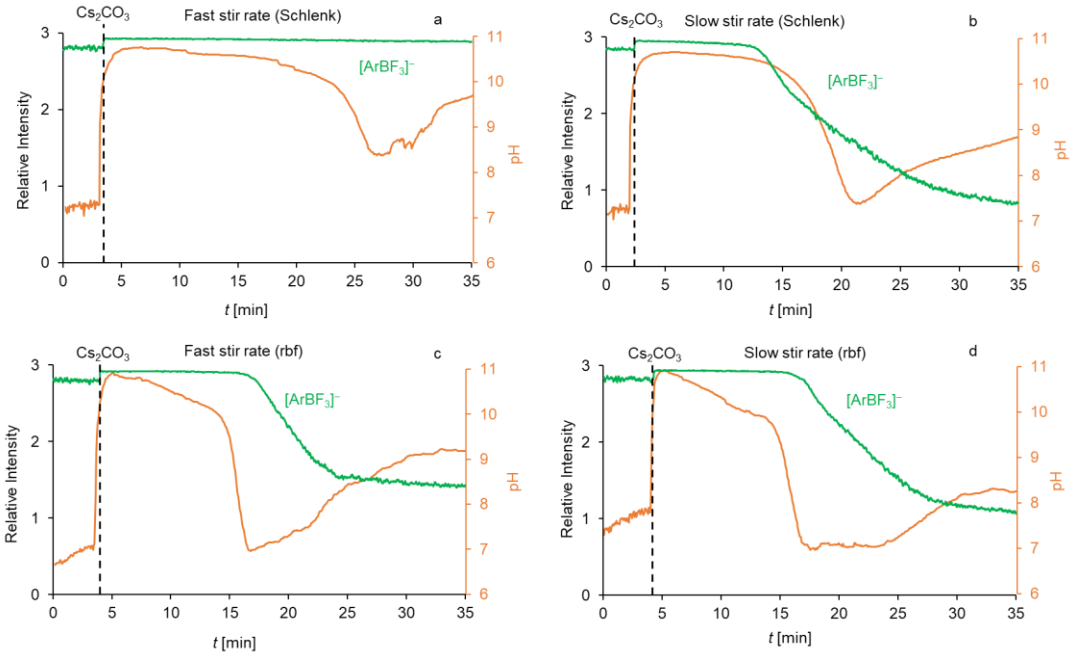

Figure 5.4. Relative species intensity and pH values for the hydrolysis of potassium p-tolyltrifluoroborate in THF/H_2O (10:1) containing Cs_2CO_3 at 55°C; reaction was performed in: a) Schlenk tube (fast stir rate); b) Schlenk tube (slow stir rate); c) rbf (fast stir rate); d) rbf (slow stir rate). The relative intensity values were determined by multiplying the intensities of F containing species by the number of F available; the sum of the result from each species represents the relative intensities of the $[ArBF_3]^-$ trace (green trace).

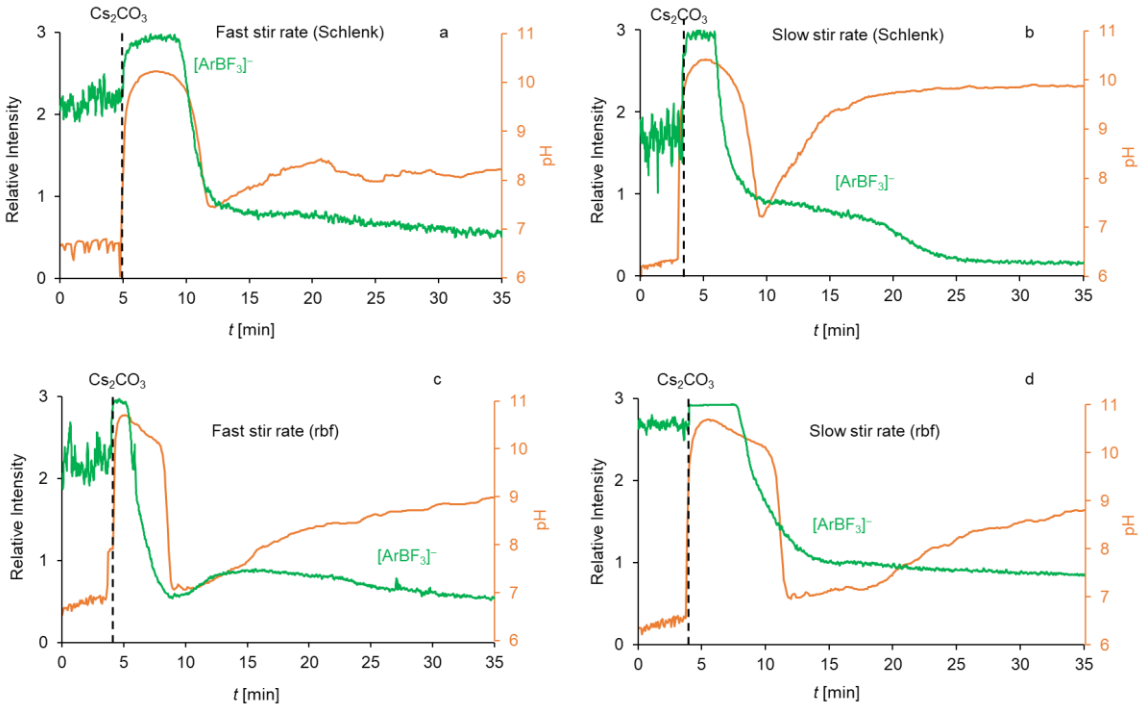

Figure 5.5. Relative species intensity and pH values for the hydrolysis of potassium cyclohexyltrifluoroborate in THF/H_2O (10:1) containing Cs_2CO_3 at 55°C; reaction was performed in: a) Schlenk tube (fast stir rate); b) Schlenk tube (slow stir rate); c) rbf (fast stir rate); d) rbf (slow stir rate). The relative intensity values were determined by multiplying the intensities of F containing species by the number of F available; the sum of the result from each species represents the relative intensities of the $[ArBF_3]^-$ trace (green trace).

5.3 Effect of flask geometry and stirring rate on hydrolysis profiles of the aryltrifluoroborates

It was also observed that different reaction vessels (Schlenk tube vs. round-bottomed flask) and changes in stirring rate could substantially affect the reaction rate. Reactions conducted in a Schlenk tube mostly had relatively low rates of hydrolysis compared with a round-bottomed flask (see Figure 5.6, Figure 5.7, and Appendix D). Lloyd-Jones[263] and Hartwig[279] determined that, in a Schlenk tube better phase contact is achieved between the bulk solvent and the basic aqueous solution. The rate of base transfer into the bulk medium is comparatively increased in a Schlenk tube which could suppress hydrolysis;[263] but hydrolysis of K[*p*-MeOC$_6$H$_4$BF$_3$] and K[CyBF$_3$] in a Schlenk tube at fast and slow stir rates respectively did not show the same behaviour (see Figure 5.7 and Appendix D).

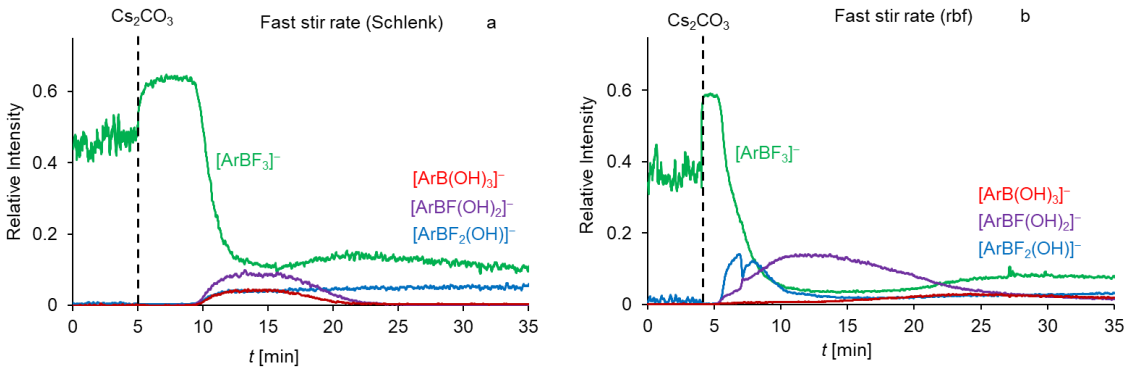

Figure 5.6. Relative species intensity for the hydrolysis of potassium cyclohexyltrifluoroborate in THF/H_2O (10:1) containing Cs_2CO_3 at 55°C; reaction was performed in: a) Schlenk tube; and b) rbf at a fast stir rate. The $[ArB(OH)_3]^-$ trace is a sum of intensities of all species with F = 0. i.e. **7** + **8** + **9** + ½**10**.

In addition, changes in stirring rate affected the induction periods. Figure 5.8a shows an example where hydrolysis of potassium p-tolyltrifluoroborate at a fast stir rate never reached the catalytic regime; whereas at a slow stir rate (Figure 5.8b), a gradual conversion was observed with an induction time of approximately 10 minutes, followed by catalytic hydrolysis. With increased stir rates, Lloyd-Jones and co-workers found that the transfer of base from aqueous to organic phase is possibly facilitated which could retard acid catalytic activity by sequestering HF.[263] However, in this study, we observed that the rates of hydrolysis for K[*p*-$MeOC_6H_4BF_3$] and K[$CyBF_3$] increased under fast stirring conditions which was unexpected (see Figure 5.7). This discrepancy with their findings could be attributed to differences in reaction vessels (PTFE *vs.* glass vessel in this study), stirring rate (100 rpm *vs.* 168 rpm for slow stirring rate and 500 rpm *vs.* 600 rpm for fast stirring rate), and the concentration of the reagents used (8 mM *vs.* 1.8 mM for the borates and 24 mM *vs.* 5.5 mM for the base).

Nonetheless, it was generally observed that the rate of hydrolysis increased with acidity of the system after addition of the base (see Appendix D). This implies that a brief induction period (as shown in the pH analysis, see Appendix D) and a drop in pH can be indicators of increased rate of solvolysis leading to consumption of $[ArBF_3]^-$, and sequestering of HF.[263] Also, a further drop in pH, could be attributed to less retardation of hydrolysis by the base, and vice versa. In respect of this, the fast hydrolysis of K[*p*-$MeOC_6H_4BF_3$] in a Schlenk tube at fast stir rate could be explained by the further drop in pH (pH dropped from 10.5 to 7.2 at the end of the induction period, see Figure 5.3), as compared with the hydrolysis at slow stirring rate (pH dropped from 10.5 to 8 at the end of the induction period, see Figure 5.3). Also, the increased rate of hydrolysis at fast stirring conditions for K[$CyBF_3$] can be explained by the slow pH recovery which indicates less hindrance by the base (see Figure 5.5).

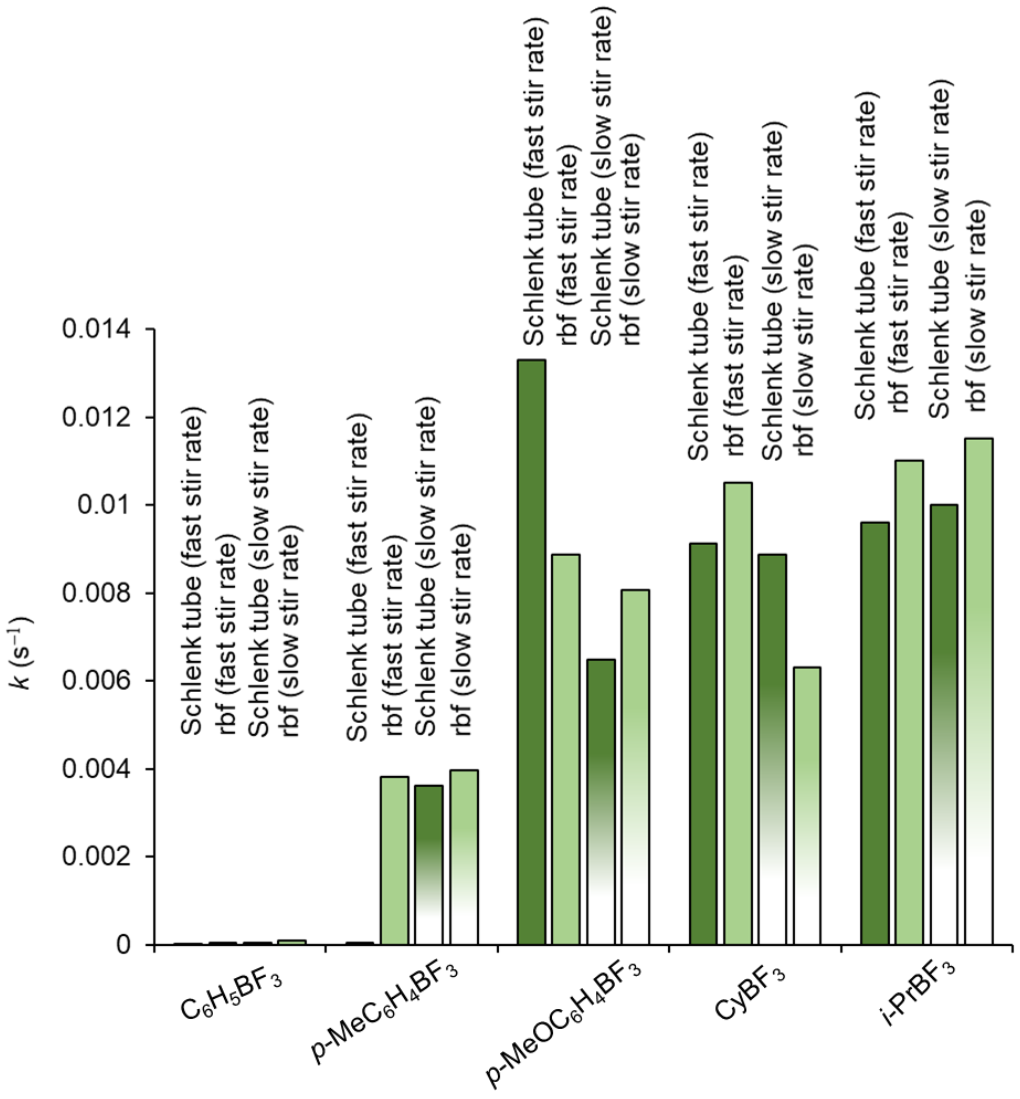

Figure 5.7. Representation of rate constants for the hydrolysis of potassium salts of A) p-methoxyphenyltrifluoroborate B) p-tolyltrifluoroborate C) cyclohexyltrifluoroborate in THF/H_2O (10:1) containing Cs_2CO_3; reaction was conducted in a Schlenk tube and round-bottomed flask at fast and slow stir rates. Rate constants were determined by linear regression of In(relative intensity) versus time (see Figure D 13 – D 22). Fully shaded bars represent fast stir rate while the half-shaded bars represent slow stir rate.

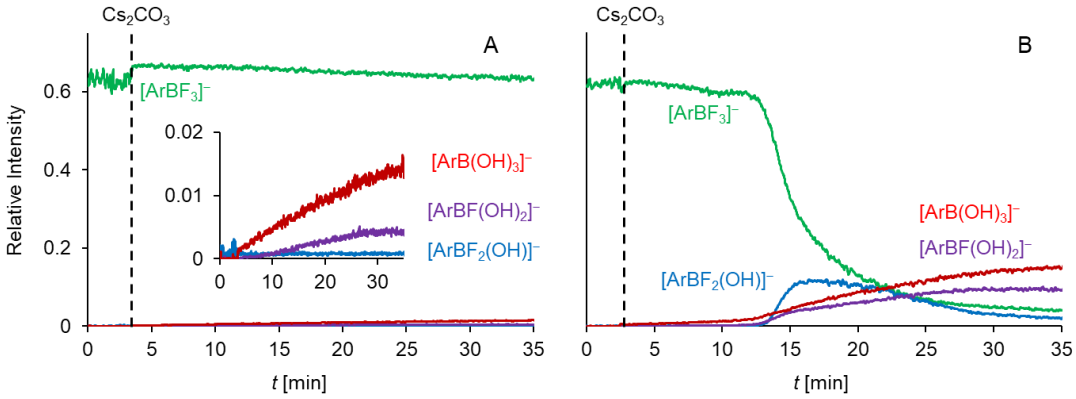

Figure 5.8. Relative species intensity for the hydrolysis of potassium p-tolyltrifluoroborate in THF/H_2O (10:1) containing Cs_2CO_3; performed at (A) a fast stir rate and (B) a slow stir rate. Inset in (A) represents hydrolyzed species; and the $[ArB(OH)_3]^-$ trace is a sum of intensities of all species with F = 0. i.e. **7** + **8** + **9** + ½**10**.

As expected, the R group had a significant effect on the conversion rate of the trifluoroborates. As shown in Figure 5.7, the reaction rate for phenyltrifluoroborate was slower than that of *p*-tolyltrifluoroborate, *p*-methoxyphenyltrifluoroborate, cyclohexyltrifluoroborate and isopropyltrifluoroborate; and as well, the induction period was relatively longer for the same substrate (see Figure 5.8 and Appendix D). This implied that the phenyl group could stabilize the borate better than the R group of the other substrates,[267] hence the order of reactivity was $C_6H_5BF_3K$ < *p*-$MeC_6H_4BF_3K$ < *p*-$MeOC_6H_4BF_3K$ < $CyBF_3K$ ~ *i*-$PrBF_3K$. These results are consistent with previous studies.[263,267]

5.4 Conclusions

Real time analysis of the hydrolysis of aryltrifluoroborates using ESI-MS confirms many of the behaviours previously revealed by ^{19}F NMR, including sensitivity to stir rates and flask geometry and the existence of significant induction periods following the addition of base. ESI-MS reveals additional details: the presence of a complex soup of reaction products, including not just partially hydrolyzed products, but also dehydrated products and aggregate species thereof. The system eventually settles into a complex equilibrium in which a wide array of species is simultaneously present. This complex speciation points to an equally complex system when aryltrifluoroborates are used as an aryl source in Suzuki-Miyaura reactions; what might on paper seem to be a single-component addition may instead have a complicated effect on the catalytic system.

5.5 Experimental

Reagents were purchased from Sigma-Aldrich and were used without further purification. Gases used were purchased from Airgas. Tetrahydrofuran was distilled over CaH_2 and stored under an inert atmosphere prior to use. The instrument used for all monitored reactions was a Waters Acquity Triple Quadrupole Detector. All ESI experiments were performed in the negative ion mode. ESI source parameters were as follows: capillary voltage was held at 3 kV, cone voltage at 12.0 V, and extraction cone at 1 V. The following settings were used to obtain optimal desolvation conditions: desolvation gas flow rate 200 L/hr, cone gas flow rate 100 L/hr, source temperature 100°C, desolvation temperature 180°C. The detector gain was set to an optimal voltage of 470 V. Scan time was set to 1 s, with an inter-scan time of 0.1 s. The collision gas flow (high purity argon) was switched off except in tandem mass spectrometric experiments (MS/MS). MS/MS experiments were conducted with a collision energy between 2-15 V. Predicted isotope pattern was overlaid on the experimental isotope pattern (see Appendix D) using an isotope pattern overlay python script.[280,281] IKA RCT B hot plate magnetic stirrer was used for all experiments. The pH measurements were recorded with an HI 2020-01 pH meter equipped with HI 10430 digital pH electrode.

A typical reaction for trifluoroborate hydrolysis is as follows. A PSI-ESI(-)-MS setup was prepared under an inert atmosphere with a potassium trifluoroborate salt (12 µmol, 1 eq) in tetrahydrofuran in a Schlenk tube and a round-bottom style flask. The reaction mixture temperature was raised to 55°C, stirring rate was set identically to all other experiments (~168 rpm and ~600 rpm for slow and fast stir rate experiments respectively). The reaction mixture was connected to the ESI source by a piece of FEP tubing, and acquisition was initiated. Cesium carbonate (36 µmol, 3 eq) was dissolved in distilled water and injected into the reaction mixture (tetrahydrofuran : water ratio 10:1). Prior to addition of the base at both stir rates, there is no phase separation. After addition of the base at both stir rates, there is a brief phase separation (lasts for about 5 seconds or less) which disappears (solution looks well mixed). The capillary sampling the solution is close to the bottom of the flask (~5-10 mm above the stirrer bar). Reactions were carried out for potassium salts of *p*-tolyltrifluoroborate (*p*-$MeC_6H_4BF_3$), *p*-methoxyphenyltrifluoroborate (*p*-$MeOC_6H_4BF_3$), cyclohexyltrifluoroborate ($CyBF_3$), phenyltrifluoroborate ($C_6H_5BF_3$), and isopropyltrifluoroborate (*i*-$PrBF_3$). Real-time pH experiments were also carried out separately following the same procedure as described for the ESI-MS experiments. Methodological optimization and careful experimental technique were required to obtain reliable equilibrium behaviour between reactions, but the observed hydrolysis species were consistent between reactions and across substrates.

Chapter 6 Standardized stirring for small scale surveys

Portions of this chapter are reproduced from a submitted manuscript “Standardized stirring for small scale surveys” I. Omari, M. Paul and J.S. McIndoe.

6.1 Introduction

Catalytic reactions are sensitive to a wide range of experimental conditions, even in homogeneous systems.[30,282–289] These conditions include variables, such as concentration of reactants and catalyst,[290] stirring rate,[291] reaction time and temperature,[292] which contribute to the outcome of a catalytic system after optimization. This chapter focuses on the influence of stirring in a small-scale cross-coupling reaction.

The effect of stirring on the rate of coupling reactions is well-established.[293–295] Lloyd-Jones and co-workers found that in the hydrolysis of organotrifluoroborates, differences in stirring rate had an impact on the reaction kinetics.[294] Gonzalez and co-workers also reported the effect of stirring rate during hydrolysis of MIDA boronates (N-methylimidodiacetic boronic acid esters) in a biphasic system.[295] In this chapter, a heterogeneous variant of the copper-free Sonogashira reaction[296–305] was studied on-line at different stirring rates, and the effect of changing the distance of a reaction vial from the centre of a stir plate was examined off-line by testing the ability of 3D printed vial holders to facilitate identical stirring conditions.

The reaction species in both cases were identified by ESI-MS. 3D printed circular and linear vial holders were designed for 10 vials. These vial holders are expected to ensure identical stirring conditions and therefore maximize the reproducibility and reliability of small-scale screening experiments,[306–310] where small differences may attract significant attention. The vial holders can be scaled up or down easily to handle larger or smaller reaction vials.

6.2 Reaction monitoring of a copper-free Sonogashira reaction at different stirring rates

In searching for heterogeneous variants of the copper-free Sonogashira reaction reported previously,[296] it was reasoned that changing the base used from 1,8-diazabicyclo[5.4.0]undec-7-ene (DBU) to caesium carbonate (Cs_2CO_3) will be the simplest modification. However, under diluted conditions for ESI-MS, caesium carbonate completely dissolved. Owing to this, calcium carbonate ($CaCO_3$) was selected; though less commonly used, it was a suitable candidate for the purpose of this work.

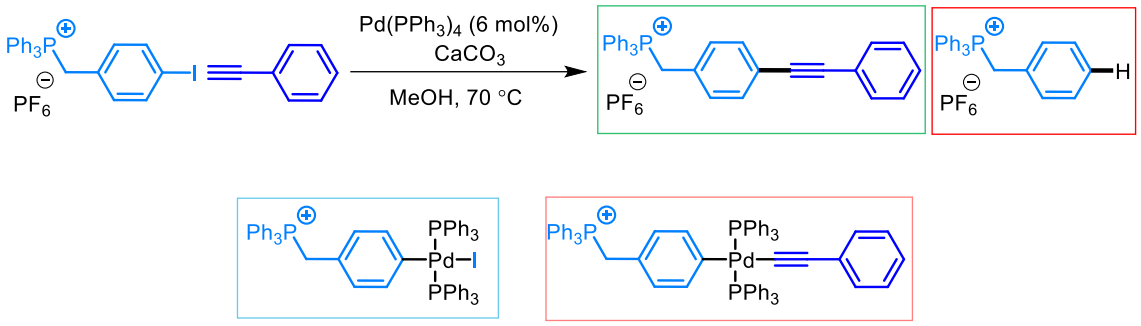

Scheme 6.1. Copper-free Sonogashira reaction in methanol at 70°C, employing a permanently charged aryl iodide and phenyl acetylene. The Sonogashira product (later shown in green) and the byproduct (later shown in red) as well as the first and second intermediate (later shown in light blue and light red) are also permanently charged and therefore detectable by ESI-MS.

The experimental conditions were then optimized to accommodate $CaCO_3$ (Scheme 6.1), and reactions were conducted in real-time at different stirring rates (60 rpm *vs.* 400 rpm) but otherwise under the same conditions. The differences between the reactions were subtle but real (see Figure 6.1), with the faster stir rate resulting in a slightly higher yield.

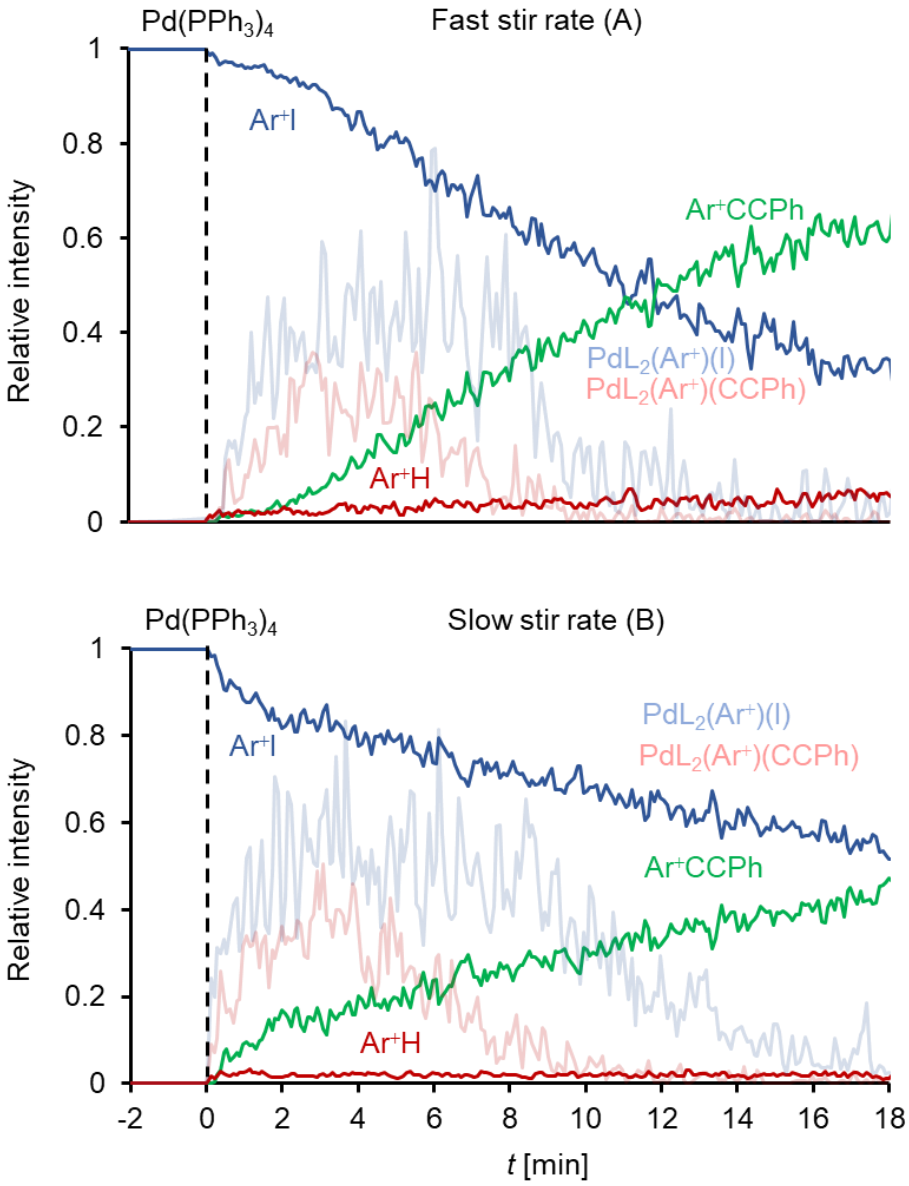

Figure 6.1. Two kinetic profiles of the copper-free Sonogashira reaction with 6 mol% of catalyst being employed. Top, at a relatively fast stirring rate and bottom, at a relatively slow stirring rate. For the purpose of illustration, the intensities of palladium intermediates were multiplied by 100. Traces were normalized to the sum of all species.

6.3 Standardizing stirring using 3D printed vial holders

It is very common in optimization of organometallic reactions (different solvents, additives, ligands, or metal centres) to charge *e.g.* 24 vials in a 6 × 4 grid and stir them all together in the same oil bath. Nonetheless, the position of a stir bar from the centre of the stir plate determines how well the reaction is stirred. In a worst-case scenario, all reactions within such an optimization attempt could stir differently and the best combination might be excluded in the next optimization step.

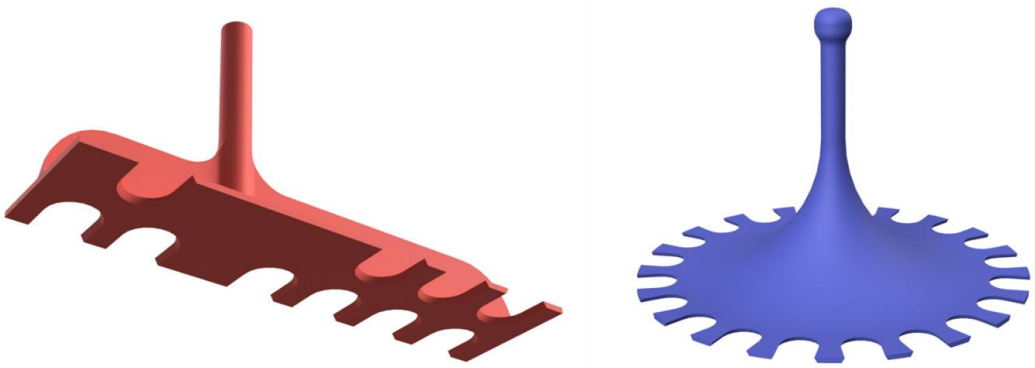

Figure 6.2. Left: Vial holder for unequal stirring. Position 0 is centred above the middle of the stir plate. Right: Vial holder for equal stirring. The middle of the holder is centred above the middle of the stir plate.

Due to this, the extent of error in differently stirred reactions was investigated. A vial holder that can hold 10 reactions at once but at deliberately different positions (see Figure 6.2, left) was designed as part of this investigation. In this setup, the vial directly next to the centre and the vial farthest from the centre were stirred most consistently, while in most others the stir bar performed a clicking or walking motion. To compare these 10 inconsistently stirred reactions, another holder was designed for equal stirring (see Figure 6.2, right). For consistency, all vials in this configuration were placed in every other slot at the same distance from the centre as the one farthest from the centre in the setup for unequal stirring. Figure 6.3 depicts the outcome obtained by means of ESI-MS after reactions were performed in vials using 3D printed linear and circular vial holders to standardize stirring.

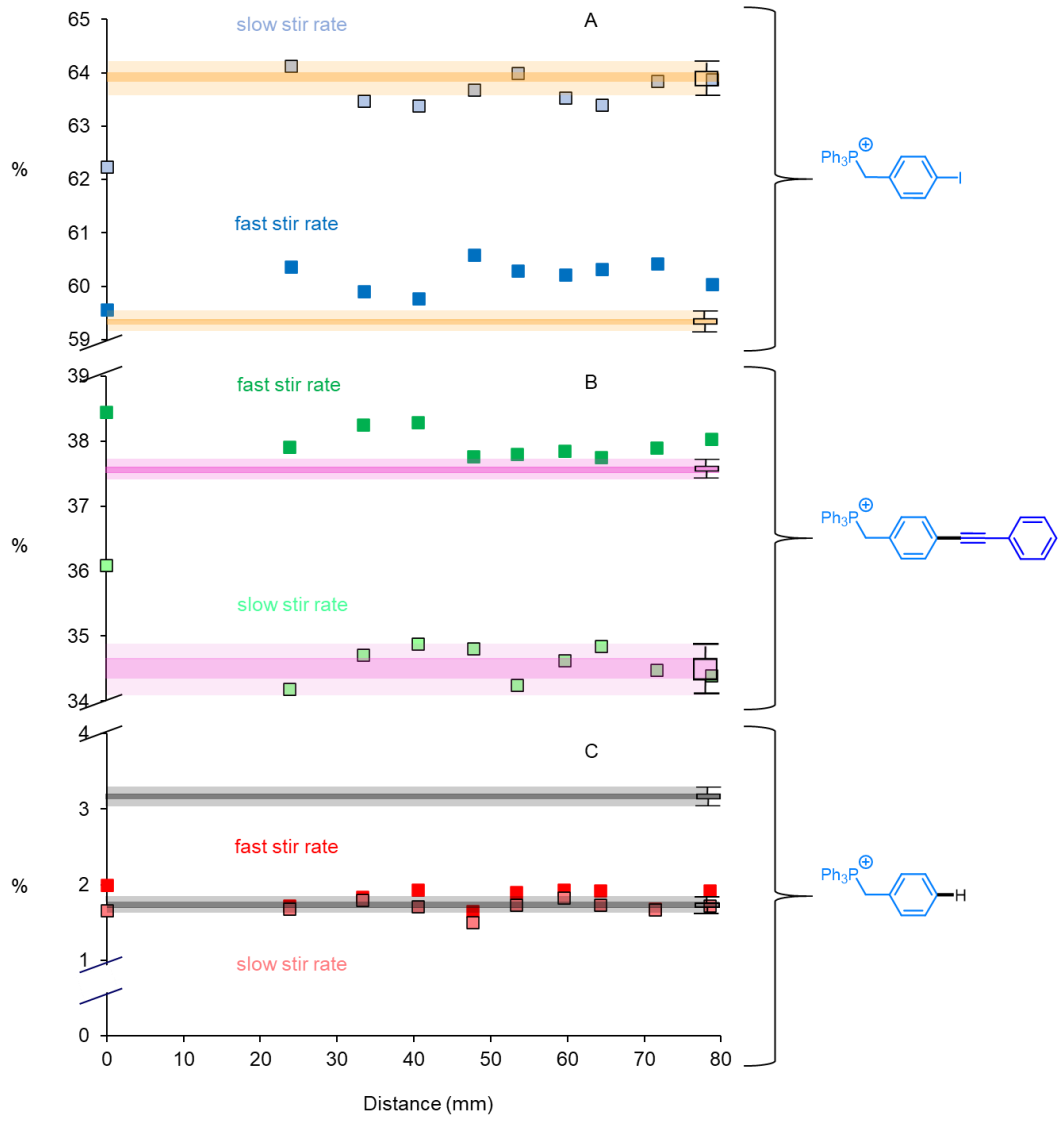

Figure 6.3. Percent yields of species of a Sonogashira reaction with a heterogeneous base ($CaCO_3$) under slow and fast stirring conditions (60 rpm and 400 rpm respectively) using 3D printed linear and circular vial holders to standardize stirring. Percent yields were calculated with the relative intensities of species obtained by ESI-MS. Distances in millimetres represent the distance from the centre of the holders to each slot for the vials. The box-and-whisker plot depicts data obtained when a circular vial holder is employed while all other data points describe results obtained when a linear vial holder is used.

As shown in Figure 6.3A, it can be observed that both under slow (60 rpm) and fast stirring (400 rpm), reactions stirred at the centre of the holder (0 mm) had a much lower content of the residual starting material Ar^+I than reactions farther away from the centre. Not surprisingly, the yields of the desired product Ar^+C_2Ph (Figure 6.3B) and the byproduct Ar^+H (Figure 6.3C) were higher at the centre. Vials placed at 24 mm through 79 mm under both stirring conditions showed a similar trend in changes in yield from one distance to the next in most cases. Also, in Figure 6.3A, at 60 rpm and 400 rpm, a range of 0.5% and 0.2% respectively can be observed when a circular vial holder was used. In addition, Figure 6.3B showed a range of 0.5% at 60 rpm and 0.2% at 400 rpm when a circular vial holder was employed. Further, Figure 6.3C displayed a range of 0.3% at 60 rpm; and 0.1% at 400 rpm when a circular vial holder was used. Also, as shown in Table 6.1, the margin of error when a circular vial holder is used for reactions stirred at 400 rpm was relatively smaller than reactions stirred at 60 rpm.

Table 6.1. Margin of error (95% confidence interval) when a circular vial holder is used.

Stirring rate (rpm)	Ar^+I (%)	Ar^+C_2Ph (%)	Ar^+H (%)
60	± 0.10	± 0.12	± 0.05
400	± 0.04	± 0.04	± 0.01

The low amounts of residual Ar^+I and higher yields of Ar^+C_2Ph shown at 0 mm using a linear vial holder can be attributed to a faster conversion rate. It is reasonable to assume that this is because the stir bar is stirring the fastest directly above the stir plate. Although experiments performed in ten vials with a linear vial holder are somewhat different from

each other (distance from the centre of the holder to each vial slot varies), more reproducible data could probably be achieved at 60 rpm considering that in Figure 6.3, the outcome of slowly stirred reactions (linear vial holder) in most cases was within 95% confidence interval of the results at same stirring rate when a circular vial holder was used (see Table 6.2).

Table 6.2. 95% confidence interval of the percent yields when a circular vial holder is used.

Stirring rate (rpm)	Ar^+I (%)	Ar^+C_2Ph (%)	Ar^+H (%)
60	(63.78, 63.98)	(34.32, 34.55)	(1.63, 1.73)
400	(59.32, 59.40)	(37.44, 37.51)	(3.16, 3.18)

The tight distribution of results revealed by employing a circular vial holder at both stirring rates demonstrates that data reproducibility could be attained with this vial holder.

6.4 Conclusion

Based on the results presented, a 3D printed circular vial holder can be recommended as a useful tool which facilitates standardized stirring and offers high precision in small-scale experiments.

6.5 Experimental

All chemicals were purchased from Sigma-Aldrich and used as received except for the HPLC grade methanol and tetrahydrofuran which were dried over calcium hydride and distilled under nitrogen before use. Argon (UHP200) was obtained from Airgas (Calgary, Canada) and employed without further purification.

In this study, both on-line and off-line experiments were carried out for fast and slow stir rate reactions. For on-line experiments, phenylacetylene (12 µmol, 1.2 eq) and calcium carbonate (0.5 mmol, 50 eq) were added to a solution of $[I(C_6H_4)CH_2PPh_3][PF_6]$ (10 µmol, 1 eq) in methanol (7 mL) in a vial charged with a stir bar under inert conditions and brought to 70°C in an oil bath. The reaction was initiated by addition of a THF solution of $Pd(PPh_3)_4$ (6 mol%) by syringe through a septum. The vial was pressurized with 3 psi argon and the reaction solution was transferred into a mass spectrometer through PEEK tubing.[64,266] An IKA C-MAG HS 7 hot plate magnetic stirrer was used for all experiments. Stirring rate was set to 400 rpm for fast stirring reactions and 60 rpm for slow stirring reactions. For off-line experiments, all reagents were prepared as described for the on-line experiments and placed in 20 vials with stir bars under inert conditions in a glovebox; however, the experiments were conducted outside the glovebox. Two sets of vials (10 vials per set) from the glovebox were arranged in a linear and circular vial holder; immersed in a heated oil-bath (70°C) for 10 minutes at both fast and slow stirring rates. The reaction was quenched after 10 min by placing the hot vials in an ice-bath for 20 min; the quenched samples were filtered and diluted with cold methanol to 1% v/v. These samples were loaded into a Hamilton GASTIGHT® syringe and transferred

through PEEK tubing directly into the mass spectrometer at a rate of 10 µL/min. The vial holders were printed on a CR-10 3D printer.

Electrospray ionization mass spectra were collected on a Waters Acquity Triple Quadrupole Detector mass spectrometer in positive ion mode. Instrument source parameters were as follows: capillary voltage was held at 3 kV, cone voltage at 10 V, and extraction cone at 0.5 V. The following settings were used for desolvation conditions: desolvation gas flow rate, 200 L/h; cone gas flow rate, 100 L/h; source temperature, 80°C; desolvation temperature, 200°C. The detector gain was set to 470 V. Scan time was set to 5 s, with an inter-scan time of 0.5 s. Low and high mass resolutions were set to 17. The relative intensities of species recorded were used for percent yield calculation. Percent yield was calculated by multiplying the ratio of the intensity of species (intensity of species of interest : total intensity of all species) by 100.

Chapter 7 Miscellaneous studies

This chapter comprises a collaborative research work with Francisco Ribeiro (visiting PhD student from Universidade de São Paulo) on the cyclization reaction of carbamate and benzoxazine by ESI-MS. My contribution to this work involved employing ESI-MS reaction monitoring for the investigation of the cyclization reactions. The study on the cyclization reaction of carbamate is a portion of a submitted manuscript; “Regio- and Diastereoselective Pd-Catalyzed Aminochlorocyclization of Allylic Carbamates: Scope, Derivatization, and Mechanism” by B. P. Spadafora, F. W. M. Ribeiro, J. E. Matsushima, E. M. Ariga, I. Omari, P. M. A. Soares, D. de Oliveira-Silva, E. Vinhato, J. S. McIndoe, T. C. Correra, and A. Rodrigues.

7.1 Real-time analysis of cyclization reaction of carbamate by ESI-MS

Palladium mediated reactions are ubiquitously used in synthetic chemistry, due to their catalytic role in cross-coupling reactions.[311–313] Among these reactions are Heck[314–316] and Suzuki[317–319] reactions, which are well-known palladium mediated reactions; and intramolecular cyclization reactions mediated by palladium[320,321]. Cyclization of carbamates mediated by Pd (II)/Cu (II) in the presence of LiCl was reported in 2004 by Liu and co-workers.[322] In the context of their study, this work aimed at employing ESI-MS to investigate their proposed reaction mechanism (scheme 7.1).

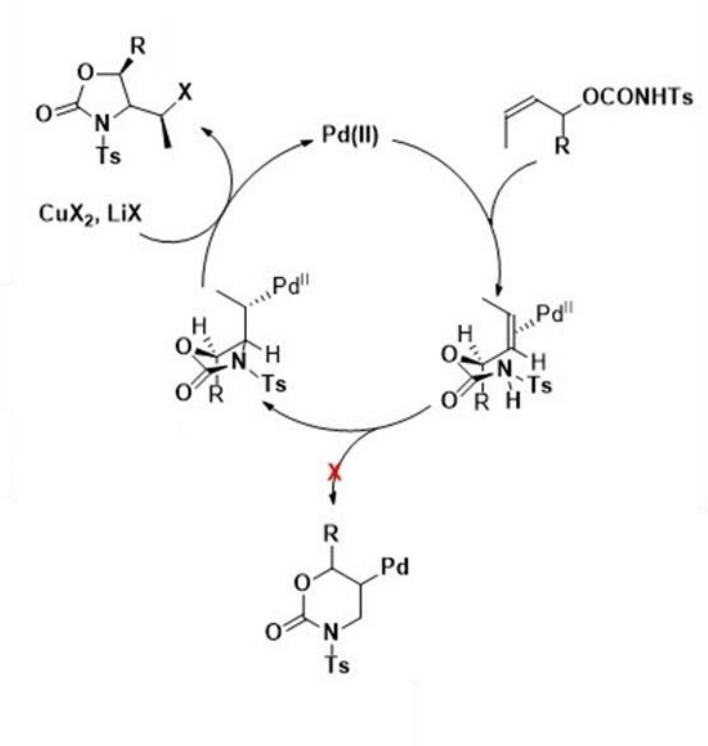

Scheme 7.1. Proposed catalytic cycle for the Pd mediated cyclization reaction by Liu *et al.*[322]

7.1.1 On-line reaction monitoring of the cyclization reaction

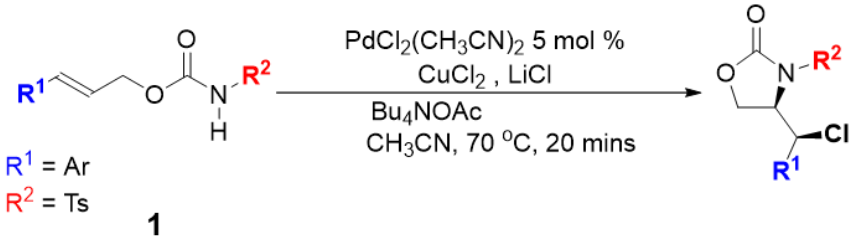

Scheme 7.2. General scheme for the cyclization reaction of carbamate (**1**) with reaction conditions used in this work.

To determine the reaction intermediates and products formed during the cyclization reaction of carbamate, PSI-ESI-MS was employed. Figure 7.1 shows real-time data of the cyclization reaction mediated by $PdCl_2(CH_3CN)_2$.

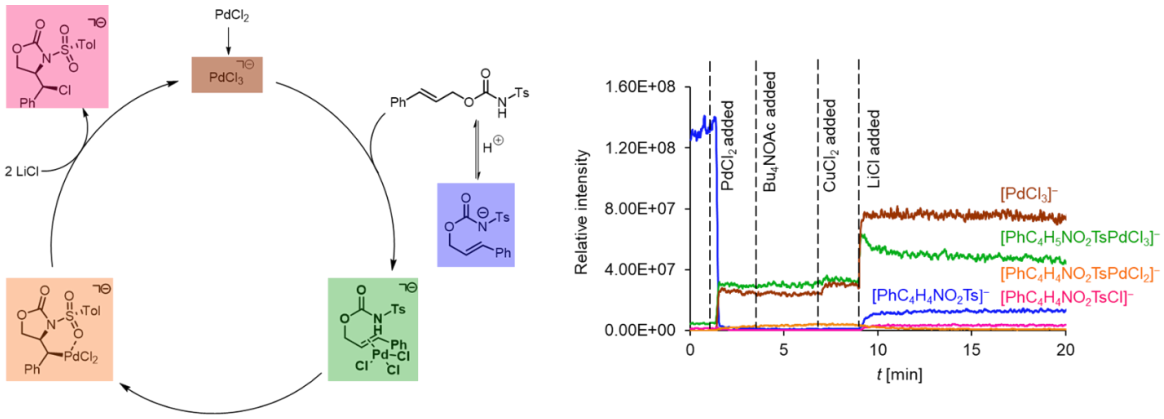

Figure 7.1. Left – Reaction mechanism for the cyclization of carbamate in CH_3CN at 70°C. Right – Evolution of species *vs.* reaction time.

The reaction proceeded after addition of $PdCl_2$ to a stirring solution of carbamate in acetonitrile. In Figure 7.1, it can be seen that upon addition of $PdCl_2$, there was a fast conversion of the carbamate which resulted into the formation of $[PhC_4H_5NO_2TsPdCl_3]^-$ (green trace), $[PdCl_3]^-$ (red trace), $[PhC_4H_4NO_2Ts]^-$ (blue trace), $[PhC_4H_4NO_2TsPdCl_2]^-$ (orange trace) and $[PhC_4H_4NO_2TsCl]^-$ (pink trace). Additions of Bu_4NOAc and $CuCl_2$ did not show any significant change in the ion intensities; but there was a small increase in the $[PdCl_3]^-$ intensity caused by Cl^- addition at 6 min (Figure 7.1). Upon addition of LiCl, the ion intensities of all products increased, meanwhile a slow decay of the intermediate $[PhC_4H_4NO_2TsPdCl_2]^-$ (orange trace) occurred. The sudden rise in intensity of the deprotonated carbamate after addition of LiCl could possibly be attributed to the increased chloride concentration. Product ion scan experiment (MS/MS) was also conducted in this work for structural information as shown in Figure 7.2. The speciation revealed in the on-line reaction monitoring gave insights into the proposed mechanism by Liu *et al*.[322]

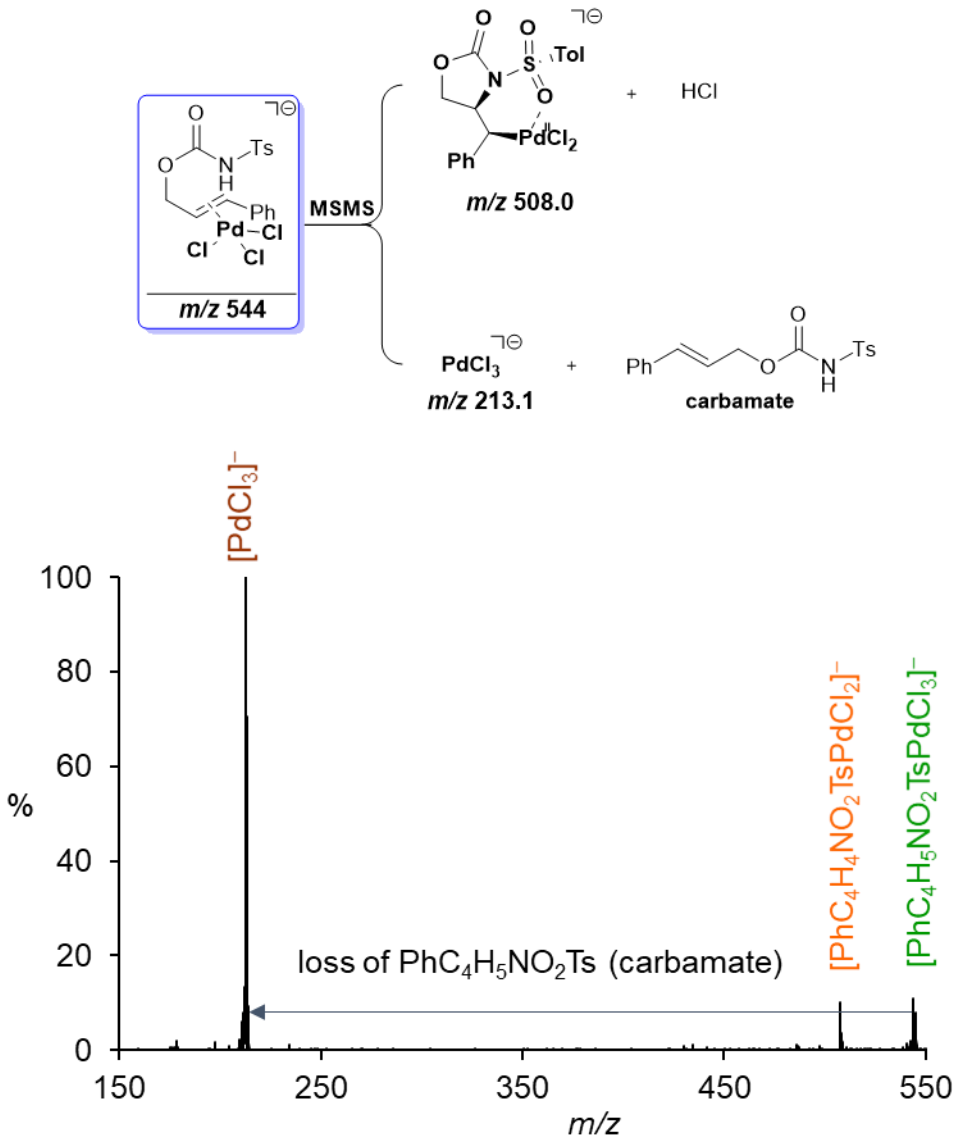

Figure 7.2. MS/MS of reaction intermediates at a collision energy of 15 V.

7.1.2 Experimental

All chemicals were purchased from Sigma-Aldrich and used without any further purification. The experiment was conducted by charging a vial with 10 mL of CH_3CN, 0.02 mol/L (1.0 mL) of carbamate, a solution of the $PdCl_2(CH_3CN)_2$ catalyst (0.004 mmol in 1.0 mL of CH_3CN diluted to a final carbamate concentration of 5%), 20 nmol/L (1.0 mL) of tetrabutylammonium acetate, 30.0 µmol/L (1.0 mL) of $CuCl_2$ and 0.07 mol/L (1.0 mL) of LiCl and a stir bar. The reaction was kept at 70°C for a total time of 20 min.

The reaction was studied by electrospray ionization mass spectrometry (ESI-MS) coupled with pressurized sample infusion (PSI), using a Waters Acquity Triple Quadrupole Detector (TQD) mass spectrometer. PSI-ESI-MS allowed real-time analysis of reaction by applying 5 psi of N_2 to the reaction vessel which enabled transfer of the reaction mixture to the ESI source via a PEEK tubing. The MS parameters used were as follows: capillary voltage 3.0 kV; cone voltage 15 V; extraction voltage 3.0 V; temperature source 90°C; cone gas flow rate 100 L/h; desolvation gas flow rate, 100 L/h; scan time was set to 5 s. MS/MS experiments were carried out with high purity argon and a collision energy between 5 to 20 V.

7.2 Cyclization reaction of benzoxazine promoted by acid catalysis

Benzoxazines are a class of thermosetting resins that were initially synthesized by Holly and Cope in 1944.[323,324] They are generally synthesized via Mannich condensation when phenol reacts with an amine and formaldehyde (example shown in Scheme 7.3).[323,325] Aversa *et al.*, synthesized N-(2-hydroxy-3,5-dimethylbenzyl)-aminopropanoic acid through a Mannich reaction where 2,4-dimethylphenol reacted with formaldehyde and 3-aminopropanoic acid in ethanol and sulfuric acid.[325]

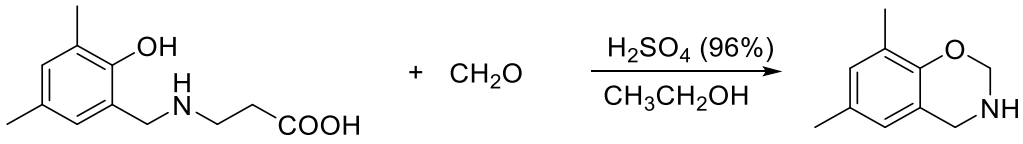

Scheme 7.3. Reaction scheme for the synthesis of a benzoxazine in ethanol and sulfuric acid.[325]

In this work ESI-MS was employed to investigate the formation of 3,4-dihydro-2H-1,3-benzoxazines in real-time. The reaction involved phenol reacting with formaldehyde and aniline in the presence of formic acid; with acetonitrile as the solvent at 80°C for 1 hour (Scheme 7.4).

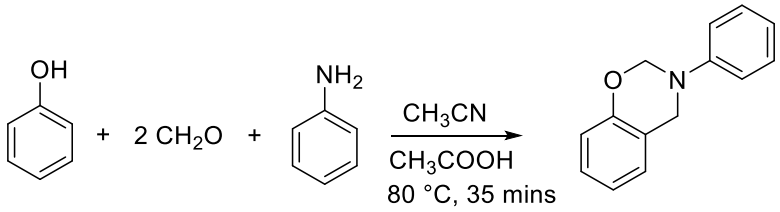

Scheme 7.4. Reaction scheme for the cyclization reaction of benzoxazine with reaction conditions used in this work.

7.2.1 On-line reaction monitoring of benzoxazine formation

By employment of PSI-ESI-MS, speciation leading to the formation of 3,4-dihydro-2H-3-phenyl-1,3-benzoxazine was examined. Figure 7.3 indicates species observed in real-time during the benzoxazine formation catalyzed by formic acid.

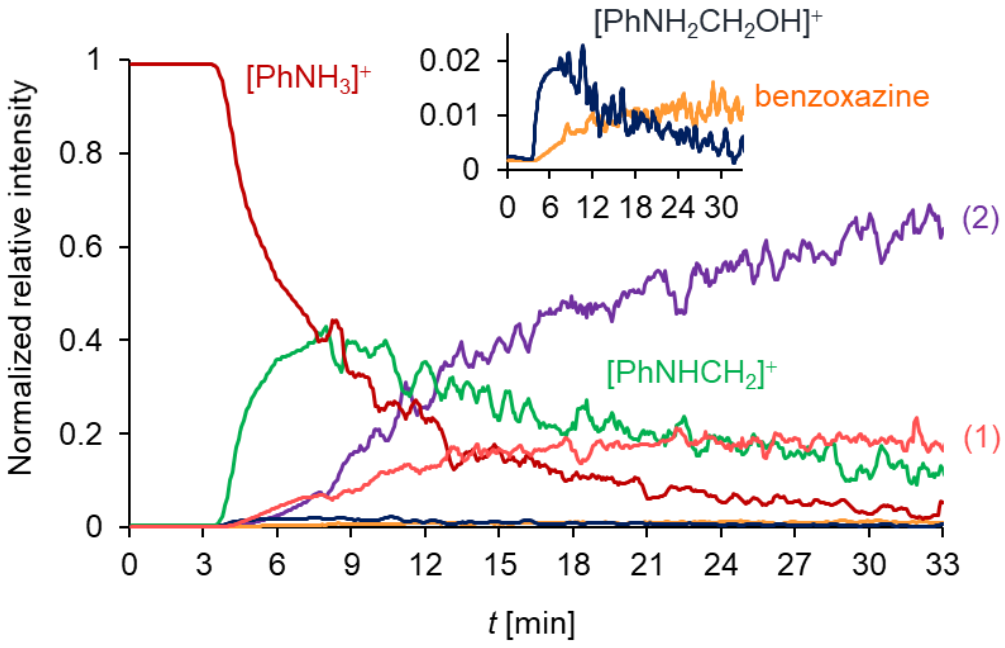

Figure 7.3. Representation of the observed speciation in real-time during the formation of benzoxazine promoted by acid catalysis. Inset: traces of a by-product and benzoxazine.

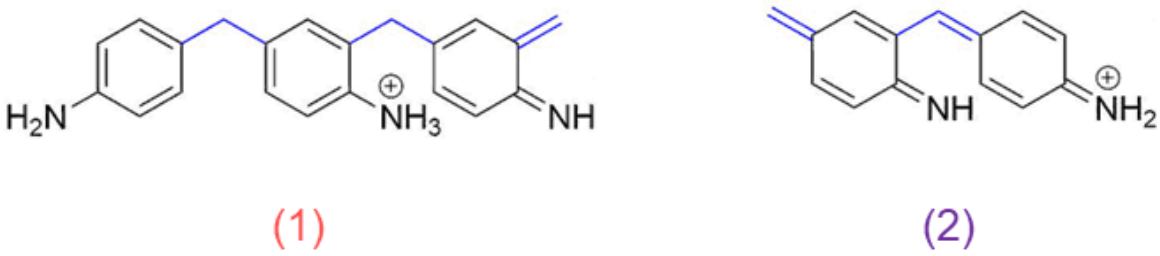

Figure 7.4. By-products observed in the on-line reaction monitoring during the formation of benzoxazine promoted by acid catalysis.

The reaction proceeded after addition of formaldehyde to a solution of formic acid, aniline and phenol in acetonitrile. Prior to the addition of formaldehyde, a protonated aniline $[PhNH_3]^+$ (red trace) emerged when aniline reacted with the formic acid. The protonated aniline species was gradually consumed in about 30 minutes following addition of the formaldehyde. As a result, $[PhNHCH_2]^+$ (green trace), $[PhNH_2CH_2OH]^+$ (deep blue trace) and benzoxazine (orange trace) were observed. In addition, two by-products were seen as light red and purple traces which were interpreted in Figure 7.4. Collectively, the observed speciation provided information for the proposed reaction meachanism in Scheme 7.5.

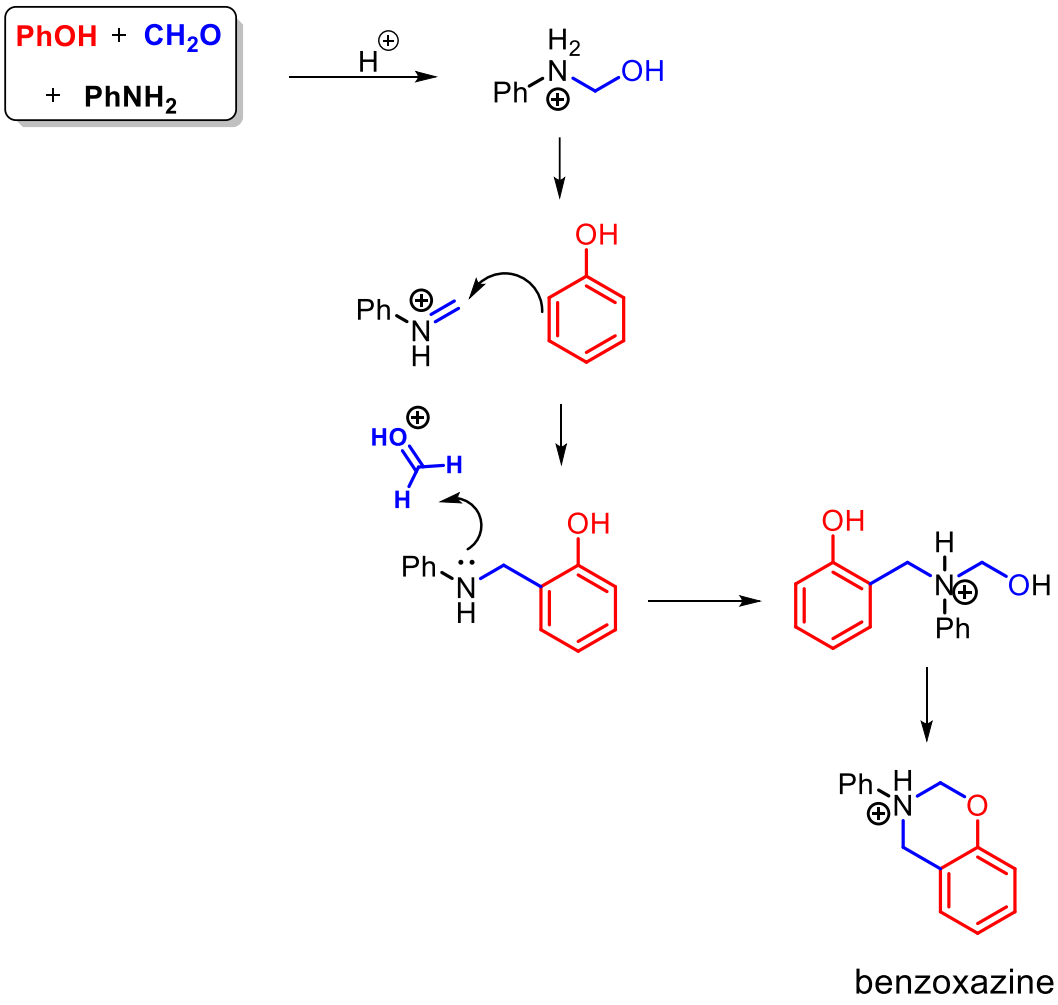

Scheme 7.5. Reaction mechanism for the cyclization of benzoxazine promoted by acid catalysis.

7.2.2 Experimental

All chemicals were purchased from Sigma-Aldrich and used without any further purification. For reaction monitoring of benzoxazine formation (3,4-dihydro-2H-3-phenyl-1,3-benzoxazine), a vial was charged with 7.0 mL of CH_3CN, 1.0 mL of 0.1% formic acid (when needed), 0.18 mmol phenol, 0.18 mmol aniline and a stir bar. The vial was sealed with a rubber septum punctured with one end of a PEEK tube; the PEEK tube was placed in the reaction solution and the other end was connected to the mass spectrometer. Finally, the vial was pressurized with 5 psi of N_2 to facilitate transfer of the reaction solution into the mass spectrometer; 0.37 mmol formaldehyde was added and the mixture was stirred for 35 minutes at 80°C. All reagents were diluted in 1.0 mL of acetonitrile.

A Waters Acquity Triple Quadrupole Detector mass spectrometer (TQD) was used for the investigation. The MS parameters used were as follows: capillary voltage 3.0 kV; cone voltage 15 V; extraction voltage 3.0 V; temperature source 90°C; gas flow rate 100 L/h; desolvation gas flow rate, 100 L/h. The detector gain was set to an optimal voltage of 470 V. Scan time was set to 1 s, with an inter-scan time of 0.1 s. MS/MS experiments were carried out with high purity argon and a collision energy between 5 to 20 V.

Chapter 8 Conclusions

This dissertation addressed disparate industrial problems, provided contributions and empirical considerations as additions to applications offered by ESI-MS and UV-Vis spectroscopy.

In an analysis of naphthenic acids in a petroleum matrix (Chapter 2), charge-tagging proved useful in selectively derivatizing target analytes for characterization by tandem ESI-MS/MS without chromatography. Despite the encouraging performance of the charge-tagged species, suppression of target analyte derivatives could be a major drawback due to interference of unreacted charge-tagged species. Therefore, it is necessary to optimize reaction conditions, such that the charge-tagged reagent is used as a limiting reagent. Nonetheless, the charge-tagging technique and tandem ESI-MS/MS may prove useful in the context of profiling the naphthenic acid components of complicated matrices, and as well, could be employed as a protocol for screening target analytes in quality control agencies.

To understand why an equimolar matrix of analytes, such as permanently charged reagents of different sizes and structure produces non-uniform response in ESI-MS, Chapter 3 described contributing factors, such as the morphology of an analyte, molecular weight, solvent and the conductivity of an analyte as parameters that can influence the signal of an analyte. These observations will provide insights into designing charge-tagged reagents for analyte characterization, and a predictive power when accounting for analytes that for reasons of high reactivity can not be isolated.

In addition, Chapter 4 employed UV-Vis spectroscopy for kinetic information on the influence of magnesium (Mg^{2+}) on Maillard reaction through off-line reaction monitoring, and ESI-MS for rapid identification of Maillard reaction species. Magnesium served as a Lewis acid catalyst, and inhibited diffusion of water molecules during the Maillard reaction. The findings in this work will enlighten brewers on the downstream impacts of magnesium ion concentrations in beer brewing. Also, the results indicate that both UV-Vis spectroscopy and ESI-MS could be used to investigate other metal-driven impacts of grain recipe variations in brewing that contribute to differences in colour and flavour outcomes of beer.

Further, Chapter 5 used ESI-MS to study the hydrolysis of organotrifluoroborates in real-time, complemented by pH analysis (not conducted simultaneously). Although meaningful data were obtained using these two separate techniques, some discrepancies in induction periods were observed comparing data from both techniques. Discrepancies in in-situ monitoring whereby different analytical techniques are used separately for an investigation of a reaction system could be resolved by combining the techniques without disturbing the reaction system, hence, in Chapter 5, an integration of ESI-MS with pH analysis could provide real-time data on speciation due to hydrolysis of the substrates as well as changes in pH simultaneously. Chapter 7 could also use ESI-MS coupled with UV-Vis spectroscopy (given the presence of unsaturated groups) to investigate the cyclization reactions of carbamate and benzoxazine. UV-Vis spectroscopy will provide information on species that are not detectable by ESI-MS but have light-absorbing groups. Thus, the employment of other analytical techniques concurrently with ESI-MS

could provide additional information on elusive reaction intermediates and facilitate interpretation of ESI-MS results.

Finally, the challenge in ensuring identical stirring conditions when conducting reactions in many reaction vials simultaneously, was addressed by employing a 3D printed circular vial holder (Chapter 6). In Chapter 6, the differential stirring effects detected in small-scale heterogeneous catalytic reactions (based on distance of the reaction vial from the central stirring point) were small and could be mitigated (though not eliminated) by ensuring reasonably fast stir rates. Also, to completely eliminate differential stirring as a cause for variation in results, circular vial holders of variable size can be 3D printed inexpensively and without the use of support material to reduce stirring effects to a minimum and to improve reproducibility in small-scale surveys.

Bibliography

(1) Thomson, J. J. *Proceedings of the Royal Society of London*; 1913.

(2) Dempster, A. J. LII. The Ionization and Dissociation of Hydrogen Molecules and the Formation of H 3 . *London, Edinburgh, Dublin Philos. Mag. J. Sci.* **1916**, *31* (185), 438–443. https://doi.org/10.1080/14786440508635520.

(3) Gross, J. H. *Mass Spectrometry: A Textbook: Second Edition*; Springer Berlin Heidelberg, 2011. https://doi.org/10.1007/978-3-642-10711-5.

(4) Bleakney, W. A New Method of Positive Ray Analysis and Its Application to the Measurement of Ionization Potentials in Mercury Vapor. *Phys. Rev.* **1929**, *34* (1), 157–160. https://doi.org/10.1103/PhysRev.34.157.

(5) Tate, J. T.; Smith, P. T. Ionization Potentials and Probabilities for the Formation of Multiply Charged Ions in the Alkali Vapors and in Krypton and Xenon. *Phys. Rev.* **1934**, *46* (9), 773–776. https://doi.org/10.1103/PhysRev.46.773.

(6) Munson, M. S. B.; Field, F. H. No Title. *J. Am. Chem. Soc.* **1966**, *88* (12), 2621–2630.

(7) Harrison, A. G. *Chemical Ionization Mass Spectrometry*; CRC Press: Boca Raton, 1992.

(8) Tanaka, K.; Waki, H.; Ido, Y.; Akita, S.; Yoshida, Y.; Yoshida, T.; Matsuo, T. Protein and Polymer Analyses up to m/z 100 000 by Laser Ionization Time-of-flight Mass Spectrometry. *Rapid Commun. Mass Spectrom.* **1988**, *2* (8), 151–153. https://doi.org/10.1002/rcm.1290020802.

(9) Dole, M.; Mack, L. L.; Hines, R. L.; Chemistry, D. O.; Mobley, R. C.; Ferguson, L. D.; Alice, M. B. Molecular Beams of Macroions. *J. Chem. Phys.* **1968**, *49* (5),

2240–2249. https://doi.org/10.1063/1.1670391.

(10) Zenobi, R.; Knochenmuss, R. Ion Formation in Maldi Mass Spectrometry. *Mass Spectrom. Rev.* **1998**, *17* (5), 337–366. https://doi.org/10.1002/(sici)1098-2787(1998)17:5<337::aid-mas2>3.0.co;2-s.

(11) Gross, J. H. Matrix-Assisted Laser Desorption/Ionization. In *Mass Spectrometry*; Springer Berlin Heidelberg, 2011; pp 507–559. https://doi.org/10.1007/978-3-642-10711-5_11.

(12) Yamashita, M.; Fenn, J. B. No Title. *J. Phys. Chem.* **1984**, *88* (20), 4451–4459.

(13) Blades, A. T.; Ikonomou, M. G.; Kebarle, P. Mechanism of Electrospray Mass Spectrometry. Electrospray as an Electrolysis Cell. *Anal. Chem.* **1991**, *63* (19), 2109–2114. https://doi.org/10.1021/ac00019a009.

(14) Taylor, G. Disintegration of Water Drops in an Electric Field. *Proc. R. Soc. London. Ser. A. Math. Phys. Sci.* **1964**, *280* (1382), 383–397. https://doi.org/10.1098/rspa.1964.0151.

(15) Schmelzeisen-Redeker, G.; Bütfering, L.; Röllgen, F. W. Desolvation of Ions and Molecules in Thermospray Mass Spectrometry. *Int. J. Mass Spectrom. Ion Process.* **1989**, *90* (2), 139–150. https://doi.org/10.1016/0168-1176(89)85004-9.

(16) Thomson, B. A.; Iribarne, J. V. Field Induced Ion Evaporation from Liquid Surfaces at Atmospheric Pressure. *J. Chem. Phys.* **1979**, *71* (11), 4451–4463. https://doi.org/10.1063/1.438198.

(17) Iribarne, J. V.; Thomson, B. A. On the Evaporation of Small Ions from Charged Droplets. *J. Chem. Phys.* **1976**, *64* (6), 2287–2294. https://doi.org/10.1063/1.432536.

(18) McQuinn, K.; Hof, F.; McIndoe, J. S. Direct Observation of Ion Evaporation from a Triply Charged Nanodroplet. *Chem. Commun.* **2007**, No. 40, 4099–4101. https://doi.org/10.1039/b711689f.

(19) Henderson, W.; McIndoe, J. S. *Mass Spectrometry of Inorganic and Organometallic Compounds*; John Wiley & Sons Ltd: West Sussex, 2005.

(20) Kebarle, P. A Brief Overview of the Present Status of the Mechanisms Involved in Electrospray Mass Spectrometry. *Journal of Mass Spectrometry*. John Wiley & Sons, Ltd July 1, 2000, pp 804–817. https://doi.org/10.1002/1096-9888(200007)35:7<804::AID-JMS22>3.0.CO;2-Q.

(21) Cole, R. B. Some Tenets Pertaining to Electrospray Ionization Mass Spectrometry. *J. Mass Spectrom.* **2000**, *35* (7), 763–772. https://doi.org/10.1002/1096-9888(200007)35:7<784::AID-JMS17>3.0.CO;2-Q.

(22) Loo, J. A. Probing Protein-Metal Ion Interactions by Electrospray Ionization Mass Spectrometry: Enolase and Nucleocapsid Protein. *Int. J. Mass Spectrom.* **2001**, *204* (1–3), 113–123. https://doi.org/10.1016/S1387-3806(00)00334-1.

(23) Feng, R.; Konishi, Y. *Analysis of Antibodies and Other Large Glycoproteins in the Mass Range of 150 000-200 000 Da by Electrospray Ionization Mass Spectrometry*; 1992; Vol. 64.

(24) Peschke, M.; Verkerk, U. H.; Kebarle, P. Features of the ESI Mechanism That Affect the Observation of Multiply Charged Noncovalent Protein Complexes and the Determination of the Association Constant by the Titration Method. *J. Am. Soc. Mass Spectrom.* **2004**, *15* (10), 1424–1434. https://doi.org/10.1016/j.jasms.2004.05.005.

(25) Clauser, K. R.; Hall, S. C.; Smith, D. M.; Webb, J. W.; Andrews, L. E.; Tran, H. M.; Epstein, L. B.; Burlingame, A. L. Rapid Mass Spectrometric Peptide Sequencing and Mass Matching for Characterization of Human Melanoma Proteins Isolated by Two-Dimensional PAGE. *Proc. Natl. Acad. Sci. U. S. A.* **1995**, *92* (11), 5072–5076. https://doi.org/10.1073/pnas.92.11.5072.

(26) Sila, A.; Bougatef, A. Antioxidant Peptides from Marine By-Products: Isolation, Identification and Application in Food Systems. A Review. *Journal of Functional Foods*. Elsevier Ltd March 1, 2016, pp 10–26. https://doi.org/10.1016/j.jff.2015.11.007.

(27) Del Gaudio, F.; Festa, C.; Mozzicafreddo, M.; Vasaturo, M.; Casapullo, A.; De Marino, S.; Riccio, R.; Monti, M. C. Biomolecular Proteomics Discloses ATP Synthase as the Main Target of the Natural Glycoside Deglucoruscin. *Mol. Biosyst.* **2016**, *12* (10), 3132–3138. https://doi.org/10.1039/c6mb00460a.

(28) Roviello, G. N. Novel Insights into Nucleoamino Acids: Biomolecular Recognition and Aggregation Studies of a Thymine-Conjugated l-Phenyl Alanine. *Amino Acids* **2018**, *50* (7), 933–941. https://doi.org/10.1007/s00726-018-2562-2.

(29) Kretz, R.; Wendt, L.; Wongkanoun, S.; Luangsa-ard, J.; Surup, F.; Helaly, S.; Noumeur, S.; Stadler, M.; Stradal, T. The Effect of Cytochalasans on the Actin Cytoskeleton of Eukaryotic Cells and Preliminary Structure–Activity Relationships. *Biomolecules* **2019**, *9* (2), 73. https://doi.org/10.3390/biom9020073.

(30) Joshi, A.; Zijlstra, H. S.; Collins, S.; McIndoe, J. S. Catalyst Deactivation Processes During 1-Hexene Polymerization. *ACS Catal.* **2020**, *10* (13), 7195–7206. https://doi.org/10.1021/acscatal.0c01607.

(31) Vikse, K. L.; Ahmadi, Z.; Manning, C. C.; Harrington, D. A.; McIndoe, J. S. Powerful Insight into Catalytic Mechanisms through Simultaneous Monitoring of Reactants, Products, and Intermediates. *Angew. Chemie Int. Ed.* **2011**, *50* (36), 8304–8306. https://doi.org/10.1002/anie.201102630.

(32) Yan, X.; Sokol, E.; Li, X.; Li, G.; Xu, S.; Cooks, R. G. On-Line Reaction Monitoring and Mechanistic Studies by Mass Spectrometry: Negishi Cross-Coupling, Hydrogenolysis, and Reductive Amination. *Angew. Chemie Int. Ed.* **2014**, *53* (23), 5931–5935. https://doi.org/10.1002/anie.201310493.

(33) Rauf, W.; Brown, J. M. Reactive Intermediates in Catalytic Alkenylation; Pathways for Mizoroki–Heck, Oxidative Heck and Fujiwara–Moritani Reactions. *Chem. Commun.* **2013**, *49* (76), 8430. https://doi.org/10.1039/c3cc44842h.

(34) Dawson, P. H. *Quadrupole Mass Spectrometry and Its Applications*; Dawson, P., Ed.; Elsevier, 2013.

(35) Borman, S.; Dagani, R.; Rawls, R. L.; Zurer, P. S. Chemistry Crystallizes Into Modern Science. *Chem. Eng. News* **1998**, *76* (2), 39–75. https://doi.org/10.1021/cen-v076n002.p039.

(36) Hu, Q.; Noll, R. J.; Li, H.; Makarov, A.; Hardman, M.; Cooks, R. G. The Orbitrap: A New Mass Spectrometer. *Journal of Mass Spectrometry*. J Mass Spectrom April 2005, pp 430–443. https://doi.org/10.1002/jms.856.

(37) Makarov, A. Electrostatic Axially Harmonic Orbital Trapping: A High-Performance Technique of Mass Analysis. *Anal. Chem.* **2000**, *72* (6), 1156–1162. https://doi.org/10.1021/ac991131p.

(38) Kim, S.; Rodgers, R. P.; Blakney, G. T.; Hendrickson, C. L.; Marshall, A. G.

Automated Electrospray Ionization FT-ICR Mass Spectrometry for Petroleum Analysis. *J. Am. Soc. Mass Spectrom.* **2009**, *20* (2), 263–268. https://doi.org/10.1016/j.jasms.2008.10.001.

(39) Scigelova, M.; Makarov, A. Orbitrap Mass Analyzer - Overview and Applications in Proteomics. In *Proteomics*; Proteomics, 2006; Vol. 1, pp 16–21. https://doi.org/10.1002/pmic.200600528.

(40) Enke, C. G. A Perspective on the Development of Tandem Mass Spectrometry. In *The Encyclopedia of Mass Spectrometry*; Elsevier, 2016; pp 68–76. https://doi.org/10.1016/b978-0-08-043848-1.00026-2.

(41) Sleno, L.; Volmer, D. A. Ion Activation Methods for Tandem Mass Spectrometry. *Journal of Mass Spectrometry*. John Wiley & Sons, Ltd October 1, 2004, pp 1091–1112. https://doi.org/10.1002/jms.703.

(42) Janusson, E. Development of Mass Spectrometry Techniques for Real-Time Reaction Monitoring, University of Victoria, 2017.

(43) Viaene, J.; Lanckmans, K.; Dejaegher, B.; Mangelings, D.; Vander Heyden, Y. Comparison of a Triple-Quadrupole and a Quadrupole Time-of-Flight Mass Analyzer to Quantify 16 Opioids in Human Plasma. *J. Pharm. Biomed. Anal.* **2016**, *127*, 49–59. https://doi.org/10.1016/j.jpba.2015.12.055.

(44) Rúbies, A.; Guo, L.; Centrich, F.; Granados, M. Analysis of Non-Steroidal Anti-Inflammatory Drugs in Milk Using QuEChERS and Liquid Chromatography Coupled to Mass Spectrometry: Triple Quadrupole versus Q-Orbitrap Mass Analyzers. *Anal. Bioanal. Chem.* **2016**, *408* (21), 5769–5778. https://doi.org/10.1007/s00216-016-9679-5.

(45) Hakme, E.; Lozano, A.; Uclés, S.; Fernández-Alba, A. R. Further Improvements in Pesticide Residue Analysis in Food by Applying Gas Chromatography Triple Quadrupole Mass Spectrometry (GC-QqQ-MS/MS) Technologies. *Anal. Bioanal. Chem.* **2018**, *410* (22), 5491–5506. https://doi.org/10.1007/s00216-017-0723-x.

(46) Fabregat-Safont, D.; Sancho, J. V; Félix Hernández, ·; María Ibáñez, ·. Rapid Tentative Identification of Synthetic Cathinones in Seized Products Taking Advantage of the Full Capabilities of Triple Quadrupole Analyzer. **2019**, *37*, 34–44. https://doi.org/10.1007/s11419-018-0432-y.

(47) Bonchio, M.; Bortolini, O.; Conte, V.; Primon, S. Aerobic Oxidation of Isopropanol Catalysed by Peroxovanadium Complexes: Mechanistic Insights. *J. Chem. Soc. Perkin Trans. 2* **2001**, No. 5, 763–765. https://doi.org/10.1039/b009958i.

(48) Gilbert, B. C.; Smith, J. R. L.; Newton, M. S.; Oakes, J.; Prats, R. P. Azo Dye Oxidation with Hydrogen Peroxide Catalysed by Manganese 1,4,7-Triazacyclononane Complexes in Aqueous Solution. *Org. Biomol. Chem.* **2003**, *1* (9), 1568–1577. https://doi.org/10.1039/b301026k.

(49) Hermanson, G. *Bioconjugate Techniques* , 2nd ed.; Elsevier Inc.: London, 2008.

(50) Yunker, L. P. E.; Ahmadi, Z.; Logan, J. R.; Wu, W.; Li, T.; Martindale, A.; Oliver, A. G.; McIndoe, J. S. Real-Time Mass Spectrometric Investigations into the Mechanism of the Suzuki-Miyaura Reaction. *Organometallics* **2018**, *37* (22), 4297–4308. https://doi.org/10.1021/acs.organomet.8b00705.

(51) Ahmadi, Z.; Yunker, L. P. E.; Oliver, A. G.; McIndoe, J. S. Mechanistic Features of the Copper-Free Sonogashira Reaction from ESI-MS. *Dalt. Trans.* **2015**, *44*

(47), 20367–20375. https://doi.org/10.1039/c5dt02889b.

(52) Vikse, K. L.; Ahmadi, Z.; Manning, C. C.; Harrington, D. A.; McIndoe, J. S. Powerful Insight into Catalytic Mechanisms through Simultaneous Monitoring of Reactants, Products, and Intermediates. *Angew. Chemie Int. Ed.* **2011**, *50* (36), 8304–8306. https://doi.org/10.1002/anie.201102630.

(53) Hambitzer, G.; Heitbaum, J. Electrochemical Thermospray Mass Spectrometry. *Anal. Chem.* **1986**, *58* (6), 1067–1070. https://doi.org/10.1021/ac00297a019.

(54) Lee, E. D.; Mueck, W.; Henion, J. D.; Covey, T. R. Real-Time Reaction Monitoring by Continuous-Introduction Ion-Spray Tandem Mass Spectrometry. *J. Am. Chem. Soc.* **1989**, *111* (13), 4600–4604.

(55) Bell, R. J.; Davey, N. G.; Martinsen, M.; Collin-Hansen, C.; Krogh, E. T.; Gill, C. G. A Field-Portable Membrane Introduction Mass Spectrometer for Real-Time Quantitation and Spatial Mapping of Atmospheric and Aqueous Contaminants. *J. Am. Soc. Mass Spectrom.* **2015**, *26*, 212–223. https://doi.org/10.1007/s13361-014-1028-3.

(56) Srinivasan, N.; Kasthurikrishnan, N.; Cooks, R. G.; Krishnan, M. S.; Tsao, G. T. On-Line Monitoring with Feedback Control of Bioreactors Using a High Ethanol Tolerance Yeast by Membrane Introduction Mass Spectrometry. *Anal. Chim. Acta* **1995**, *316* (2), 269–276. https://doi.org/10.1016/0003-2670(95)00362-4.

(57) Brodbelt, J. S.; Cooks, R. G.; Tou, J. C.; Kallos, G. J.; Dryzga, M. D. In Vivo Mass Spectrometric Determination of Organic Compounds in Blood with a Membrane Probe. *Anal. Chem.* **1987**, *59* (3), 454–458. https://doi.org/10.1021/ac00130a017.

(58) Termopoli, V.; Torrisi, E.; Famiglini, G.; Palma, P.; Zappia, G.; Cappiello, A.; Vandergrift, G. W.; Zvekic, M.; Krogh, E. T.; Gill, C. G. Mass Spectrometry Based Approach for Organic Synthesis Monitoring. *Anal. Chem.* **2019**, *91* (18), 11916–11922. https://doi.org/10.1021/acs.analchem.9b02681.

(59) Nelson, J. H. L.; Friesen, D. A.; Gill, C. G.; Krogh, E. T. On-Line Measurement of Oxidative Degradation Kinetics for Trace Gasoline Contaminants in Aqueous Solutions and Natural Water by Membrane Introduction Tandem Mass Spectrometry. *J. Environ. Sci. Heal. Part A* **2010**, *45* (13), 1720–1731. https://doi.org/10.1080/10934529.2010.513250.

(60) Letourneau, D. R.; Gill, C. G.; Krogh, E. T. Photosensitized Degradation Kinetics of Trace Halogenated Contaminants in Natural Waters Using Membrane Introduction Mass Spectrometry as an in Situ Reaction Monitor. *Photochem. Photobiol. Sci.* **2015**, *14* (11), 2108–2118. https://doi.org/10.1039/c5pp00286a.

(61) Zhang, H.; Li, N.; Wang, Y.; Zhao, D.; He, J.; You, H.; Jiang, J. Real-Time Monitoring of the Degradation of Cu(II)-EDTA in H2O2/UV Using Illumination-Assisted Droplet Spray Ionization Mass Spectrometry. *Chemosphere* **2017**, *184*, 932–938. https://doi.org/10.1016/j.chemosphere.2017.06.064.

(62) Pulliam, C. J.; Bain, R. M.; Osswald, H. L.; Snyder, D. T.; Fedick, P. W.; Ayrton, S. T.; Flick, T. G.; Cooks, R. G. Simultaneous Online Monitoring of Multiple Reactions Using a Miniature Mass Spectrometer. *Anal. Chem.* **2017**, *89* (13), 6969–6975. https://doi.org/10.1021/acs.analchem.7b00119.

(63) Yunker, L. P. E.; Stoddard, R. L.; Mcindoe, J. S. Practical Approaches to the ESI-MS Analysis of Catalytic Reactions. **2014**. https://doi.org/10.1002/jms.3303.

(64) Vikse, K. L.; Ahmadi, Z.; Luo, J.; Van Der Wal, N.; Daze, K.; Taylor, N.; McIndoe, J. S. Pressurized Sample Infusion: An Easily Calibrated, Low Volume Pumping System for ESI-MS Analysis of Reactions. *Int. J. Mass Spectrom.* **2012**, *323–324*, 8–13. https://doi.org/10.1016/j.ijms.2012.03.007.

(65) Janusson, E.; Zijlstra, H. S.; Nguyen, P. P. T.; Macgillivray, L.; Martelino, J.; McIndoe, J. S. Real-Time Analysis of Pd2(Dba)3 Activation by Phosphine Ligands. *Chem. Commun.* **2017**, *53* (5), 854–856. https://doi.org/10.1039/c6cc08824d.

(66) Gellrich, U.; Meißner, A.; Steffani, A.; Kähny, M.; Drexler, H. J.; Heller, D.; Plattner, D. A.; Breit, B. Mechanistic Investigations of the Rhodium Catalyzed Propargylic CH Activation. *J. Am. Chem. Soc.* **2014**, *136* (3), 1097–1104. https://doi.org/10.1021/ja411204d.

(67) Yunker, L. P. E.; Ahmadi, Z.; Logan, J. R.; Wu, W.; Li, T.; Martindale, A.; Oliver, A. G.; McIndoe, J. S. Real-Time Mass Spectrometric Investigations into the Mechanism of the Suzuki-Miyaura Reaction. *Organometallics* **2018**, *37* (22), 4297–4308. https://doi.org/10.1021/acs.organomet.8b00705.

(68) Yeung, D.; Penafiel, J.; Zijlstra, H. S.; McIndoe, J. S. Oxidation of Titanocene(III): The Deceptive Simplicity of a Color Change. *Inorg. Chem.* **2018**, *57* (1), 457–461. https://doi.org/10.1021/acs.inorgchem.7b02705.

(69) Vikse, K. L.; Woods, M. P.; McIndoe, J. S. Pressurized Sample Infusion for the Continuous Analysis of Air- and Moisture-Sensitive Reactions Using Electrospray Ionization Mass Spectrometry. *Organometallics* **2010**, *29* (23), 6615–6618. https://doi.org/10.1021/om1008082.

(70) Vicent, C.; Gusev, D. G. ESI-MS Insights into Acceptorless Dehydrogenative Coupling of Alcohols. *ACS Catal.* **2016**, *6* (5), 3301–3309. https://doi.org/10.1021/acscatal.6b00623.

(71) Omari, I.; Zhu, H.; McGarvey, G. B.; McIndoe, J. S. Acid-Selective Mass Spectrometric Analysis of Petroleum Fractions. *Int. J. Mass Spectrom.* **2019**, *435*, 315–320. https://doi.org/10.1016/j.ijms.2018.10.029.

(72) Zhu, H.; Janusson, E.; Luo, J.; Piers, J.; Islam, F.; McGarvey, G. B.; Oliver, A. G.; Granot, O.; McIndoe, J. S. Phenol-Selective Mass Spectrometric Analysis of Jet Fuel. *Analyst* **2017**, *142* (17), 3278–3284. https://doi.org/10.1039/C7AN00908A.

(73) Janusson, E.; McGarvey, G. B.; Islam, F.; Rowan, C.; McIndoe, J. S. Selective Mass Spectrometric Analysis of Thiols Using Charge-Tagged Disulfides. *Analyst* **2016**, *141* (19), 5520–5526. https://doi.org/10.1039/C6AN01210H.

(74) Thomas, G. T.; MacGillivray, L.; Dean, N. L.; Stoddard, R. L.; Yunker, L. P. E.; McIndoe, J. S. Confounding Contaminants in Mass Spectrometric Reaction Monitoring. *Int. J. Mass Spectrom.* **2019**, *441*, 14–18. https://doi.org/10.1016/j.ijms.2019.04.001.

(75) Theron, R.; Wu, Y.; Yunker, L. P. E.; Hesketh, A. V.; Pernik, I.; Weller, A. S.; McIndoe, J. S. Simultaneous Orthogonal Methods for the Real-Time Analysis of Catalytic Reactions. *ACS Catal.* **2016**, *6* (10), 6911–6917. https://doi.org/10.1021/acscatal.6b01489.

(76) Perkampus, H.-H. *UV-VIS Spectroscopy and Its Applications*, 1st ed.; Springer-Verlag, 1992.

(77) Rao, C. N. . *Chromophores and Transitions*; Butterworth and Co. Ltd: London,

1975.

(78) Li, Y.; Hong, X. M.; Collard, D. M.; El-Sayed, M. A. Suzuki Cross-Coupling Reactions Catalyzed by Palladium Nanoparticles in Aqueous Solution. *Org. Lett.* **2000**, *2* (15), 2385–2388. https://doi.org/10.1021/ol0061687.

(79) Sawoo, S.; Srimani, D.; Dutta, P.; Lahiri, R.; Sarkar, A. Size Controlled Synthesis of Pd Nanoparticles in Water and Their Catalytic Application in C-C Coupling Reactions. **2009**. https://doi.org/10.1016/j.tet.2009.03.062.

(80) Phan, N. T. S.; Van Der Sluys, M.; Jones, C. W. On the Nature of the Active Species in Palladium Catalyzed Mizoroki-Heck and Suzuki-Miyaura Couplings - Homogeneous or Heterogeneous Catalysis, a Critical Review. *Advanced Synthesis and Catalysis*. John Wiley & Sons, Ltd April 1, 2006, pp 609–679. https://doi.org/10.1002/adsc.200505473.

(81) Ohde, H.; Wai, C. M.; Kim, H.; Kim, J.; Ohde, M. Hydrogenation of Olefins in Supercritical CO2 Catalyzed by Palladium Nanoparticles in a Water-in-CO2 Microemulsion. *J. Am. Chem. Soc.* **2002**, *124* (17), 4540–4541. https://doi.org/10.1021/ja012232j.

(82) Bauer, M.; Kauf, T.; Christoffers, J.; Bertagnolli, H. Investigations into the Metal Species of the Homogeneous Iron(III) Catalyzed Michael Addition Reactions. *Phys. Chem. Chem. Phys.* **2005**, *7* (13), 2664–2670. https://doi.org/10.1039/b501204j.

(83) Owens, G. S.; Durazo, A.; Abu-Omar, M. M. Kinetics of MTO-Catalyzed Olefin Epoxidation in Ambient Temperature Ionic Liquids: UV/Vis and 2H NMR Study. *Chem. - A Eur. J.* **2002**, *8* (13), 3053–3059. https://doi.org/10.1002/1521-

3765(20020703)8:13<3053::AID-CHEM3053>3.0.CO;2-G.

(84) Hughey, C. A.; Rodgers, R. P.; Marshall, A. G.; Walters, C. C.; Qian, K.; Mankiewicz, P. Acidic and Neutral Polar NSO Compounds in Smackover Oils of Different Thermal Maturity Revealed by Electrospray High Field Fourier Transform Ion Cyclotron Resonance Mass Spectrometry. *Org. Geochem.* **2004**, *35* (7), 863–880. https://doi.org/10.1016/J.ORGGEOCHEM.2004.02.008.

(85) Rodgers, R. P.; Schaub, T. M.; Marshall, A. G. Petroleomics: MS Returns to Its Roots. *Anal. Chem.* **2005**, *77* (1), 20 A-27 A. https://doi.org/10.1021/ac053302y.

(86) Dalmaschio, G. P.; Malacarne, M. M.; de Almeida, V. M. D. L.; Pereira, T. M. C.; Gomes, A. O.; de Castro, E. V. R.; Greco, S. J.; Vaz, B. G.; Romão, W. Characterization of Polar Compounds in a True Boiling Point Distillation System Using Electrospray Ionization FT-ICR Mass Spectrometry. *Fuel* **2014**, *115*, 190–202. https://doi.org/10.1016/J.FUEL.2013.07.008.

(87) Kane, R. D.; Cayard, M. S. Understanding Critical Factors 11, That Influence Refinery Crude Corrosiveness. *Mater. Perform.* **1999**, *38* (7), 48–54.

(88) Meredith, W.; Kelland, S.-J.; Jones, D. . Influence of Biodegradation on Crude Oil Acidity and Carboxylic Acid Composition. *Org. Geochem.* **2000**, *31* (11), 1059–1073. https://doi.org/10.1016/S0146-6380(00)00136-4.

(89) Slavcheva, E.; Shone, B.; Turnbull, A. Review of Naphthenic Acid Corrosion in Oilrefining. *Br. Corros. J.* **1999**, *34* (2), 125–131. https://doi.org/10.1179/000705999101500761.

(90) Headley, J. V.; Peru, K. M.; Barrow, M. P. Mass Spectrometric Characterization of Naphthenic Acids in Environmental Samples: A Review. *Mass Spectrom. Rev.*

2009, *28* (1), 121–134. https://doi.org/10.1002/mas.20185.

(91) Barrow, M. P.; Headley, J. V.; Peru, K. M.; Derrick, P. J. Data Visualization for the Characterization of Naphthenic Acids within Petroleum Samples. *Energy and Fuels* **2009**, *23* (5), 2592–2599. https://doi.org/10.1021/ef800985z.

(92) Mark P. Barrow, †; Liam A. McDonnell, †; Xidong Feng, †; Jérémie Walker, ‡ and; Peter J. Derrick*, †. Determination of the Nature of Naphthenic Acids Present in Crude Oils Using Nanospray Fourier Transform Ion Cyclotron Resonance Mass Spectrometry: The Continued Battle Against Corrosion. **2003**. https://doi.org/10.1021/AC020388B.

(93) Turnbull, A.; Slavcheva, E.; Shone, B. Factors Controlling Naphthenic Acid Corrosion. *CORROSION* **1998**, *54* (11), 922–930. https://doi.org/10.5006/1.3284811.

(94) and, N. A. T.; Winans*, R. E.; and, J. H. S.; Robinson, R. C. On the Nature and Origin of Acidic Species in Petroleum. 1. Detailed Acid Type Distribution in a California Crude Oil. **2001**. https://doi.org/10.1021/EF010106V.

(95) Wang, X.; Kasperski, K. L. Analysis of Naphthenic Acids in Aqueous Solution Using HPLC-MS/MS. *Anal. Methods* **2010**, *2* (11), 1715. https://doi.org/10.1039/c0ay00204f.

(96) Clemente, J. S.; Yen, T.-W.; Fedorak, P. M. Development of a High Performance Liquid Chromatography Method to Monitor the Biodegradation of Naphthenic Acids. *J. Environ. Eng. Sci.* **2003**, *2* (3), 177–186. https://doi.org/10.1139/s03-011.

(97) Holowenko, F. M.; MacKinnon, M. D.; Fedorak, P. M. Characterization of Naphthenic Acids in Oil Sands Wastewaters by Gas Chromatography-Mass

Spectrometry. *Water Res.* **2002**, *36* (11), 2843–2855. https://doi.org/10.1016/S0043-1354(01)00492-4.

(98) Seifert, W. K.; Teeter, R. M.; Howells, W. G.; Cantow, M. J. R. Analysis of Crude Oil Carboxylic Acids after Conversion to Their Corresponding Hydrocarbons. *Anal. Chem.* **1969**, *41* (12), 1638–1647. https://doi.org/10.1021/ac60281a006.

(99) Fan, T. P. Characterization of Naphthenic Acids in Petroleum by Fast Atom Bombardment Mass Spectrometry. *Energy & Fuels* **1991**, *5* (3), 371–375. https://doi.org/10.1021/ef00027a003.

(100) St. John, W. P.; Rughani, J.; Green, S. A.; McGinnis, G. D. Analysis and Characterization of Naphthenic Acids by Gas Chromatography- Electron Impact Mass Spectrometry of Tert.-Butyldimethylsilyl Derivatives. *J. Chromatogr. A* **1998**, *807* (2), 241–251. https://doi.org/10.1016/S0021-9673(98)00085-5.

(101) Chang S. Hsu, *,†; G. J. Dechert, †; W. K. Robbins, † and; Fukuda‡, E. K. Naphthenic Acids in Crude Oils Characterized by Mass Spectrometry. **1999**. https://doi.org/10.1021/EF9901746.

(102) Lo, C. C.; Brownlee, B. G.; Bunce, N. J. Mass Spectrometric and Toxicological Assays of Athabasca Oil Sands Naphthenic Acids. *Water Res.* **2006**, *40* (4), 655–664. https://doi.org/10.1016/J.WATRES.2005.12.008.

(103) Walter E. Rudzinski, *; Leon Oehlers, and; Zhang, Y.; Najera, B. Tandem Mass Spectrometric Characterization of Commercial Naphthenic Acids and a Maya Crude Oil. **2002**. https://doi.org/10.1021/EF020013T.

(104) Kim, S.; Stanford, L. A.; Rodgers, R. P.; Marshall, A. G.; Walters, C. C.; Qian, K.; Wenger, L. M.; Mankiewicz, P. Microbial Alteration of the Acidic and Neutral

Polar NSO Compounds Revealed by Fourier Transform Ion Cyclotron Resonance Mass Spectrometry. *Org. Geochem.* **2005**, *36* (8), 1117–1134. https://doi.org/10.1016/J.ORGGEOCHEM.2005.03.010.

(105) Pål V. Hemmingsen, *,†; Sunghwan Kim, ‡; Hanne E. Pettersen, †; Ryan P. Rodgers, ‡; Johan Sjöblom, † and; Marshall‡, A. G. Structural Characterization and Interfacial Behavior of Acidic Compounds Extracted from a North Sea Oil. **2006**. https://doi.org/10.1021/EF0504321.

(106) Zhan, D.; Fenn, J. B. Electrospray Mass Spectrometry of Fossil Fuels. *Int. J. Mass Spectrom.* **2000**, *194* (2–3), 197–208. https://doi.org/10.1016/S1387-3806(99)00186-4.

(107) Miyabayashi, K.; Naito, Y.; Miyake, M.; Tsujimoto, K. Quantitative Capability of Electrospray Ionization Fourier Transform Ion Cyclotron Resonance Mass Spectrometry for a Complex Mixture. *Eur. J. Mass Spectrom.* **2000**, *6* (3), 251–258. https://doi.org/10.1255/ejms.346.

(108) Duncan, K. D.; Letourneau, D. R.; Vandergrift, G. W.; Jobst, K.; Reiner, E.; Gill, C. G.; Krogh, E. T. A Semi-Quantitative Approach for the Rapid Screening and Mass Profiling of Naphthenic Acids Directly in Contaminated Aqueous Samples. *J. Mass Spectrom.* **2016**, *51* (1), 44–52. https://doi.org/10.1002/jms.3721.

(109) Duncan, K. D.; Volmer, D. A.; Gill, C. G.; Krogh, E. T. Rapid Screening of Carboxylic Acids from Waste and Surface Waters by ESI-MS/MS Using Barium Ion Chemistry and On-Line Membrane Sampling. *J. Am. Soc. Mass Spectrom.* **2016**, *27* (3), 443–450. https://doi.org/10.1007/s13361-015-1311-y.

(110) Fenn, J. B.; Mann, M.; Meng, C. K.; Wong, S. F.; Whitehouse, C. M. Electrospray

Ionization for Mass Spectrometry of Large Biomolecules. *Science* **1989**, *246* (4926), 64–71. https://doi.org/10.1126/SCIENCE.2675315.

(111) Marshall, A. G.; Schweikhard, L. Fourier Transform Ion Cyclotron Resonance Mass Spectrometry: Technique Developments. *Int. J. Mass Spectrom. Ion Process.* **1992**, *118–119*, 37–70. https://doi.org/10.1016/0168-1176(92)85058-8.

(112) Marshall, A. G.; Hendrickson, C. L.; Jackson, G. S. Fourier Transform Ion Cyclotron Resonance Mass Spectrometry: A Primer. *Mass Spectrom. Rev.* **1998**, *17* (1), 1–35. https://doi.org/10.1002/(SICI)1098-2787(1998)17:1<1::AID-MAS1>3.0.CO;2-K.

(113) Jonathan Amster, I. Fourier Transform Mass Spectrometry. *J. Mass Spectrom.* **1996**, *31* (12), 1325–1337. https://doi.org/10.1002/(SICI)1096-9888(199612)31:12<1325::AID-JMS453>3.0.CO;2-W.

(114) Dienes, T.; Pastor, S. J.; Schürch, S.; Scott, J. R.; Yao, J.; Cui, S.; Wilkins, C. L. Fourier Transform Mass Spectrometry—Advancing Years (1992-Mid. 1996). *Mass Spectrom. Rev.* **1996**, *15* (3), 163–211. https://doi.org/10.1002/(SICI)1098-2787(1996)15:3<163::AID-MAS2>3.0.CO;2-G.

(115) and, K. Q.; Robbins, W. K.; Christine A. Hughey, †; Helen J. Cooper; Ryan P. Rodgers, and; Alan G. Marshall*, †. Resolution and Identification of Elemental Compositions for More than 3000 Crude Acids in Heavy Petroleum by Negative-Ion Microelectrospray High-Field Fourier Transform Ion Cyclotron Resonance Mass Spectrometry. **2001**. https://doi.org/10.1021/EF010111Z.

(116) Barrow, M. P.; Headley, J. V.; Peru, K. M.; Derrick, P. J. Fourier Transform Ion Cyclotron Resonance Mass Spectrometry of Principal Components in Oilsands

Naphthenic Acids. *J. Chromatogr. A* **2004**, *1058* (1–2), 51–59. https://doi.org/10.1016/j.chroma.2004.08.082.

(117) Clingenpeel, A. C.; Rowland, S. M.; Corilo, Y. E.; Zito, P.; Rodgers, R. P. Fractionation of Interfacial Material Reveals a Continuum of Acidic Species That Contribute to Stable Emulsion Formation. *Energy & Fuels* **2017**, *31* (6), 5933–5939. https://doi.org/10.1021/acs.energyfuels.7b00490.

(118) Rowland, S. M.; Robbins, W. K.; Corilo, Y. E.; Marshall, A. G.; Rodgers, R. P. Solid-Phase Extraction Fractionation To Extend the Characterization of Naphthenic Acids in Crude Oil by Electrospray Ionization Fourier Transform Ion Cyclotron Resonance Mass Spectrometry. *Energy & Fuels* **2014**, *28* (8), 5043–5048. https://doi.org/10.1021/ef5015023.

(119) Mapolelo, M. M.; Rodgers, R. P.; Blakney, G. T.; Yen, A. T.; Asomaning, S.; Marshall, A. G. Characterization of Naphthenic Acids in Crude Oils and Naphthenates by Electrospray Ionization FT-ICR Mass Spectrometry. *Int. J. Mass Spectrom.* **2011**, *300* (2–3), 149–157. https://doi.org/10.1016/j.ijms.2010.06.005.

(120) Rekha, V. V.; Ramani, M. V.; Ratnamala, A.; Rupakalpana, V.; Subbaraju, G. V.; Satyanarayana, C.; Rao, C. S. A Simple, Efficient, Green, Cost Effective and Chemoselective Process for the Esterification of Carboxylic Acids. *Org. Process Res. Dev.* **2009**, *13* (4), 769–773. https://doi.org/10.1021/op900096y.

(121) Spinella, S.; Maiorana, A.; Qian, Q.; Dawson, N. J.; Hepworth, V.; McCallum, S. A.; Ganesh, M.; Singer, K. D.; Gross, R. A. Concurrent Cellulose Hydrolysis and Esterification to Prepare a Surface-Modified Cellulose Nanocrystal Decorated with Carboxylic Acid Moieties. *ACS Sustain. Chem. Eng.* **2016**, *4* (3), 1538–1550.

https://doi.org/10.1021/acssuschemeng.5b01489.

(122) Zeng, Q.; Song, Z.; Qin, H.; Cheng, H.; Chen, L.; Pan, M.; Heng, Y.; Qi, Z. Ionic Liquid [BMIm][HSO4] as Dual Catalyst-Solvent for the Esterification of Hexanoic Acid with n-Butanol. *Catal. Today* **2020**, *339*, 113–119. https://doi.org/10.1016/j.cattod.2019.03.052.

(123) Fox M. A.; Whitesell J. K. *Organic Chemistry*, 3rd ed.; Jones and Bartlett Publishers, Inc.: London, 2004.

(124) Hoffmann, C.; Faure, A.-C.; Vancaeyzeele, C.; Roux, S.; Tillement, O.; Pauthe, E.; Goubard, F. Labeling of Fibronectin by Fluorescent and Paramagnetic Nanoprobes for Exploring the Extracellular Matrix: Bioconjugate Synthesis Optimization and Biochemical Characterization. *Anal. Bioanal. Chem.* **2011**, *399* (4), 1653–1663. https://doi.org/10.1007/s00216-010-4476-z.

(125) Darr, A.; Calabro, A. Synthesis and Characterization of Tyramine-Based Hyaluronan Hydrogels. *J. Mater. Sci. Mater. Med.* **2009**, *20* (1), 33–44. https://doi.org/10.1007/s10856-008-3540-0.

(126) Havre, T. E.; Sjöblom, J.; Vindstad, J. E. Oil/Water-Partitioning and Interfacial Behavior of Naphthenic Acids. *J. Dispers. Sci. Technol.* **2003**, *24* (6), 789–801. https://doi.org/10.1081/DIS-120025547.

(127) Shepherd, A. G.; van Mispelaar, V.; Nowlin, J.; Genuit, W.; Grutters, M. Analysis of Naphthenic Acids and Derivatization Agents Using Two-Dimensional Gas Chromatography and Mass Spectrometry: Impact on Flow Assurance Predictions †. *Energy & Fuels* **2010**, *24* (4), 2300–2311. https://doi.org/10.1021/ef900949m.

(128) Patiny, L.; Borel, A. ChemCalc: A Building Block for Tomorrow's Chemical

Infrastructure. *J. Chem. Inf. Model.* **2013**, *53* (5), 1223–1228. https://doi.org/10.1021/ci300563h.

(129) Zhou, S.; Cook, K. D. A Mechanistic Study of Electrospray Mass Spectrometry: Charge Gradients within Electrospray Droplets and Their Influence on Ion Response. *J. Am. Soc. Mass Spectrom.* **2001**, *12* (2), 206–214. https://doi.org/10.1016/S1044-0305(00)00213-0.

(130) Cech, N. B.; Enke, C. G. Practical Implications of Some Recent Studies in Electrospray Ionization Fundamentals. *Mass Spectrom. Rev.* **2001**, *20* (6), 362–387. https://doi.org/10.1002/mas.10008.

(131) Amad, M. H.; Cech, N. B.; Jackson, G. S.; Enke, C. G. Importance of Gas-Phase Proton Affinities in Determining the Electrospray Ionization Response for Analytes and Solvents. *J. Mass Spectrom.* **2000**, *35* (7), 784–789. https://doi.org/10.1002/1096-9888(200007)35:7<784::AID-JMS17>3.0.CO;2-Q.

(132) Chalcraft, K. R.; Lee, R.; Mills, C.; Britz-McKibbin, P. Virtual Quantification of Metabolites by Capillary Electrophoresis-Electrospray Ionization-Mass Spectrometry: Predicting Ionization Efficiency Without Chemical Standards. *Anal. Chem.* **2009**, *81* (7), 2506–2515. https://doi.org/10.1021/ac802272u.

(133) Kiontke, A.; Oliveira-Birkmeier, A.; Opitz, A.; Birkemeyer, C. Electrospray Ionization Efficiency Is Dependent on Different Molecular Descriptors with Respect to Solvent PH and Instrumental Configuration. *PLoS One* **2016**, *11* (12), e0167502. https://doi.org/10.1371/journal.pone.0167502.

(134) Henriksen, T.; Juhler, R. K.; Svensmark, B.; Cech, N. B. The Relative Influences of Acidity and Polarity on Responsiveness of Small Organic Molecules to

Analysis with Negative Ion Electrospray Ionization Mass Spectrometry (ESI-MS). *J. Am. Soc. Mass Spectrom.* **2005**, *16* (4), 446–455. https://doi.org/10.1016/j.jasms.2004.11.021.

(135) Mandra, V. J.; Kouskoura, M. G.; Markopoulou, C. K. Using the Partial Least Squares Method to Model the Electrospray Ionization Response Produced by Small Pharmaceutical Molecules in Positive Mode. *Rapid Commun. Mass Spectrom.* **2015**, *29* (18), 1661–1675. https://doi.org/10.1002/rcm.7263.

(136) Cheng, Z. L.; Siu, K. W. M.; Guevremont, R.; Berman, S. S. Electrospray Mass Spectrometry: A Study on Some Aqueous Solutions of Metal Salts☆. *J. Am. Soc. Mass Spectrom.* **1992**, *3* (4), 281–288. https://doi.org/10.1016/1044-0305(92)87055-4.

(137) Kebarle, P.; Peschke, M. On the Mechanisms by Which the Charged Droplets Produced by Electrospray Lead to Gas Phase Ions. *Anal. Chim. Acta* **2000**, *406* (1), 11–35. https://doi.org/10.1016/S0003-2670(99)00598-X.

(138) Fenn, J. B. Ion Formation from Charged Droplets: Roles of Geometry, Energy, and Time. *J. Am. Soc. Mass Spectrom.* **1993**, *4* (7), 524–535. https://doi.org/10.1016/1044-0305(93)85014-O.

(139) Wang, G.; Cole, R. B. Charged Residue versus Ion Evaporation for Formation of Alkali Metal Halide Cluster Ions in ESI. *Anal. Chim. Acta* **2000**, *406* (1), 53–65. https://doi.org/10.1016/S0003-2670(99)00599-1.

(140) Tang, L.; Kebarle, P. Dependence of Ion Intensity in Electrospray Mass Spectrometry on the Concentration of the Analytes in the Electrosprayed Solution. *Anal. Chem.* **1993**, *65* (24), 3654–3668. https://doi.org/10.1021/ac00072a020.

(141) Fei, Z.; Zhu, D.-R.; Yan, N.; Scopelliti, R.; Katsuba, S. A.; Laurenczy, G.; Chisholm, D. M.; McIndoe, J. S.; Seddon, K. R.; Dyson, P. J. Electrostatic and Non-Covalent Interactions in Dicationic Imidazolium-Sulfonium Salts with Mixed Anions. *Chem. - A Eur. J.* **2014**, *20* (15), 4273–4283. https://doi.org/10.1002/chem.201303520.

(142) Bini, R.; Bortolini, O.; Chiappe, C.; Pieraccini, D.; Siciliano, T. Development of Cation/Anion "Interaction" Scales for Ionic Liquids through ESI-MS Measurements. *J. Phys. Chem. B* **2007**, *111* (3), 598–604. https://doi.org/10.1021/jp0663199.

(143) Bruins, A. P. Mechanistic Aspects of Electrospray Ionization. *J. Chromatogr. A* **1998**, *794* (1–2), 345–357. https://doi.org/10.1016/S0021-9673(97)01110-2.

(144) Kebarle, P.; Tang, L. From Ions in Solution to Ions in the Gas Phase - the Mechanism of Electrospray Mass Spectrometry. *Anal. Chem.* **1993**, *65* (22), 972A-986A. https://doi.org/10.1021/ac00070a001.

(145) Cole, R. B.; Harrata, A. K. Charge-State Distributuion and Electric-Discharge Suppression in Negative-Ion Electrospray Mass Spectrometry Using/Chlorinated Solvents. *Rapid Commun. Mass Spectrom.* **1992**, *6* (8), 536–539. https://doi.org/10.1002/rcm.1290060811.

(146) Cole, R. B.; Harrata, A. K. Solvent Effect on Analyte Charge State, Signal Intensity, and Stability in Negative Ion Electrospray Mass Spectrometry; Implications for the Mechanism of Negative Ion Formation. *J. Am. Soc. Mass Spectrom.* **1993**, *4* (7), 546–556. https://doi.org/10.1016/1044-0305(93)85016-Q.

(147) Stassen, H. K.; Ludwig, R.; Wulf, A.; Dupont, J. Imidazolium Salt Ion Pairs in

Solution. *Chem. - A Eur. J.* **2015**, *21* (23), 8324–8335. https://doi.org/10.1002/chem.201500239.

(148) Pape, J.; Vikse, K. L.; Janusson, E.; Taylor, N.; McIndoe, J. S. Solvent Effects on Surface Activity of Aggregate Ions in Electrospray Ionization. *Int. J. Mass Spectrom.* **2014**, *373*, 66–71. https://doi.org/10.1016/j.ijms.2014.09.009.

(149) Bortolini, O.; Chiappe, C.; Ghilardi, T.; Massi, A.; Pomelli, C. S. Dissolution of Metal Salts in Bis(Trifluoromethylsulfonyl)Imide-Based Ionic Liquids: Studying the Affinity of Metal Cations Toward a "Weakly Coordinating" Anion. *J. Phys. Chem. A* **2015**, *119* (21), 5078–5087. https://doi.org/10.1021/jp507437g.

(150) Hunt, P. A. Why Does a Reduction in Hydrogen Bonding Lead to an Increase in Viscosity for the 1-Butyl-2,3-Dimethyl-Imidazolium-Based Ionic Liquids? †. *J. Phys. Chem. B* **2007**, *111* (18), 4844–4853. https://doi.org/10.1021/jp067182p.

(151) Kohagen, M.; Brehm, M.; Lingscheid, Y.; Giernoth, R.; Sangoro, J.; Kremer, F.; Naumov, S.; Iacob, C.; Kärger, J.; Valiullin, R.; et al. How Hydrogen Bonds Influence the Mobility of Imidazolium-Based Ionic Liquids. A Combined Theoretical and Experimental Study of 1- *n* -Butyl-3-Methylimidazolium Bromide. *J. Phys. Chem. B* **2011**, *115* (51), 15280–15288. https://doi.org/10.1021/jp206974h.

(152) Izgorodina, E. I.; MacFarlane, D. R. Nature of Hydrogen Bonding in Charged Hydrogen-Bonded Complexes and Imidazolium-Based Ionic Liquids. *J. Phys. Chem. B* **2011**, *115* (49), 14659–14667. https://doi.org/10.1021/jp208150b.

(153) Katsyuba, S. A.; Vener, M. V.; Zvereva, E. E.; Fei, Z.; Scopelliti, R.; Laurenczy, G.; Yan, N.; Paunescu, E.; Dyson, P. J. How Strong Is Hydrogen Bonding in Ionic

Liquids? Combined X-Ray Crystallographic, Infrared/Raman Spectroscopic, and Density Functional Theory Study. *J. Phys. Chem. B* **2013**, *117* (30), 9094–9105. https://doi.org/10.1021/jp405255w.

(154) Fumino, K.; Reimann, S.; Ludwig, R. Probing Molecular Interaction in Ionic Liquids by Low Frequency Spectroscopy: Coulomb Energy, Hydrogen Bonding and Dispersion Forces. *Phys. Chem. Chem. Phys.* **2014**, *16* (40), 21903–21929. https://doi.org/10.1039/C4CP01476F.

(155) Dhumal, N. R.; Noack, K.; Kiefer, J.; Kim, H. J. Molecular Structure and Interactions in the Ionic Liquid 1-Ethyl-3-Methylimidazolium Bis(Trifluoromethylsulfonyl)Imide. *J. Phys. Chem. A* **2014**, *118* (13), 2547–2557. https://doi.org/10.1021/jp502124y.

(156) Skarmoutsos, I.; Welton, T.; Chemical, P. H.-P. C.; 2014, U. The Importance of Timescale for Hydrogen Bonding in Imidazolium Chloride Ionic Liquids. *Phys. Chem. Chem. Phys.* **2014**, *16*, 3675–3685. https://doi.org/10.1039/c3cp54551b.

(157) Janusson, E.; Hesketh, A. V.; Bamford, K. L.; Hatlelid, K.; Higgins, R.; McIndoe, J. S. Spatial Effects on Electrospray Ionization Response. *Int. J. Mass Spectrom.* **2015**, *388*, 1–8. https://doi.org/10.1016/J.IJMS.2015.07.016.

(158) Song, L. D.; Rosen, M. J. Surface Properties, Micellization, and Premicellar Aggregation of Gemini Surfactants with Rigid and Flexible Spacers. *Langmuir* **1996**, *12* (5), 1149–1153. https://doi.org/10.1021/la950508t.

(159) Zook, D. R.; Bruins, A. P. On Cluster Ions, Ion Transmission, and Linear Dynamic Range Limitations in Electrospray (Ionspray) Mass Spectrometry. *Int. J. Mass Spectrom. Ion Process.* **1997**, *162* (1–3), 129–147. https://doi.org/10.1016/S0168-

1176(96)04511-9.

(160) Yunker, L. P. E.; Ahmadi, Z.; Logan, J. R.; Wu, W.; Li, T.; Martindale, A.; Oliver, A. G.; McIndoe, J. S. Real-Time Mass Spectrometric Investigations into the Mechanism of the Suzuki–Miyaura Reaction. *Organometallics* **2018**, *37* (22), 4297–4308. https://doi.org/10.1021/acs.organomet.8b00705.

(161) Belli, R. G.; Wu, Y.; Ji, H.; Joshi, A.; Yunker, L. P. E.; McIndoe, J. S.; Rosenberg, L. Competitive Ligand Exchange and Dissociation in Ru Indenyl Complexes. *Inorg. Chem.* **2019**, *58* (1), 747–755. https://doi.org/10.1021/acs.inorgchem.8b02915.

(162) Luo, J.; Wu, Y.; Zijlstra, H. S.; Harrington, D. A.; McIndoe, J. S. Mass Transfer and Convection Effects in Small-Scale Catalytic Hydrogenation. *Catal. Sci. Technol.* **2017**, *7* (12), 2609–2615. https://doi.org/10.1039/C7CY00492C.

(163) Yan, X.; Sokol, E.; Li, X.; Li, G.; Xu, S.; Cooks, R. G. On-Line Reaction Monitoring and Mechanistic Studies by Mass Spectrometry: Negishi Cross-Coupling, Hydrogenolysis, and Reductive Amination. *Angew. Chemie Int. Ed.* **2014**, *53* (23), 5931–5935. https://doi.org/10.1002/anie.201310493.

(164) Medeiros, G. A.; da Silva, W. A.; Bataglion, G. A.; Ferreira, D. A. C.; de Oliveira, H. C. B.; Eberlin, M. N.; Neto, B. A. D. Probing the Mechanism of the Ugi Four-Component Reaction with Charge-Tagged Reagents by ESI-MS(/MS). *Chem. Commun.* **2014**, *50* (3), 338–340. https://doi.org/10.1039/C3CC47156J.

(165) Ingram, A. J.; Boeser, C. L.; Zare, R. N. Going beyond Electrospray: Mass Spectrometric Studies of Chemical Reactions in and on Liquids. *Chem. Sci.* **2016**, *7* (1), 39–55. https://doi.org/10.1039/C5SC02740C.

(166) Theron, R.; Wu, Y.; Yunker, L. P. E.; Hesketh, A. V.; Pernik, I.; Weller, A. S.; McIndoe, J. S. Simultaneous Orthogonal Methods for the Real-Time Analysis of Catalytic Reactions. *ACS Catal.* **2016**, *6* (10), 6911–6917. https://doi.org/10.1021/acscatal.6b01489.

(167) Chantooni, M. K.; Kolthoff, I. M. Hydration of Ions in Acetonitrile. *J. Am. Chem. Soc.* **1967**, *89* (7), 1582–1586. https://doi.org/10.1021/ja00983a008.

(168) De Vos, N.; Maton, C.; Stevens, C. V. Electrochemical Stability of Ionic Liquids: General Influences and Degradation Mechanisms. *ChemElectroChem* **2014**, *1* (8), 1258–1270. https://doi.org/10.1002/celc.201402086.

(169) Abbott, A. P.; Mckenzie, K. J. Application of Ionic Liquids to the Electrodeposition of Metals. *Phys. Chem. Chem. Phys.* **2006**, *8*, 4265–4279. https://doi.org/10.1039/b607329h.

(170) Rohner, T. C.; Lion, N.; Girault, H. H. Electrochemical and Theoretical Aspects of Electrospray Ionisation. *Phys. Chem. Chem. Phys.* **2004**, *6*, 3056–3068. https://doi.org/10.1039/b316836k.

(171) Liu, P.; Lu, M.; Zheng, Q.; Zhang, Y.; Dewald, H. D.; Chen, H. Recent Advances of Electrochemical Mass Spectrometry. *Analyst* **2013**, *138* (19), 5519. https://doi.org/10.1039/c3an00709j.

(172) Kay, R. L.; Zawoyski, C.; Evans, D. F. The Conductance of the Symmetrical Tetraalkylammonium Halides and Picrates in Methanol at 25 and 10° [1]. *J. Phys. Chem.* **1965**, *69* (12), 4208–4215. https://doi.org/10.1021/j100782a024.

(173) Evans, D. F.; Zawoyski, C.; Kay, R. L. The Conductance of the Symmetrical Tetraalkylammonium Halides and Picrates in Acetonitrile at 25° [1]. *J. Phys. Chem.*

1965, *69* (11), 3878–3885. https://doi.org/10.1021/j100895a040.

(174) Kay, R. L.; Hawes, J. L. The Association of Cesium Chloride in Anhydrous Methanol at 25°. *J. Phys. Chem.* **1965**, *69* (8), 2787–2788. https://doi.org/10.1021/j100892a505.

(175) Miller, P. E.; Denton, M. B. The Transmission Properties of an RF-Only Quadrupole Mass Filter. *Int. J. Mass Spectrom. Ion Process.* **1986**, *72* (3), 223–238. https://doi.org/10.1016/0168-1176(86)80021-0.

(176) Turecek, F.; Gu, M.; Shaffer, S. A. Novel Tandem Quadrupole-Acceleration-Deceleration Mass Spectrometer for Neutralization-Reionization Studies. *J. Am. Soc. Mass Spectrom.* **1992**, *3* (5), 493–501. https://doi.org/10.1016/1044-0305(92)85026-G.

(177) Ahmadi, Z.; Yunker, L. P. E.; Oliver, A. G.; McIndoe, J. S. Mechanistic Features of the Copper-Free Sonogashira Reaction from ESI-MS. *Dalt. Trans.* **2015**, *44* (47), 20367–20375. https://doi.org/10.1039/C5DT02889B.

(178) Ahmadi, Z.; McIndoe, J. S. A Mechanistic Investigation of Hydrodehalogenation Using ESI-MS. *Chem. Commun.* **2013**, *49* (98), 11488. https://doi.org/10.1039/c3cc46271d.

(179) Hellwig, M.; Henle, T. Baking, Ageing, Diabetes: A Short History of the Maillard Reaction. *Angewandte Chemie - International Edition*. Wiley-VCH Verlag July 14, 2014, pp 10316–10329. https://doi.org/10.1002/anie.201308808.

(180) Nursten, H. The Chemistry of Non Enzymatic Browning. In Maillard Reaction - Chemistry, Biochemistry and Implications. **2005**, 5–29.

(181) O'Brien, J.; Morrissey, P. A. Nutritional and Toxicological Aspects of the Maillard

Browning Reaction in Foods. *Crit. Rev. Food Sci. Nutr.* **1989**, *28* (3), 211–248. https://doi.org/10.1080/10408398909527499.

(182) Van Boekel, M. A. J. S. Effect of Heating on Maillard Reactions in Milk. In *Food Chemistry*; Elsevier, 1998; Vol. 62, pp 403–414. https://doi.org/10.1016/S0308-8146(98)00075-2.

(183) Ames, J. M. Control of the Maillard Reaction in Food Systems. *Trends in Food Science and Technology*. Elsevier July 1, 1990, pp 150–154. https://doi.org/10.1016/0924-2244(90)90113-D.

(184) Ames, J. M.; Arnoldi, A.; Bates, L.; Negroni, M. Analysis of the Methanol-Extractable Nonvolatile Maillard Reaction Products of a Model Extrusion-Cooked Cereal Product. *J. Agric. Food Chem.* **1997**, *45* (4), 1256–1263. https://doi.org/10.1021/jf9606316.

(185) Morales, F. J.; Van Boekel, M. A. J. S. A Study on Advanced Maillard Reaction in Heated Casein/Sugar Solutions: Colour Formation. *Int. Dairy J.* **1998**, *8* (10–11), 907–915. https://doi.org/10.1016/S0958-6946(99)00014-X.

(186) Nursten, H. E. Recent Developments in Studies of the Maillard Reaction. *Food Chem.* **1981**, *6* (3), 263–277. https://doi.org/10.1016/0308-8146(81)90014-5.

(187) Heyns, K.; Meinecke, K.-H. Über Bildung Und Darstellung von D-Glucosamin Aus Fructose Und Ammoniak. *Chem. Ber.* **2006**, *86* (11), 1453–1462. https://doi.org/10.1002/cber.19530861115.

(188) Hodge, J. E. Dehydrated Foods, Chemistry of Browning Reactions in Model Systems. *J. Agric. Food Chem.* **1953**, *1* (15), 928–943. https://doi.org/10.1021/jf60015a004.

(189) Kunze, W. Technology of Brewing & Malting; VLB: Berlin, 2004; pp 90–95, 217.

(190) Köller, H. Magnesium Ion Catalysed Isomerization of Humulone: A New Route to Pure Isohumulones. *J. Inst. Brew.* **1969**, *75* (2), 175–179. https://doi.org/10.1002/j.2050-0416.1969.tb03197.x.

(191) De Keukeleire, D. Fundamentals of Beer and Hop Chemistry. *Quim. Nova* **2000**, *23* (1), 108–112. https://doi.org/10.1590/S0100-40422000000100019.

(192) Langstaff, S. A.; Lewis, M. J. The Mouthfeel of Beer - A Review. *J. Inst. Brew.* **1993**, *99* (1), 31–37. https://doi.org/10.1002/j.2050-0416.1993.tb01143.x.

(193) Lewis, M. J.; Bamforth, C. W. Inorganic Ions. In *Essays in Brewing Science*; Springer US: Boston, MA, 2006; pp 69–73. https://doi.org/10.1007/0-387-33011-9_7.

(194) Pohl, P. Metals in Beer. *Beer Heal. Dis. Prev.* **2009**, 349–358. https://doi.org/10.1016/B978-0-12-373891-2.00033-X.

(195) Comrie, A. A. D. Brewing Liquor-A Review. *J. Inst. Brew.* **1967**, *73* (4), 335–346. https://doi.org/10.1002/j.2050-0416.1967.tb03050.x.

(196) Taylor, J. R. N.; Daiber, K. H. Effect of Calcium Ions in Sorghum Beer Mashing. *J. Inst. Brew.* **1988**, *94* (2), 68–70. https://doi.org/10.1002/j.2050-0416.1988.tb04559.x.

(197) Parkin, E.; Shellhammer, T. Toward Understanding the Bitterness of Dry-Hopped Beer. *J. Am. Soc. Brew. Chem.* **2017**, *75* (4), 363–368. https://doi.org/10.1094/ASBCJ-2017-4311-01.

(198) McLaughlin, I. R.; Lederer, C.; Shellhammer, T. H. Bitterness-Modifying Properties of Hop Polyphenols Extracted from Spent Hop Material. *J. Am. Soc.*

Brew. Chem. **2008**, *66* (3), 174–183. https://doi.org/10.1094/ASBCJ-2008-0619-01.

(199) O'Brien, J.; Morrissey, P. A. Metal Ion Complexation by Products of the Maillard Reaction. *Food Chem.* **1997**, *58* (1–2), 17–27. https://doi.org/10.1016/S0308-8146(96)00162-8.

(200) Rizzi, G. P. Effects of Cationic Species on Visual Color Formation in Model Maillard Reactions of Pentose Sugars and Amino Acids. *J. Agric. Food Chem.* **2008**, *56* (16), 7160–7164. https://doi.org/10.1021/jf801197n.

(201) Rizzi, G. P. Control of Color Formation by Ionic Species in Non-Enzymic Browning Reactions; 2010; pp 121–128. https://doi.org/10.1021/bk-2010-1042.ch012.

(202) Bastgen, N.; Becher, T.; Titze, J. Influencing Factors on Hop Isomerization Beyond the Conventional Range. *J. Am. Soc. Brew. Chem.* **2019**, *77* (2), 126–133. https://doi.org/10.1080/03610470.2019.1587734.

(203) Agu, R. C. Effect of Some Metal Ions on Proteinase Activity of Sorghum and Barley Malts. *Tech. Q. MBAA Commun.* **2006**, *43* (2), 109–114.

(204) Bromberg, S. K.; Bower, P. A.; Duncombe, G. R.; Fehring, J.; Gerber, L.; Lau, V. K.; Tata, M. Requirements for Zinc, Manganese, Calcium, and Magnesium in Wort. *J. Am. Soc. Brew. Chem.* **1997**, *55* (3), 123–128. https://doi.org/10.1094/ASBCJ-55-0123.

(205) Walker, G. M. Magnesium as a Stress-Protectant for Industrial Strains of *Saccharomyces Cerevisiae*. *J. Am. Soc. Brew. Chem.* **1998**, *56* (3), 109–113. https://doi.org/10.1094/ASBCJ-56-0109.

(206) Birch, R. M.; Dumont, A.; Walker, G. M. The Role of Magnesium and Calcium in Governing Yeast Agglomeration. *Food Technol. Biotechnol.* **2002**, *40* (3), 199–205.

(207) Matiacevich, S. B.; Santagapita, P. R.; Buera, M. del P. The Effect of MgCl2 on the Kinetics of the Maillard Reaction in Both Aqueous and Dehydrated Systems. *Food Chem.* **2010**, *118* (1), 103–108. https://doi.org/10.1016/J.FOODCHEM.2009.04.084.

(208) Santagapita, P. R.; Matiacevich, S. B.; Buera, M. del P. Non-Enzymatic Browning Kinetics in Sucrose-Glycine Aqueous and Dehydrated Model Systems in Presence of MgCl2. *Food Res. Int.* **2018**, *114*, 97–103. https://doi.org/10.1016/J.FOODRES.2018.07.049.

(209) Vanderhaegen, B.; Neven, H.; Verachtert, H.; Derdelinckx, G. The Chemistry of Beer Aging – A Critical Review. *Food Chem.* **2006**, *95* (3), 357–381. https://doi.org/10.1016/J.FOODCHEM.2005.01.006.

(210) Vanderhaegen, B.; Delvaux, F.; Daenen, L.; Verachtert, H.; Delvaux, F. R. Aging Characteristics of Different Beer Types. *Food Chem.* **2007**, *103* (2), 404–412. https://doi.org/10.1016/J.FOODCHEM.2006.07.062.

(211) Rivero, D.; Pérez-Magariño, S.; González-Sanjosé, M. L.; Valls-Belles, V.; Pilar Codoñer, A.; Pilar Muñiz. Inhibition of Induced DNA Oxidative Damage by Beers: Correlation with the Content of Polyphenols and Melanoidins. *J. Agric. Food Chem.* **2005**, *53* (9), 3637–3642. https://doi.org/10.1021/JF048146V.

(212) Woffenden, H. M.; Ames, J. M.; Chandra, S.; Monica Anese, A.; Nicoli, M. C. Effect of Kilning on the Antioxidant and Pro-Oxidant Activities of Pale Malts. *J.*

Agric. Food Chem. **2002**, *50* (17), 4925–4933. https://doi.org/10.1021/JF020312G.

(213) Steinhart, H. The Maillard Reaction. Chemistry, Biochemistry and Implications. By Harry Nursten. *Angew. Chemie Int. Ed.* **2005**, *44* (46), 7503–7504. https://doi.org/10.1002/anie.200585332.

(214) Cämmerer, B.; Chodakowski, K.; Gienapp, C.; Wohak, L.; Hartwig, A.; Kroh, L. W. Pro-Oxidative Effects of Melanoidin–Copper Complexes on Isolated and Cellular DNA. *Eur. Food Res. Technol.* **2012**, *234* (4), 663–670. https://doi.org/10.1007/s00217-012-1675-1.

(215) Hoff, S.; Lund, M. N.; Petersen, M. A.; Jespersen, B. M.; Andersen, M. L. Influence of Malt Roasting on the Oxidative Stability of Sweet Wort. *J. Agric. Food Chem.* **2012**, *60* (22), 5652–5659. https://doi.org/10.1021/jf300749r.

(216) Carvalho, D. O.; Øgendal, L. H.; Andersen, M. L.; Guido, L. F. High Molecular Weight Compounds Generated by Roasting Barley Malt Are Pro-Oxidants in Metal-Catalyzed Oxidations. *Eur. Food Res. Technol.* **2016**, *242* (9), 1545–1553. https://doi.org/10.1007/s00217-016-2655-7.

(217) Shellhammer, T. H.; Bamforth, C. W. Assessing Color Quality of Beer. In *ACS Symposium Series*; American Chemical Society, 2008; Vol. 983, pp 192–202. https://doi.org/10.1021/bk-2008-0983.ch015.

(218) Coghe, S.; Adriaenssens, B.; Leonard, S.; Delvaux, F. R. Fractionation of Colored Maillard Reaction Products from Dark Specialty Malts. *J. Am. Soc. Brew. Chem.* **2004**, *62* (2), 79–86. https://doi.org/10.1094/ASBCJ-62-0079.

(219) Cortés, N.; Kunz, T.; Furukawa Suárez, A.; Hughes, P. Development and Correlation Between the Organic Radical Concentration in Different Malt Types

and Oxidative Beer Stability. *J. Am. Soc. Brew. Chem* **2010**, *68* (2), 107–113. https://doi.org/10.1094/ASBCJ-2010-0412-01.

(220) Kunz, T.; Kroh, L. W.; Methner, F.-J.; Berlin, T. U. Influence of Intermediate Maillard Reaction Products with Enediol Structure on the Oxidative Stability of Beverages 1. *J. Am. Soc. Brew. Chem* **2013**, *71* (3), 114–123. https://doi.org/10.1094/ASBCJ-2013-0429-01.

(221) Kwak, E.-J.; Lim, S.-I. The Effect of Sugar, Amino Acid, Metal Ion, and NaCl on Model Maillard Reaction under PH Control. *Amino Acids* **2004**, *27* (1), 85–90. https://doi.org/10.1007/s00726-004-0067-7.

(222) Otter, G. E.; Taylor, L. Determination of the Sugar Composition of Wort and Beer by Gas Liquid Chromatography. *J. Inst. Brew.* **1967**, *73* (6), 570–576. https://doi.org/10.1002/j.2050-0416.1967.tb03086.x.

(223) Nie, C.; Wang, C.; Zhou, G.; Dou, F.; Huang, M. Effects of Malting Conditions on the Amino Acid Compositions of Final Malt. *African J. Biotechnol.* **2010**, *9* (53), 9018–9025. https://doi.org/10.5897/AJB10.370.

(224) Ajandouz, E. H.; Tchiakpe, L. S.; Dalle Ore, F.; Benajiba, A.; Puigserver, A. Effects of PH on Caramelization and Maillard Reaction Kinetics in Fructose-Lysine Model Systems. *J. Food Sci.* **2001**, *66* (7), 926–931. https://doi.org/10.1111/j.1365-2621.2001.tb08213.x.

(225) Swinehart, D. F. The Beer-Lambert Law. *Journal of Chemical Education*. 1962, pp 333–335. https://doi.org/10.1021/ed039p333.

(226) Kuo, D. L. Magnesium Chloride Catalysed Acylation Reaction. *Tetrahedron* **1992**, *48* (42), 9233–9236. https://doi.org/10.1016/S0040-4020(01)85613-1.

(227) Hodge, J. E. Dehydrated Foods, Chemistry of Browning Reactions in Model Systems. *J. Agric. Food Chem.* **1953**, *1* (15), 928–943. https://doi.org/10.1021/jf60015a004.

(228) Arosha N. Wijewickreme; David D. Kitts, * and; Durance, T. D. Reaction Conditions Influence the Elementary Composition and Metal Chelating Affinity of Nondialyzable Model Maillard Reaction Products. *J. Agric. Food Chem.* **1997**, *45* (12), 4577–4583. https://doi.org/10.1021/JF970041N.

(229) Ramonaitytė, D. T.; Keršienė, M.; Adams, A.; Tehrani, K. A.; Kimpe, N. De. The Interaction of Metal Ions with Maillard Reaction Products in a Lactose–Glycine Model System. *Food Res. Int.* **2009**, *42* (3), 331–336. https://doi.org/10.1016/J.FOODRES.2008.12.008.

(230) Gomyo, T.; Horikoshi, M. On the Interaction of Melanoidin with Metallic Ions. *Agric. Biol. Chem.* **1976**, *40* (1), 33–40. https://doi.org/10.1271/bbb1961.40.33.

(231) Yoshihiro Yoshimura, *; Tsutomu Iijima; Takaho Watanabe, and; Nakazawa, H. Antioxidative Effect of Maillard Reaction Products Using Glucose−Glycine Model System. **1997**. https://doi.org/10.1021/JF9609845.

(232) Rufián-Henares, J. A.; de la Cueva, S. P. Antimicrobial Activity of Coffee Melanoidins□A Study of Their Metal-Chelating Properties. *J. Agric. Food Chem.* **2009**, *57* (2), 432–438. https://doi.org/10.1021/jf8027842.

(233) Cui, H.; Hayat, K.; Jia, C.; Duhoranimana, E.; Huang, Q.; Zhang, X.; Ho, C.-T. Synergistic Effect of a Thermal Reaction and Vacuum Dehydration on Improving Xylose–Phenylalanine Conversion to *N* -(1-Deoxy- d -Xylulos-1-Yl)-Phenylalanine during an Aqueous Maillard Reaction. *J. Agric. Food Chem.* **2018**,

66 (38), 10077–10085. https://doi.org/10.1021/acs.jafc.8b04448.

(234) Tang, W.; Cui, H.; Sun, F.; Yu, X.; Hayat, K.; Hussain, S.; Tahir, M. U.; Zhang, X.; Ho, C.-T. *N* -(1-Deoxy- d -Xylulos-1-Yl)-Glutathione: A Maillard Reaction Intermediate Predominating in Aqueous Glutathione-Xylose Systems by Simultaneous Dehydration-Reaction. *J. Agric. Food Chem.* **2019**, *67* (32), 8994–9001. https://doi.org/10.1021/acs.jafc.9b04694.

(235) Wang, J.; Lu, Y.-M.; Liu, B.-Z.; He, H.-Y. Electrospray Positive Ionization Tandem Mass Spectrometry of Amadori Compounds. *J. Mass Spectrom.* **2008**, *43* (2), 262–264. https://doi.org/10.1002/jms.1290.

(236) Nashalian, O.; Yaylayan, V. A. In Situ Formation of the Amino Sugars 1-Amino-1-Deoxy-Fructose and 2-Amino-2-Deoxy-Glucose under Maillard Reaction Conditions in the Absence of Ammonia. *Food Chem.* **2016**, *197*, 489–495. https://doi.org/10.1016/J.FOODCHEM.2015.10.140.

(237) Omari, I.; Randhawa, P.; Randhawa, J.; Yu, J.; McIndoe, J. S. Structure, Anion, and Solvent Effects on Cation Response in ESI-MS. *J. Am. Soc. Mass Spectrom.* **2019**, *30* (9), 1750–1757. https://doi.org/10.1007/s13361-019-02252-0.

(238) Hemmler, D.; Roullier-Gall, C.; Marshall, J. W.; Rychlik, M.; Taylor, A. J.; Schmitt-Kopplin, P. Evolution of Complex Maillard Chemical Reactions, Resolved in Time. *Sci. Rep.* **2017**, *7* (1), 3227. https://doi.org/10.1038/s41598-017-03691-z.

(239) Wunderlich, S.; Back, W. Overview of Manufacturing Beer: Ingredients, Processes, and Quality Criteria. *Beer Heal. Dis. Prev.* **2009**, 3–16. https://doi.org/10.1016/B978-0-12-373891-2.00001-8.

(240) Fix, G. *Principles of Brewing Science: A Study of Serious Brewing Issues*, 2nd ed.; Brewers Publication: Boulder, 1999.

(241) Jones, M.; Pragnell, M. J.; Pierce, J. S. Absorption of Amino Acids by Yeasts From a Semi-Defined Medium Simulating Wort. *J. Inst. Brew.* **1969**, *75* (6), 520–536. https://doi.org/10.1002/j.2050-0416.1969.tb03243.x.

(242) Romkes1, S. C. E.; Lewis, M. J. Some Factors Which Affect Amino Acid Uptake by Saccharomyces Carlsbergensis. *Appl. Microbiol.* **1971**, *21* (5), 799–805.

(243) Patiny, L.; Borel, A. ChemCalc: A Building Block for Tomorrow's Chemical Infrastructure. *J. Chem. Inf. Model.* **2013**, *53* (5), 1223–1228. https://doi.org/10.1021/ci300563h.

(244) Hall, D. G. Structure, Properties, and Preparation of Boronic Acid Derivatives. Overview of Their Reactions and Applications, in Boronic Acids: Preparation and Applications in Organic Synthesis and Medicine (Ed D. G. Hall). In *Boronic Acids*; Wiley-VCH Verlag GmbH & Co. KGaA, Weinheim, FRG.: Weinheim, Germany, 2011; Vol. 1, pp 1–133. https://doi.org/10.1002/9783527639328.ch1.

(245) Doucet, H. Suzuki–Miyaura Cross-Coupling Reactions of Alkylboronic Acid Derivatives or Alkyltrifluoroborates with Aryl, Alkenyl or Alkyl Halides and Triflates. *European J. Org. Chem.* **2008**, *2008* (12), 2013–2030. https://doi.org/10.1002/ejoc.200700984.

(246) Knapp, D. M.; Gillis, E. P.; Burke, M. D. A General Solution for Unstable Boronic Acids: Slow-Release Cross-Coupling from Air-Stable MIDA Boronates. *J. Am. Chem. Soc.* **2009**, *131* (20), 6961–6963. https://doi.org/10.1021/ja901416p.

(247) Li, J.; Grillo, A. S.; Burke, M. D. From Synthesis to Function via Iterative

Assembly of N-Methyliminodiacetic Acid Boronate Building Blocks. *Acc. Chem. Res.* **2015**, *48* (8), 2297–2307. https://doi.org/10.1021/acs.accounts.5b00128.

(248) Dick, G. R.; Knapp, D. M.; Gillis, E. P.; Burke, M. D. General Method for Synthesis of 2-Heterocyclic N-Methyliminodiacetic Acid Boronates. *Org. Lett.* **2010**, *12* (10), 2314–2317. https://doi.org/10.1021/ol100671v.

(249) Gillis, E. P.; Burke, M. D. [Bicyclic Borane Framework] Iterative Cross-Couplng with MIDA Boronates: Towards a General Platform for Small Molecule Synthesis. *Aldrichimica Acta* **2009**, *42* (1), 17–27.

(250) A. Molander, G.; Jean-Gérard, L. Cross-Coupling Reactions of Organotrifluoroborate Salts. In *Organic Reactions*; John Wiley & Sons, Inc.: Hoboken, NJ, USA, 2012; Vol. 79, pp 1–316. https://doi.org/10.1002/0471264180.or079.01.

(251) Cella, R.; Cunha, R. L. O. R.; Reis, A. E. S.; Pimenta, D. C.; Klitzke, C. F.; Stefani, H. A. Suzuki-Miyaura Cross-Coupling Reactions of Aryl Tellurides with Potassium Aryltrifluoroborate Salts. *J. Org. Chem.* **2006**, *71* (1), 244–250. https://doi.org/10.1021/jo052061r.

(252) Yuen, A. K. L.; Hutton, C. A. Deprotection of Pinacolyl Boronate Esters via Hydrolysis of Intermediate Potassium Trifluoroborates. *Tetrahedron Lett.* **2005**, *46* (46), 7899–7903. https://doi.org/10.1016/j.tetlet.2005.09.101.

(253) Molander, G. A.; Ribagorda, M. Expanding Organoboron Chemistry: Epoxidation of Potassium Organotrifluoroborates. *J. Am. Chem. Soc.* **2003**, *125* (37), 11148–11149. https://doi.org/10.1021/ja0351140.

(254) Du, X.; Suguro, M.; Hirabayashi, K.; Mori, A.; Nishikata, T.; Hagiwara, N.;

Kawata, K.; Okeda, T.; Wang, H. F.; Fugami, K.; et al. Mizoroki-Heck Type Reaction of Organoboron Reagents with Alkenes and Alkynes. A Pd(II)-Catalyzed Pathway with Cu(OAc)2 as an Oxidant. *Org. Lett.* **2001**, *3* (21), 3313–3316. https://doi.org/10.1021/ol016529y.

(255) Wright, S. W.; Hageman, D. L.; McClure, L. D. Fluoride-Mediated Boronic Acid Coupling Reactions. *J. Org. Chem.* **1994**, *59* (20), 6095–6097. https://doi.org/10.1021/jo00099a049.

(256) Batey, R. A.; Quach, T. D. Synthesis and Cross-Coupling Reactions of Tetraalkylammonium Organotrifluoroborate Salts. *Tetrahedron Lett.* **2001**, *42* (52), 9099–9103. https://doi.org/10.1016/S0040-4039(01)01983-9.

(257) Darses, S.; Genet, J. P. Potassium Organotrifluoroborates: New Perspectives in Organic Synthesis. *Chemical Reviews*. American Chemical Society January 2008, pp 288–325. https://doi.org/10.1021/cr0509758.

(258) Stefani, H. A.; Cella, R.; Vieira, A. S. Recent Advances in Organotrifluoroborates Chemistry. *Tetrahedron*. Pergamon April 30, 2007, pp 3623–3658. https://doi.org/10.1016/j.tet.2007.01.061.

(259) Lennox, A. J. J.; Lloyd-Jones, G. C. Selection of Boron Reagents for Suzuki-Miyaura Coupling. *Chemical Society Reviews*. Royal Society of Chemistry January 7, 2014, pp 412–443. https://doi.org/10.1039/c3cs60197h.

(260) Molander, G. A.; Ito, T. Cross-Coupling Reactions of Potassium Alkyltrifluoroborates with Aryl and 1-Alkenyl Trifluoromethanesulfonates. *Org. Lett.* **2001**, *3* (3), 393–396. https://doi.org/10.1021/ol006896u.

(261) Molander, G. A.; Biolatto, B. Efficient Ligandless Palladium-Catalyzed Suzuki

Reactions of Potassium Aryltrifluoroborates. *Org. Lett.* **2002**, *4* (11), 1867–1870. https://doi.org/10.1021/ol025845p.

(262) Molander, G. A.; Biolatto, B. Palladium-Catalyzed Suzuki-Miyaura Cross-Coupling Reactions of Potassium Aryl- and Heteroaryltrifluoroborates. *J. Org. Chem.* **2003**, *68* (11), 4302–4314. https://doi.org/10.1021/jo0342368.

(263) Lennox, A. J. J.; Lloyd-Jones, G. C. Organotrifluoroborate Hydrolysis: Boronic Acid Release Mechanism and an Acid-Base Paradox in Cross-Coupling. *J. Am. Chem. Soc.* **2012**, *134* (17), 7431–7441. https://doi.org/10.1021/ja300236k.

(264) Lennox, A. J. J.; Lloyd-Jones, G. C. The Slow-Release Strategy in Suzuki-Miyaura Coupling. *Isr. J. Chem.* **2010**, *50* (5–6), 664–674. https://doi.org/10.1002/ijch.201000074.

(265) Butters, M.; Harvey, J. N.; Jover, J.; Lennox, A. J. J.; Lloyd-Jones, G. C.; Murray, P. M. Aryl Trifluoroborates in Suzuki-Miyaura Coupling: The Roles of Endogenous Aryl Boronic Acid and Fluoride. *Angew. Chemie Int. Ed.* **2010**, *49* (30), 5156–5160. https://doi.org/10.1002/anie.201001522.

(266) Yunker, L. P. E.; Stoddard, R. L.; McIndoe, J. S. Practical Approaches to the ESI-MS Analysis of Catalytic Reactions. *Journal of Mass Spectrometry*. John Wiley & Sons, Ltd January 1, 2014, pp 1–8. https://doi.org/10.1002/jms.3303.

(267) Ting, R.; Harwig, C. W.; Lo, J.; Li, Y.; Adam, M. J.; Ruth, T. J.; Perrin, D. M. Substituent Effects on Aryltrifluoroborate Solvolysis in Water: Implications for Suzuki-Miyaura Coupling and the Design of Stable 18F-Labeled Aryltrifluoroborates for Use in PET Imaging. *J. Org. Chem.* **2008**, *73* (12), 4662–4670. https://doi.org/10.1021/jo800681d.

(268) Pape, J.; Vikse, K. L.; Janusson, E.; Taylor, N.; Mcindoe, J. S. Solvent Effects on Surface Activity of Aggregate Ions in Electrospray Ionization. **2014**. https://doi.org/10.1016/j.ijms.2014.09.009.

(269) Meng, C. K.; Fenn, J. B. Formation of Charged Clusters during Electrospray Ionization of Organic Solute Species. *Org. Mass Spectrom.* **1991**, *26* (6), 542–549. https://doi.org/10.1002/oms.1210260604.

(270) Hao, C.; March, R. E. Electrospray Ionization Tandem Mass Spectrometric Study of Salt Cluster Ions: Part 2 ? Salts of Polyatomic Acid Groups and of Multivalent Metals. *J. Mass Spectrom.* **2001**, *36* (5), 509–521. https://doi.org/10.1002/jms.150.

(271) Rettig, S. J.; Trotter, J. Crystal and Molecular Structure of Phenylboronic Acid, $C_6H_5B(OH)_2$. *Can. J. Chem.* **1977**, *55* (17), 3071–3075. https://doi.org/10.1139/v77-430.

(272) Snyder, H. R.; Kuck, J. A.; Johnson, R. J. Organoboron Compounds, and the Study of Reaction Mechanisms. Primary Aliphatic Boronic Acids. *J. Am. Chem. Soc.* **1938**, *60* (1), 105–111. https://doi.org/10.1021/ja01268a033.

(273) Fujita, N.; Shinkai, S.; James, T. D. Boronic Acids in Molecular Self-Assembly. *Chem. – An Asian J.* **2008**, *3* (7), 1076–1091. https://doi.org/10.1002/asia.200800069.

(274) Giri, R. R.; Ozaki, H.; Morigaki, T.; Taniguchi, S.; Takanami, R. UV Photolysis of Perfluorooctanoic Acid (PFOA) in Dilute Aqueous Solution. *Water Sci. Technol.* **2011**, *63* (2), 276–282. https://doi.org/10.2166/wst.2011.050.

(275) Thomas, A. A.; Denmark, S. E. Pre-Transmetalation Intermediates in the Suzuki-Miyaura Reaction Revealed: The Missing Link. *Science (80-.).* **2016**, *352* (6283),

329–332. https://doi.org/10.1126/science.aad6981.

(276) Thomas, A. A.; Wang, H.; Zahrt, A. F.; Denmark, S. E. Structural, Kinetic, and Computational Characterization of the Elusive Arylpalladium(II)Boronate Complexes in the Suzuki-Miyaura Reaction. *J. Am. Chem. Soc.* **2017**, *139* (10), 3805–3821. https://doi.org/10.1021/jacs.6b13384.

(277) Kuivila, H. G.; Reuwer Jr., J. F.; Mangravite, J. A. Electrophilic Displacement Reactions: XV. Kinetics and Mechanism of the Base-Catalyzed Protodeboronation of Areneboronic Acids. *Can. J. Chem.* **1963**, *41* (12), 3081–3090. https://doi.org/10.1139/v63-451.

(278) Omari, I.; Randhawa, P.; Randhawa, J.; Yu, J.; Mcindoe, J. S. Structure, Anion, and Solvent Effects on Cation Response in ESI-MS. *J. Am. Soc. Mass Spectrom.* **2019**, *30* (9), 1750–1757. https://doi.org/10.1021/JASMS.8B06089;ISSUE:ISSUE:10.1021.

(279) Carrow, B. P.; Hartwig, J. F. Distinguishing between Pathways for Transmetalation in Suzuki-Miyaura Reactions. *J. Am. Chem. Soc.* **2011**, *133* (7), 2116–2119. https://doi.org/10.1021/ja1108326.

(280) Łacki, M. K.; Startek, M.; Valkenborg, D.; Gambin, A. IsoSpec: Hyperfast Fine Structure Calculator. *Anal. Chem.* **2017**, *89* (6), 3272–3277. https://doi.org/10.1021/acs.analchem.6b01459.

(281) Yunker, L. P. E.; Donnecke, S.; Ting, M.; Yeung, D.; McIndoe, J. S. PythoMS: A Python Framework to Simplify and Assist in the Processing and Interpretation of Mass Spectrometric Data. *J. Chem. Inf. Model.* **2019**, *59* (4), 1295–1300. https://doi.org/10.1021/acs.jcim.9b00055.

(282) Liu, R. Y.; Dennis, J. M.; Buchwald, S. L. The Quest for the Ideal Base: Rational Design of a Nickel Precatalyst Enables Mild, Homogeneous C-N Cross-Coupling. *J. Am. Chem. Soc.* **2020**, *142* (9), 4500–4507. https://doi.org/10.1021/jacs.0c00286.

(283) Pang, H.; Wang, Y.; Gallou, F.; Lipshutz, B. H. Fe-Catalyzed Reductive Couplings of Terminal (Hetero)Aryl Alkenes and Alkyl Halides under Aqueous Micellar Conditions. *J. Am. Chem. Soc.* **2019**, *141* (43), 17117–17124. https://doi.org/10.1021/jacs.9b04510.

(284) Handa, S.; Jin, B.; Bora, P. P.; Wang, Y.; Zhang, X.; Gallou, F.; Reilly, J.; Lipshutz, B. H. Sonogashira Couplings Catalyzed by Fe Nanoparticles Containing Ppm Levels of Reusable Pd, under Mild Aqueous Micellar Conditions. *ACS Catal.* **2019**, *9* (3), 2423–2431. https://doi.org/10.1021/acscatal.9b00007.

(285) Ton, S. J.; Fogg, D. E. The Impact of Oxygen on Leading and Emerging Ru-Carbene Catalysts for Olefin Metathesis: An Unanticipated Correlation between Robustness and Metathesis Activity. *ACS Catal.* **2019**, *9* (12), 11329–11334. https://doi.org/10.1021/acscatal.9b03285.

(286) Anand, M.; Nørskov, J. K. Scaling Relations in Homogeneous Catalysis: Analyzing the Buchwald-Hartwig Amination Reaction. *ACS Catal.* **2020**, *10* (1), 336–345. https://doi.org/10.1021/acscatal.9b04323.

(287) Prieto, G. Carbon Dioxide Hydrogenation into Higher Hydrocarbons and Oxygenates: Thermodynamic and Kinetic Bounds and Progress with Heterogeneous and Homogeneous Catalysis. *ChemSusChem* **2017**, *10* (6), 1056–1070. https://doi.org/10.1002/cssc.201601591.

(288) Cook, A.; Prakash, S.; Zheng, Y. L.; Newman, S. G. Exhaustive Reduction of Esters Enabled by Nickel Catalysis. *J. Am. Chem. Soc.* **2020**, *142* (18), 8109–8115. https://doi.org/10.1021/jacs.0c02405.

(289) Verheyen, T.; Van Turnhout, L.; Vandavasi, J. K.; Isbrandt, E. S.; De Borggraeve, W. M.; Newman, S. G. Ketone Synthesis by a Nickel-Catalyzed Dehydrogenative Cross-Coupling of Primary Alcohols. *J. Am. Chem. Soc.* **2019**, *141* (17), 6869–6874. https://doi.org/10.1021/jacs.9b03280.

(290) Zapf, A.; Beller, M. Palladium Catalyst Systems for Cross-Coupling Reactions of Aryl Chlorides and Olefins. *Chem. – A Eur. J.* **2001**, *7* (13), 2908–2915. https://doi.org/10.1002/1521-3765(20010702)7:13<2908::AID-CHEM2908>3.0.CO;2-R.

(291) Castanet, A. S.; Colobert, F.; Desmurs, J. R.; Schlama, T. Biaryl Synthesis via Suzuki Coupling Promoted by Catalytic Amounts of Quaternary Ammonium Salts. In *Journal of Molecular Catalysis A: Chemical*; Elsevier, 2002; Vol. 182–183, pp 481–487. https://doi.org/10.1016/S1381-1169(01)00489-7.

(292) Li, Z.; Ke, F.; Deng, H.; Xu, H.; Xiang, H.; Zhou, X. Synthesis of Disulfides and Diselenides by Copper-Catalyzed Coupling Reactions in Water. *Org. Biomol. Chem.* **2013**, *11* (18), 2943–2946. https://doi.org/10.1039/c3ob40464a.

(293) Luo, J.; Wu, Y.; Zijlstra, H. S.; Harrington, D. A.; Scott McIndoe, J. Mass Transfer and Convection Effects in Small-Scale Catalytic Hydrogenation. *Cite this Catal. Sci. Technol* **2017**, *7*, 2609. https://doi.org/10.1039/c7cy00492c.

(294) Lennox, A. J. J.; Lloyd-Jones, G. C. Organotrifluoroborate Hydrolysis: Boronic Acid Release Mechanism and an Acid-Base Paradox in Cross-Coupling. *J. Am.*

Chem. Soc. **2012**, *134* (17), 7431–7441. https://doi.org/10.1021/ja300236k.

(295) Gonzalez, J. A.; Ogba, O. M.; Morehouse, G. F.; Rosson, N.; Houk, K. N.; Leach, A. G.; Cheong, P. H. Y.; Burke, M. D.; Lloyd-Jones, G. C. MIDA Boronates Are Hydrolysed Fast and Slow by Two Different Mechanisms. *Nat. Chem.* **2016**, *8* (11), 1067–1075. https://doi.org/10.1038/nchem.2571.

(296) Ahmadi, Z.; Yunker, L. P. E.; Oliver, A. G.; McIndoe, J. S. Mechanistic Features of the Copper-Free Sonogashira Reaction from ESI-MS. *Dalt. Trans.* **2015**, *44* (47), 20367–20375. https://doi.org/10.1039/c5dt02889b.

(297) Gazvoda, M.; Virant, M.; Pinter, B.; Košmrlj, J. Mechanism of Copper-Free Sonogashira Reaction Operates through Palladium-Palladium Transmetallation. *Nat. Commun.* **2018**, *9* (1), 1–9. https://doi.org/10.1038/s41467-018-07081-5.

(298) Ljungdahl, T.; Bennur, T.; Dallas, A.; Emtenäs, H.; Mårtensson, J. Two Competing Mechanisms for the Copper-Free Sonogashira Cross-Coupling Reaction. *Organometallics* **2008**, *27* (11), 2490–2498. https://doi.org/10.1021/om800251s.

(299) Vikse, K. L.; Ahmadi, Z.; Manning, C. C.; Harrington, D. A.; McIndoe, J. S. Powerful Insight into Catalytic Mechanisms through Simultaneous Monitoring of Reactants, Products, and Intermediates. *Angew. Chemie Int. Ed.* **2011**, *50* (36), 8304–8306. https://doi.org/10.1002/anie.201102630.

(300) Jutand, A.; Négri, S.; Principaud, A. Formation of ArPdXL(Amine) Complexes by Substitution of One Phosphane Ligand by an Amine in *Trans*- $ArPdX(PPh_3)_2$ Complexes. *Eur. J. Inorg. Chem.* **2005**, *2005* (4), 631–635. https://doi.org/10.1002/ejic.200400413.

(301) Gelman, D.; Buchwald, S. L. Efficient Palladium-Catalyzed Coupling of Aryl Chlorides and Tosylates with Terminal Alkynes: Use of a Copper Cocatalyst Inhibits the Reaction. *Angew. Chemie Int. Ed.* **2003**, *42* (48), 5993–5996. https://doi.org/10.1002/anie.200353015.

(302) Urgaonkar, S.; Verkade, J. G. Ligand-, Copper-, and Amine-Free Sonogashira Reaction of Aryl Iodides and Bromides with Terminal Alkynes. *J. Org. Chem.* **2004**, *69* (17), 5752–5755. https://doi.org/10.1021/jo049325e.

(303) Lipshutz, B. H.; Chung, D. W.; Rich, B. Sonogashira Couplings of Aryl Bromides: Room Temperature, Water Only, No Copper. *Org. Lett.* **2008**, *10* (17), 3793–3796. https://doi.org/10.1021/ol801471f.

(304) Karak, M.; Barbosa, L. C. A.; Hargaden, G. C. Recent Mechanistic Developments and next Generation Catalysts for the Sonogashira Coupling Reaction. *RSC Advances*. Royal Society of Chemistry October 23, 2014, pp 53442–53466. https://doi.org/10.1039/c4ra09105a.

(305) Komáromi, A.; Novák, Z. Efficient Copper-Free Sonogashira Coupling of Aryl Chlorides with Palladium on Charcoal. *Chem. Commun.* **2008**, No. 40, 4968–4970. https://doi.org/10.1039/b810928a.

(306) Noordzij, G. J.; Dietz, C. H. J. T.; Leoné, N.; Wilsens, C. H. R. M.; Rastogi, S. Small-Scale Screening of Novel Biobased Monomers: The Curious Case of 1,3-Cyclopentanediol. *RSC Adv.* **2018**, *8* (70), 39818–39828. https://doi.org/10.1039/C8RA08811J.

(307) Truppo, M. D.; Rozzell, J. D.; Moore, J. C.; Turner, N. J. Rapid Screening and Scale-up of Transaminase Catalysed Reactions. *Org. Biomol. Chem.* **2009**, *7* (2),

395–398. https://doi.org/10.1039/b817730a.

(308) Santanilla, A. B.; Regalado, E. L.; Pereira, T.; Shevlin, M.; Bateman, K.; Campeau, L. C.; Schneeweis, J.; Berritt, S.; Shi, Z. C.; Nantermet, P.; et al. Nanomole-Scale High-Throughput Chemistry for the Synthesis of Complex Molecules. *Science (80-.).* **2015**, *347* (6217), 49–53. https://doi.org/10.1126/science.1259203.

(309) Isbrandt, E. S.; Sullivan, R. J.; Newman, S. G. High Throughput Strategies for the Discovery and Optimization of Catalytic Reactions. *Angew. Chemie Int. Ed.* **2019**, *58* (22), 7180–7191. https://doi.org/10.1002/anie.201812534.

(310) Monfette, S.; Blacquiere, J. M.; Fogg, D. E. The Future, Faster: Roles for High-Throughput Experimentation in Accelerating Discovery in Organometallic Chemistry and Catalysis. *Organometallics* **2011**, *30* (1), 36–42. https://doi.org/10.1021/om1010319.

(311) Shi, S.; Szostak, M. Decarbonylative Cyanation of Amides by Palladium Catalysis. *Org. Lett.* **2017**, *19* (12), 3095–3098. https://doi.org/10.1021/acs.orglett.7b01199.

(312) Brals, J.; Smith, J. D.; Ibrahim, F.; Gallou, F.; Handa, S. Micelle-Enabled Palladium Catalysis for Convenient Sp2-Sp3 Coupling of Nitroalkanes with Aryl Bromides in Water under Mild Conditions. *ACS Catal.* **2017**, *7* (10), 7245–7250. https://doi.org/10.1021/acscatal.7b02663.

(313) Cresswell, A. J.; Lloyd-Jones, G. C. Room-Temperature Gold-Catalysed Arylation of Heteroarenes: Complementarity to Palladium Catalysis. *Chem. - A Eur. J.* **2016**, *22* (36), 12641–12645. https://doi.org/10.1002/chem.201602893.

(314) Jagtap, S. Heck Reaction—State of the Art. *Catalysts* **2017**, *7* (9), 267.

https://doi.org/10.3390/catal7090267.

(315) Kurandina, D.; Rivas, M.; Radzhabov, M.; Gevorgyan, V. Heck Reaction of Electronically Diverse Tertiary Alkyl Halides. *Org. Lett.* **2018**, *20* (2), 357–360. https://doi.org/10.1021/acs.orglett.7b03591.

(316) de Vries, J. G. The Heck Reaction in the Production of Fine Chemicals. *Can. J. Chem.* **2001**, *79* (5–6), 1086–1092. https://doi.org/10.1139/v01-033.

(317) Chen, Z.; Vorobyeva, E.; Mitchell, S.; Fako, E.; Ortuño, M. A.; López, N.; Collins, S. M.; Midgley, P. A.; Richard, S.; Vilé, G.; et al. A Heterogeneous Single-Atom Palladium Catalyst Surpassing Homogeneous Systems for Suzuki Coupling. *Nature Nanotechnology*. Nature Publishing Group June 25, 2018, pp 702–707. https://doi.org/10.1038/s41565-018-0167-2.

(318) Liu, C.; Li, G.; Shi, S.; Meng, G.; Lalancette, R.; Szostak, R.; Szostak, M. Acyl and Decarbonylative Suzuki Coupling of N-Acetyl Amides: Electronic Tuning of Twisted, Acyclic Amides in Catalytic Carbon-Nitrogen Bond Cleavage. *ACS Catal.* **2018**, *8* (10), 9131–9139. https://doi.org/10.1021/acscatal.8b02815.

(319) Kubo, T.; Scheutz, G. M.; Latty, T. S.; Sumerlin, B. S. Synthesis of Functional and Boronic Acid-Containing Aliphatic Polyesters: Via Suzuki Coupling. *Chem. Commun.* **2019**, *55* (39), 5655–5658. https://doi.org/10.1039/c9cc01975h.

(320) Kumar Mondal, S.; Ali, S. A.; Kumar Manna, S.; Mandal, A.; Kumar Senapati, B.; Hossain, M.; Samanta, S. Palladium-Catalyzed Intramolecular Cyclization: Access to Rare Pentacyclic *N* -Fused Heterocycles. *ChemistrySelect* **2017**, *2* (29), 9312–9318. https://doi.org/10.1002/slct.201701800.

(321) El-Atawy, M. A.; Ferretti, F.; Ragaini, F. Palladium-Catalyzed Intramolecular

Cyclization of Nitroalkenes: Synthesis of Thienopyrroles. *European J. Org. Chem.* **2017**, *2017* (14), 1902–1910. https://doi.org/10.1002/ejoc.201700165.

(322) A., L.; X., L.; G., L. A Novel Highly Regio- and Diastereoselective Haloamination of Alkenes Catalyzed by Divalent Palladium. *Tetrahedron Lett.* **2004**, *45*, 1785–1788.

(323) Wang, Y.; You, S.; Hu, J.; Zhang, K. Synthesis and Properties of Benzoxazine Monomers Bearing Both 3-Methyltetrahydrophtalimide and Nitrile Groups: Para-Para vs. Ortho-Ortho. *Macromol. Res.* **2020**, *28* (1), 74–81. https://doi.org/10.1007/s13233-020-8018-z.

(324) Holly, F. W.; Cope, A. C. Condensation Products of Aldehydes and Ketones with O-Aminobenzyl Alcohol and o-Hydroxybenzylamine. *J. Am. Chem. Soc.* **1944**, *66* (11), 1875–1879. https://doi.org/10.1021/ja01239a022.

(325) Aversa, M. C.; Giannetto, P.; Caristi, C.; Ferlazzo, A. Behaviour of an N-(o-Hydroxybenzyl)-β-Amino-Acid in the Presence of Dehydrating Agents. Synthesis of a 3,4-Dihydro-2H-1,3-Benzoxazine. *J. Chem. Soc. - Ser. Chem. Commun.* **1982**, *0* (8), 469–470. https://doi.org/10.1039/C39820000469.

(326) Speier, J. L.; Webster, J. A.; Barnes, G. H. The Addition of Silicon Hydrides to Olefinic Double Bonds. Part II. The Use of Group VIII Metal Catalysts. *J. Am. Chem. Soc.* **1957**, *79* (4), 974–979. https://doi.org/10.1021/ja01561a054.

(327) Benkeser, R. A.; Kang, J. The Composition of Speier's Catalyst. *J. Organomet. Chem.* **1980**, *185* (1), C9–C12. https://doi.org/10.1016/S0022-328X(00)94412-7.

(328) Behr, A.; Naendrup, F.; Obst, D. Platinum-Catalysed Hydrosilylation of Unsaturated Fatty Acid Esters. *Adv. Synth. Catal.* **2002**, *344* (10), 1142–1145.

https://doi.org/10.1002/1615-4169(200212)344:10<1142::AID-ADSC1142>3.0.CO;2-P.

(329) Skoda-Földes, R.; Kollár, L.; Heil, B. Homogeneous Catalytic Hydrosilylation of the CC Double Bond with Platinum Catalysts. *J. Organomet. Chem.* **1989**, *366* (1–2), 275–279. https://doi.org/10.1016/0022-328X(89)87333-4.

(330) Stein, J.; Lewis, L. N.; Gao, Y.; Scott, R. A. In Situ Determination of the Active Catalyst in Hydrosilylation Reactions Using Highly Reactive Pt(0) Catalyst Precursors. *J. Am. Chem. Soc.* **1999**, *121* (15), 3693–3703. https://doi.org/10.1021/ja9825377.

(331) Li, C.; Li, D.; Zhao, Z. S.; Duan, X. M.; Hou, W. Platinum Nanoparticles from Hydrosilylation Reaction: Carbosilane Dendrimer as Capping Agent. *Colloids Surfaces A Physicochem. Eng. Asp.* **2010**, *366* (1–3), 45–49. https://doi.org/10.1016/j.colsurfa.2010.05.013.

(332) Lewis, L. N.; Colbom, R. E.; Grade, H.; Bryant, G. L.; Sumpter, C. A.; Scott, R. A. *Mechanism of Formation of Platinum(O) Complexes Containing Silicon-Vinyl Ligands*; 1995; Vol. 14.

(333) Harada, M.; Einaga, H. Formation Mechanism of Pt Particles by Photoreduction of Pt Ions in Polymer Solutions. **2006**. https://doi.org/10.1021/la052378m.

(334) Wojnicki, M.; Kwolek, P. Reduction of Hexachloroplatinate(IV) Ions with Methanol under UV Radiation. *J. Photochem. Photobiol. A Chem.* **2016**, *314*, 133–142. https://doi.org/10.1016/j.jphotochem.2015.08.020.

(335) Hossain, M. J.; Rahman, M. S.; Rahman, • M S; Ali, • M A; Nandi, • N C; Noor, • P; Ahmed, • K N; Akhter, • S. Optimized Reduction Conditions for the

Microfluidic Synthesis of 1.3 ± 0.3 Nm Pt Clusters. *J. Nanostructure Chem. 6*. https://doi.org/10.1007/s40097-015-0179-5.

Appendix A
Acid-selective mass spectrometric analysis of petroleum fractions

Section A1. NMR spectra for synthesized imidazolium salts

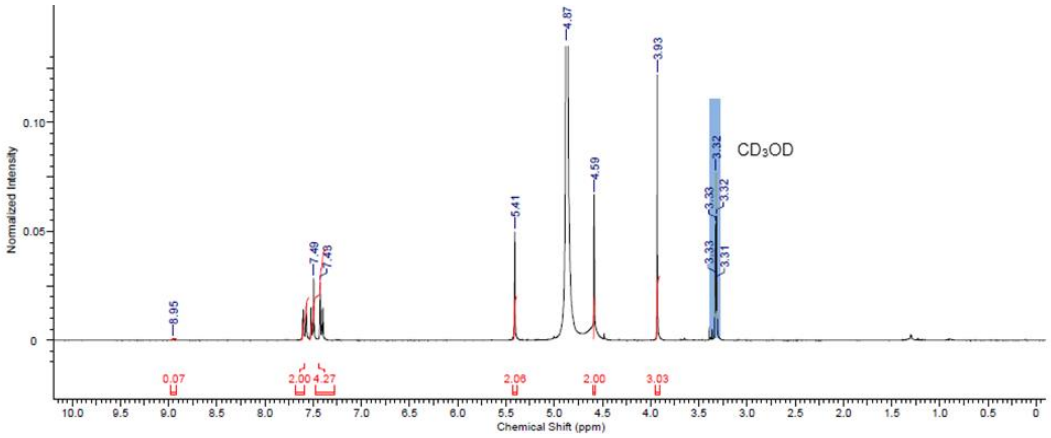

Figure A.1. 1H NMR (300 MHz, CD_3OD) spectrum of 3-(4-(bromomethyl) benzyl)-1-methylimidazolium hexafluorophosphate, CD_3OD solvent; 298 K.

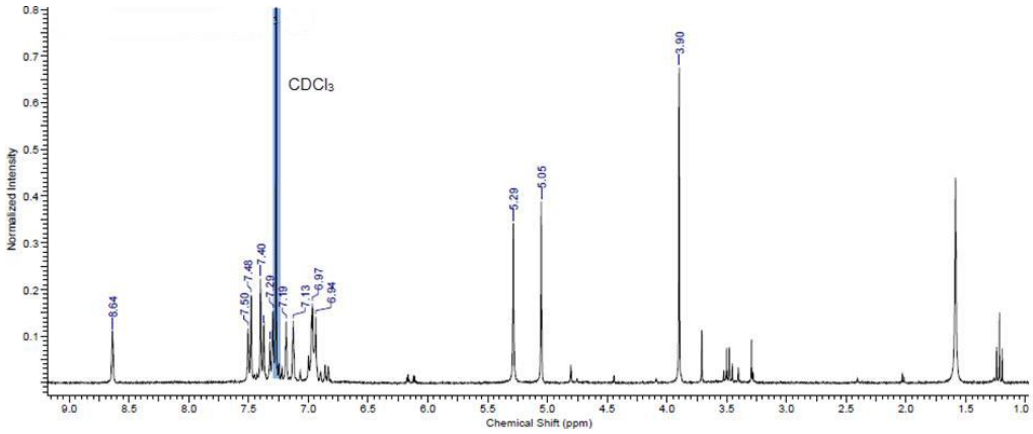

Figure A.2. 1H NMR (300 MHz, $CDCl_3$) spectrum of 3-(4-(hydroxymethyl) benzyl)-1-methylimidazolium hexafluorophosphate, $CDCl_3$ solvent; 298 K.

Appendix B
Structure, anion, and solvent effects on cation response in ESI-MS

Section B1. ESI-MS spectra for synthesized salts and analyte response

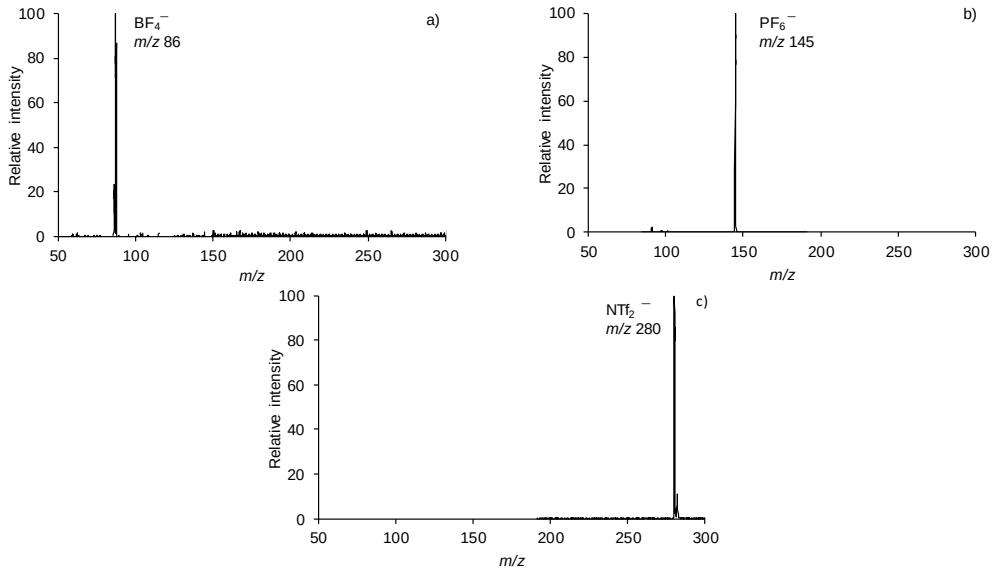

Figure B.1. Negative ion ESI mass spectrum of the synthesized salts in methanol: a) $[BF_4]^-$; b) $[PF_6]^-$; and c) $[NTf_2]^-$.

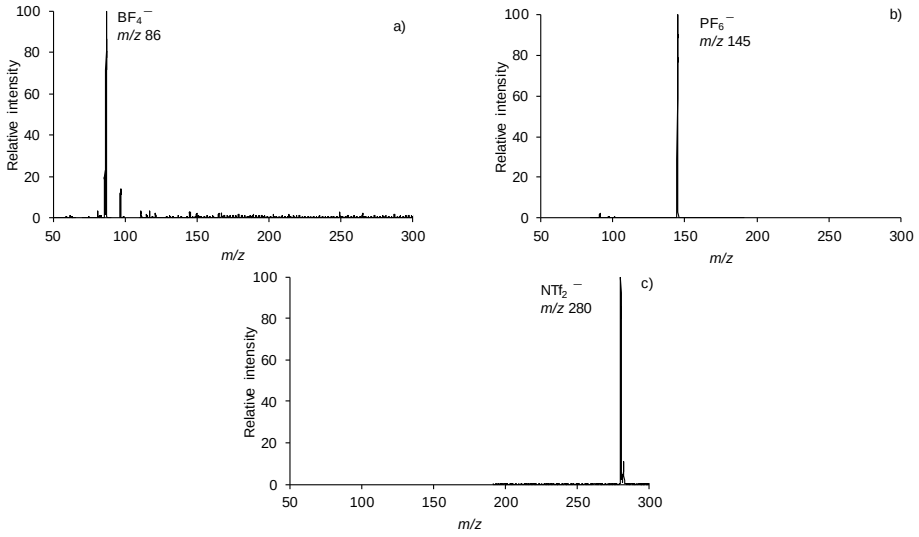

Figure B.2. Negative ion ESI mass spectrum of the synthesized salts in water/acetonitrile: a) $[BF_4]^-$; b) $[PF_6]^-$; and c) $[NTf_2]^-$.

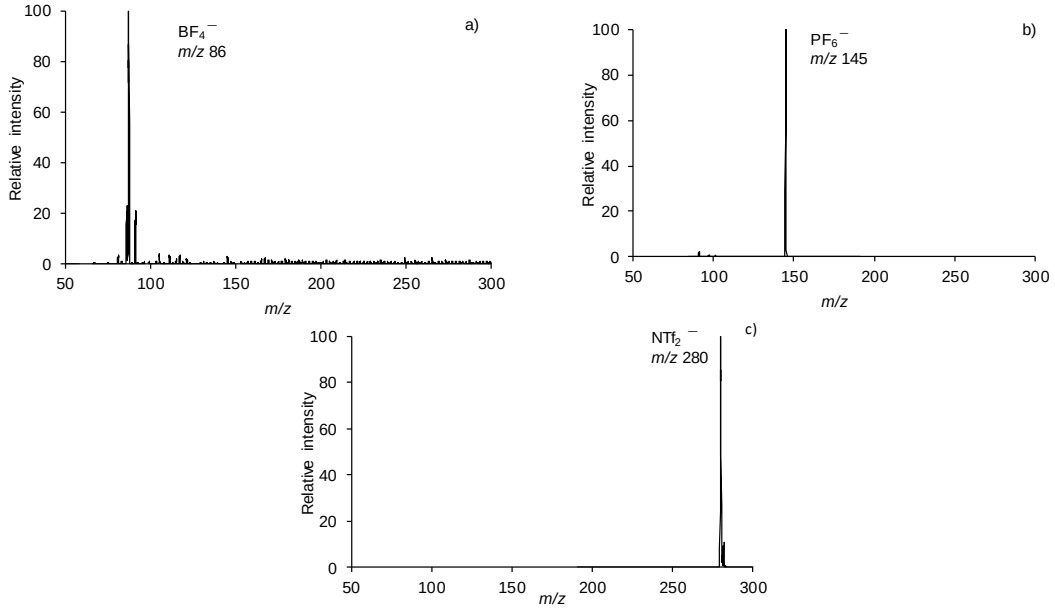

Figure B.3. Negative ion ESI mass spectrum of the synthesized salts in acetonitrile: a) $[BF_4]^-$; b) $[PF_6]^-$; and c) $[NTf_2]^-$.

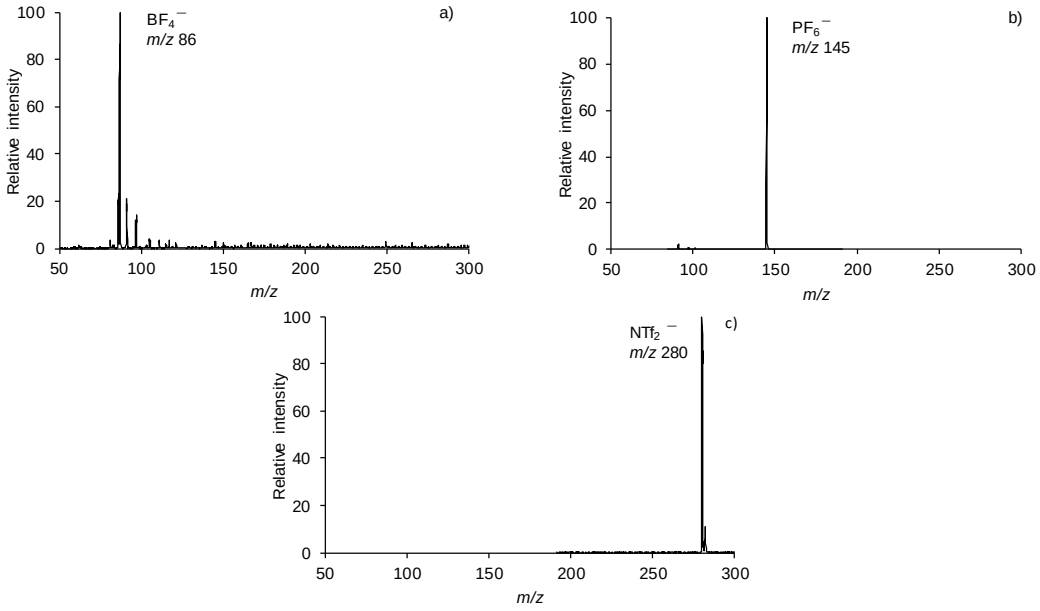

Figure B.4. Negative ion ESI mass spectrum of the synthesized salts in dichloromethane: a) $[BF_4]^-$; b) $[PF_6]^-$; and c) $[NTf_2]^-$.

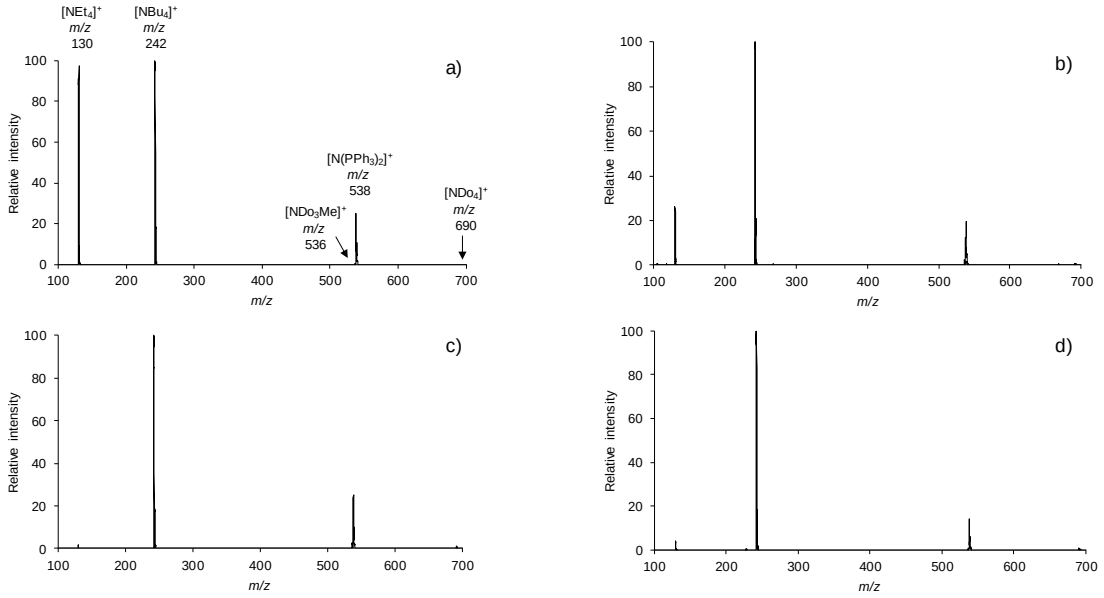

Figure B.5. Positive ion ESI mass spectrum of an equimolar mixture of six cations $[NEt_4]^+$ (*m/z* 130), Cs^+ (*m/z* 132), $[NBu_4]^+$ (*m/z* 242), $[N(PPh_3)_2]^+$ (*m/z* 538), $[NDo_3Me]^+$ (*m/z* 536), $[NDo_4]^+$ (*m/z* 690), paired with various counterions in dichloromethane: a) Cl^-; b) $[BF_4]^-$; c) $[PF_6]^-$; and d) $[NTf_2]^-$.

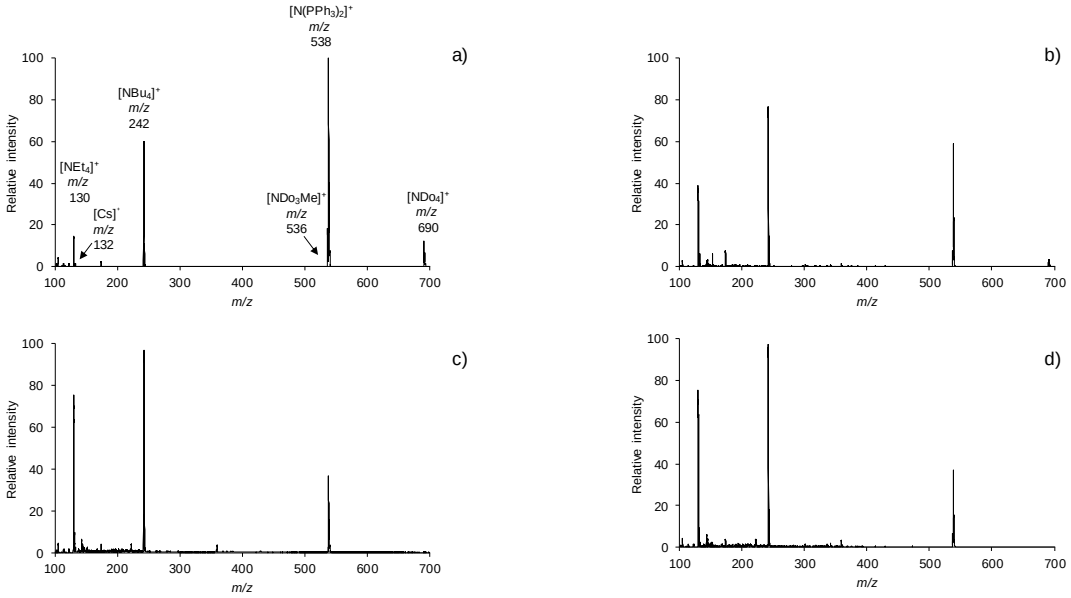

Figure B.6. Positive ion ESI mass spectrum of an equimolar mixture of six cations $[NEt_4]^+$ (*m/z* 130), Cs^+ (*m/z* 132), $[NBu_4]^+$ (*m/z* 242), $[N(PPh_3)_2]^+$ (*m/z* 538), $[NDo_3Me]^+$ (*m/z* 536), $[NDo_4]^+$ (*m/z* 690), paired with various counterions in water/acetonitrile: a) Cl^-; b) $[BF_4]^-$; c) $[PF_6]^-$; and d) $[NTf_2]^-$.

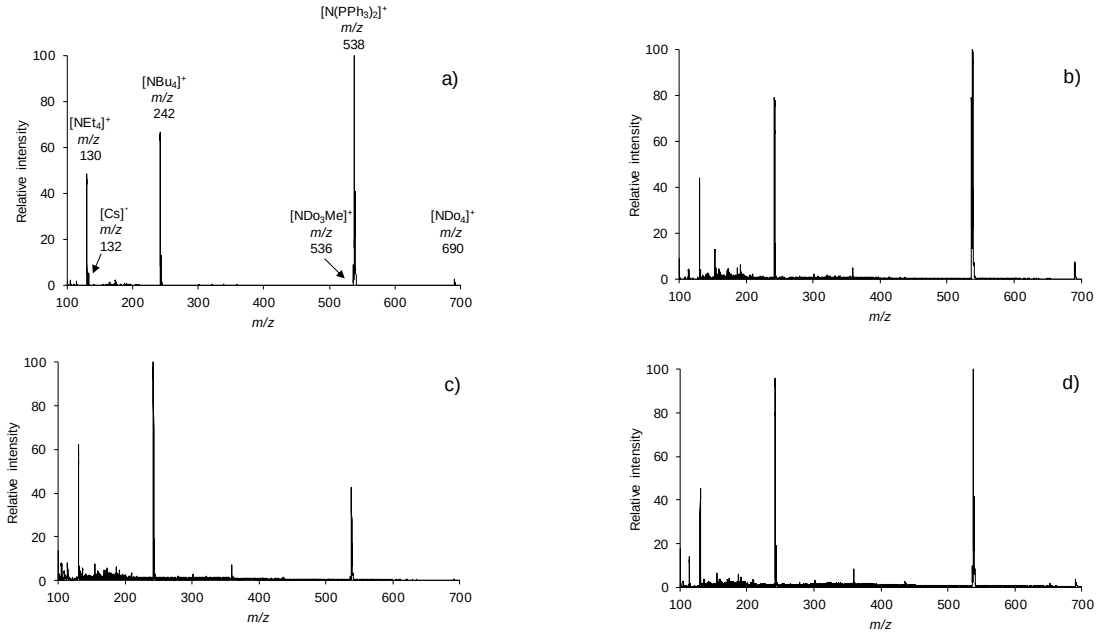

Figure B.7. Positive ion ESI mass spectrum of an equimolar mixture of six cations $[NEt_4]^+$ (*m/z* 130), Cs^+ (*m/z* 132), $[NBu_4]^+$ (*m/z* 242), $[N(PPh_3)_2]^+$ (*m/z* 538), $[NDo_3Me]^+$ (*m/z* 536), $[NDo_4]^+$ (*m/z* 690), paired with various counterions in methanol: a) Cl^-; b) $[BF_4]^-$; c) $[PF_6]^-$; and d) $[NTf_2]^-$.

Appendix C
Magnesium-accelerated Maillard reactions in beer brewing

Section C1. ESI-MS/MS of Maillard reaction species

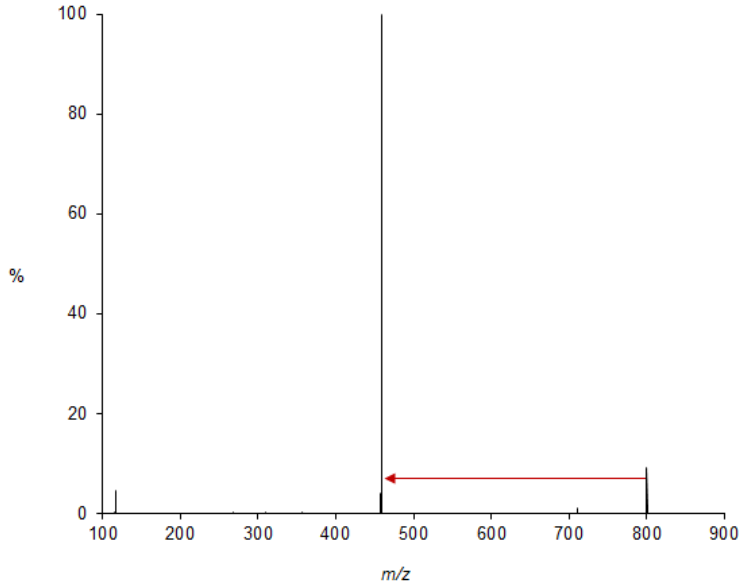

Figure C.1. ESI-MS/MS spectra of a precursor ion at m/z 800.0308 and a product ion at *m/z* 458.0179 of a maltose-proline system.

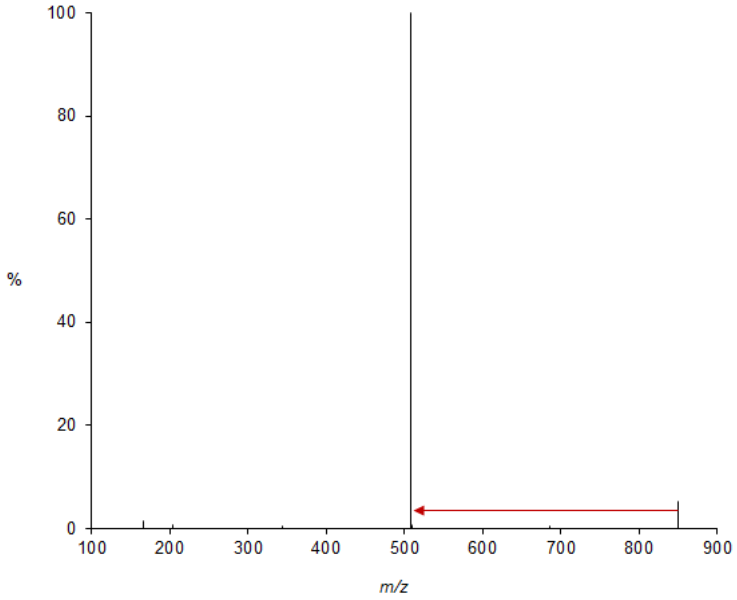

Figure C.2. ESI-MS/MS spectra of a precursor ion at m/z 850.0030 and a product ion at *m/z* 508.0730 of a maltose-proline system.

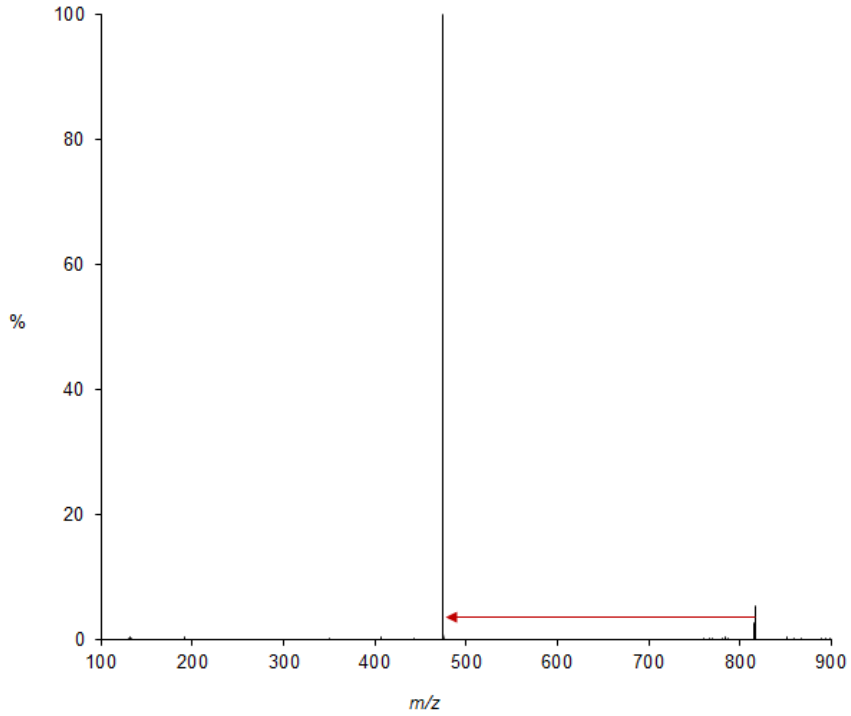

Figure C.3. ESI-MS/MS spectra of a precursor ion at m/z 816.0049 and a product ion at *m/z* 474.1030 of a maltose-leucine system.

Section C2. Change of absorbance over time

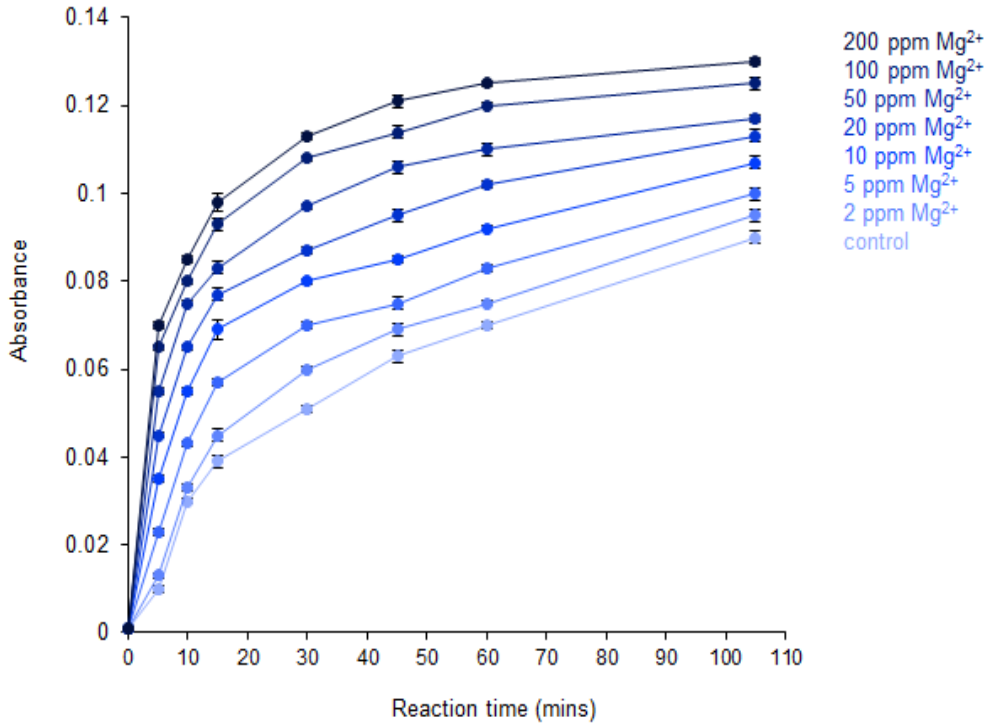

Figure C.4. Representation of the influence of Mg^{2+} on the change of absorbance over time of a maltose-leucine model system. The standard deviation of the mean (n = 3) is represented by the vertical bars.

Section C3. ESI-MS Mass Spectra

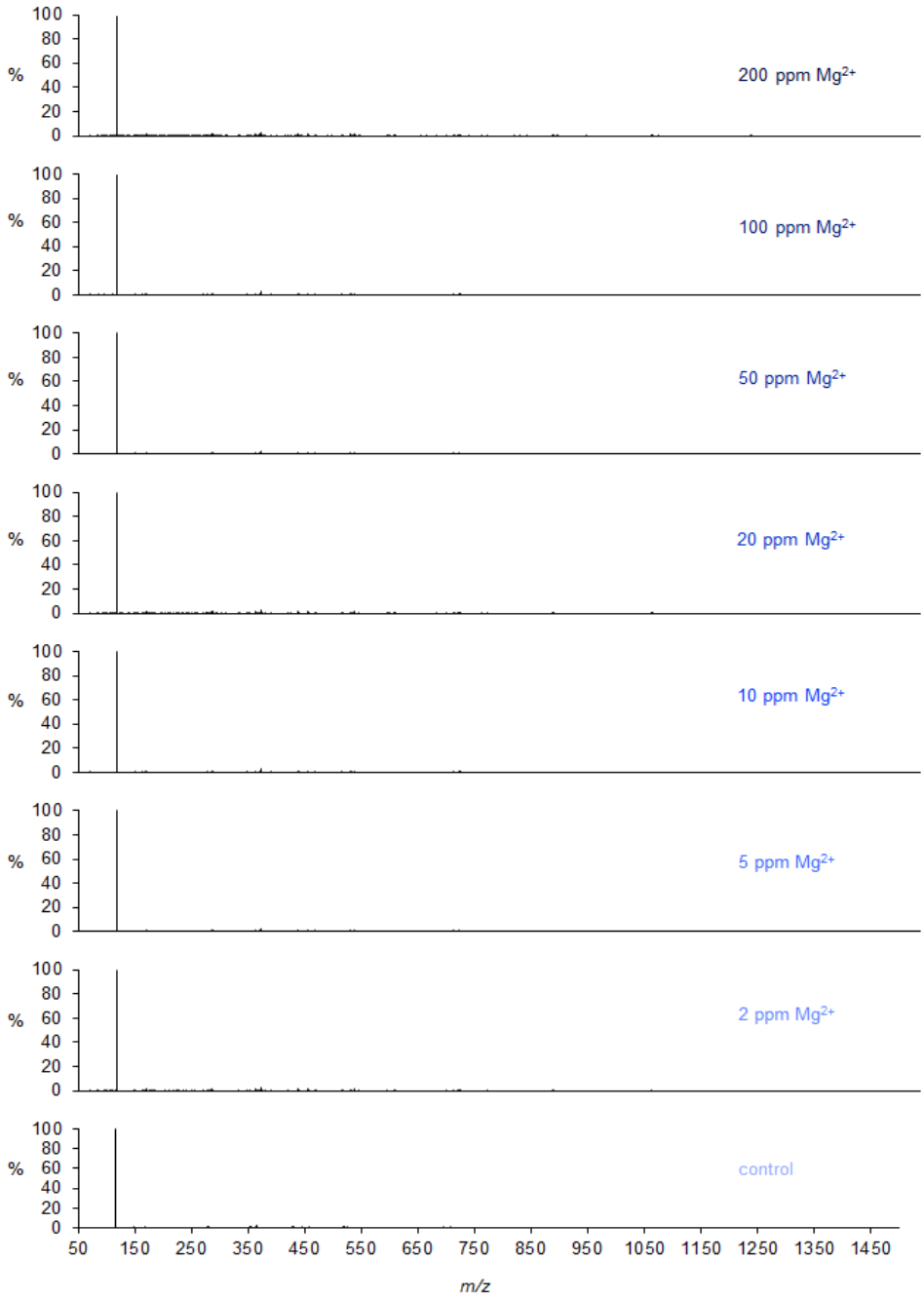

Figure C.5. Positive ion mode ESI-MS of the Maillard reaction species of maltose-proline system at room temperature with various concentrations of magnesium.

.

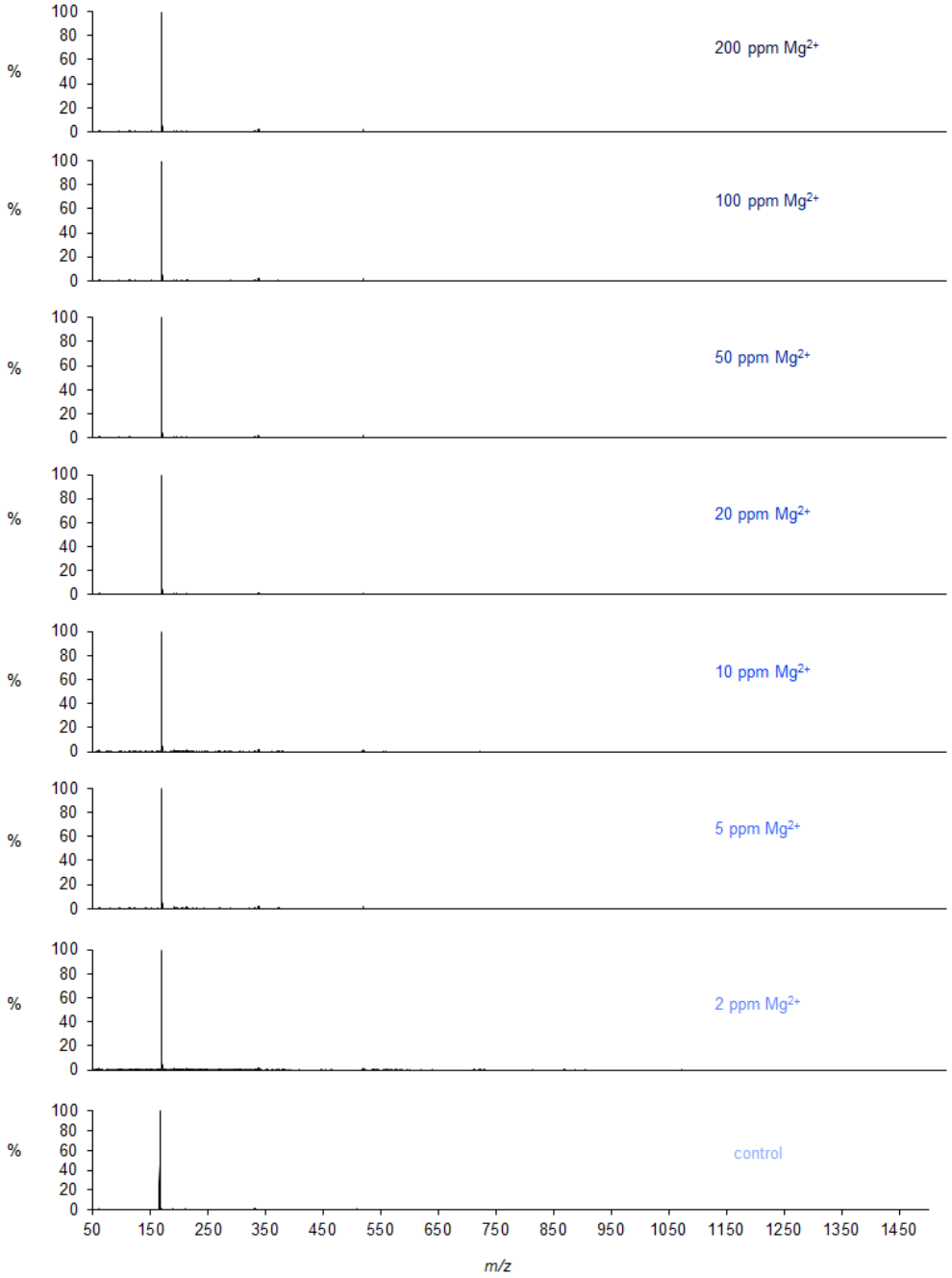

Figure C.6. Positive ion mode ESI-MS of the Maillard reaction species of maltose-phenylalanine system at room temperature with various concentrations of magnesium.

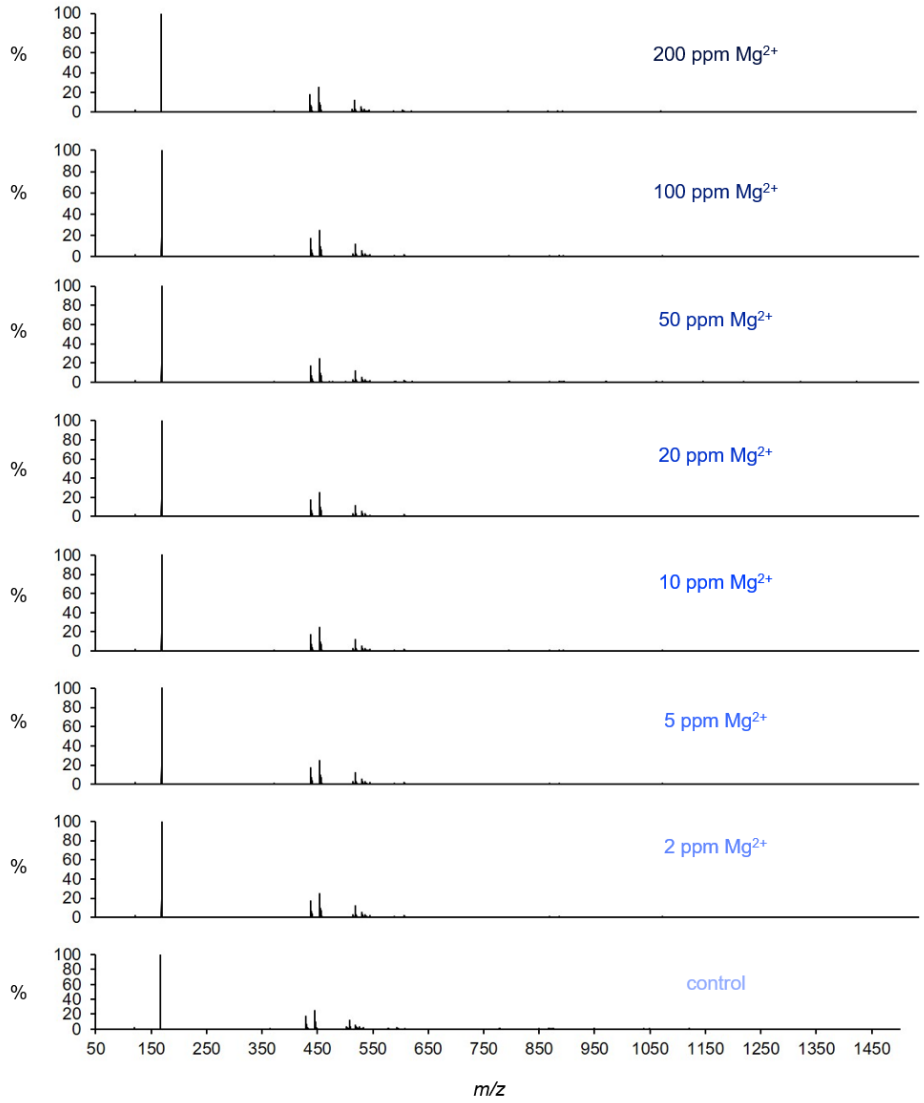

Figure C.7. Positive ion mode ESI-MS of the Maillard reaction species of maltose-phenylalanine system after reflux at 130°C for 105 mins with various concentrations of magnesium.

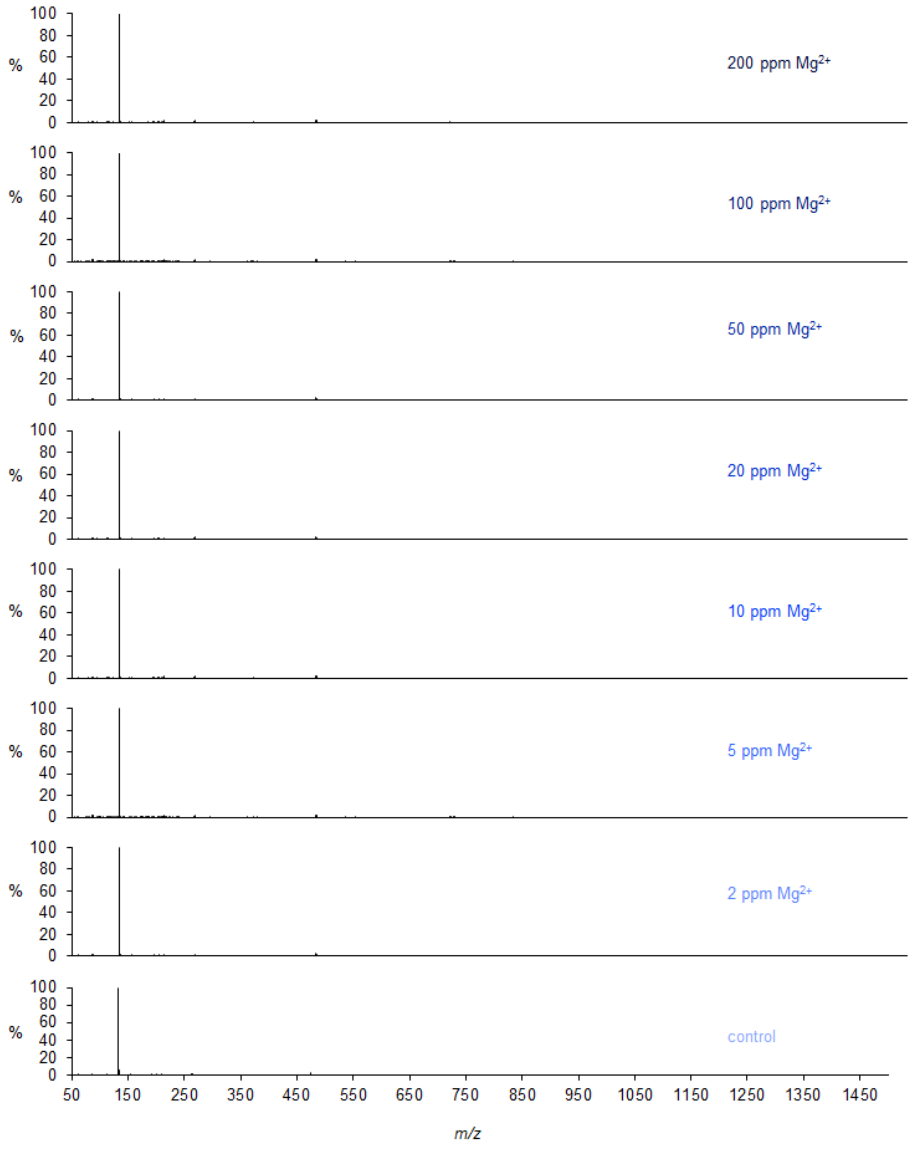

Figure C.8. Positive ion mode ESI-MS of the Maillard reaction species of maltose-leucine system at room temperature with various concentrations of magnesium.

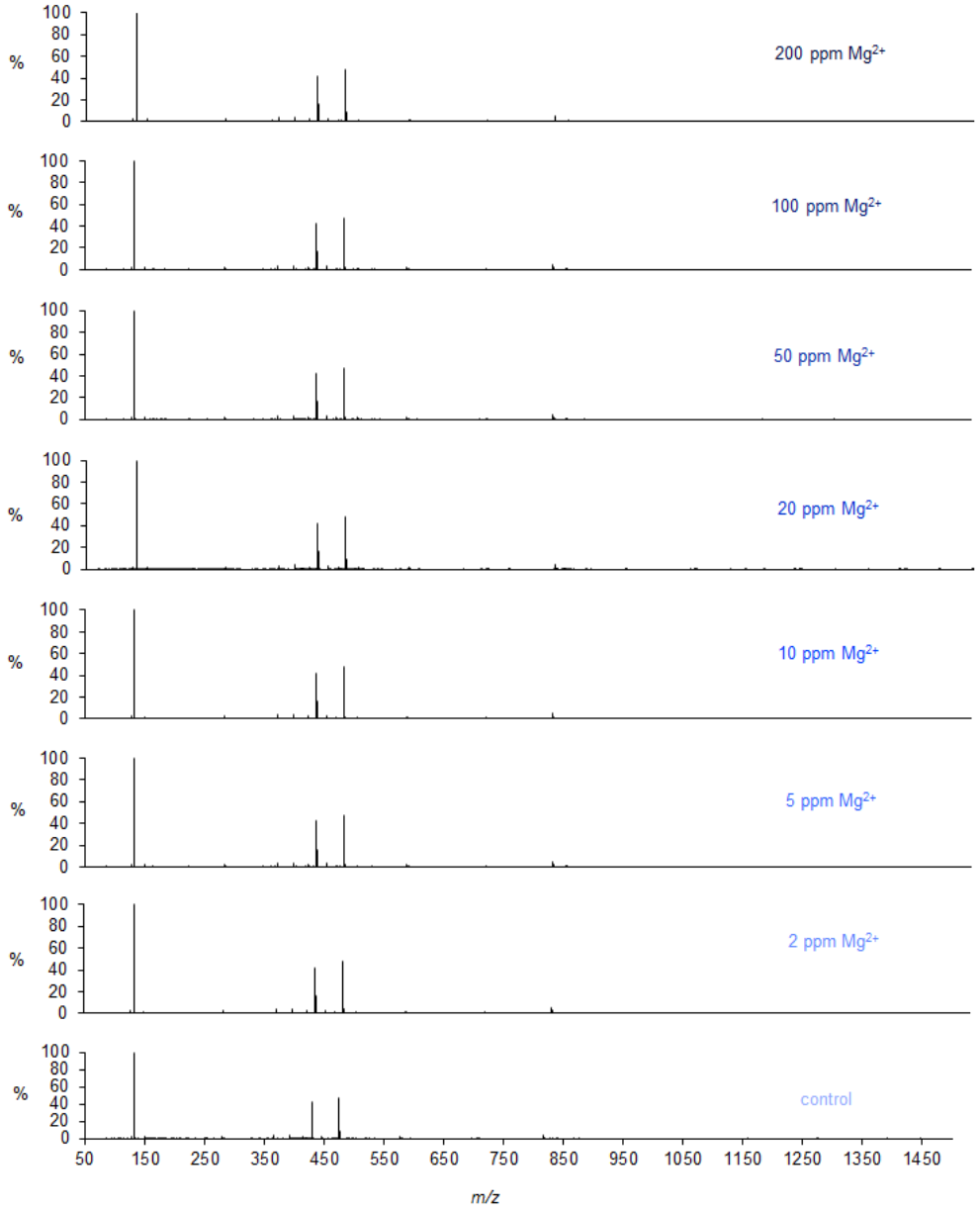

Figure C.9. Positive ion mode ESI-MS of the Maillard reaction species of maltose-leucine system after reflux at 130ºC for 105 mins with various concentrations of magnesium.

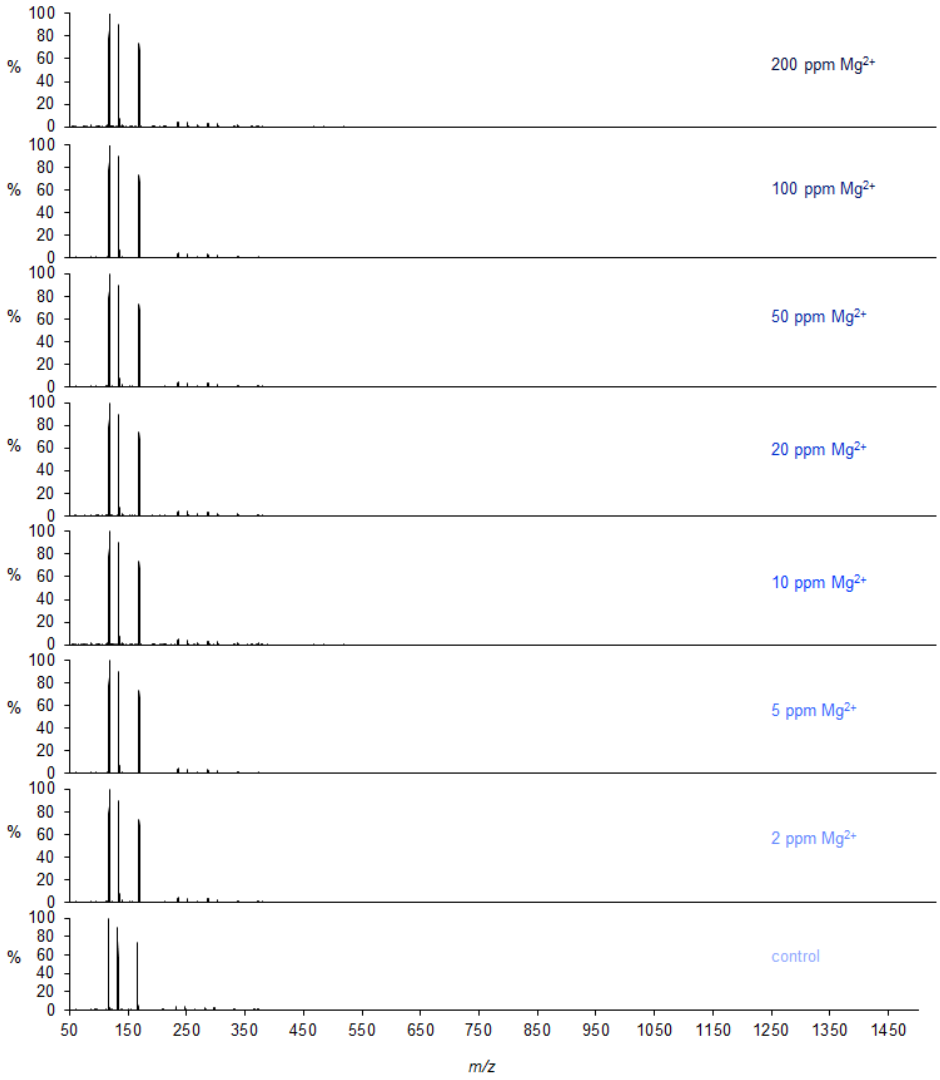

Figure C.10. Positive ion mode ESI-MS of the Maillard reaction species of maltose-proline/phenylalanine/leucine system at room temperature with various concentrations of magnesium.

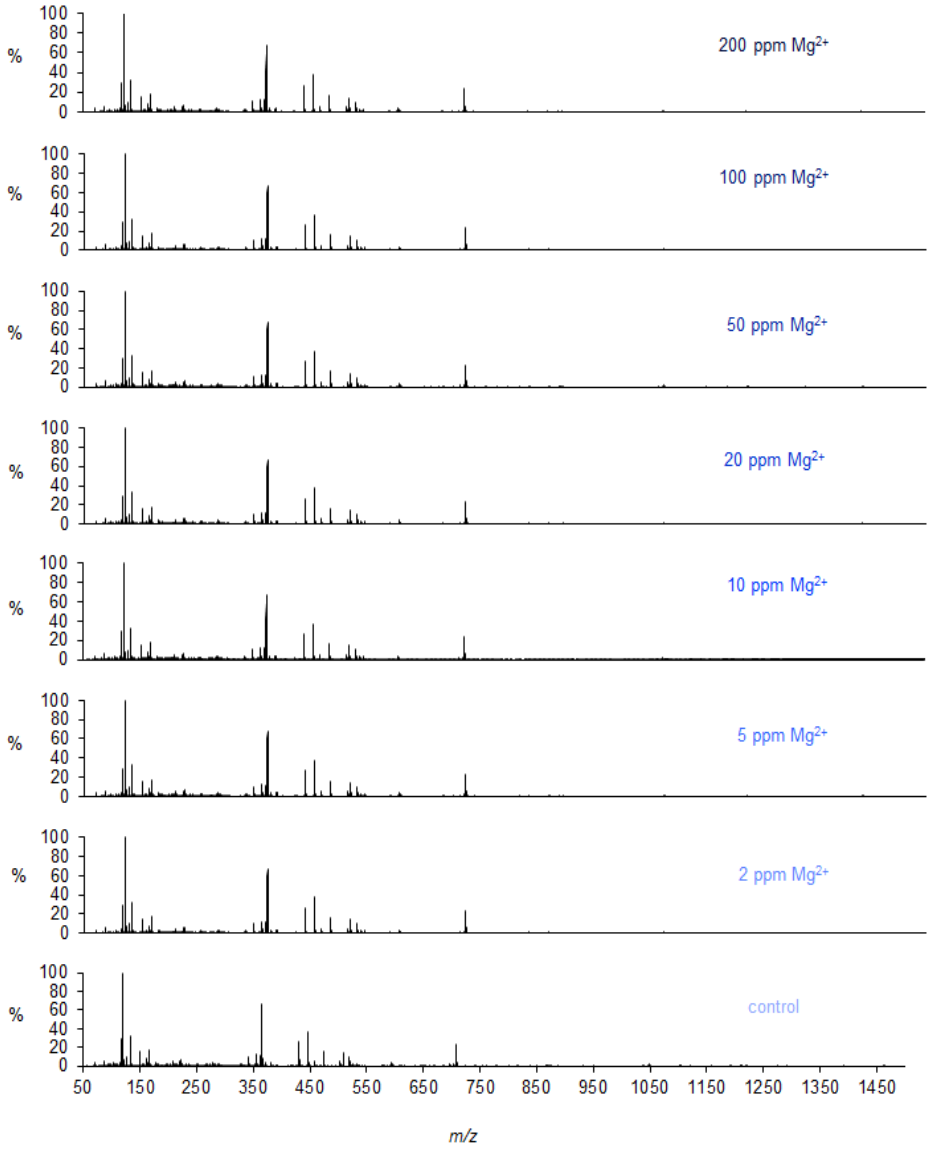

Figure C.11. Positive ion mode ESI-MS of the Maillard reaction species of maltose-proline-phenylalanine-leucine system after reflux at 130ºC for 105 mins with various concentrations of magnesium.

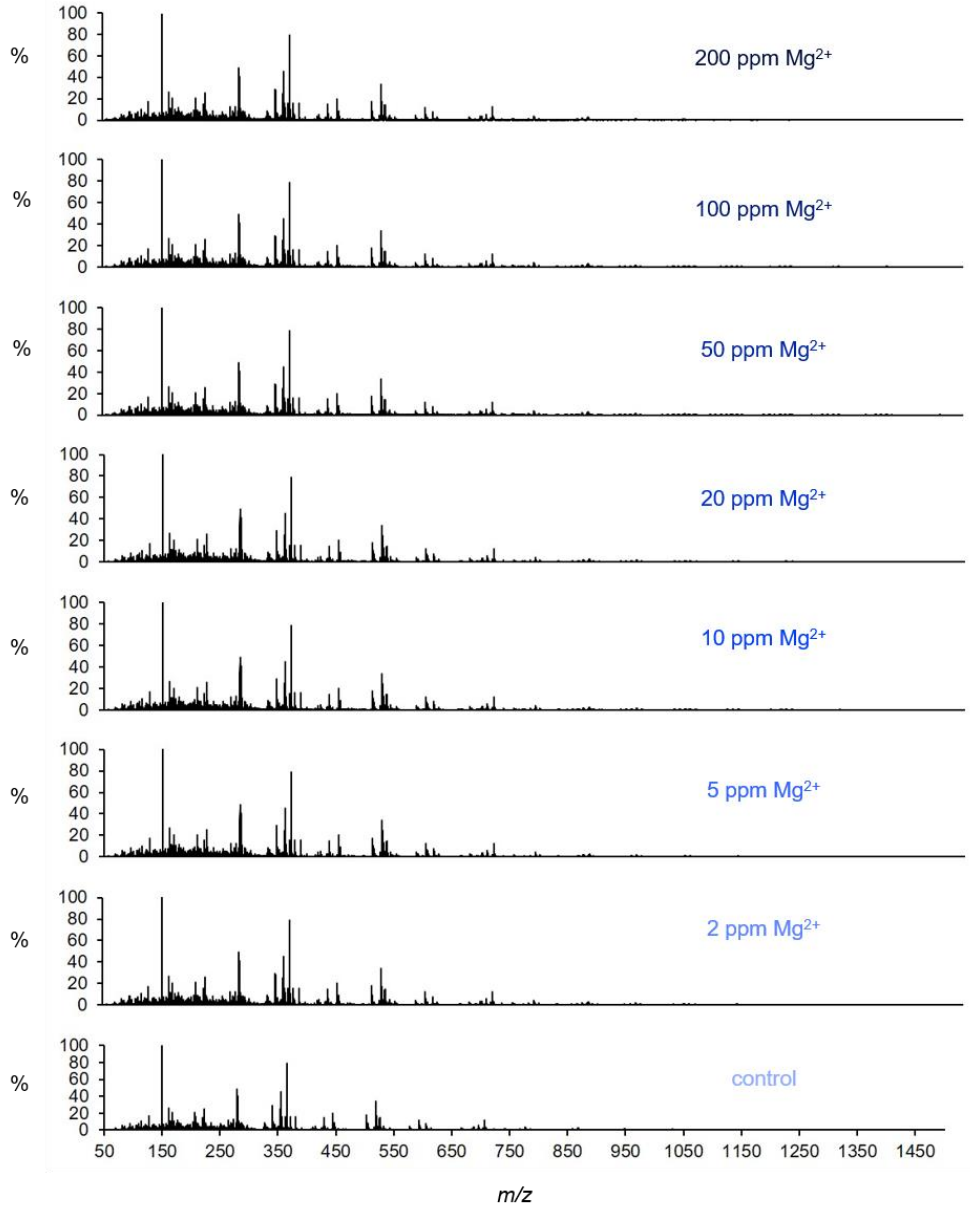

Figure C.12. Positive ion mode ESI-MS of the Maillard reaction species of wort at room temperature with various concentrations of Mg^{2+} (2 ppm through 200 ppm); and a control (no Mg^{2+} added).

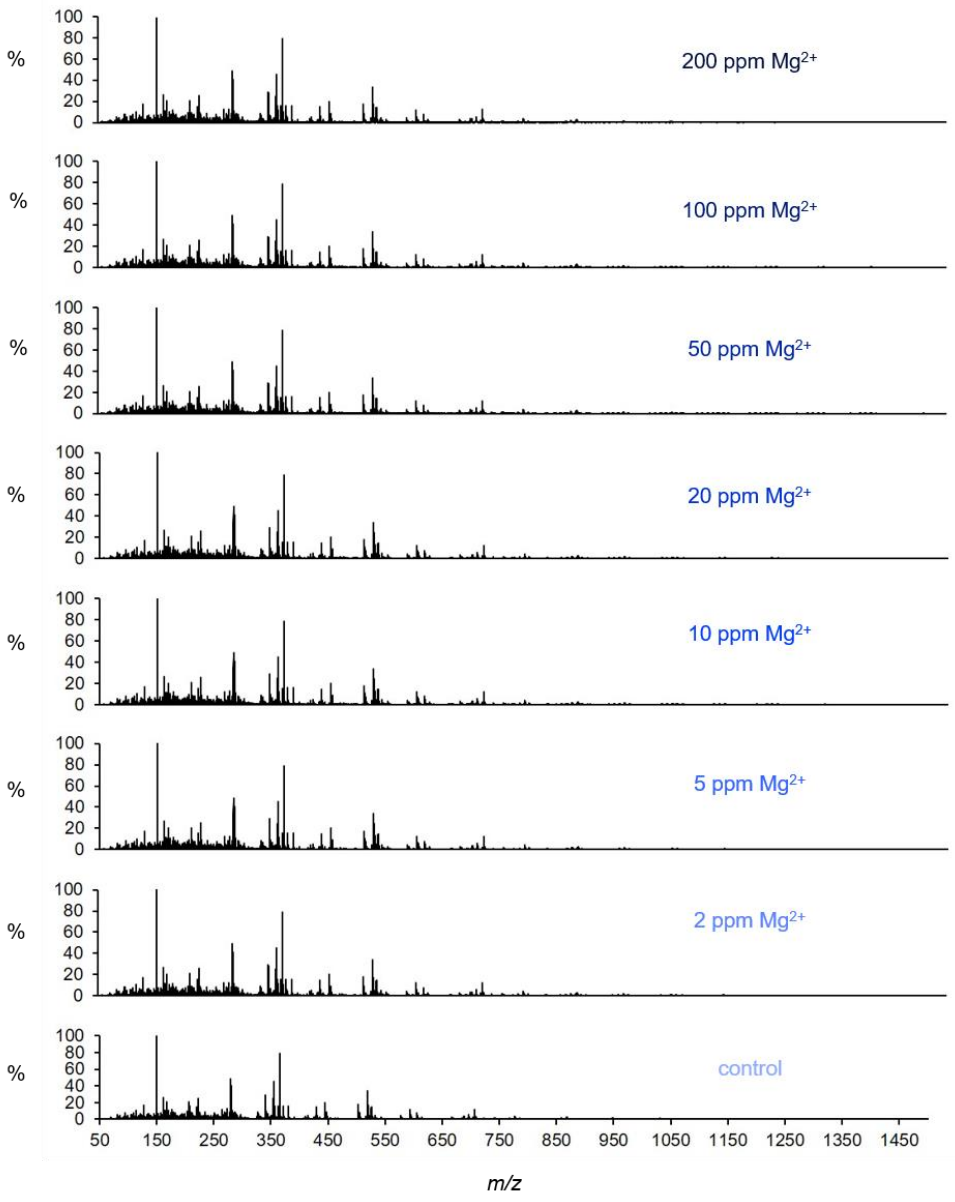

Figure C.13. Positive ion mode ESI-MS of the Maillard reaction species of wort after reflux at 130°C for 105 mins with various concentrations of Mg^{2+} (2 ppm through 200 ppm); and a control (no Mg^{2+} added).

Appendix D
Dynamic ion speciation during hydrolysis of aryltrifluoroborates

Section D1. Effect of flask geometry and stirring rate on hydrolysis profiles of the aryltrifluoroborates

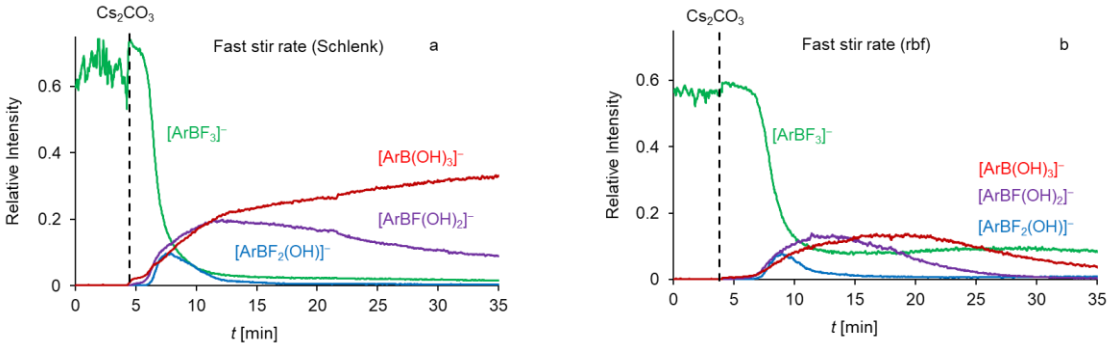

Figure D.1. Relative species intensity for the hydrolysis of potassium p-methoxyphenyltrifluoroborate in THF/H_2O (10:1) containing Cs_2CO_3 at 55°C; reaction was performed in: a) Schlenk tube; and b) rbf at a fast stir rate. The $[ArB(OH)_3]^-$ trace is a sum of intensities of all species with F=0. i.e. **7** + **8** + **9** + ½**10**. An example where hydrolysis of potassium p-tolyltrifluoroborate at a fast stir rate never reached the catalytic regime is shown in (a).

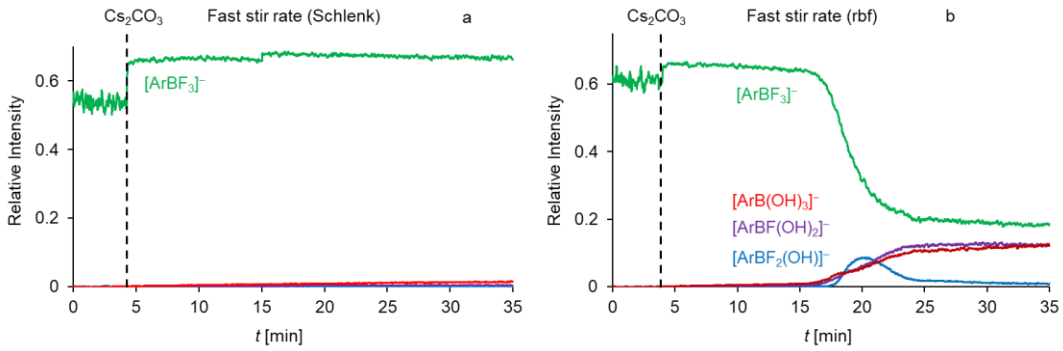

Figure D.2. Relative species intensity for the hydrolysis of potassium p-tolyltrifluoroborate in THF/H_2O (10:1) containing Cs_2CO_3 at 55°C; reaction was performed in: a) Schlenk tube; and b) rbf at a fast stir rate. The $[ArB(OH)_3]^-$ trace is a sum of intensities of all species with F=0. i.e. **7** + **8** + **9** + ½**10**.

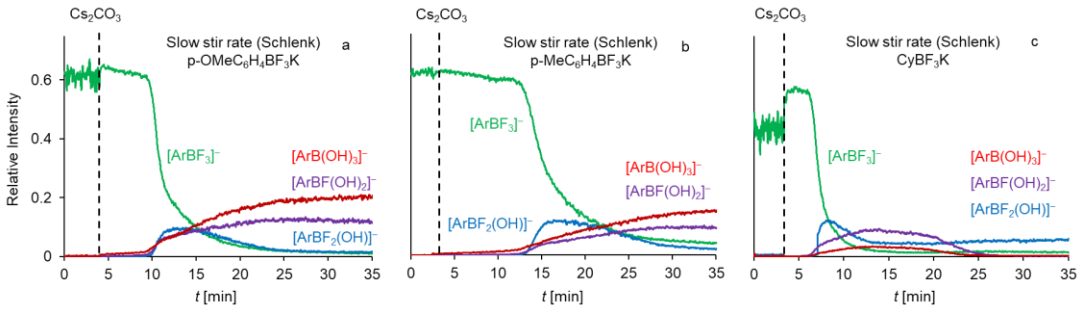

Figure D.3. Relative species intensity for the hydrolysis of potassium salts of a) p-methoxyphenyltrifluoroborate; b) 4-tolyltrifluoroborate; c) cyclohexyltrifluoroborate in THF/H_2O (10:1) containing Cs_2CO_3 at 55°C; reaction was performed in a Schlenk tube at a slow stir rate. The $[ArB(OH)_3]^-$ trace is a sum of intensities of all species with F=0. i.e. **7** + **8** + **9** + ½**10**.

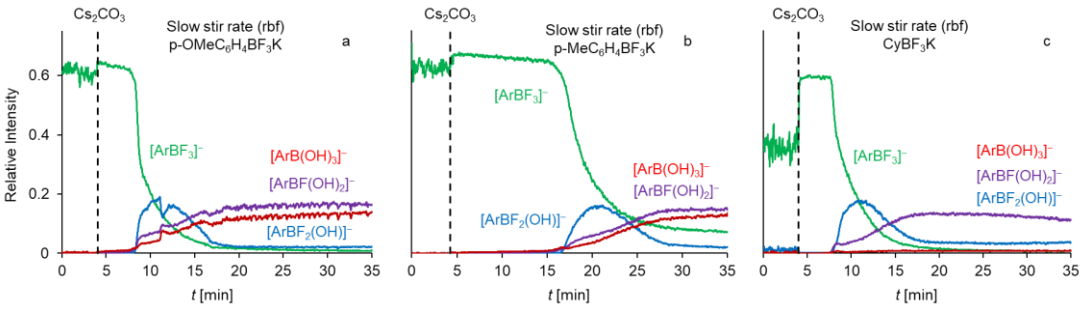

Figure D.4. Relative species intensity for the hydrolysis of potassium salts of a) p-methoxyphenyltrifluoroborate; b) 4-tolyltrifluoroborate; c) cyclohexyltrifluoroborate in THF/H_2O (10:1) containing Cs_2CO_3 at 55°C; reaction was performed in a round-bottomed flask (rbf) at a slow stir rate. The $[ArB(OH)_3]^-$ trace is a sum of intensities of all species with F=0. i.e. **7** + **8** + **9** + ½**10**.

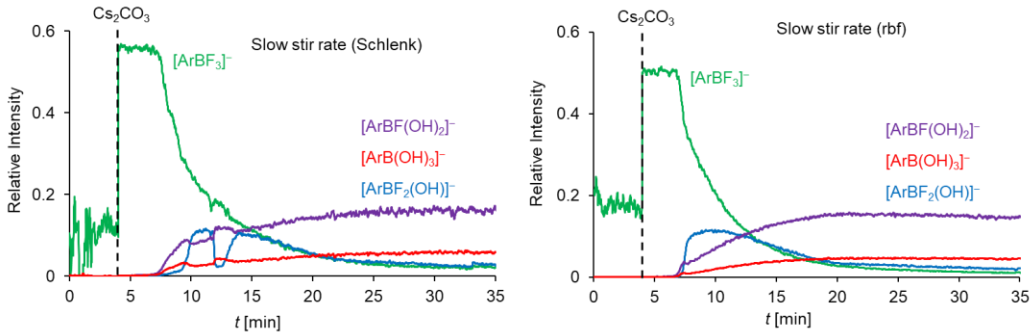

Figure D.5. Relative species intensity for the hydrolysis of potassium isopropyltrifluoroborate in THF/H_2O (10:1) containing Cs_2CO_3 at 55°C; reaction was performed in: a) Schlenk tube; and b) rbf at a slow stir rate. The $[ArB(OH)_3]^-$ trace is a sum of intensities of all species with F=0. i.e. **7** + **8** + **9** + ½**10**.

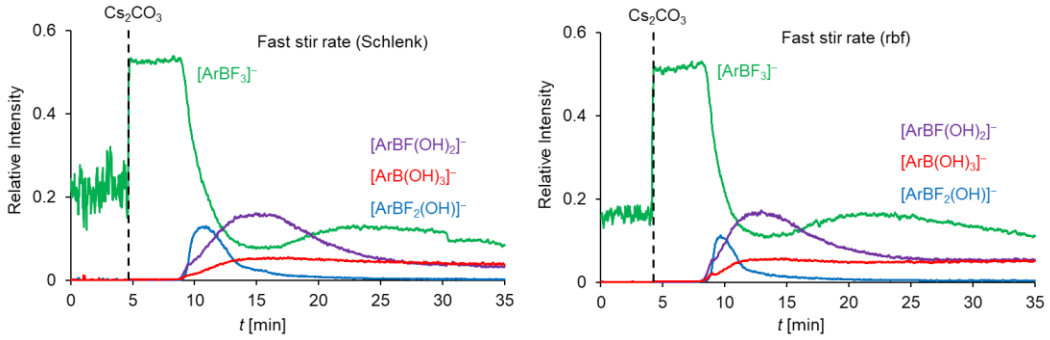

Figure D.6. Relative species intensity for the hydrolysis of potassium isopropyltrifluoroborate in THF/H_2O (10:1) containing Cs_2CO_3 at 55°C; reaction was performed in: a) Schlenk tube; and b) rbf at a fast stir rate. The $[ArB(OH)_3]^-$ trace is a sum of intensities of all species with F=0. i.e. **7** + **8** + **9** + ½**10**.

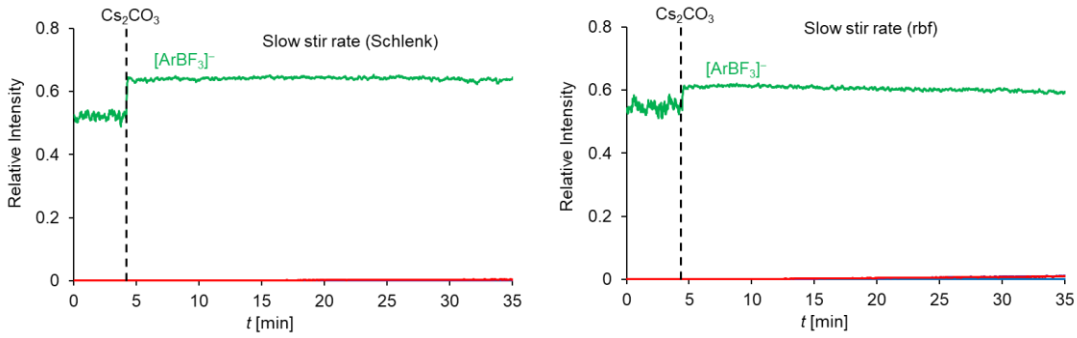

Figure D.7. Relative species intensity for the hydrolysis of potassium phenyltrifluoroborate in THF/H_2O (10:1) containing Cs_2CO_3 at 55°C; reaction was performed in: a) Schlenk tube; and b) rbf at a slow stir rate. The $[ArB(OH)_3]^-$ trace is a sum of intensities of all species with F=0. i.e. **7** + **8** + **9** + ½**10**.

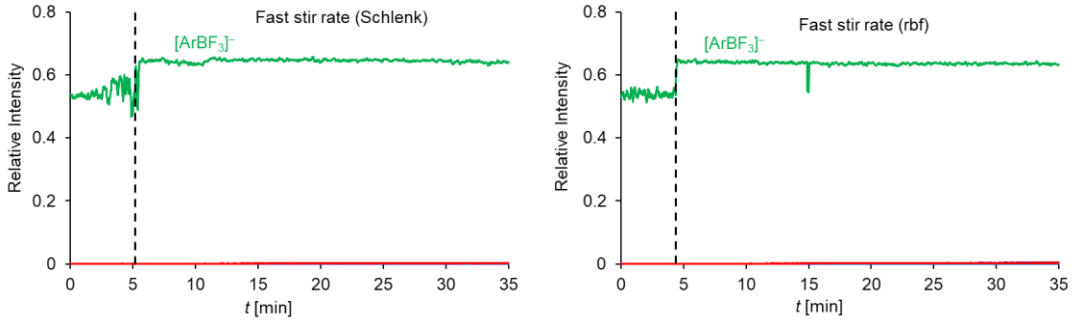

Figure D.8. Relative species intensity for the hydrolysis of potassium phenyltrifluoroborate in THF/H_2O (10:1) containing Cs_2CO_3 at 55°C; reaction was performed in: a) Schlenk tube; and b) rbf at a fast stir rate. The $[ArB(OH)_3]^-$ trace is a sum of intensities of all species with F=0. i.e. **7** + **8** + **9** + ½**10**.

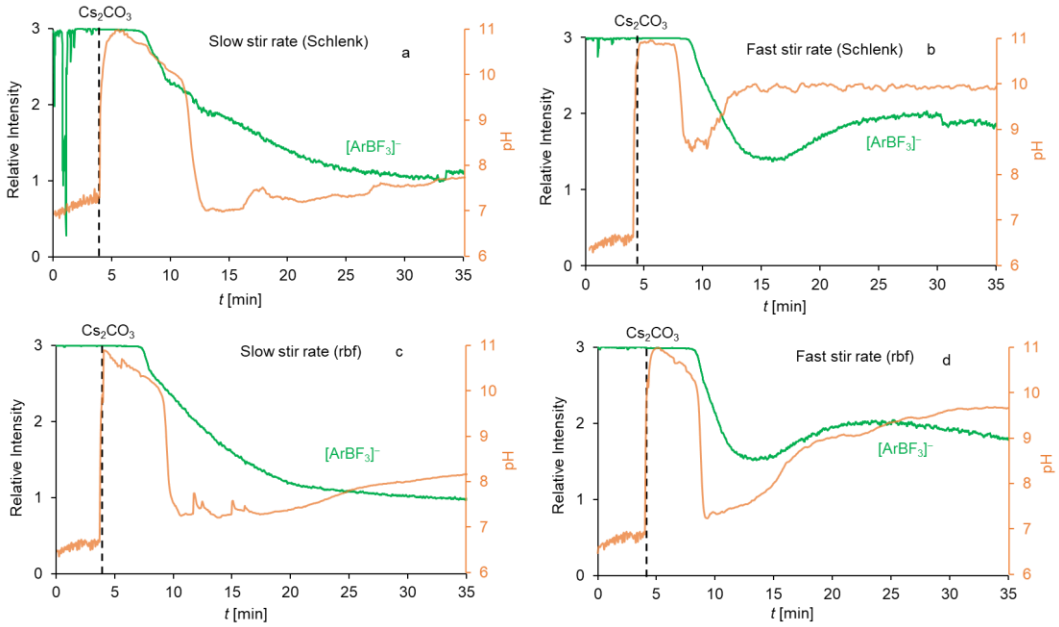

Figure D.9. Relative species intensity and pH values for the hydrolysis of potassium isopropyltrifluoroborate in THF/H_2O (10:1) containing Cs_2CO_3 at 55°C; reaction was performed in: a) Schlenk tube (slow stir rate); b) Schlenk tube (fast stir rate); c) rbf (slow stir rate); d) rbf (fast stir rate). The relative intensity values were determined by multiplying the intensities of F containing species by the number of F available; the sum of the result from each species represents the relative intensities of the $[ArBF_3]^-$ trace (green trace).

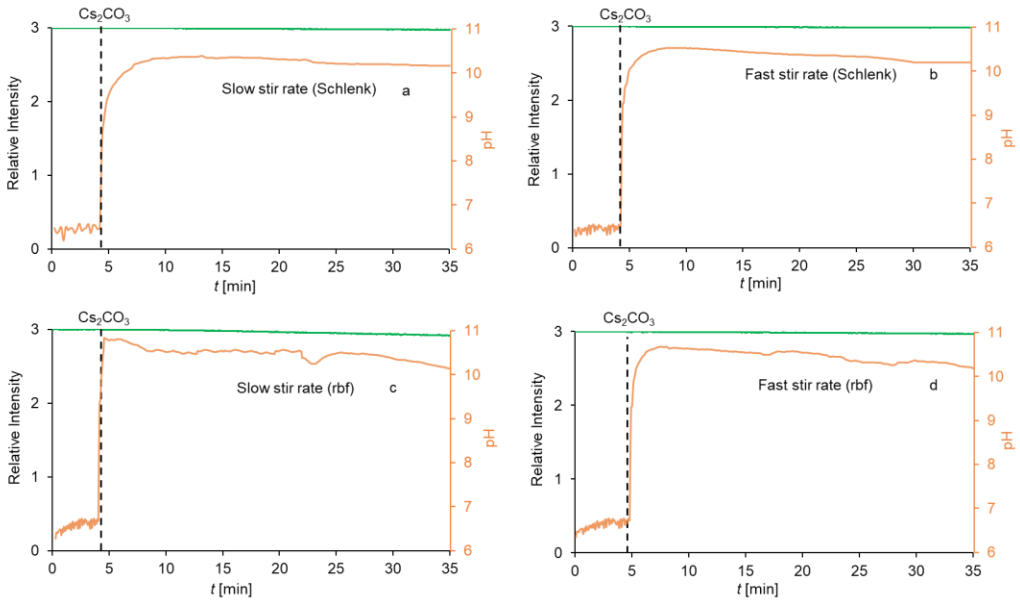

Figure D.10. Relative species intensity and pH values for the hydrolysis of potassium phenyltrifluoroborate in THF/H_2O (10:1) containing Cs_2CO_3 at 55°C; reaction was performed in: a) Schlenk tube (slow stir rate); b) Schlenk tube (fast stir rate); c) rbf (slow stir rate); d) rbf (fast stir rate). The relative intensity values were determined by multiplying the intensities of F containing species by the number of F available; the sum of the result from each species represents the relative intensities of the $[ArBF_3]^-$ trace (green trace).

Section D2. Additional MS data

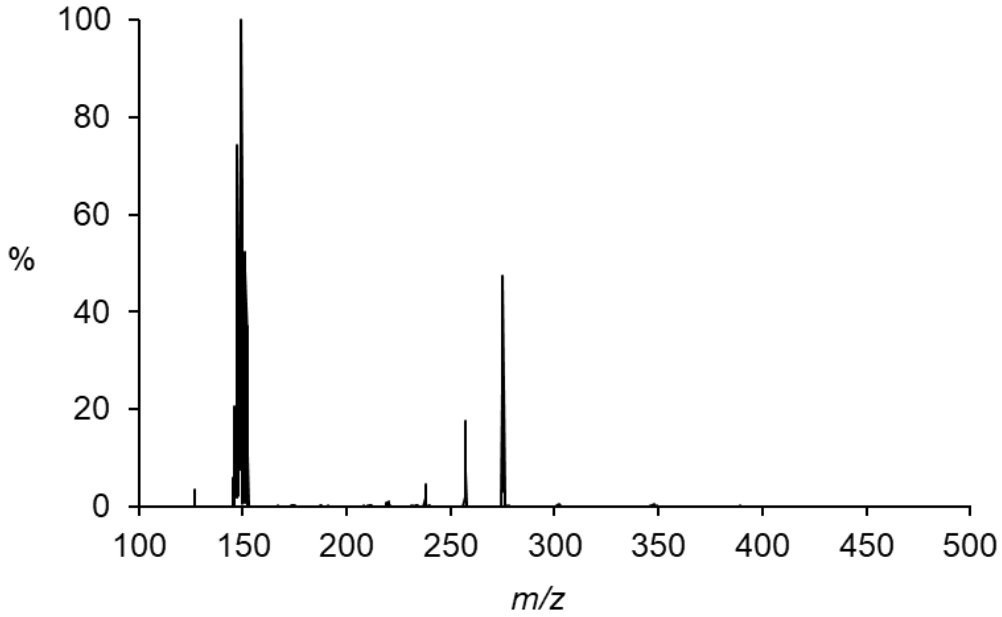

Figure D.11. Negative ion mass spectrum of the hydrolysis of potassium cyclohexyltrifluoroborate in THF (55°C) after 20 minutes of addition of water and Cs_2CO_3.

Table D.1. Mass and assignment of species observed during hydrolysis of potassium cyclohexyltrifluoroborate substrate

m/z	Assignment
151	$[ArBF_3]^-$
149	$[ArBF_2(OH)]^-$
147	$[ArBF(OH)_2]^-$
145	$[ArB(OH)_3]^-$
127	$[ArBO_2H]^-$
236	$[(ArB)_2O_3H]^-$
258	$[(ArB)_2O_3H_2F]^-$
276	$[(ArBO_2H_2)_2F]^-$
341	$[(ArBF_3)_2K]^-$
435	$[(ArBF_3)_2Cs]^-$

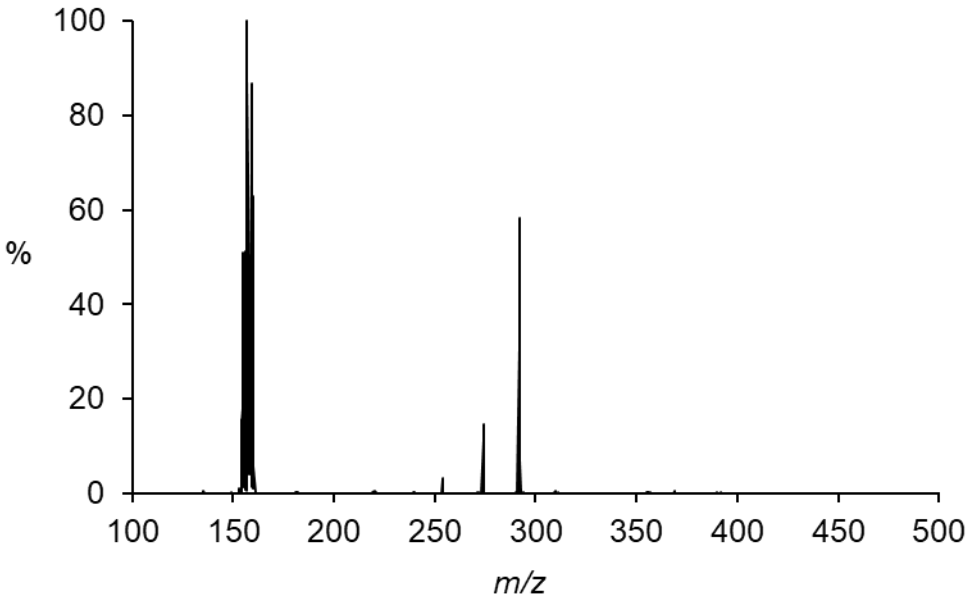

Figure D.12. Negative ion mass spectrum of the hydrolysis of potassium p-tolyltrifluoroborate in THF (55°C) after 20 minutes of addition of water and Cs_2CO_3.

Table D.2. Mass and assignment of species observed during hydrolysis of potassium p-tolyltrifluoroborate substrate.

m/z	Assignment
159	$[ArBF_3]^-$
157	$[ArBF_2(OH)]^-$
155	$[ArBF(OH)_2]^-$
153	$[ArB(OH)_3]^-$
135	$[ArBO_2H]^-$
254	$[(ArB)_2O_3H]^-$
274	$[(ArB)_2O_3H_2F]^-$
292	$[(ArBO_2H_2)_2F]^-$
357	$[(ArBF_3)_2K]^-$
451	$[(ArBF_3)_2Cs]^-$

Section D3. First-order plots

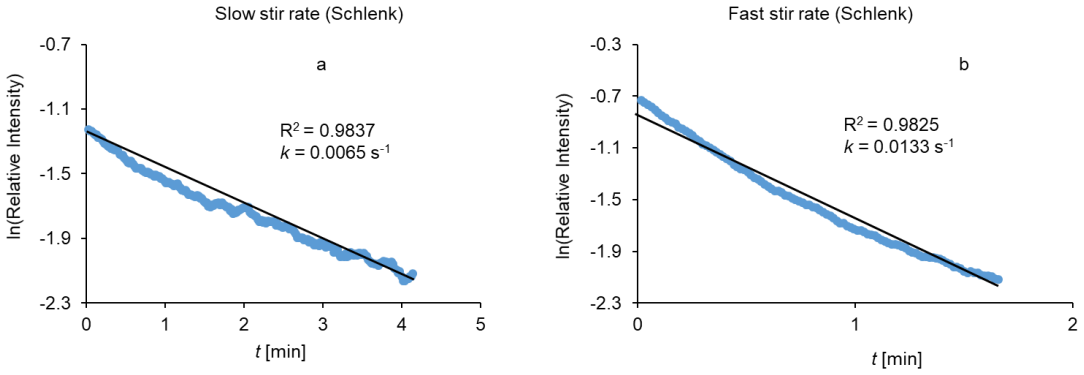

Figure D.13. Linear regression of ln(relative intensity) versus time. The first order plot was determined for $[ArBF_3]^-$ as a result of hydrolysis of potassium p-methoxyphenyltrifluoroborate in THF/H_2O (10:1) containing Cs_2CO_3 at 55°C; reaction was performed in a Schlenk tube at: a) a slow stir rate; b) a fast stir rate.

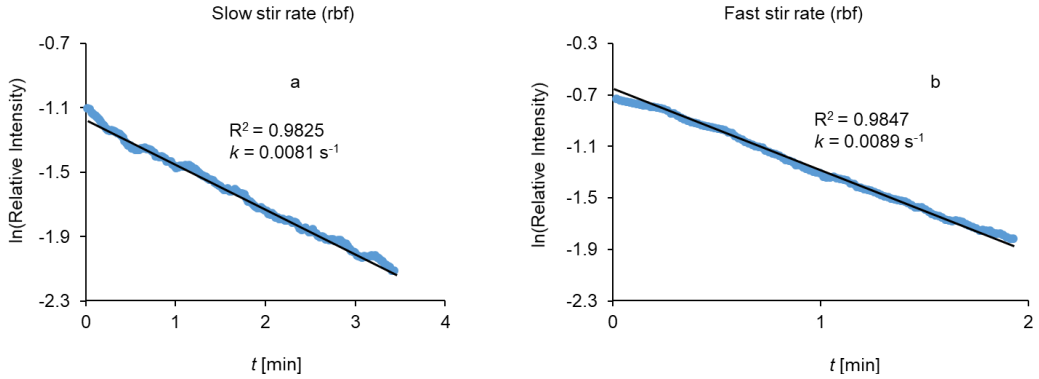

Figure D.14. Linear regression of ln(relative intensity) versus time. The first order plot was determined for $[ArBF_3]^-$ as a result of hydrolysis of potassium p-methoxyphenyltrifluoroborate in THF/H_2O (10:1) containing Cs_2CO_3 at 55°C; reaction was performed in a rbf at: a) a slow stir rate; b) a fast stir rate.

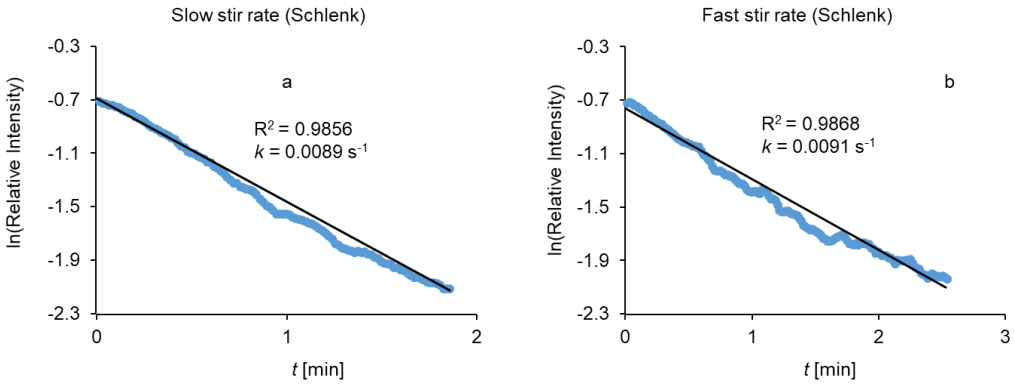

Figure D.15. Linear regression of ln(relative intensity) versus time. The first order plot was determined for $[ArBF_3]^-$ as a result of hydrolysis of potassium cyclohexyltrifluoroborate in THF/H_2O (10:1) containing Cs_2CO_3 at 55°C; reaction was performed in a Schlenk tube at: a) a slow stir rate; b) a fast stir rate.

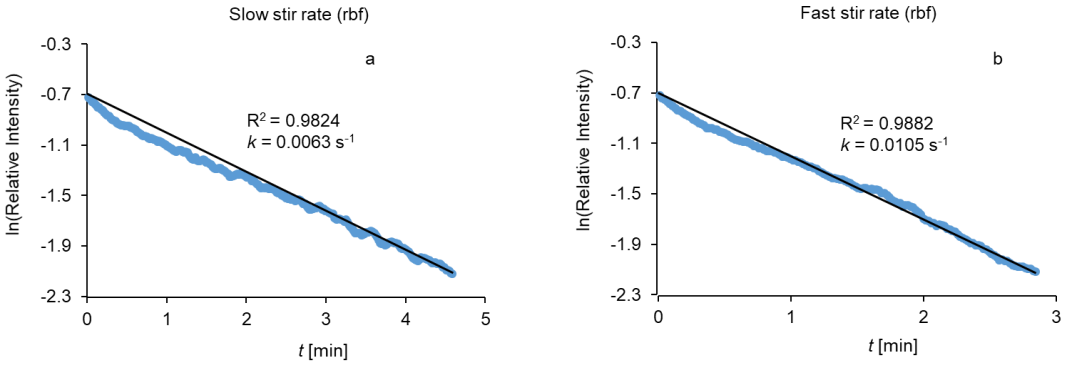

Figure D.16. Linear regression of ln(relative intensity) versus time. The first order plot was determined for $[ArBF_3]^-$ as a result of hydrolysis of potassium cyclohexyltrifluoroborate in THF/H_2O (10:1) containing Cs_2CO_3 at 55°C; reaction was performed in a rbf at: a) a slow stir rate; b) a fast stir rate.

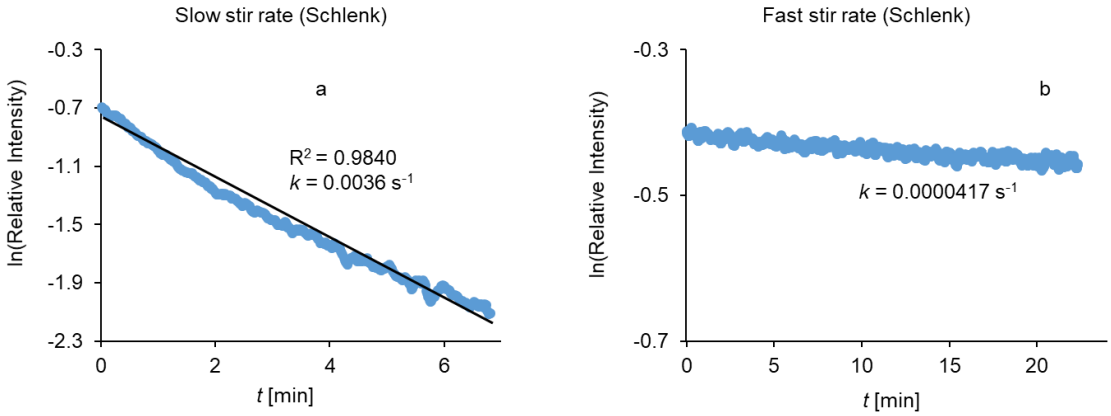

Figure D.17. Linear regression of ln(relative intensity) versus time. The first order plot was determined for $[ArBF_3]^-$ as a result of hydrolysis of potassium p-tolyltrifluoroborate in THF/H_2O (10:1) containing Cs_2CO_3 at 55°C; reaction was performed in a Schlenk tube at: a) a slow stir rate; b) a fast stir rate.

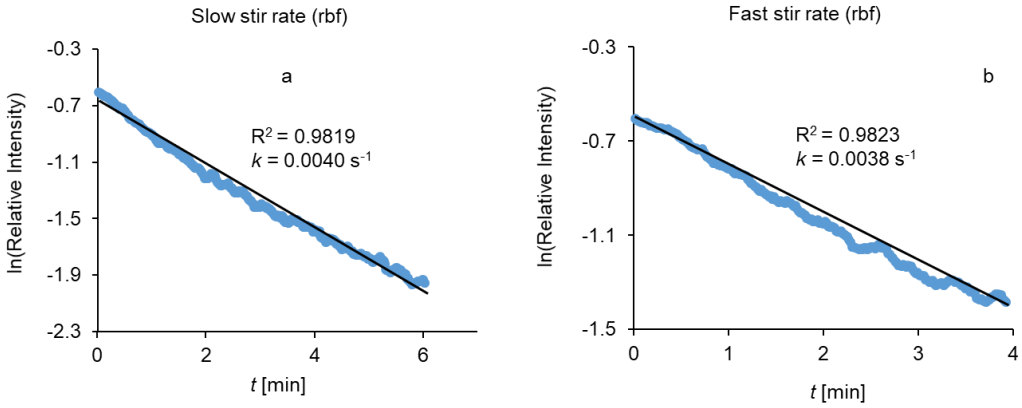

Figure D.18. Linear regression of ln(relative intensity) versus time. The first order plot was determined for $[ArBF_3]^-$ as a result of hydrolysis of potassium p-tolyltrifluoroborate in THF/H_2O (10:1) containing Cs_2CO_3 at 55°C; reaction was performed in a rbf at: a) a slow stir rate; b) a fast stir rate.

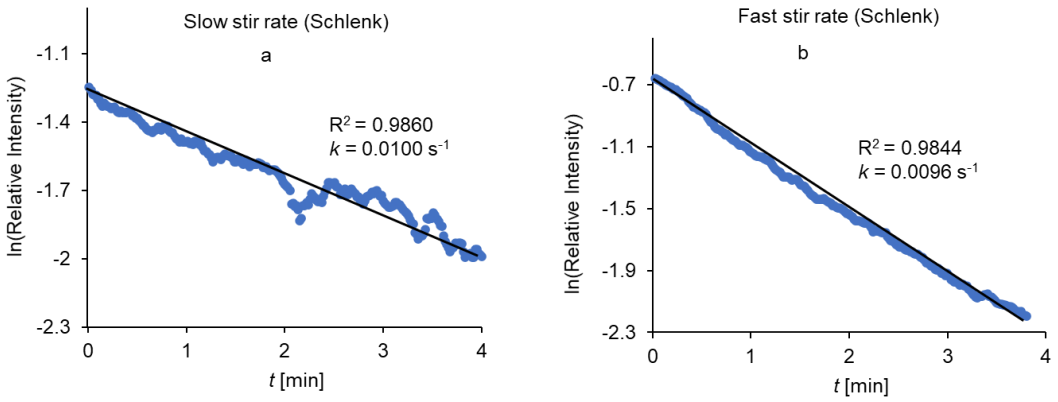

Figure D.19. Linear regression of ln(relative intensity) versus time. The first order plot was determined for $[ArBF_3]^-$ as a result of hydrolysis of potassium isopropyltrifluoroborate in THF/H_2O (10:1) containing Cs_2CO_3 at 55°C; reaction was performed in a Schlenk tube at: a) a slow stir rate; b) a fast stir rate.

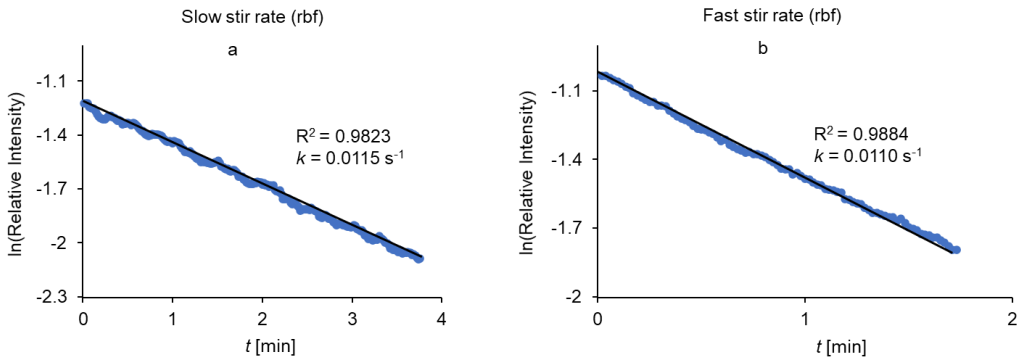

Figure D.20. Linear regression of ln(relative intensity) versus time. The first order plot was determined for $[ArBF_3]^-$ as a result of hydrolysis of potassium isopropyltrifluoroborate in THF/H_2O (10:1) containing Cs_2CO_3 at 55°C; reaction was performed in a rbf at: a) a slow stir rate; b) a fast stir rate.

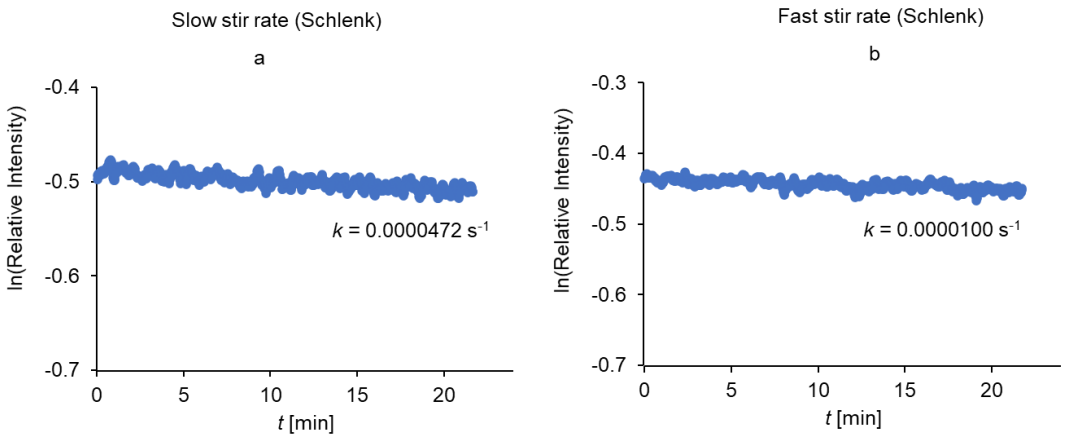

Figure D.21. Linear regression of ln(relative intensity) versus time. The first order plot was determined for $[ArBF_3]^-$ as a result of hydrolysis of potassium phenyltrifluoroborate in THF/H_2O (10:1) containing Cs_2CO_3 at 55°C; reaction was performed in a Schlenk tube at: a) a slow stir rate; b) a fast stir rate.

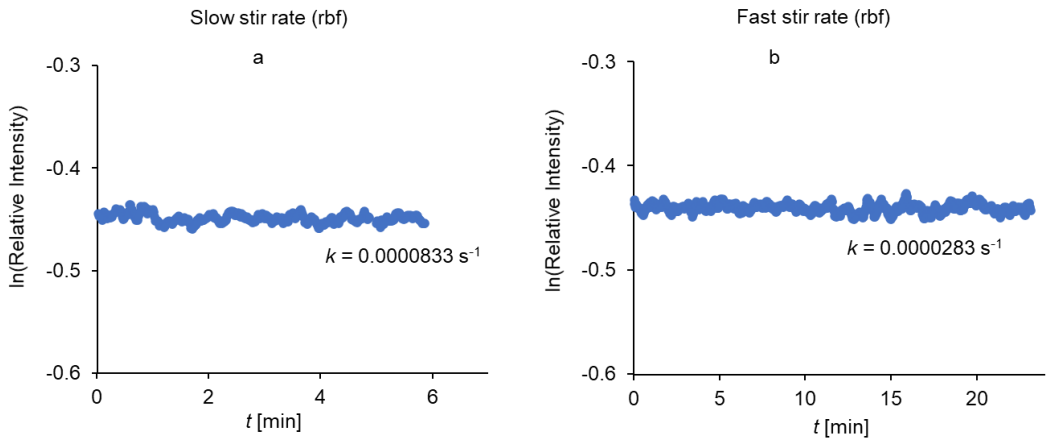

Figure D.22. Linear regression of ln(relative intensity) versus time. The first order plot was determined for $[ArBF_3]^-$ as a result of hydrolysis of potassium phenyltrifluoroborate in THF/H_2O (10:1) containing Cs_2CO_3 at 55°C; reaction was performed in a rbf at: a) a slow stir rate; b) a fast stir rate.

Section D4. Overlaid isotope patterns

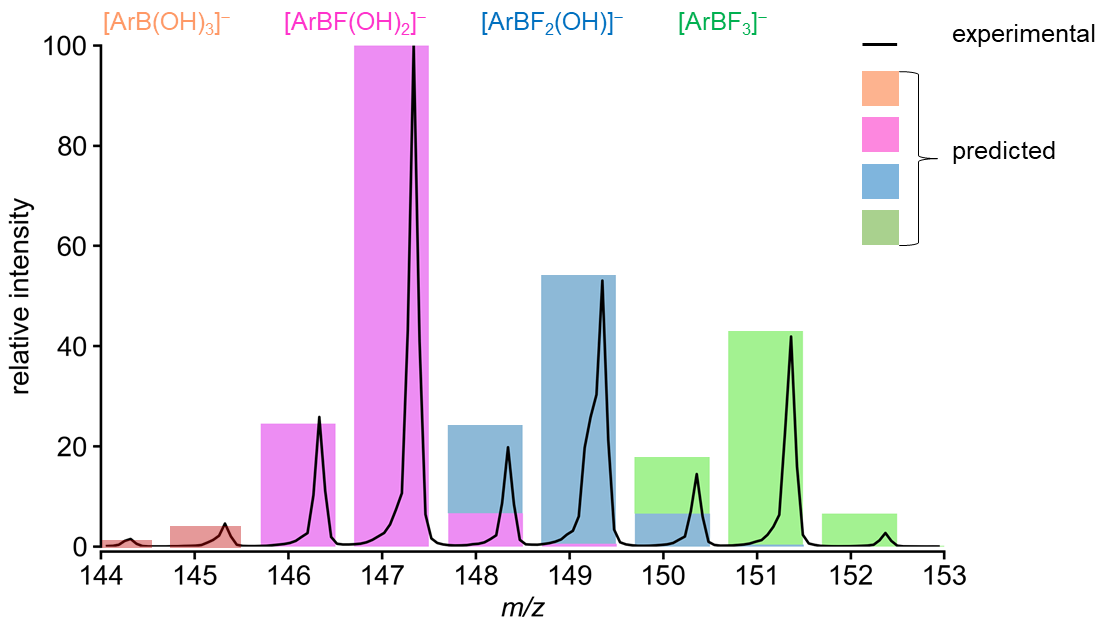

Figure D.23. Overlaid predicted isotope pattern on the experimental isotope pattern for $[ArBF_3]^-$ (green), $[ArBF_2(OH)]^-$ (blue), $[ArBF(OH)_2]^-$ (purple) and $[ArB(OH)_3]^-$ (red). Species are from hydrolysis of potassium cyclohexyltrifluoroborate in THF/H_2O.

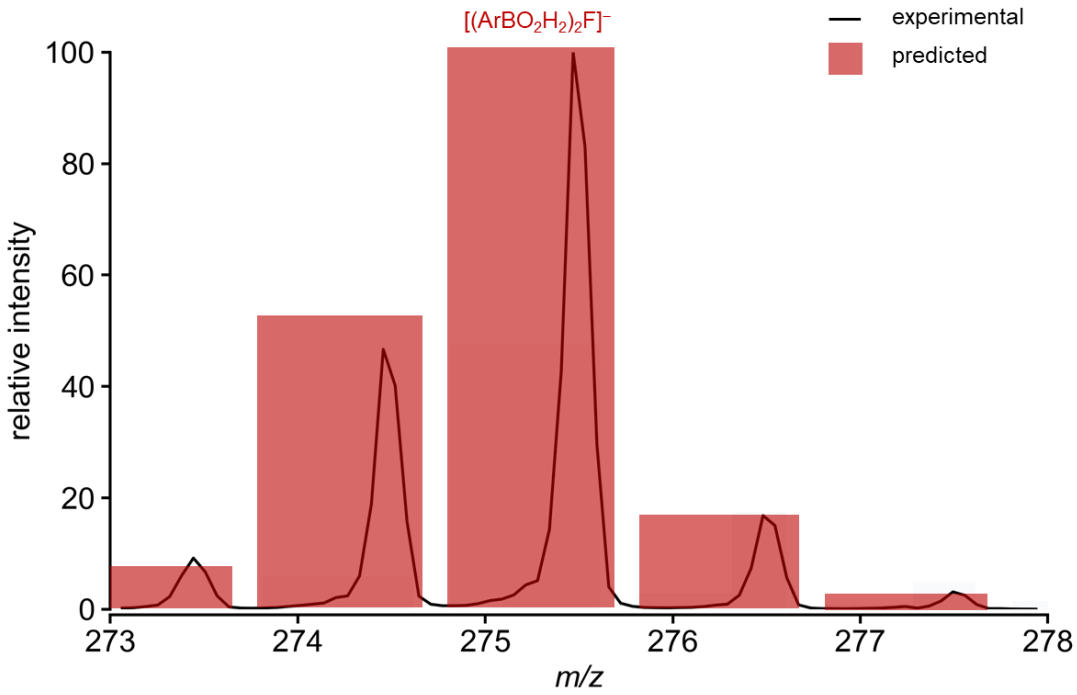

Figure D.24. Overlaid predicted isotope pattern on the experimental isotope pattern for $[(ArBO_2H_2)_2F]^-$ (red). Species is from hydrolysis of potassium cyclohexyltrifluoroborate in THF/H_2O.

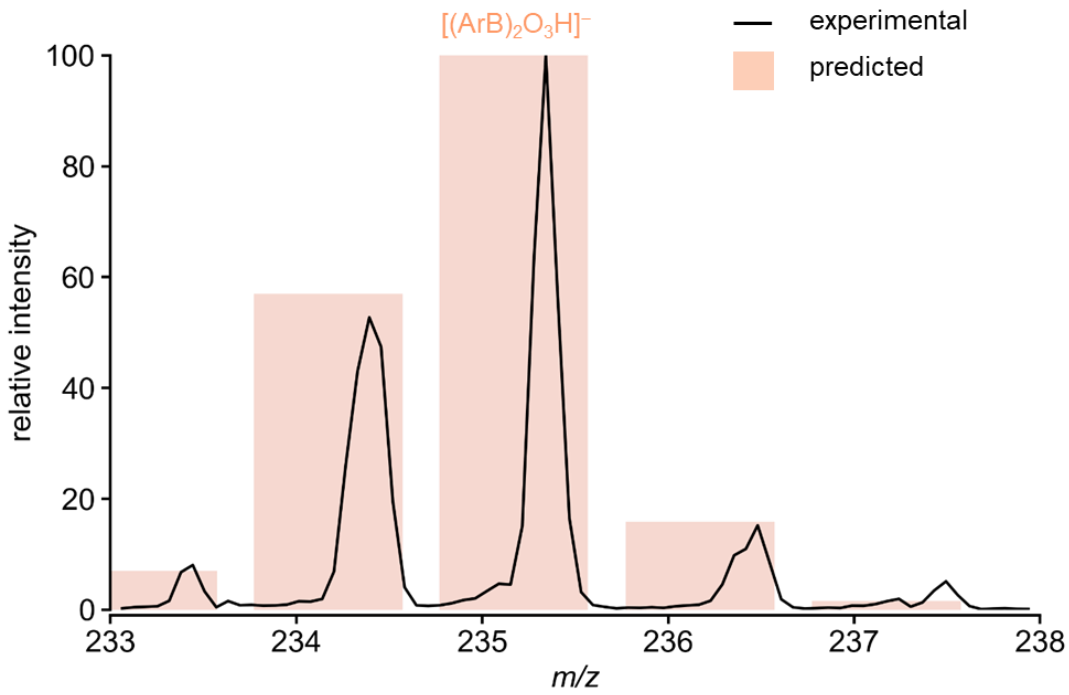

Figure D.25. Overlaid predicted isotope pattern on the experimental isotope pattern for $[(ArB)_2O_3H]^-$ (red). Species is from hydrolysis of potassium cyclohexyltrifluoroborate in THF/H_2O.

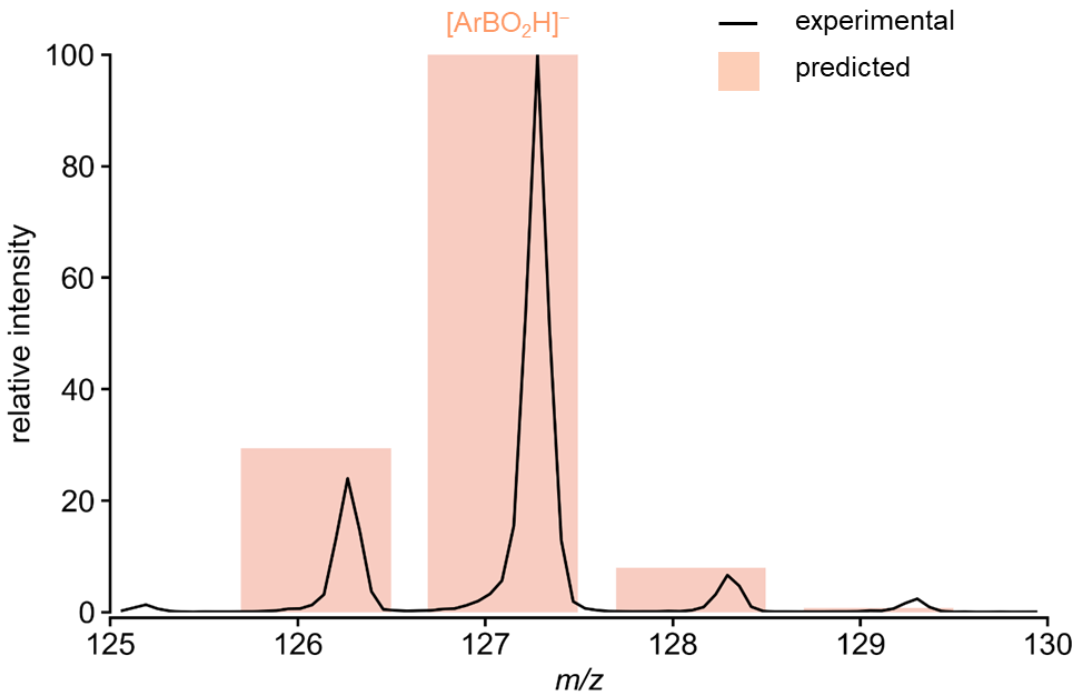

Figure D.26. Overlaid predicted isotope pattern on the experimental isotope pattern for $[ArBO_2H]^-$ (red). Species is from hydrolysis of potassium cyclohexyltrifluoroborate in THF/H_2O.

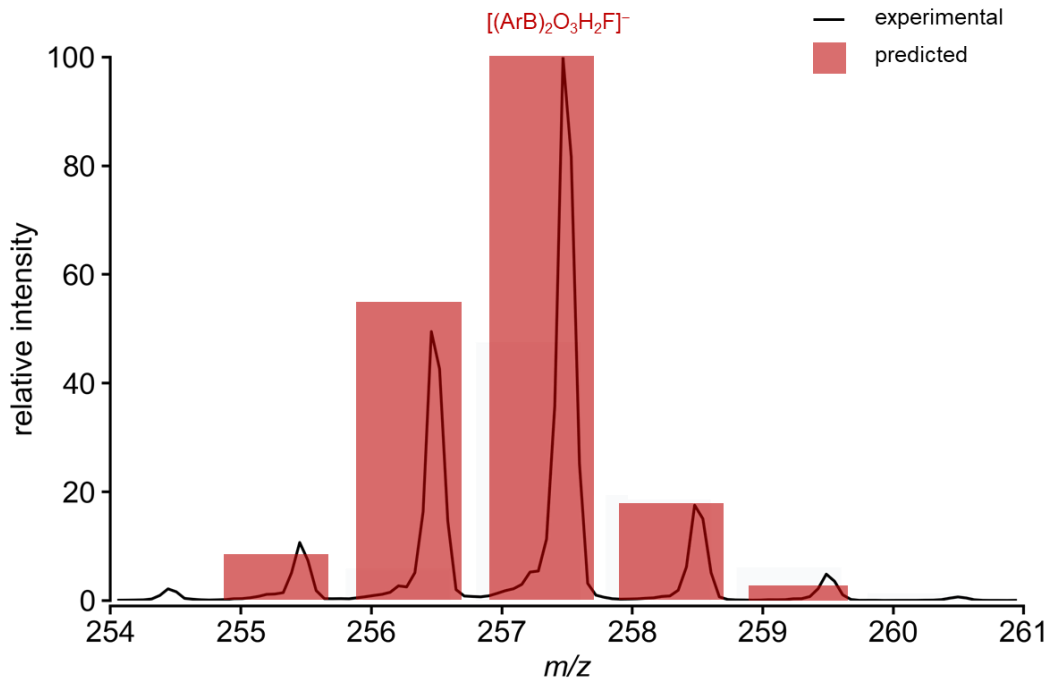

Figure D.27. Overlaid predicted isotope pattern on the experimental isotope pattern for $[(ArB)_2O_3H_2F]^-$ (red). Species is from hydrolysis of potassium cyclohexyltrifluoroborate in THF/H_2O.

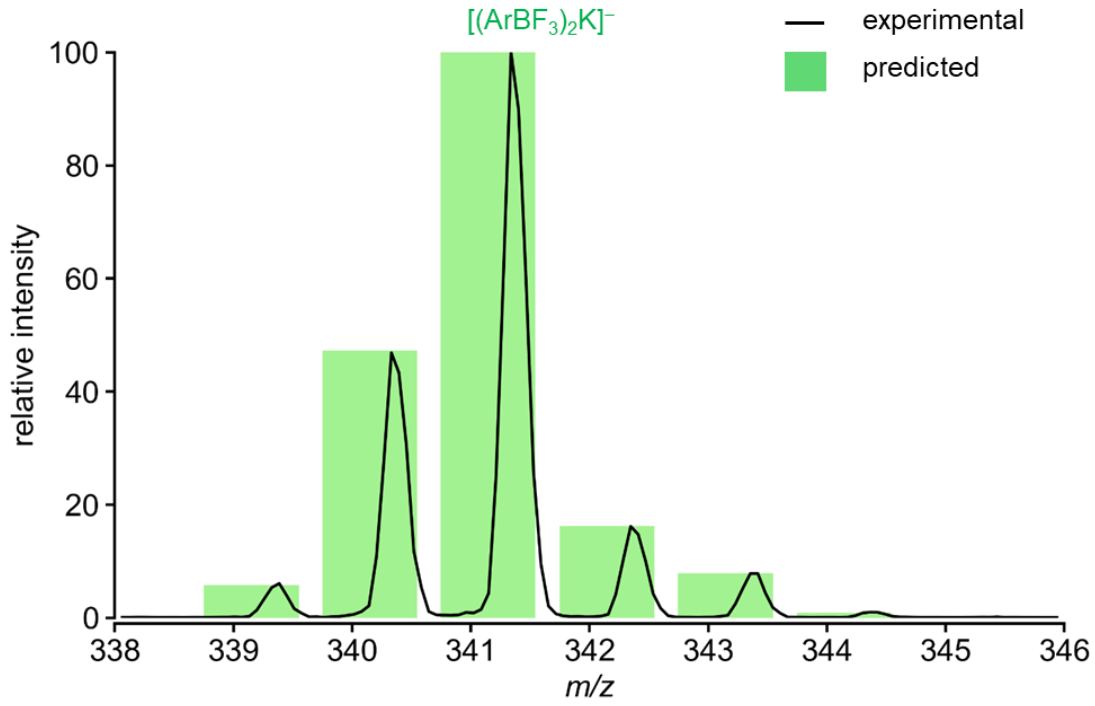

Figure D.28. Overlaid predicted isotope pattern on the experimental isotope pattern for $[(ArBF_3)_2K]^-$ (green). Species is from hydrolysis of potassium cyclohexyltrifluoroborate in THF/H_2O.

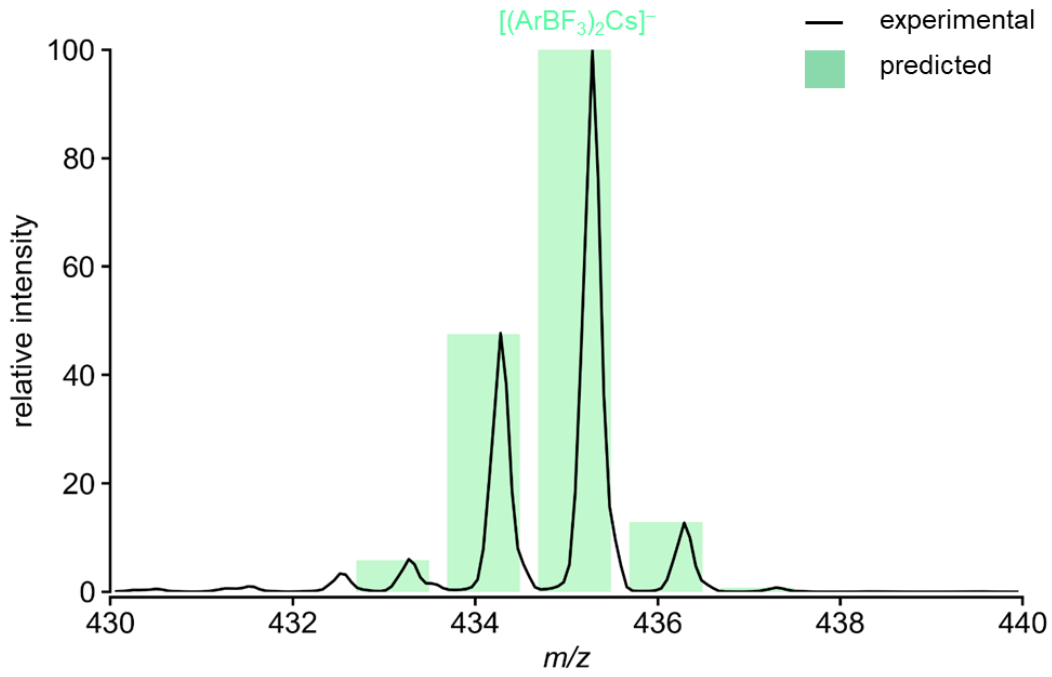

Figure D.29. Overlaid predicted isotope pattern on the experimental isotope pattern for $[(ArBF_3)_2Cs]^-$ (green). Species is from hydrolysis of potassium cyclohexyltrifluoroborate in THF/H_2O.

Section D5. ESI-MS/MS of aggregate species

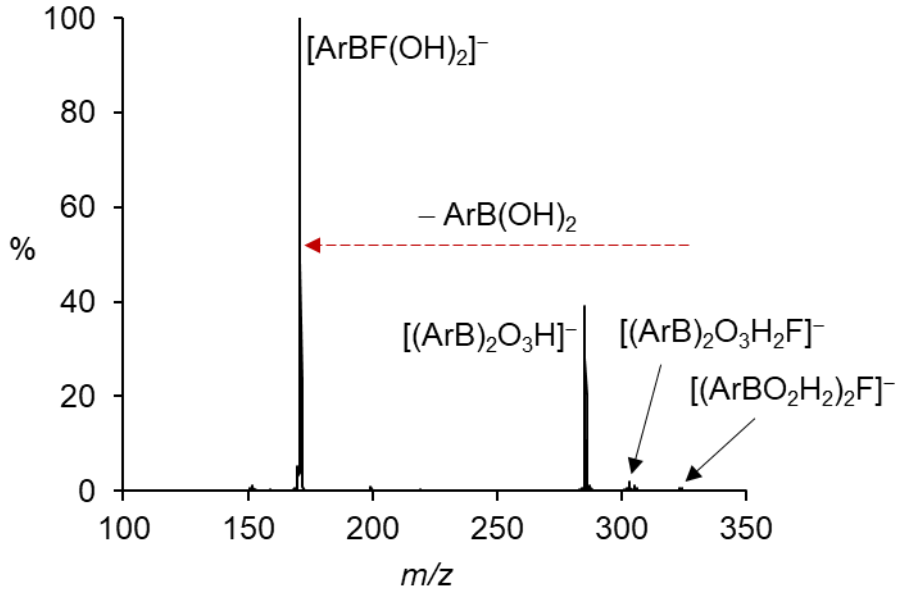

Figure D.30. MS/MS product ion spectrum of $[(ArBO_2H_2)_2F]^-$ (mixed dimer) from hydrolysis of potassium p-methoxyphenyltrifluoroborate substrate. Mixed dimer comprises: $[ArBF(OH)_2]^-$ and $ArB(OH)_2$ (neutral species, not observed).

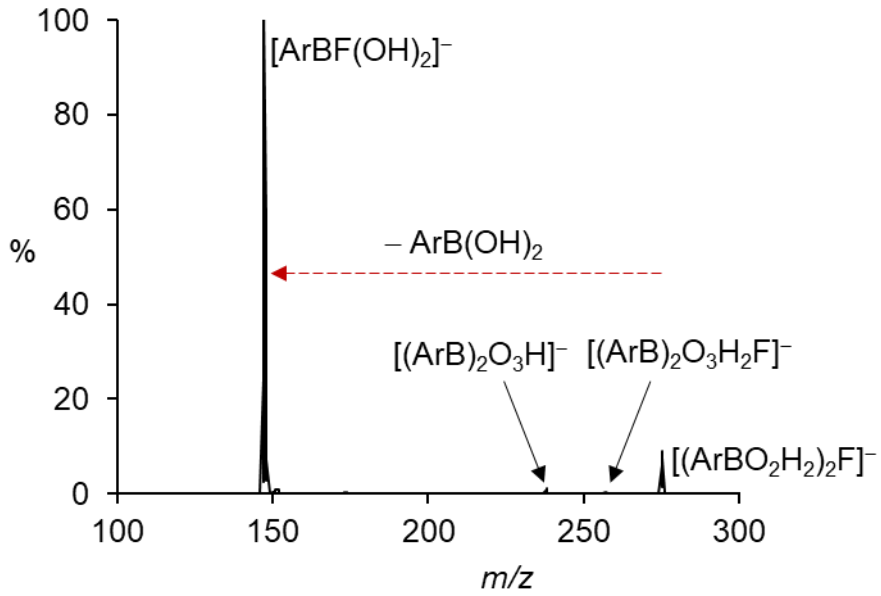

Figure D.31. MS/MS product ion spectrum of $[(ArBO_2H_2)_2F]^-$ (mixed dimer) from hydrolysis of potassium cyclohexyltrifluoroborate substrate. Mixed dimer comprises: $[ArBF(OH)_2]^-$ and $ArB(OH)_2$ (neutral species, not observed).

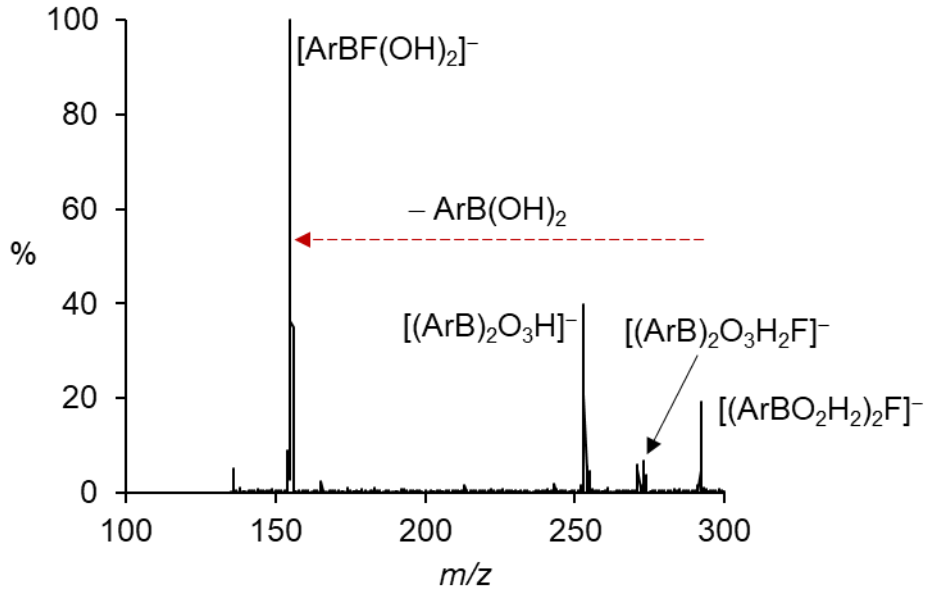

Figure D.32. MS/MS product ion spectrum of $[(ArBO_2H_2)_2F]^-$ (mixed dimer) from hydrolysis of potassium p-tolyltrifluoroborate substrate. Mixed dimer comprises: $[ArBF(OH)_2]^-$ and $ArB(OH)_2$ (neutral species, not observed).